

Simulations of solutal Marangoni convection in two liquid layers: complex and transient patterns

Dissertation

zur Erlangung des akademischen Grades

**Doktoringenieur
(Dr.-Ing.)**

vorgelegt der
Fakultät für Maschinenbau der
Technischen Universität Ilmenau

von Herrn

M.Sc. Thomas Köllner

geboren am 03.01.1986 in Rudolstadt/Deutschland

Erster Gutachter:	Priv.-Doz. Dr. Thomas Boeck
Zweiter Gutachter:	apl. Prof. Dr.-Ing. habil. Christian Karcher
Dritter Gutachter:	Prof. Dr. Michael Bestehorn
Tag der Einreichung:	06.07.2015
Tag der mündlichen Prüfung:	11.11.2015

urn:nbn:de:gbv:ilm1-2015000626

Zusammenfassung

Stofftransport über die Grenzfläche zwischen nicht mischbarer Flüssigkeiten ist in der Lage Konvektion durch Dichtegradienten (Rayleigh-Konvektion) oder Gradienten in der Grenzflächenspannung (Marangoni-Konvektion) zu erzeugen. Direkte numerische Simulationen eines Zweischichtsystems wurden durchgeführt, um zwei klassische Experimente aus diesem Bereich zu reproduzieren und zu erklären.

Dazu wurden die Navier-Stokes-Boussinesq- und die Transportgleichung für einen gelösten Stoff in zwei, durch eine ebene Grenzfläche gekoppelten Schichten, für all drei Raumdimensionen gelöst. Eine Pseudo-Spektral-Methode wurde zur numerischen Lösung der Gleichungen eingesetzt, wobei Fourier-Moden in beiden horizontalen Richtungen und Chebyshev-Moden in der vertikalen Richtung eingesetzt wurden. Der anfänglich nur in einer Phase gelöste Stoff diffundiert in die andere Phase, welches im Laufe des Stofftransportes Konvektion auslöst. Zwei unterschiedliche Stoffsysteme wurden simuliert, zuerst das ternäre Gemisch aus Cyclohexanol, Wasser und Butanol. Dabei ist Butanol zu Beginn nur in der oberen organischen Phase gelöst. Da Butanol die Grenzflächenspannung sowie Dichte verringert, entsteht Marangoni-Konvektion mit einer stabilisierenden Dichteschichtung. Die durchgeführten Simulationen reproduzierten erfolgreich die experimentell bekannten mehrskaligen Strömungsmuster. Eine zweistufige Hierarchie von Konvektionszellen wurde beobachtet: große, langsam wachsende Zellen, welche kleinere, stetig bewegte Zellen einschließen. Die Ursache für den Musteraufbau wurde durch zwei Mechanismen, Vergrößerung und eine lokale Instabilität, erklärt. Die zeitliche Entwicklung der Muster wurde mit zwei unabhängigen Experimenten aus der Literatur verglichen. Dazu wurden Längenskalen und der optische Fluss aus Schlierenbildern abgeleitet. Neben einer guten qualitativen Übereinstimmung erschienen jedoch Simulationen verlangsamt im Vergleich mit den Experimenten. Parameterstudien zeigten, dass Konzentrationsänderungen von Butanol teilweise durch eine Reskalierung von Länge und Zeit berücksichtigt werden können.

Bei dem zweiten Stoffsystem wurde die Übergangskomponente durch Isopropanol ersetzt (ähnliche Eigenschaften wie Butanol) und nun in der unteren wässrigen Phase gelöst. Hierfür konnten Simulationen die experimentell beobachteten Strukturen (Eruptionen) reproduzieren und deren Ursprung durch die Wechselwirkung von Rayleigh- und Marangoni-Konvektion erklären. Ein Vergleich mit experimentellen Ergebnissen zeigte eine gute qualitative Übereinstimmung, jedoch waren auch hier die experimentell ermittelten Geschwindigkeiten höher. Parameterstudien ergaben, dass Variationen in der Ausgangskonzentration teilweise durch eine Reskalierung der Zeit berücksichtigt werden können.

Abstract

Mass transfer through the interface between immiscible liquids potentially causes convection by interfacial tension gradients (Marangoni convection) and by density differences (Rayleigh convection). Three-dimensional direct numerical simulations of two liquid layers were carried out to explain and to firstly reproduce classical experimental observations of Marangoni convection. The Navier-Stokes-Boussinesq equations were solved with a plane interface that couples layers. A pseudospectral-numerical method was employed with Fourier-modes in both horizontal directions and Chebyshev modes for the vertical direction. Initially, the solute is dissolved only in one of the quiescent, equally sized layers. As it starts to diffuse in the other layer convection is triggered.

Two kinds of mass-transfer systems were simulated: First, the ternary system made of cyclohexanol, water and butanol, which is initially dissolved in the lighter organic phase. Since butanol lowers interfacial tension as well as density, Marangoni convection under a stabilizing density stratification evolves. Simulations successfully reproduce multiscale flow patterns that were reported by experiments. Especially, we observe a two-level hierarchy of convection cells that consist of large, slowly growing cells that host smaller, rapidly changing cells. These multiscale patterns are explained by the action of coarsening and a local instability. The temporal development was compared to two independent experiments from literature by measuring length scales and the optical flow of shadowgraph images. Overall, experiments qualitatively agree but appeared accelerated in time versus simulations. Parametric studies revealed that the concentration changes of butanol can be partly accounted for by a scale transformation.

For a second configuration, the transferred solute is changed to isopropanol (similar properties as butanol) and now dissolved in the lower aqueous phase. Former experimental observation of structures called eruptions could be reproduced, and their origin was explained by the coupling of Rayleigh and Marangoni convection. A comparison with recent experimental results showed a good qualitative agreement, but experimentally measured velocity appeared roughly twice as high as the simulated ones. Parametric studies showed that variations in initial concentration could be partly accounted for by another scale transformation.

Contents

1	Introduction	1
2	Solutal Marangoni convection in two-layer systems	3
2.1	Literature review on Marangoni convection	3
2.2	Mass transfer between plane layers: paradigmatic system	7
2.3	Mechanisms of convection	10
2.4	Pattern formation during mass transfer	12
2.4.1	Marangoni convection with stable density stratification	12
2.4.2	Rayleigh-Marangoni convection	15
3	Theoretical analysis	18
3.1	Nondimensionalization and scale invariance	18
3.1.1	Marangoni scaling	20
3.1.2	Viscous scaling	22
3.1.3	Diffusive scaling	23
3.2	Symmetry of motion for Stokes flow	25
3.3	Equilibration under pure diffusion	26
3.4	Neutral linear stability for the pure Marangoni case	29
3.4.1	Steady basic state	31
3.4.2	Non-linear basic state: frozen time analysis	32
3.5	Application of linear theory	35
3.6	Conclusion	38
4	Numerical methods	40
4.1	Pressure-free formulation	40
4.2	Discretization of the governing equations	42
4.3	Application of boundary and matching conditions	45
4.4	Workflow	48
5	Results on Marangoni convection with stable density stratification	49
5.1	Cyclohexanol-water-butanol system	50
5.1.1	Physical modeling	50
5.1.2	Sample configurations	54
5.2	Marangoni convection in the reference configuration	55
5.2.1	Overview	55
5.2.2	States of convection: onset	63
5.2.3	States of convection: growth and saturation of initial ROs	66

5.2.4	States of convection: hierarchical patterns	68
5.3	Comparison of simulations with experiments	71
5.3.1	Experimental procedure	72
5.3.2	Qualitative comparison	73
5.3.3	Horizontal size of RC-Is	73
5.3.4	Horizontal size of RC-IIs	77
5.3.5	Optical flow	78
5.4	Discussion: mechanism of multiscale structures	82
5.4.1	Coarsening of hierarchical pattern: general properties	82
5.4.2	Coarsening of hierarchical pattern: vertical length scales	83
5.4.3	Substructuring of hierarchical pattern	85
5.5	Role of gravity and geometrical constraints	88
5.5.1	Impact of density stratification	88
5.5.2	Impact of geometrical constraints	91
5.6	Two-dimensional geometry	95
5.7	Discussion and conclusion	98
6	Marangoni convection in a HS cell	101
6.1	Methods	102
6.1.1	Experiments	102
6.1.2	Theoretical Hele-Shaw model	103
6.1.3	Discussion of the Hele-Shaw model	104
6.2	Results	107
6.2.1	<i>Thin</i> and <i>vertically</i> oriented Hele-Shaw cell	107
6.2.2	<i>Thin</i> and <i>horizontally</i> oriented Hele-Shaw cell	108
6.2.3	<i>Thick</i> and <i>vertically</i> oriented Hele-Shaw cell	109
6.2.4	<i>Thick</i> and <i>horizontally</i> oriented Hele-Shaw cell	110
6.3	Density convection in horizontal orientation	111
6.4	Discussion and conclusion	113
7	Results on Rayleigh-Marangoni convection	115
7.1	Introduction	115
7.2	Sample configurations	116
7.3	Rayleigh-Marangoni convection in the reference configuration	121
7.3.1	Early phase of convection	121
7.3.2	Onset time and onset wavenumbers	125
7.3.3	Long term evolution	127
7.4	Comparison to experiments	131
7.4.1	Typical patterns	131
7.4.2	Quantitative comparison - optical flow	135
7.5	Parametric study	138
7.5.1	Variation of concentration	138
7.5.2	Pure Rayleigh convection	139
7.5.3	Two-dimensional simulations	144
7.6	Discussion	144
7.6.1	Onset of convection	144
7.6.2	Mechanism of eruptions	147

7.6.3	Reproduction of experiments	147
7.7	Conclusion	150
8	Conclusion and Recommendations	152
A	Thermal model	156
B	Material properties	158
B.1	Water-cyclohexanol-butanol system	158
B.2	Water-cyclohexanol-isopropanol system	160
C	Kinetic energy balance	164
D	Supplementary numerical results	167
D.1	Marangoni convection	167
D.2	Rayleigh-Marangoni convection	169
E	Image processing	171
	Bibliography	173
	List of Symbols	186
	Danksagung	189

Chapter 1

Introduction

The transfer of substances between two liquid phases occurs in numerous of natural as well as technological processes. E.g., when Champagne is uncorked [136], supersaturated CO_2 is released to the ambient air while producing the well-known bubbling. Many industrial processes involve solvent extraction [85] that relies on the solute's relative solubility between phases and has specific applications in the fields of hydrometallurgy, pharmacy, petrochemistry and wastewater treatment [108].

The theoretical description of such *mass transfer* processes involves various physical phenomena [25] (e.g. chemical reaction, mixing, hydrodynamic instabilities, the heat of solution, adsorption of surfactants, electromagnetic effects, emulsification, solubilization). Understanding these phenomena and their coupling are crucial for the design of unit operations system and the development of novel processes.

The present thesis is dedicated to such a transport phenomenon, namely, the convection due to gradients in interfacial tension, which is known as solutal *Marangoni convection*.

The physics of interfaces deals with all sorts of phenomena that are related to the common boundary between two different phases of matter, such as solid/liquid, liquid/liquid or liquid/gas. The main macroscopic mechanical property of an interface is its *interfacial tension* [69] – like the pressure is for the ambient air. It represents the force per unit length normal to a "virtual" cut through the interface. Microscopically, it is attributed to the unbalanced molecular attraction that tends to pull molecules into the interior of a phase [189]. The consequences of interfacial tension^I (known as capillary phenomena) are readily observed by the peculiar shape of liquid interfaces from drops or soap films [74].

The theoretical connection between gradients in interfacial tension (due to inhomogeneities in composition or temperature) and observable motions near the interface was made (more or less independently) by three people: Thomson (1855), Van der Mensbrugghe (1869) and Marangoni (1871) (cf. Ref. [203]) by the analysis of experiments. However, Marangoni was primarily credited for this by the scientific community. Nowadays, several thousands of scientific publications (more than three thousand include "Marangoni" in their title) deal with all kinds of questions related to Marangoni convection. An important, canonical problem

^IThe interface between a condensed phase and non-condensed (e.g. water/air) is in particular called surface and consequently it possesses a surface tension.

was established by Sternling & Scriven in 1959 [219]; they were able to predict under which circumstances Marangoni convection can be expected when a solute is transported from one immiscible phase to another. This fostered several experimental works, e.g. Refs. [143, 166], which confirmed the theoretical predictions of Sternling & Scriven but also showed that even in a careful experiment, very complex, transient convective patterns arise, which could not be reproduced by the mathematical methods at that time. And even fifty years later many of those – now classical – observations still lack a numerical study.

This thesis endeavors to reproduce such experiments of solutal Marangoni convection in their fully transient, three-dimensional continuum-mechanical description by means of numerical simulation. Specifically, two different material systems are examined, which showed rather different convective structures [197]: (1) The transport of butanol from a cyclohexanol-rich into a water-rich phase, showing *hierarchical patterns* of Marangoni cells [197, 198], which were attributed to the stationary Marangoni instability according to the theory of Sterling & Scriven. (2) The transport of isopropanol from an aqueous to a cyclohexanol-rich phase, exhibiting *eruptions*, which were attributed to the interplay between buoyant convection and the Marangoni effect.

The scientific value of the following theoretical study is twofold. (1) The used models are probed whether they are able to reproduce the experimental observation or not, which may lead to a refined theoretical description afterward. (2) Experimental observations of Marangoni convection are usually limited to a few physical properties, whereas simulations include detailed knowledge of all physical properties from the supposed model. This complete knowledge in turn leads to a better picture of the involved physical mechanisms.

This dissertation consists of eight chapters. Ch. 2 reviews the key literature relevant to the stated issues and introduces the paradigmatic model, used to describe mass-transfer experiments. It also reviews those two sample systems that are studied subsequently and formulates the detailed aims of this thesis. Chapter 3 derives general conclusions from the paradigmatic model and treats the stability of solute diffusion perturbed by Marangoni convection. The methods employed for numerical simulations are described in Ch. 4. The results of numerical simulations and their comparison to experimental observation is presented and discussed in Chs. 5-7. Especially, the case when stationary Marangoni instability is prevailing is treated: at an extended interface in Ch. 5 and inside a Hele-Shaw cell in Ch. 6. Chapter 7 treats a case where buoyant convection is the prevailing source for convection. Finally, conclusion and recommendations for further work are outlined in Ch. 8.

Chapter 2

Solutal Marangoni convection in two-layer systems

2.1 Literature review on Marangoni convection

The modern, academic research on interfacial tension driven flows dates back to Thompson in 1855 [229], who suggested surface tension gradients as the source for convective patterns in drops at an alcohol-water interface. However, it was Carlo Marangoni(1871) [153], who has been credited for his experiments and their interpretation in terms of surface-tension-driven flows.

In the first half of the 20th century numerous experiments [125, 148] were carried out related to the action of Marangoni convection – see excellent review of Scriven & Sternling [203] from 1960 or Ref. [188]. A distinctly influential study – viewed from the perspective of hydrodynamics – was provided by the seminal work of Bénard [16]. He observed highly regular patterns of convection cells that were caused by a steady temperature gradient across a liquid layer. His work received significant attention since it was tractable for a quantitative, theoretical description, which was initiated by Rayleigh(1916) [182]. Rayleigh attempted to explain Bénard’s cells by solving linearized model equations, which describe the onset of buoyancy driven flow from a quiescent state of steady heat conduction. Rayleigh showed that convection could be expected when the nondimensional group

$$Ra = \frac{\Delta\rho g L^3}{\mu\kappa}, \quad (2.1)$$

(the Rayleigh number) exceeds a certain value depending on the boundary conditions. The Rayleigh number compares the density difference $\Delta\rho$ between top and bottom owing to a temperature difference (density should be lower at the bottom for convection), gravitational acceleration g , the height of the layer L with the dynamic viscosity μ and the thermal diffusivity κ .

Roughly, forty years later in 1958, Pearson [172] published a pioneering work that also treated Bénard’s problem. He also analyzed the steady heat transfer state – similar to Rayleigh [182] – but now included that interfacial tension depends on the temperature but disregarded the variation of density. Observation of drying films of paint drew his attention to the fact that no matter what orientation the film possessed against gravitational acceleration,

patterns of convection were observed – which was in contrast to the buoyancy based model by Rayleigh [182].

By this, Pearson showed that the steady state of heat conduction is also unstable if the dimensionless parameter Ma , defined by

$$Ma = \frac{\Delta\sigma L}{\mu\kappa}, \quad (2.2)$$

exceeds a critical positive value, e.g. $Ma_{crit} \approx 80$ (for an isothermal, no-slip bottom and a "insulating", stress-free surface) with critical a wavelength $\lambda \approx 2\pi L/2$ of sinusoidal perturbations. The non-dimensional group Ma is called the Marangoni number; it expresses the relative importance of the characteristic surface tension difference $\Delta\sigma$ to opposing viscous forces. The effect that surface tension changes by temperature gradients is also known as *thermocapillarity*. A sound physical introduction to Marangoni convection is given in Sec. 2.3

Motivated by experimental observations on spontaneous interfacial motions during mass transfer [122, 133, 137, 207, 213], Sternling & Scriven [219] tackled the mass-transfer analog of Pearson's problem in a similarly important paper in 1959. They analyzed the linear stability of diffusive solute transfer through the interface of two semi-infinite layers. They predicted that stationary and oscillatory types of motion might appear depending on: the Marangoni number, the ratios of viscosity and diffusivities between layers as well as the direction of transport. Their analysis showed great success in explaining the onset of convection during mass transfer up to excluded physical effect such as: adsorption of surfactants, heat of solution, deformable interfaces or buoyant effect – which were treated by other authors later following their example.

Another important theoretical work was provided by Nield [165] in 1964. He solved the mathematical problem of Rayleigh and Pearson (single layer) with both effects acting in parallel, using the help of a digital computer. He showed that the marginal Marangoni and Rayleigh number (i.e. the threshold for onset of convection) are now coupled by the approximate formula

$$Ra/Ra_c + Ma/Ma_c = 1, \quad (2.3)$$

where Ra_c and Ma_c are the values with the other effect respectively excluded, e.g. $Ra_c \approx 669$, $Ma_{crit} \approx 80$. Later, Palmer & Berg (1971) [169] confirmed this with convection experiments using silicone oil. Then at the beginning of the Sixties, investigations of surface tension driven phenomena branched, i.e. becoming more and more specialized.

One direction was the fundamental visual observation of convective patterns during the transfer of a solute through a plane interface [9, 78, 141, 143, 143, 166, 197, 198], in the spirit of Bénard's experiments. However, in contrast to Bénard's thermal set up, mass transfer appeared more involved. A complete experimental and theoretical description could not be obtained due to the time-dependent, multiscale and irregular structures.

Several reason for the increased difficulty – compared to the thermal setup – can be noted: (1) Observed patterns are usually time-dependent since only a limited amount of solute can be transfer with a usual experimental setup – which is in contrast to the thermal setup where a steady supply of heat could be maintained without mechanical disturbance of the system. (2) In systems composed of two *liquid* layers, usually, the transport properties of both phases have to be accounted for in detail, which consequently extends the set of free parameters of a theoretical model. (3) Solute transfer inherently implies phase change

effects, making experiments more demanding and theoretical modeling more uncertain. (4) The change of interfacial tension by solute concentration is usually much higher than by temperature variation, which leads to increased nonlinearity and therefore to more complex dynamics.

The present work will study this issues from the theoretical point of view since nowadays scientific methods – especially computing resources – are available to simulate these time-dependent three-dimensional processes in detail. Before concentrating on the principal topic of this thesis in Secs. 2.2-2.4, the general review on solutal Marangoni convection is continued by further addressing some new important subtopics.

The oscillatory mode of solutal Marangoni instability, predicted by Sternling & Scriven, was first detected by Linde and coworkers in the 1960s [139, 140, 145, 198]. Single capillary waves sustained by Marangoni convection are triggered when a gas/liquid system is heated from the air side (if the kinematic viscosity of the air is higher) or for example if acetone is adsorbed from air into water. The complex patterns observed could be traced back essentially to the interaction of three dominant wave types [50, 76, 147, 162, 163, 183].

Many efforts [22, 23, 30, 54, 66, 115, 194, 226] have been undertaken – rather successfully – to describe polygonal convection patterns in the classical setup of Bénard, i.e. the transport of heat trough a liquid layer into the ambient air – referred as *Bénard-Marangoni convection*. Also, the thermal problem of two liquid layers between isothermal solids has been studied experimentally [100, 230] and theoretical [29, 72, 99] see [164] for further references. Furthermore, thermal Marangoni convection has been studied for temperature gradient applied parallel to the interface [56], especially in liquid bridges [124, 232] which appear in applications of crystal growth.

Heat of solution: The transfer of solute – i.e. a solution in one phase and dissolution in the other – between phases is accompanied by the release or consumption of latent heat. This was studied experimentally [87, 158, 174, 244] and theoretically [58, 90, 173, 216]. Generally, it was found that heat release can trigger Marangoni instability [173] as well as a Rayleigh instability. However, in ternary systems the impact of temperature variation on interfacial tension was experimentally assessed as insignificant [87] compared to the compositional impact for a large number of material systems (mainly mixtures of organic liquids and water).

The coupling between the thermal and the solutal Marangoni effect is of peculiar importance in liquid/gas system, in particular where *evaporation* or *condensation* takes place. Berg *et al.* [19] outstandingly demonstrated the influence of Marangoni convection for evaporating liquids with and without surface active agents (*surfactants*). The convection patterns were only sustained in thicker layers (those were attributed to buoyant convection) when the interface was contaminated with surfactants. Thereafter, numerous works dealt with related topics, e.g.: Marangoni instability in evaporating droplets [5, 34, 60, 150], theoretical works in layered systems with evaporation [33, 159, 231], experimental observations of interesting circular patterns during evaporation of binary mixture [247], uneven drying of thin films [242], onset of convection in drying polymer solution [62], Marangoni patterns during the evaporation of a planar liquid layer of hydrofluoroethers [46, 49].

Generally, Marangoni convection at dispersed, pendant or sessile *droplets* is an active and broad field of research. Especially, the motion of drops on solid substrates poses an extra difficulty due to the physics of triple line motion [211]. Some examples of recent studies are self-propulsion of liquid droplets [109, 243], spreading and dissolving droplets [21, 131, 177] and Marangoni induced agitation [79]. Moreover, computer simulations of evaporating pinned ses-

sile water droplets of submicrometer size [204] have shown that the thermal Marangoni flow loses its importance for very small droplets with diameters $L \leq 10^{-5}$ m. The coalescence of neighboring sessile droplets of different but miscible liquids is suppressed by a Marangoni flow [35, 102, 103]. Wegner performed extensive studies (experimental and numerical) on mass transfer at single dispersed, rising drops [71, 234–236, 238] showing how the Marangoni effect influences mass transfer and motion.

Interfaces often contain traces of *surfactants* [63]; sometimes roughly labeled as contaminants. Surfactants have a high technological relevance in all branches of chemical engineering as: emulsifier, dispersants, foaming agents, detergents, wetting agents [17]. Their special physical properties result from their adsorption at interfaces, by this, very small amounts can alter interfacial tension significantly [63]. Although, the effect of interfacial adsorption is out of the scope of our following theoretical studies, we will include this important class of substances in our review.

The adsorption of surfactants causes a new dynamical effect: When, for any reason, an interface expands locally, interfacial surfactant concentration Γ (in mol/m²) locally decreases. This concentration gradients cause an interfacial tension gradient opposite to the initial expansion and consequently damps the motion. This effect has been referred to as *Gibbs elasticity*, or more appropriately, as the *Plateau-Marangoni-Gibbs* effect [203].

Numerous studies addressed the effect of adsorbed surfactants on convection, of which Berg and Acrivos [18] provided a theoretical explanation by extending Pearsons model by an insoluble surfactant. They demonstrated that the Plateau-Marangoni-Gibbs effect may increase the critical Marangoni number thousand-fold. This fact makes experiments with free water surfaces (since they have high surface tension) very demanding by means of purifying components since very small amounts of contamination may cause this effects.

The transport of a soluble surfactant was considered by linear stability analysis [39, 89, 214]. In particular, the linear stability analysis (for stationary Marangoni instability) [214] showed that a second threshold for the smallest amplifiable wavelength appears, which is (beside other quantities) proportional to the square root of the *Gibbs length* δ_G , i.e. $\lambda_{min} \propto \sqrt{\delta_G}$. The Gibbs length is the thickness of a virtual layer that contains as much of the surfactant as is adsorbed $\delta_G = \Gamma/c$ (here c means the bulk concentration at the interface).

Recently, periodic non-linear oscillations of interfacial tension were measured during mass transfer of typical surfactants in a liquid-liquid system with plane interface. Namely, in the system *water/dichloromethane* with CTAB as diffusing species [129], here, the system alternates between phases of strong convection with simultaneously low interfacial tension and phases of weak convection with high interfacial tension. Experiments in *heptane/water* with oxyethylated alcohols [121] showed that for a given experimental geometry the occurrence of periodic oscillation vitally depends on the used surfactants and their initial concentration, especially a partition coefficient near unity was mentioned as requirement for oscillations. Corresponding numerical simulations of a simplified model system [121] showed an explanation. In this study, a single convection cell covered the whole interface, which is suddenly increasing in strength. Further experimental studies [223] in the same system *heptane/water* with oxyethylated alcohols as diffusing species discussed the influence of the surfactant properties on the occurrence of the periodic oscillation, e.g. the critical micelle concentration and the partition coefficient.

Periodic decay and re-amplification of Marangoni convection was also observed for a point-like source of surfactant located under an air-liquid interface. There, a flow was caused by the

combined action of adsorption-desorption kinetics and geometric confinement [117–120]. In further studies, the interaction of Marangoni convection and buoyancy-driven convection led to oscillations of an organic drop, which was placed in an aqueous surfactant solution with vertical concentration gradient [116].

Recently, the coupling between *chemical reactions* and Marangoni convection – via production of heat or surface active products – has received considerable attention [6, 59, 67, 149, 187, 199]. For instance, the shape of propagating autocatalytic reaction fronts [186], front velocity [210] or the dissolution of alkyl formates in water with their subsequent hydrolysis has been studied [40].

Finally, let us note some studies with direct impact on *applications*. Besides the observation of fundamental processes, the description of the integral amount of transferred mass between phases – commonly noted as *mass transfer studies* – has a long history in chemical engineering for various configurations [10, 39, 78, 97, 138, 207, 237]. Especially, it is aimed at accelerating the rate of mass or heat transfer in different configuration: mass transfer enhancement due to the Marangoni effect in extraction [4, 10, 39, 97, 237], distillation [73, 181], efficiency of cooling devices [105, 106] or enhanced oil recovery by gas injection changing interfacial tension [221] [104]. Moreover, the occurrence of Marangoni effects in LiBr absorbers was observed [53, 93].

Another topic is the drying of lacquers or polymer solutions on which many industrial applications such as coating or printing are based on [24, 86, 94, 220]. The goal of a smooth surface finish is sometimes not achieved because the solvent evaporation can trigger Marangoni convection, which may in turn cause marked surface corrugations [14]. Moreover, the impact of Marangoni convection on the film thickness during wire coating was studied [167]. Another, related application is "Marangoni drying" that influences drying by contacting a thin film of water with a vapor of organic liquid [95, 154].

2.2 Mass transfer between plane layers: paradigmatic system

After broadly overviewing relevant studies on solutal Marangoni convection, this section will further pinpoint the objectives and defining the scope of this thesis by introducing our *paradigmatic theoretical model*. This model will be the basis of the numerical studies.

Fig. 2.1 shows the geometry of the paradigmatic model (PM). The system consist of two liquid phases (synonymously called layers), which are indicated by a number in brackets (1) and (2) for the bottom and top phase, receptively.¹ Each phase occupies a rectangular cuboid $\Omega^{(1)} = (0, L_x) \times (0, L_y) \times (-d^{(1)}, 0) \subset \mathbb{R}^3$ and $\Omega^{(2)} = (0, L_x) \times (0, L_y) \times (0, d^{(2)}) \subset \mathbb{R}^3$, whose extent is taken as time *independent*. These cuboids are separated by the *interface* $\Omega^{(s)} = (0, L_x) \times (0, L_y) \times \{0\} \subset \mathbb{R}^3$, thus the interface is *plane* and *undeformable*, consequently. Usually the layer heights are taken as equal, i.e. $d^{(1)} = d^{(2)}$. The spatial domain Ω of the system is the union of the layers and the interface $\Omega = \Omega^{(1)} \cup \Omega^{(2)} \cup \Omega^{(s)}$.

Both layers consist of a fluid with a potentially dissolved solute. The amount of solute is described by the field of molar concentration $c^{(i)}(\mathbf{x}, t)$ at the point $\mathbf{x} = (x, y, z) \in \Omega$ and time $t \in \mathbb{R}^+$. The fluid moves with the mass averaged velocity $\mathbf{u}^{(i)}(\mathbf{x}, t)$ and its dynamic pressure is $p_d(\mathbf{x}, t)$. The fluid's mass density $\rho^{(i)}$ is assumed to depend linearly on solute concentration

$$\rho^{(i)} = \rho_{ref}^{(i)} + \rho_{ref}^{(i)} \beta_c^{(i)} c^{(i)}, \quad (2.4)$$

¹The notion of "top" and "bottom" displays that the acceleration of gravity acts against the z-direction

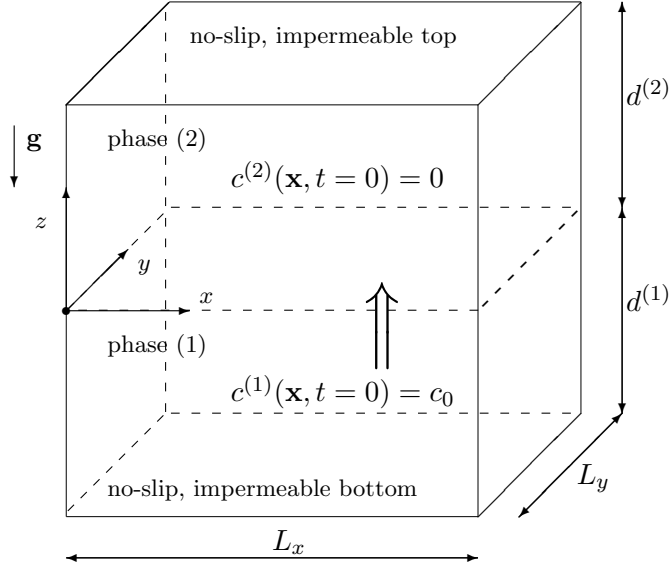


Figure 2.1: Sketch of the two-layer-mass-transfer system.

where $\beta_c^{(i)}$ is the solutal expansion coefficient and $\rho_{ref}^{(i)}$ is the reference density (the one without solute), each in layer (i) respectively. Furthermore, we assume that layers are stable stratified, $\rho^{(2)} < \rho^{(1)}$, which is crucial for the assumption that the interface is plane.^{II} A second material law is that interfacial tension σ depends linearly on solute concentrations

$$\sigma = \sigma_{ref} + \sigma_{ref} \alpha_c c^{(1)} \quad \text{for } z = 0, \quad (2.5)$$

where α_c is the solutal interfacial tension coefficient and σ_{ref} the reference interfacial tension (without solute). In literature, it is widely customary to change signs in the material laws, e.g. writing " $\sigma = \sigma_{ref} - \sigma_{ref} \alpha_c c^{(1)}$ " if $\alpha_c < 0$. This custom is not followed in this work since interfacial tension may also rise for certain solutes (although $\alpha_c < 0$ is more common) and for the density dependence on solute both signs are equally observed.

The fluid motion and the distribution of solute obey the following equations

$$\partial_t \mathbf{u}^{(i)} + \mathbf{u}^{(i)} \cdot \nabla \mathbf{u}^{(i)} = - \frac{\nabla p_d^{(i)}}{\rho_{ref}^{(i)}} + \nu^{(i)} \Delta \mathbf{u}^{(i)} + c^{(i)} \beta_c^{(i)} \mathbf{g} \quad \text{for } \mathbf{x} \in \Omega^{(i)}, \quad (2.6)$$

$$\nabla \cdot \mathbf{u}^{(i)} = 0 \quad \text{for } \mathbf{x} \in \Omega^{(i)}, \quad (2.7)$$

$$\partial_t c^{(i)} + \mathbf{u}^{(i)} \cdot \nabla c^{(i)} = D^{(i)} \Delta c^{(i)} \quad \text{for } \mathbf{x} \in \Omega^{(i)}. \quad (2.8)$$

Equation (2.6) is known as the Navier-Stokes-Boussinesq equation (NSB equation) describing transport of momentum in a Newtonian liquid, whereas density changes are only regarded in the buoyancy term $c^{(i)} \beta_c^{(i)} \mathbf{g}$. Equation (2.7) enforces the fluid being incompressible and Eq. (2.8) describes the transport of solute by advection $\mathbf{u}^{(i)} \cdot \nabla c^{(i)}$ and diffusion $D^{(i)} \Delta c^{(i)}$.

^{II}Consult Smith [217] for condition to apply the plane layer model, which is usually a good approximation for deep layers; moreover see discussion in Ref. [164] that qualifies the plane interface assumption as essential for the framework of Boussinesq approximation in the present context of natural convection.

Transport parameter appearing in Eqs. (2.6-2.8) are kinematic viscosity $\nu^{(i)}$ and the diffusivity of the solute $D^{(i)}$. These are constant in each layer but usually differ between layers. Note that "(i)" is just a dummy index that takes values of $i \in \{1, 2\}$.

Both layers are coupled at the plane interface ($z = 0$) through the *matching conditions*:

$$u_x^{(1)} = u_x^{(2)}, \quad u_y^{(1)} = u_y^{(2)}, \quad (2.9)$$

$$u_z^{(1)} = u_z^{(2)} = 0, \quad (2.10)$$

$$D^{(1)}\partial_z c^{(1)} = D^{(2)}\partial_z c^{(2)}, \quad (2.11)$$

$$c^{(1)}H = c^{(2)}, \quad (2.12)$$

$$\sigma_{ref}\alpha_c\partial_x c^{(1)} = -\mu^{(2)}\partial_z u_x^{(2)} + \mu^{(1)}\partial_z u_x^{(1)}, \quad (2.13)$$

$$\sigma_{ref}\alpha_c\partial_y c^{(1)} = -\mu^{(2)}\partial_z u_y^{(2)} + \mu^{(1)}\partial_z u_y^{(1)}. \quad (2.14)$$

These relations enforce: the continuity of velocity at the interface (2.9), the assumption of a plane, undeformable interface (2.10), the continuity of solute flux through the interface (2.11), Henry's model of partitioning (2.12) (by means of the partitioning constant H – also called Henry's constant) and the balance of tangential stresses (by means of dynamic viscosity $\mu^{(i)} = \nu^{(i)}\rho_{ref}^{(i)}$) between layers with interfacial tension gradients (2.13),(2.14).

The velocity, the solute and the pressure are periodic at the boundary of the $x - y$ dimension, which reads as follows

$$\mathbf{u}^{(i)}(x + L_x, y, z, t) = \mathbf{u}^{(i)}(x, y, z, t), \quad \mathbf{u}^{(i)}(x, y + L_y, z, t) = \mathbf{u}^{(i)}(x, y, z, t), \quad (2.15)$$

$$c^{(i)}(x + L_x, y, z, t) = c^{(i)}(x, y, z, t), \quad c^{(i)}(x, y + L_y, z, t) = c^{(i)}(x, y, z, t), \quad (2.16)$$

$$p_d^{(i)}(x + L_x, y, z, t) = p_d^{(i)}(x, y, z, t), \quad p_d^{(i)}(x, y + L_y, z, t) = p_d^{(i)}(x, y, z, t), \quad (2.17)$$

with periodicity lengths L_x, L_y . At the bottom ($z = -d^{(1)}$) and the top ($z = d^{(2)}$), no-slip and impermeability is imposed by

$$\partial_z c^{(1)} = u_z^{(1)} = u_x^{(1)} = u_y^{(1)} = 0 \quad \text{for } z = -d^{(1)}, \quad (2.18)$$

$$\partial_z c^{(2)} = u_z^{(2)} = u_x^{(2)} = u_y^{(2)} = 0 \quad \text{for } z = d^{(2)}. \quad (2.19)$$

These kinds of models are heavily used in the field of fluid mechanics, describing mass transfer, furthermore, they are the classical conceptual framework of solutal Marangoni convection [25, 164, 219]. For a discussion of the physical basis and the inherent assumption of the presented model equations consult Refs. [50, 164]. In general, the model rests on the theory of classical continuum mechanics (especially in the connection with interfaces see [69] and on linear non-equilibrium thermodynamics [15, 57]).

In this thesis, we are concerned with two initial states. First, solute initially dissolved in layer (1),

$$\mathbf{u}^{(1)} = \mathbf{u}^{(2)} = 0 + \mathcal{N}(\mathbf{x}), \quad (2.20)$$

$$c^{(1)} = c_0, \quad c^{(2)} = 0, \quad (2.21)$$

with concentration c_0 , thus, transport from bottom to top (1) \rightarrow (2). This situation is depicted in Fig. 2.1. Second, just the reversed transport direction (2) \rightarrow (1) is considered:

$$\mathbf{u}^{(1)} = \mathbf{u}^{(2)} = 0 + \mathcal{N}(\mathbf{x}), \quad (2.22)$$

$$c^{(1)} = 0, \quad c^{(2)} = c_0. \quad (2.23)$$

In order to trigger convection, the initial velocity fields is set to be nonzero by a sort of white noise $\mathcal{N}(\mathbf{x})$ ^{III}. In the following Eqs. (2.6)-(2.19) are referred to as the *paradigmatic model*, which is abbreviated as PM.

The same equations are able to describe the extensively studied thermal problem [50, 165, 172, 182, 217, 246], i.e. the model describing internal energy changes due to temperature gradients but with a uniform composition. In this case, the solutal properties can be bijectively identified by the thermal ones, e.g. the temperature $T^{(i)}$ is identified by the concentration $T^{(1)} \cong Hc^{(1)}, T^{(2)} \cong c^{(2)}$. This unique identification and the thermal equations are collected in App. A

The presented equations give rise to a semi-dynamical system since from a given initial state a unique state in the future is specified implicitly.^{IV} In this context, we introduce some further abbreviatory notion: The *state* of the system is denoted by a tuple X , composed of velocity and concentration fields in space (not in time)

$$X = [\mathbf{u}^{(1)}(\mathbf{x}), \mathbf{u}^{(2)}(\mathbf{x}), c^{(1)}(\mathbf{x}), c^{(2)}(\mathbf{x})], \quad (2.24)$$

which belongs to an abstract state space V [185]. Note that in the incompressible equation pressure p_d is uniquely determined by this state X (up to an additive constant). A state X given at $t_0 = 0$ is called *initial state* (or synonymously initial condition). Given a specific initial state X_0 , our paradigmatic model Eqs. (2.6)-(2.19) gives rise to a unique solution $X(t)$ with $X(0) = X_0$.

2.3 Mechanisms of convection

In this section, the different convection regimes that the PM is able to describe are categorized by their instability behavior. This and quoted experimental patterns prepare us to formulate the aims and scope of the present thesis in the subsequent Sec. 2.4.

Depending on the physical parameters, rather different material systems with various dynamics can be described. Nevertheless, they all share that solute spreads over both layers, which finally amounts to a *global equilibrium* with $c^{(1)} = 1/(H+1)$, $c^{(2)} = H/(H+1)$, $\mathbf{u}^{(i)} = 0$ (assuming that $D^{(i)} > 0$, $0 < H < \infty$ and $d^{(1)} = d^{(2)}$). The hydrodynamic processes in the "interim period" are governed by the action of gravitational acceleration (*Rayleigh effect*) and interfacial tension gradients (*Marangoni effect*), which are able to render the pure diffusional equilibration unstable, i.e. the system evolves in a state of *convection* $\mathbf{u}^{(i)} \neq 0$. Both sources for convection will be explained next.

In Fig. 2.2(a), a situation short after initialization is depicted. In this figure, dark color depicts a high concentration. Thus, a transport (2) \rightarrow (1) is shown. At the interface, a positive perturbation of solute concentration is considered. Furthermore, assume that solute decreases interfacial tension, $\alpha_c < 0$. Inevitably, interfacial tension gradients will create a flow

^{III}This is done since it is desired that those perturbations not introduce a "qualitative" impact on the dynamics, while the particular choice is detailed later.

^{IV} Here we assumed that this rather casually stated mathematical problem is well-posed. Surely, a rigorous mathematical treatment is needed to decide the well-posedness since the underlying function spaces had to be specified, which is not done here as common for the engineering mathematics. Moreover, the question of well-posedness of the Navier-Stokes equation is still an open problem [61, 185] for a general class of initial and boundary conditions

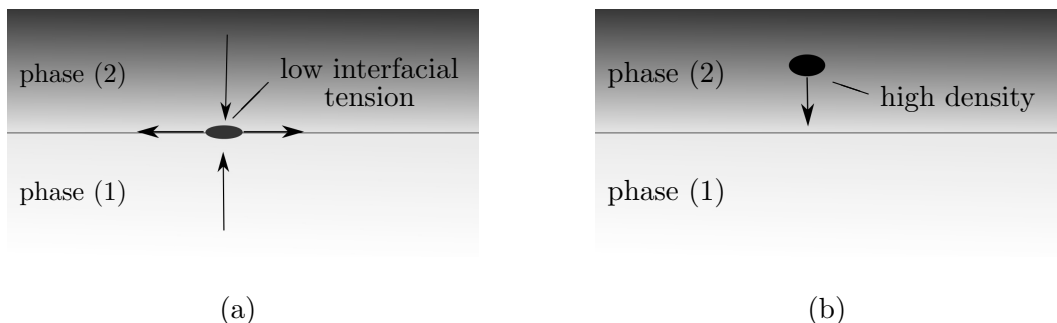


Figure 2.2: Sketch of Marangoni effect (a) and Rayleigh effect (b). Dark color depicts high concentration and arrows depict fluid motion. Solute increases density but lowers interfacial tension.

that spreads solute tangentially away from this initial variation [cf. "Marangoni condition" of Eq.(2.13)]. The ensuing flow carries fluid from the bulk to the interface. The flow can be considered symmetric to the interface if: vertical boundaries are far away, the ensuing flow is not strong (Stokes flow cf. Sec. 3.2), and density gradients can be neglected.^V

The subsequent impact on the interfacial concentration depends on the relative size of diffusivities – whether $D^{(1)} > D^{(2)}$ or $D^{(1)} < D^{(2)}$ – since the assumed perturbation could be amplified or damped by the ensuing motion. If transport is *from* the phase with *lower* diffusivity *into* the phase with *higher* diffusivity, the interfacial concentration will decrease from the point where bulk fluid impinges the interface, consequently, concentration is highest at the inflow and convection is amplified. This behavior is explained by considering the approximately parallel flow of fluid near the interface, here the phase with stronger diffusion will force the interfacial concentration closer to its bulk value than the other phase with lower diffusivity. In the sketched situation of transport (2) \rightarrow (1), Marangoni instability requires $D^{(2)} < D^{(1)}$, because in this way concentration will decrease from the point of inflow.

These considerations are formalized in the classical analysis of stationary instability, i.e. disregarding oscillatory instabilities, cf. Sec. 3.4. The conditions on physical properties for such a stationary Marangoni instability (in line with the verbal explanation) are sketched in Fig. 2.3; they are fulfilled if the term $\xi\psi\frac{\partial\sigma}{\partial c}$ is positive, whereas ξ and ψ are defined in the legend of Fig. 2.3 and account for the direction of transport and the relative size of diffusivities, respectively.

The strength of Marangoni convection can be estimated by relating the competing effects of solute transport to the interface and diffusion of solute gradients. The velocity of convective motion can be estimated from the stress balance at the interface Eq. (2.13). Consider a driving difference of interfacial tension $\Delta\sigma$, then a flow of magnitude U is established of order $U \sim \Delta\sigma/\mu^{(2)}$ – where we assumed that $\mu^{(1)} \ll \mu^{(2)}$. Thus a convection time t_{Ma} for the transport over a distance l is established by $t_{Ma} = \mu^{(2)}l/\Delta\sigma$, parallelly, a diffusion time for

^VIn this work, exclusively liquid/liquid layers will be considered; these usually have high Schmidt numbers $Sc^{(i)} = \nu^{(i)}/D^{(i)} > 1000$. For gas/liquid system or for the thermal problem, this is not the case, which can give rise to oscillatory instabilities due to the additional time scales.

equilibrating over a distance l is $t_d = l^2/D^{(2)}$. When the time for diffusion is large compared to the convective time, concentration differences are expected to be effectively converted into motion. Therefore, the higher the Marangoni number

$$Ma = t_d/t_{Ma} = \Delta\sigma l/(\mu^{(2)}D^{(2)}), \quad (2.25)$$

is, the stronger is the transport of bulk fluid with high concentration differences to the interface.

The second source for convection is sketched in Fig. 2.2(b). Here, again a transport of solute from the top to the bottom is depicted. A portion of fluid with higher concentration is sketched that – taking $\beta_c^{(i)} > 0$ – has a higher density than fluid at the same vertical level. Necessarily, a flow sets in that lowers the dense fluid against the lighter fluid. A self-sustained motion, i.e. Rayleigh convection, might be triggered. In the sketched situation the perturbation is amplified since a dense layer (dark color) overlays a light layer. However, if the direction of transport is reversed or the dependence of density on solute changes its sign ($\beta_c^{(i)} < 0$), the diffusive equilibration might be stable. This consideration is also condensed in Fig. 2.3: Rayleigh convection is expected if $\xi \frac{\partial \rho}{\partial c} < 0$. Note that this is a rather simple picture since the coupling between both effects and oscillatory instabilities are neglected, for a more comprehensive account consult Ref. [164].

The presented characterization of main convective regimes triggered by mass transfer in liquid/liquid system has been theoretically and experimentally confirmed, e.g. demonstrated by the quoted experimental shadowgraphs in Fig. 2.3. However, a detailed theoretical prediction of the complex and transient patterns in a realistic three-dimensional two-layer system is poorly available. This leads us to formulate the aims of this thesis and to provide a review on characteristic convective structures this thesis want to reproduce.

2.4 Pattern formation during mass transfer

It is our aim to reproduce closely experimentally observed structures (Fig. 2.3) that are triggered by mass transfer. Consequently, the paradigmatic model is probed whether it is able to reproduce these patterns. In the following two subsections, observation regarding type I (Sec. 2.4.1) and type III (Sec. 2.4.2) systems are reviewed, and open questions are explicated as well as our strategy to solve them.

2.4.1 Marangoni convection with stable density stratification

Perhaps the most frequently studied regime is that of type I [9, 78, 141, 143, 143, 166, 197, 198]; this might be due to its complex but also highly ordered patterns (see cell pattern type I in Fig.2.3). The process of mass transfer and the corresponding patterns driven by the Marangoni effect were experimentally observed via optical methods. These methods are mainly schlieren shadowgraphs or simply shadowgraph methods, i.e. they prescribing horizontal concentration gradients in x - y planes near the interface [160].

To overcome the vague description, "interfacial turbulence", of early scientific works [219], Orell & Westwater [166] made a first attempt to classify experimentally observed patterns in terms of: polygonal cells, stripes and ripples. After half a century of work, Linde *et al.* [146]

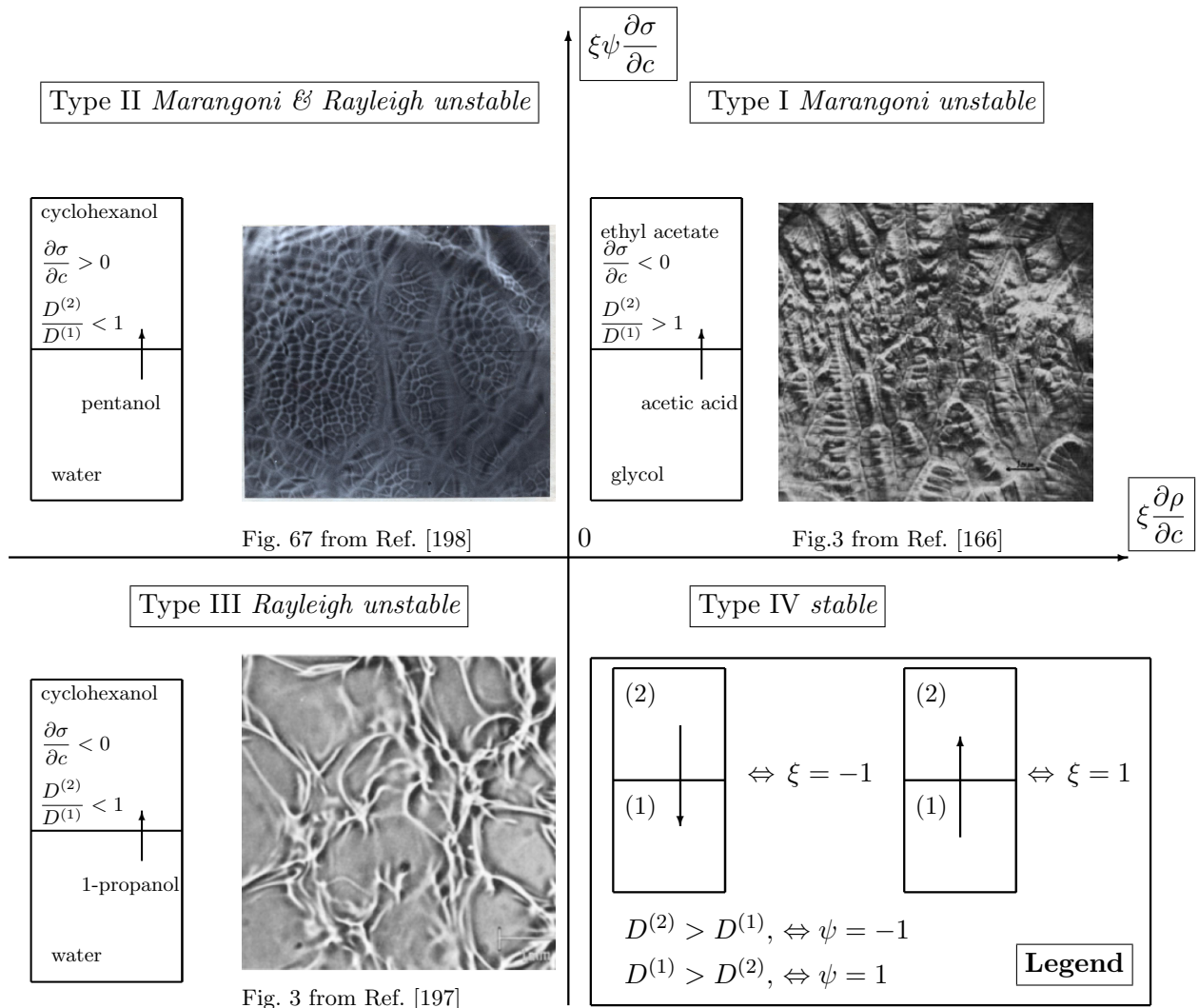


Figure 2.3: Scheme representing conditions for the stationary Marangoni instability, cf. Eq. (3.110), and Rayleigh instability (cf. Ref. [20]) in the paradigmatic system. The value of ψ and ξ code the direction of mass transfer and the ratio of diffusivities, which is noted in the legend in quadrant four. A characteristic experimental pattern is shown for each quadrant. Note that for type I also Rayleigh and for type III also Marangoni effects impact the nonlinear process of natural convection.

finally proposed a complete classification of the highly complex and unsteady patterns in the form of a few hypotheses, based on a broad range of experiments. His hypotheses are briefly quoted from Ref. [146]:

- L₁ "Interfacial convection is built up of three basic structures: (a) Marangoni roll cells (b) relaxation oscillation and (c) synchronized relaxation oscillation waves.
- L₂ Each of these structures may occur in n different hierarchy steps of different size, which we call n th order, referring to the number of substructures which are embedded. Substructure(s) of all three types can occur in any of the three patterns.
- L₃ Driving force of all these structures is the Marangoni shear stress, $d\sigma/dC \cdot \partial C/\partial x$, operating on different length scales.
- L₄ Interfacial convection can consist of numerous periodic cycles of amplification and decay of the three basic structures. The complexity in large containers, whose size exceeds the largest wavelength, arises from the fact that structures of different types or of a different hierarchy might occur simultaneously in different regions of the container".

Linde's first point (L₁) proposes three main structures that should cover all patterns in mass transfer system of type I.

The first structure is the Marangoni *roll cell* RC, sketched in the left column of Fig. 2.4. These RCs are similar to the polygonal cells studied in Bénard-Marangoni convection [36, 66, 114]. They form a relatively stable polygonal network, which is driven by low interfacial tension in the cell centers and high at the boundaries. This interfacial tension distribution results from the inflow in the cell centers and outflow at the cell borders.^{VI} Such structures are seen in Fig. 2.3 type II.

The second structure identified by Linde is the *relaxation oscillation* of Marangoni roll cells-ROs, cf. middle column of Fig. 2.4. This patterns is proposed to have the same origin as the RC but is highly unsteady. Individual cells grow fast in size and thereby compressing neighboring structures. After the spreading of an individual cell, the motion will cease (relaxation). Note that this pattern shares features to the observed eruptions in Rayleigh unstable system (see next Sec. 2.4.2), but has been observed [146] in systems where Rayleigh convection is not likely to be amplified.

The third basic structures according to Linde are the *synchronized relaxation oscillations waves* - ROWs. Mostly, they appear as aligned (straight or circular concentric) convection cells that move in a common direction. The concentric type has been termed *ripples* by Orell and Westwater [166]. Both types are divided into approximately equidistant relaxation zones [199] and can occur either as a single structure or in the form of a substructure (see L₂). Fig.2.3 (type I) shows a mixture of ROWs and RCs.

At present, only the simplest Marangoni roll cells without substructure have been thoroughly investigated by experiments and two-dimensional simulations, including recent work [37, 47, 65, 80, 152, 206]. Especially, no one-to-one comparison between experimental observations and simulations of the three-dimensional problem has been carried out. In this view, several open questions remained unsolved:

^{VI} Linde also reported on RC with a reversed flow orientation in chemical system involving the transport of strong surfactant [143], which is out of the scope of the present work since in this system the adsorbed amount of surfactant has to be taken into account in the mass balance.

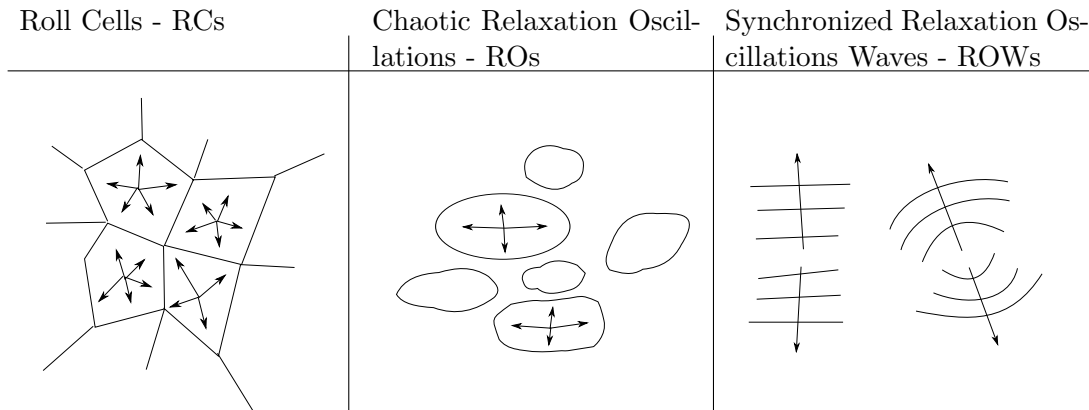


Figure 2.4: Sketch of basic Marangoni patterns according to theory of Linde [146]. Lines depict the highest contrast in experimental shadowgraph images and arrows fluid velocity at the interface.

(M₁) Is the paradigmatic model, introduced in Sec. 2.2, able to describe experimentally observed patterns [143, 146, 166], triggered by mass transfer? Or, are other physical effects (e.g. adsorption of surfactants, interfacial deformation, heat of solution, wall effects) necessary to understand the pattern formation?

(M₂) What physical mechanism are responsible for the appearance of basic structures (L₁), hierarchy formation (L₂) and "periodic cycles" (L₄). Thus, can we confirm the hypotheses of Linde?

(M₃) Can we perform a quantitative one-to-one comparison between experimental observation and numerical simulation, and what is its outcome?

(M₄) How do physical parameters influence Marangoni convection, and can we make further fundamental predictions for this equilibration process?

These open issues will be addressed by three-dimensional simulations of a sample system made of cyclohexanol, water and butanol in Ch. 5. The simulated data will be compared to classical experimental observation from literature [198] and recent experiments of Karin Schwarzenberger and Kerstin Eckert [111]. In the preceding Ch. 3, theoretical work on the PM is presented as an aid for the interpretation of numerical results. Especially, we will use linear stability methods to obtain information on convection onset. Chapter 6 will study convection not in a three-dimensional box as introduced by the PM, but in a Hele-Shaw cell, i.e. liquid confined in a narrow gap between two plates. This will further assess question M₃.

2.4.2 Rayleigh-Marangoni convection

As a second parameter regime, we will study a type III system (see Fig 2.3), i.e. where Rayleigh convection is the primary mechanism. Particular attention is given to a system that nevertheless showed a distinct impact by the Marangoni effect in terms of a structure noted

as "eruptions." In this view, the state of these systems is classified as Rayleigh-Marangoni convection.

An early observation of a type III system ^{VII} was published by Kroepelin & Neumann (1957) [123]. They considered the transport of acetic acid from ethyl acetate into water (see Fig. 2.5) inside a kind of Hele-Shaw cell. They observed Rayleigh convection (reproduced in Fig. 2.5) in both phases and vigorous movements at the interface, which they called eruptions (from the german word "Eruptionen"). They also mentioned the analogy of this Rayleigh induced eruptions with eruption triggered by forced convection. The experiments on the plane interface were motivated from their former experiments at pending drops [122].

Orell & Westwater [166] also studied this combination of materials, but at an extended interface. They characterized the interfacial structures as "interfacial turbulence, chaotic and unorganized activity", but did not provide images of this regime. Due to this "unorganized" appearance this convective regime received less attention and its structures are often just termed as "interfacial turbulence".

Further similar observation were published from Berg & Morig's experiments [20] of a benzene-chlorobenzene - water system with the transport of acetic acid between phases (in a Hele-Shaw cell). With this system, they could alter the density dependence of the phases on acetic acid by the concentration of chlorobenzene. Especially, they compared an experiment from type II and one from type III; they noted that no difference between convective pattern is evident. Nevertheless, their observation for the type III regime resembled the observations of Kroepelin & Neumann.

Fortunately, Schwarz [197, 198] paid more attention to this convection regime and published observation in the material system cyclohexanol/water+1-propanol (see Fig.2.3 type III). For this, he reported on erratic motions of circular spreadings (german "Spreitungen"), which he also called eruptions [197]. These structures of interfacial convection showed a close similarity to the dynamics reported on the ROs (Fig. 2.4) of Linde but are obviously triggered by Rayleigh convection. Schwarz reported such eruption for numerous systems that are designated to type III in his doctoral thesis [198].

In a broader context, numerous authors have studied the interplay between buoyant convection and the Marangoni effect. For instance, early studies on thermal convection revealed the damping effect of dissolved surfactant [18, 55, 170, 246]. Or recently, studies (see review [117]) on the localized addition of surfactants under a surface showed an oscillatory behavior.

Similar to the eruptions in the layered systems, the coupling of buoyant convection and the Marangoni effect manifests in droplet geometries: For instance Lappa *et al.* observed structures like eruptions (they called shooting) at dissolving drops [127, 128]. Also, a comprehensive study of dissolving droplets has been performed by Agble and coworkers [2-4] in binary systems. They showed that additionally introduced surfactants trigger irregular Marangoni convection with otherwise only buoyant convection.

Despite this interest, the detailed theoretical reproduction of classically observed eruptions

^{VII}Let us roughly estimate physical parameters, to check if it is indeed of type III (Fig 2.3). Water is denser ($\rho^{(1)} \approx 1\text{kg/l}$) than ethyl acetate ($\rho^{(2)} \approx 0.9\text{kg/l}$) viscosity of the pure liquids is $\mu^{(1)} \approx 1\text{mPas}$, $\mu^{(2)} \approx 0.4\text{mPas}$ (from handbook [135]). The diffusivity of acetic acid in the pure liquids under infinite dilution is also found in Ref. [135], namely, $D^{(1)} = 1.29 \times 10^{-9} \text{ m/s}^2$, $D^{(2)} = 2.18 \times 10^{-9} \text{ m/s}^2$. The density dependence is estimated as $\partial\rho^{(1,2)}/\partial c > 0$ since acetic acid is denser than water and ethyl acetate. Interfacial tension decrease via adding acetic acid $\partial\sigma/\partial c < 0$ [166]. As a result of our estimation, for transport (2) \rightarrow (1) (the situation shown in Fig. 2.5) the system belongs to the third quadrant, i.e. type III *Rayleigh unstable*.

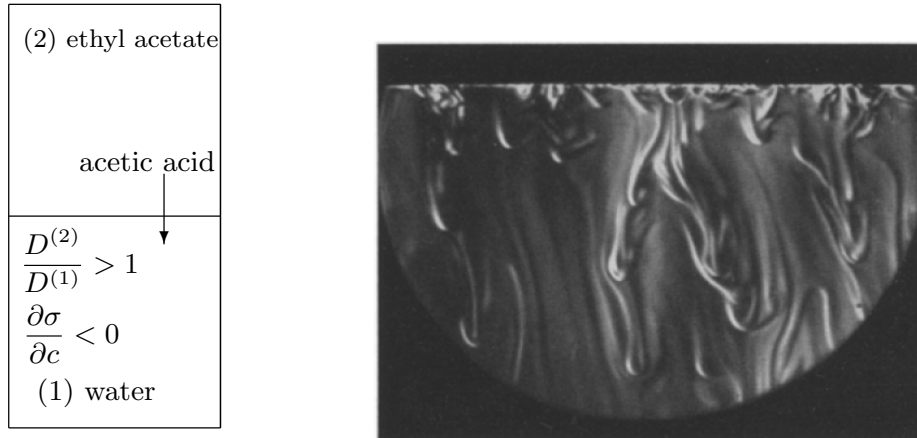


Figure 2.5: Eruptions and solutal plumes during transport of acetic acid from ethyl acetate into water. The shadowgraph image is reproduced from [123] and shows the water-rich phase.

from mass transfer experiments [20, 123, 166] is still lacking. Therefore – as in the former Marangoni case – no one-to-one comparison between experimental observation of complex and time-dependent structures and theoretical predictions is available. Consequently, several open questions remain:

- (R₁) Is the introduced PM able to reproduce the experimentally observed structures?
- (R₂) What physical mechanisms are responsible for the observed eruptions?
- (R₃) Can we perform a one-to-one comparison between experimental observations and a numerical simulation?
- (R₄) How do physical parameters fundamentally influence the equilibration process of type III?

In line with the proposed strategy to study Marangoni convection (Sec. 2.4.1), we will study "Rayleigh-Marangoni convection" for a realistic mass transfer system, namely, the ternary system cyclohexanol/water+2-propanol ($\hat{=}$ isopropanol). For a similar system, experimental results have been already reported [197, 198] (done with 1-propanol instead of 2-propanol isopropanol). However, for the isopropanol system, detailed experimental data has been provided by Karin Schwarzenberger and Kerstin Eckert to us.

Chapter 7 will present three-dimensional simulations and compare them to corresponding experiments. We will comprehensively study properties of convection and especially the way eruptions are produced. Furthermore, the variations of the initial concentration and the disregard of the Marangoni effect ($\alpha_c = 0$) are addressed by parametric studies.

Chapter 3

Theoretical analysis

This chapter is devoted to the analysis of our PM equations from Sec. 2.2. It is organized as follows.

Different units are introduced to nondimensionalize the governing equation in Sec. 3.1. In Sec. 3.2, a symmetry property of the PM is shown that appears in the limit of vanishing buoyancy ($G = 0$), and when viscous momentum transport dominates (Stokes flow). Sec. 3.3 presents the development of solute profiles under pure diffusion in the limit of two semi-infinite layers. Sec. 3.4 formulates the linear stability problem of a diffusive basic state. Based on this, classical stability results are reviewed (Sec. 3.4.1), and new results on the stability of the nonlinear diffusive profiles (only Marangoni effect) are derived in Sec. 3.4.2. Section 3.5 applies these new results to a specific system and compares them to nonlinear simulations. This chapter is finally summarized in Sec. 3.6.

3.1 Nondimensionalization and scale invariance

The present section reformulates the dimensional PM (introduced in Sec. 2.2) into different nondimensional forms. The essential physical parameters that govern the paradigmatic problem are gained by measuring independent (x, y, z, t) and dependent $(\mathbf{u}^{(i)}, c^{(i)}, p_d^{(i)})$ physical quantities in intrinsic units. The first two choices of units show a valuable scale invariance in the case of two semi-infinite domains, i.e. the change in the initial concentration does not alter the nondimensional problem. After that, the basis for numerical simulations is prepared by introducing units based on the layer height as reference length, which is in contrast to the first two. For an independent account of nondimensional equations for our specific problem consult Ref. [50, 164].

The PM relates fields $(\mathbf{u}^{(i)}, c^{(i)}, p_d^{(i)})$ via Eqs. (2.6)-(2.19), describing balance laws and boundary conditions. If an initial state X_0 is presupposed, a unique solution $X(t)$ will solve the problem. However, in Eqs. (2.6)-(2.19) numerous free physical and geometrical variables appear. These depend on the peculiar physical system under study. Let us gather those properties into a set \mathcal{P} and call them the *dimensional parameters*. Exemplary, these parameters can be read up in Eqs. (2.6)-(2.19) for example they are $\mathcal{P} = \{\nu^{(i)}, \rho_{ref}^{(i)}, \sigma_0, \alpha_c, c_0, L_x, d^{(1)}, \dots\}$. However, not any change in the dimensional parameters \mathcal{P} lead to another mathematical problem, which is trivially observed when doubling α_c and halving σ_0 for instance since they only appear as a product in the PM. See Barenblatt [11] for a comprehensive and general account on this issue.

In order to reduce the number of governing parameters in a corresponding nondimensional problem, units are defined in terms of the dimensional parameters \mathcal{P} . For nondimensionalization four basic units are chosen: length \tilde{L} , time \tilde{T} , mass \tilde{M} and molar concentration \tilde{C} while the other units are derived (in the sense of SI-unit system): velocity \tilde{L}/\tilde{T} and pressure $\tilde{M}/(\tilde{T}^2\tilde{L})$. In these terms, nondimensional variables (with a hat) are generated by

$$\hat{\mathbf{u}}^{(i)}(\mathbf{x}/\tilde{L}, t/\tilde{T}) = \mathbf{u}^{(i)}(\mathbf{x}, t) \cdot \tilde{T}/\tilde{L}, \quad (3.1)$$

$$\hat{c}^{(i)}(\mathbf{x}/\tilde{L}, t/\tilde{T}) = c^{(i)}(\mathbf{x}, t)/\tilde{C}, \quad (3.2)$$

$$\hat{p}_d^{(i)}(\mathbf{x}/\tilde{L}, t/\tilde{T}) = p_d^{(i)}(\mathbf{x}, t) \cdot (\tilde{T}^2\tilde{L})/\tilde{M}, \quad (3.3)$$

$$\hat{\mathbf{x}} = \mathbf{x}/\tilde{L}, \quad (3.4)$$

$$\hat{t} = t/\tilde{T}, \quad (3.5)$$

Note that the new functions, e.g. $\hat{\mathbf{u}}(\hat{\mathbf{x}}, \hat{t})$, are treated as a functions defined on the new domain $\hat{\Omega} = \{\mathbf{x}/\tilde{L} : \mathbf{x} \in \Omega\}$ of the scaled coordinate $\hat{\mathbf{x}}$, and also differential operators (e.g. $\hat{\nabla}, \partial_{\hat{t}}$) are acting on this new set of independent variables. Right away, we limit our considerations to a unit of mass that is related to the density of the lower layer $\tilde{M} = \rho_{ref}^{(1)}\tilde{L}^3$ and set the unit for molar concentration equal to the initial molar concentration in one layer $\tilde{C} = c_0$.

With these choices, the PM is reformulated. The equations that change non-trivially, i.e. where new parameters appear are listed in the following. For the bulk, they read

$$\frac{D\hat{\mathbf{u}}^{(i)}}{D\hat{t}} = \hat{c}^{(i)}\beta_c^{(i)}\mathbf{g}\frac{c_0\tilde{T}^2}{\tilde{L}} - \frac{\hat{\nabla}\hat{p}_d^{(i)}\rho_{ref}^{(1)}}{\rho_{ref}^{(i)}} + \frac{\tilde{T}}{\tilde{L}^2}\nu^{(i)}\hat{\Delta}\hat{\mathbf{u}}^{(i)}, \quad (3.6)$$

$$\partial_{\hat{t}}\hat{c}^{(i)} = -\hat{\mathbf{u}}^{(i)} \cdot \hat{\nabla}\hat{c}^{(i)} + \frac{\tilde{T}}{\tilde{L}^2}D^{(i)}\hat{\Delta}\hat{c}^{(i)}. \quad (3.7)$$

For the matching conditions at $\hat{z} = 0$, it is

$$\frac{\tilde{T}\sigma_0\alpha_c c_0}{\tilde{L}\mu^{(1)}}\hat{\nabla}_s\hat{c} = -\frac{\mu^{(2)}}{\mu^{(1)}}\partial_{\hat{z}}\hat{\mathbf{u}}^{(2)} + \partial_{\hat{z}}\hat{\mathbf{u}}^{(1)}, \quad (3.8)$$

$$\partial_{\hat{z}}\hat{c}^{(1)} = \frac{D^{(2)}}{D^{(1)}}\partial_{\hat{z}}\hat{c}^{(2)}, \quad (3.9)$$

$$\hat{c}^{(1)}H = \hat{c}^{(2)}. \quad (3.10)$$

$$(3.11)$$

For the boundary,¹ it yields

$$\hat{c}^{(i)}(\hat{x} + L_x/\tilde{L}, \hat{y}, \hat{z}) = \hat{c}^{(i)}(\hat{x}, \hat{y}, \hat{z}), \quad (3.12)$$

$$\hat{c}^{(i)}(\hat{x}, \hat{y} + L_y/\tilde{L}, \hat{z}) = \hat{c}^{(i)}(\hat{x}, \hat{y}, \hat{z}), \quad (3.13)$$

$$\partial_{\hat{z}}\hat{c}^{(1)} = \hat{u}_z^{(1)} = \hat{u}_x^{(1)} = \hat{u}_y^{(1)} = 0 \quad \text{for } \hat{z} = -d^{(1)}/\tilde{L}, \quad (3.14)$$

$$\partial_{\hat{z}}\hat{c}^{(2)} = \hat{u}_z^{(2)} = \hat{u}_x^{(2)} = \hat{u}_y^{(2)} = 0 \quad \text{for } \hat{z} = d^{(2)}/\tilde{L}, \quad (3.15)$$

and initial conditions read

$$\hat{\mathbf{u}}^{(1)} = \hat{\mathbf{u}}^{(2)} = 0 + \mathcal{N}/\left(\frac{\tilde{L}}{\tilde{T}}\right). \quad (3.16)$$

¹We omitted to write all periodicity conditions for the other variables.

Before discussing the first set of units, we analyze the nondimensional equations whether they can be made invariant under a change of initial concentration c_0 . In order to eliminate c_0 in Eqs. (3.6)-(3.8) length and time have to be related to the concentration unit. Thus, consider $\tilde{T} \propto c_0^a$ and $\tilde{L} \propto c_0^b$, then it is sufficient for the elimination of c_0 in Eqs. (3.6)-(3.8) if

$$1 + 2a - b = 0, \quad (3.17)$$

$$a - 2b = 0, \quad (3.18)$$

$$1 + a - b = 0, \quad (3.19)$$

hold. It is readily shown that all three relations cannot apply. However when one relation is omitted, it is well possible. This leads to two subcases: pure Rayleigh and pure Marangoni convection. For pure Rayleigh ($\alpha_c = 0$) only Eqs. (3.17) and (3.18) have to be regarded, which yields

$$\tilde{L} \propto c_0^{-1/3}, \quad \tilde{T} \propto c_0^{-2/3} \Rightarrow \tilde{U} \propto c_0^{+1/3}. \quad (3.20)$$

On the other hand, when buoyant effects are disregarded ($\beta_c^{(i)} = 0$), only Eqs. (3.18) and (3.19) need to be considered, consequently

$$\tilde{L} \propto c_0^{-1}, \quad \tilde{T} \propto c_0^{-2} \Rightarrow \tilde{U} \propto c_0^{+1}. \quad (3.21)$$

Note that these choices generates boundary and initial conditions Eqs. (3.12)-(3.16) that depend on c_0 , especially, the position of the boundary (e.g. $d^{(1)}/\tilde{L}$) and the periodicity lengths (L_y/\tilde{L}) change.

However, in the limit of an infinite spatial domain $\Omega = \mathbb{R}^3$, the nondimensional problem is almost invariant under a change of c_0 , which is discussed in the next subsection for the Marangoni case.

3.1.1 Marangoni scaling

When buoyant effects are disregarded $\beta_c^{(i)}=0$, Eqs. (3.6)-(3.8) are independent of $\Delta\sigma = |\sigma_{ref}\alpha_c c_0|$ for the following *interfacial units*

$$L_{int} = \frac{\mu^{(1)}\nu^{(1)}}{\Delta\sigma}, \quad (3.22)$$

$$T_{int} = \frac{\mu^{(1)}\mu^{(1)}\nu^{(1)}}{(\Delta\sigma)^2}, \quad (3.23)$$

$$U_{int} = L_{int}/T_{int} = \frac{\Delta\sigma}{\mu^{(1)}}. \quad (3.24)$$

This directly applies the idea expressed in Eq. (3.21). Though, α_c is not allowed to change sign^{II}. Surely, other choices are possible, e.g. $\nu^{(1)}$ could be replaced by $D^{(1)}$.

Note that the tangential stress balance (3.8) becomes

$$sgn(\alpha_c)\partial_x c^{(1)} = -\mu^{(2)}/\mu^{(1)}\partial_z u_x^{(2)} + \partial_z u_x^{(1)}, \quad (3.25)$$

$$sgn(\alpha_c)\partial_y c^{(1)} = -\mu^{(2)}/\mu^{(1)}\partial_z u_y^{(2)} + \partial_z u_y^{(1)}. \quad (3.26)$$

^{II}Nevertheless, the sign change of α could also be allowed, meaning a change of sign would change the sign of nondimensional coordinates, which would complicate the discussion.

It does not contain the absolute value of c_0 .

Obviously, the nondimensional domain $\hat{\Omega}$ changes in size by variation of $L_{int} \propto (\Delta\sigma)^{-1}$. Nevertheless, as noted before, we proceed by considering an infinite domain $\Omega = \mathbb{R}^3$. Thus, boundary conditions get invariant. However, the initial conditions for the velocity field are still involved by

$$\hat{\mathbf{u}}^{(1)} = \hat{\mathbf{u}}^{(2)} = \mathcal{N}(\hat{\mathbf{x}}L_{int})/U_{int}. \quad (3.27)$$

Thus once a dimensional noise \mathcal{N} is given, it breaks the scale invariance even in the infinite case.

For example consider the dimensional noise as a sum of Fourier modes [with some fixed expansion coefficients $a(\mathbf{k}_j)$]

$$\mathcal{N}(\mathbf{x}) = \sum_j a(\mathbf{k}_j)e^{i\mathbf{k}_j\mathbf{x}}, \quad (3.28)$$

then its nondimensional counterpart is

$$\hat{\mathcal{N}} = \frac{1}{U_{int}} \sum_j a(\mathbf{k}_j)e^{i\mathbf{k}_j\hat{\mathbf{x}}L_{int}}. \quad (3.29)$$

Consider *increasing* interfacial tension difference $\Delta\sigma$ and note that $U_{int} \propto \Delta\sigma$, $L_{int} \propto (\Delta\sigma)^{-1}$; consequently, $\hat{\mathcal{N}}$ decreases and the spectrum is shifted to smaller wavenumbers. So if initial perturbations are "relatively structureless", the main impact (of increasing $\Delta\sigma$) will be a decrease of amplitude and therefore onset of convection might appear later – in those nondimensional terms since any other terms are unchanged. However, the impact of initial perturbations on the long-term dynamics is unclear a priori.

But the question remains, in what situations can the finitely sized system ($L_y, L_x, d^{(1)}, d^{(2)} < \infty$) be approximately described by the infinite one? For the author a rigorous mathematical answer seem rather involved since the governing equations have elliptic and parabolic properties, thus the full domain is immediately impacted by changes of field quantities, also very far away from the interface. Nevertheless, in Ch. 5, these ideas are practically applied to the simulations that investigate a change in initial concentrations.

Before proceeding with the system of units actually used for simulations, a last issue, namely, the impact of buoyancy is discussed. Therefore, consider the application of interfacial units [Eqs. (3.22)-(3.24)] in Eq. (3.6), which yields

$$\partial_t \hat{\mathbf{u}}^{(1)} = -\hat{\mathbf{u}}^{(1)} \cdot \nabla \hat{\mathbf{u}}^{(1)} - \nabla \hat{p}_d^{(1)} + \Delta \hat{\mathbf{u}}^{(1)} - \hat{c}^{(1)} Mo \mathbf{e}_z, \quad (3.30)$$

$$\partial_t \hat{\mathbf{u}}^{(2)} = -\hat{\mathbf{u}}^{(2)} \cdot \nabla \hat{\mathbf{u}}^{(2)} - \frac{\nabla \hat{p}_d^{(2)}}{\rho} + \nu \Delta \hat{\mathbf{u}}^{(2)} - \hat{c}^{(2)} Mo \beta \mathbf{e}_z, \quad (3.31)$$

where a new dimensionless parameter appears: the Morton number

$$Mo = \frac{c_0 \beta_c^{(1)} (\mu^{(1)})^3 \nu^{(1)} g}{(\Delta\sigma)^3}. \quad (3.32)$$

The Morton number measures the relative impact of buoyant forces. Consequently, if buoyant effects are compensated by a hydrostatic pressure

$$\nabla p_d^{(1)} \sim c^{(1)} M o e_z \quad (3.33)$$

the effects of scale variance can still persist.

Finally, let us conclude with the four necessary conditions for the scale invariance under a variation of $\Delta\sigma$. (1) The system has to obey the PM, and the rest of parameters are unchanged. (2) The system has to be practically semi-infinite, i.e. no outer length is present. (3) When buoyant effects are present, the Morton number has to be constant (including trivially zero). (4) Initial conditions have to be rescaled since they introduce an outer scale.

3.1.2 Viscous scaling

In the present section, the basis for our later numerical investigations is derived: the nondimensional equations in viscous scales. The intrinsic units are based on the layer height and the characteristic time of viscous equilibration across the layer height $d^{(1)}$. They read

$$L_{vis} = d^{(1)}, \quad (3.34)$$

$$T_{vis} = (d^{(1)})^2 / \nu^{(1)}, \quad (3.35)$$

$$U_{vis} = L_{vis} / T_{vis} = \frac{\nu^{(1)}}{d^{(1)}}. \quad (3.36)$$

Recall that units for mass and molar concentration are set by $\tilde{M} = \rho_{ref}^{(1)}$, $\tilde{C} = c_0$ and that pressure is measured by $\tilde{P} = \nu^{(1)} \mu^{(1)} / (d^{(1)})^2$; furthermore, dynamic and kinematic viscosity are coupled via the reference densities $\mu^{(i)} = \rho_{ref}^{(i)} \nu^{(i)}$.

The nondimensionalization [i.e. application of (3.1)-(3.5)] yields the following equations in the bulk

$$\partial_t \hat{\mathbf{u}}^{(1)} = -\hat{\mathbf{u}}^{(1)} \cdot \hat{\nabla} \hat{\mathbf{u}}^{(1)} - \hat{\nabla} \hat{p}_d^{(1)} + \hat{\Delta} \hat{\mathbf{u}}^{(1)} - \hat{c}^{(1)} G \mathbf{e}_z, \quad (3.37)$$

$$\hat{\nabla} \cdot \hat{\mathbf{u}}^{(1)} = 0, \quad (3.38)$$

$$\partial_t \hat{\mathbf{u}}^{(2)} = -\hat{\mathbf{u}}^{(2)} \cdot \hat{\nabla} \hat{\mathbf{u}}^{(2)} - \frac{1}{\rho} \hat{\nabla} \hat{p}_d^{(2)} + \nu \hat{\Delta} \hat{\mathbf{u}}^{(2)} - \hat{c}^{(2)} G \beta \mathbf{e}_z, \quad (3.39)$$

$$\hat{\nabla} \cdot \hat{\mathbf{u}}^{(2)} = 0, \quad (3.40)$$

$$\partial_t \hat{c}^{(1)} = -\hat{\mathbf{u}}^{(1)} \cdot \hat{\nabla} \hat{c}^{(1)} + \frac{1}{S_C^{(1)}} \hat{\Delta} \hat{c}^{(1)}, \quad (3.41)$$

$$\partial_t \hat{c}^{(2)} = -\hat{\mathbf{u}}^{(2)} \cdot \hat{\nabla} \hat{c}^{(2)} + \frac{D}{S_C^{(1)}} \hat{\Delta} \hat{c}^{(2)}. \quad (3.42)$$

No-slip and impermeable boundary conditions are imposed for the solid walls at the bottom and top:

$$\partial_{\hat{z}} \hat{c}^{(1)} = \hat{u}_z^{(1)} = \hat{u}_x^{(1)} = \hat{u}_y^{(1)} = 0 \quad \text{for } \hat{z} = -1 \quad (3.43)$$

$$\partial_{\hat{z}} \hat{c}^{(2)} = \hat{u}_z^{(2)} = \hat{u}_x^{(2)} = \hat{u}_y^{(2)} = 0 \quad \text{for } \hat{z} = d. \quad (3.44)$$

The matching conditions at the plane interface ($\hat{z}=0$) are:

$$\hat{u}_x^{(1)} = \hat{u}_x^{(2)}, \quad \hat{u}_y^{(1)} = \hat{u}_y^{(2)}, \quad \hat{u}_z^{(1)} = \hat{u}_z^{(2)} = 0, \quad \partial_{\hat{z}} \hat{c}^{(1)} = D \partial_{\hat{z}} \hat{c}^{(2)}, \quad H \hat{c}^{(1)} = \hat{c}^{(2)}, \quad (3.45)$$

$$\frac{Ma}{S_C^{(1)}} \partial_{\hat{x}} \hat{c}^{(1)} = -\mu \partial_{\hat{z}} \hat{u}_x^{(2)} + \partial_{\hat{z}} \hat{u}_x^{(1)}, \quad \frac{Ma}{S_C^{(1)}} \partial_{\hat{y}} \hat{c}^{(1)} = -\mu \partial_{\hat{z}} \hat{u}_y^{(2)} + \partial_{\hat{z}} \hat{u}_y^{(1)}. \quad (3.46)$$

Periodicity is enforced by

$$\hat{c}^{(i)}(\hat{x} + l_x, \hat{y}, \hat{z}) = \hat{c}^{(i)}(\hat{x}, \hat{y}, \hat{z}), \quad \hat{c}^{(i)}(\hat{x}, \hat{y} + l_y, \hat{z}) = \hat{c}^{(i)}(\hat{x}, \hat{y}, \hat{z}), \quad (3.47)$$

$$\hat{p}_d^{(i)}(\hat{x} + l_x, \hat{y}, \hat{z}) = \hat{p}_d^{(i)}(\hat{x}, \hat{y}, \hat{z}), \quad \hat{p}_d^{(i)}(\hat{x}, \hat{y} + l_y, \hat{z}) = \hat{p}_d^{(i)}(\hat{x}, \hat{y}, \hat{z}), \quad (3.48)$$

$$\hat{\mathbf{u}}^{(i)}(\hat{x} + l_x, \hat{y}, \hat{z}) = \hat{\mathbf{u}}^{(i)}(\hat{x}, \hat{y}, \hat{z}), \quad \hat{\mathbf{u}}^{(i)}(\hat{x}, \hat{y} + l_y, \hat{z}) = \hat{\mathbf{u}}^{(i)}(\hat{x}, \hat{y}, \hat{z}). \quad (3.49)$$

Initial conditions for transport (1) \rightarrow (2) are

$$\hat{\mathbf{u}}^{(1)} = \hat{\mathbf{u}}^{(2)} = 0 + \mathcal{N}(\hat{\mathbf{x}}d^{(1)})/U_{vis}, \quad (3.50)$$

$$c^{(1)} = 1, \quad c^{(2)} = 0. \quad (3.51)$$

Still we let the initial velocity perturbation \mathcal{N} unspecified.

Several nondimensional parameters arise in these equation; Tab. 3.1 lists them. The physical importance of the Marangoni number Ma and the Rayleigh number $Ra = G Sc^{(1)}$ as a measure for the expected convection strength was already noted in the previous chapter. Let us note that due to the boundary conditions that describe the system as closed, the layer heights may have low impact on the dynamics, when convection and mass flux is mainly restricted to a zone near the interface. Such a situation will be called a *deep layer regime* in the following.

The essential nondimensional parameters $\hat{\mathcal{P}}$, i.e. the minimal set of governing parameters for a unique definition of the nondimensional problem is given by

$$\hat{\mathcal{P}} = \{G, Sc^{(1)}, Ma, H, \rho, \nu, D, \beta, d, l_x, l_y\}, \quad (3.52)$$

being eleven in number. This is a seemingly large parameter space, though several constraints may be noted: (1) In the later course, we will restrict to equal layer heights $d = 1$ and mostly to situations with a square base $l_x = l_y$. (2) We aim to study situations with a large base, i.e. when the system state \hat{X} exhibits some internal translation invariance $\hat{X}(\hat{\mathbf{x}}) \approx \langle \hat{X}(\hat{\mathbf{x}} + (\lambda \mathbf{e}_x + \mu \mathbf{e}_y)) \rangle_e$ with some $\lambda, \mu \ll l_x, l_y$, at least in the sense of an ensemble average. (3) Also, parameter space is constrained by focusing on liquid/liquid system in this work. There ratios of diffusivity $D = D^{(2)}/D^{(1)}$ and ratios of viscosities $\nu = \nu^{(2)}/\nu^{(1)}$ are approximately linked by the Stokes-Einstein relations, i.e. $D^{(i)} \sim 1/(\nu^{(i)} \rho_{ref}^{(i)})$ [52, 70]. (4) The Schmidt number in liquids is usually large $Sc^{(i)} \geq 1000$.

3.1.3 Diffusive scaling

For completeness, we will give the equations when the nondimensionalization is based on a diffusive time. It is presented here because of its frequent appearance in literature as well as its application in linear stability analysis.

Relative to equations in viscous units (Sec. 3.1.2), the viscous time Eq. (3.35) is replaced by the characteristic time for diffusion in the lower layer:

$$T_{diff} = (d^{(1)})^2/D^{(1)}. \quad (3.53)$$

Consequently, the unit for velocity changes accordingly

$$U_{diff} = L_{diff}/T_{diff} = \frac{D^{(1)}}{d^{(1)}}. \quad (3.54)$$

dimensionless quantity	definition
Grashof number	$G = \frac{c_0 \beta_c^{(1)} g L^3}{(\nu^{(1)})^2}$
Schmidt number in (1)	$Sc^{(1)} = \frac{\nu^{(1)}}{D^{(1)}}$
Marangoni number	$Ma = \frac{c_0 \alpha_c \sigma_{ref} L}{\rho^{(1)} \nu^{(1)} D^{(1)}}$
partition coefficient	$H = c_{eq}^{(2)} / c_{eq}^{(1)}$
density ratio	$\rho = \frac{\rho_{ref}^{(2)}}{\rho_{ref}^{(1)}}$
kinematic viscosity ratio	$\nu = \frac{\nu^{(2)}}{\nu^{(1)}}$
diffusivity ratio	$D = \frac{D^{(2)}}{D^{(1)}}$
layer height ratio	$d = \frac{d^{(2)}}{d^{(1)}}$
solutal expansion coefficient ratio	$\beta = \frac{\beta_c^{(2)}}{\beta_c^{(1)}}$
horizontal domain size	$l_x = L_x / d^{(1)}$
horizontal domain size	$l_y = L_y / d^{(1)}$
Rayleigh number	$Ra = G Sc^{(1)} = \frac{c_0 \beta_c^{(1)} g L^3}{\nu^{(1)} D^{(1)}}$
Schmidt number in (2)	$Sc^{(2)} = Sc^{(1)} \nu / D = \frac{\nu^{(2)}}{D^{(2)}}$
dynamic viscosity ratio	$\mu = \nu \rho$

Table 3.1: Nondimensional parameters, the last three depend on the parameters above.

Relative to the presentation in Sec. 3.1.2, the following equations change:

$$\partial_{\hat{t}}\hat{\mathbf{u}}^{(1)} = -\hat{\mathbf{u}}^{(1)} \cdot \hat{\nabla}\hat{\mathbf{u}}^{(1)} - \hat{\nabla}\hat{p}_d^{(1)} + Sc^{(1)}\hat{\Delta}\hat{\mathbf{u}}^{(1)} - \hat{c}^{(1)}RaSc^{(1)}\mathbf{e}_z, \quad (3.55)$$

$$\partial_{\hat{t}}\hat{\mathbf{u}}^{(2)} = -\hat{\mathbf{u}}^{(2)} \cdot \hat{\nabla}\hat{\mathbf{u}}^{(2)} - \frac{1}{\rho}\hat{\nabla}\hat{p}_d^{(2)} + Sc^{(1)}\nu\hat{\Delta}\hat{\mathbf{u}}^{(2)} - \hat{c}^{(2)}Ra\beta Sc^{(1)}\mathbf{e}_z, \quad (3.56)$$

$$\partial_{\hat{t}}\hat{c}^{(1)} = -\hat{\mathbf{u}}^{(1)} \cdot \hat{\nabla}\hat{c}^{(1)} + \hat{\Delta}\hat{c}^{(1)}, \quad (3.57)$$

$$\partial_{\hat{t}}\hat{c}^{(2)} = -\hat{\mathbf{u}}^{(2)} \cdot \hat{\nabla}\hat{c}^{(2)} + D\hat{\Delta}\hat{c}^{(2)}, \quad (3.58)$$

and in the matching conditions ($\hat{z} = 0$)

$$Ma\partial_{\hat{x}}\hat{c}^{(1)} = -\mu\partial_{\hat{z}}\hat{u}_x^{(2)} + \partial_{\hat{z}}\hat{u}_x^{(1)}, \quad (3.59)$$

$$Ma\partial_{\hat{y}}\hat{c}^{(1)} = -\mu\partial_{\hat{z}}\hat{u}_y^{(2)} + \partial_{\hat{z}}\hat{u}_y^{(1)}, \quad (3.60)$$

Here the Rayleigh rather than the Grashof number is used for brevity.

3.2 Symmetry of motion for Stokes flow

In the course of this work, it will turn out that convection, in the chosen sample system, is in the Stokes flow regime, i.e. viscous force outweighs inertia. In this regime, the momentum balance can be reduced to the time-independent Stokes equations. By additionally neglecting buoyancy terms ($G = 0$), these Stokes equations read

$$0 = -\nabla p_d^{(1)} + \Delta\mathbf{u}^{(1)}, \quad (3.61)$$

$$0 = -\nabla p_d^{(2)} + \mu\Delta\mathbf{u}^{(2)}, \quad (3.62)$$

in viscous units with hats dropped.

The analysis of Stokes equations (3.61)-(3.62) with boundary conditions (3.43)-(3.46) reveals that the flow governed by these equations possesses a mirror symmetry at the interface for equally sized layers $d = 1$. This mirror symmetry is expressed for $z > 0$ by

$$\begin{aligned} u_z^{(1)}(x, y, -z) &= -u_z^{(2)}(x, y, z), \quad u_x^{(1)}(x, y, -z) = u_x^{(2)}(x, y, z), \\ u_y^{(1)}(x, y, -z) &= u_y^{(2)}(x, y, z) \end{aligned} \quad (3.63)$$

or with the Cartesian tensor $T = \mathbf{e}_x\mathbf{e}_x + \mathbf{e}_y\mathbf{e}_y - \mathbf{e}_z\mathbf{e}_z$ expressed as

$$T \cdot \mathbf{u}^{(1)}(T \cdot \mathbf{x}) = \mathbf{u}^{(2)}(\mathbf{x}) \text{ for } z > 0 \quad (3.64)$$

A proof of Eq. (3.63) is sketched as follows: Consider a solution is known for the bottom $p_d^{(1)}(\mathbf{x}), \mathbf{u}^{(1)}(\mathbf{x})$ layer. Then insert the proposed velocity (3.63) in Eq. (3.62). We find that the pressures are related by $\nabla p_d^{(2)} = \mu T \nabla p_d^{(1)}(T \cdot \mathbf{x})$ by using Eq. (3.61), therewith indeed the proposed velocity solves Eq. (3.62). Furthermore, the proposed velocity field obeys the boundary conditions that are periodicity, no-slip at the bottom and continuity at $z = 0$. These condition are simply enforced by (3.63). Consequently, by explicitly constructing a symmetric velocity field in layer (2) from any solution in layer (1), it follows that any solution of the given problem obeys the mirror symmetry.

Furthermore, note that these arguments fail for $G \neq 0$ because – in this case – the concentration fields appear in the momentum balance. By this, we can not construct the pressure gradient in the layer (2) if $\text{curl}(c^{(i)}(\mathbf{x})\mathbf{e}_z) \neq 0$.

The consequences of this symmetry property are twofold: Firstly, results from a full simulation may show this interesting behavior; therefore, this relation can be used to check the numerical code and enriches the interpretation of results. Secondly, when Stokes flow with $G = 0$ is assumed, the Stokes equations have to be calculated in one layer only. This reduction is possible since the boundary condition can be reformulated with the help of Eq. (3.63), thereby saving numerical cost. Also, note that for Stokes flow, several semi-analytical methods exist [179, 227], especially useful for moving boundary problems.

3.3 Equilibration under pure diffusion

When fluid motion is absent $\mathbf{u}^{(i)} = 0$, then solute spreads by molecular diffusion only. In this case, the *dimensional* governing equations reduce to

$$\partial_t c^{(1)} = D^{(1)} \Delta c^{(1)} \text{ for } -d^{(1)} < z < 0 \quad (3.65)$$

$$\partial_t c^{(2)} = D^{(2)} \Delta c^{(2)} \text{ for } 0 < z < d^{(2)}. \quad (3.66)$$

Initially at $t = 0$, it is assumed that solute is present only in the top layer,

$$c^{(1)} = 0, \quad c^{(2)} = c_0. \quad (3.67)$$

Furthermore, the matching condition (at $z = 0$) are

$$\partial_z c^{(1)} D^{(1)} = \partial_z c^{(2)} D^{(2)}, \quad c^{(1)} H = c^{(2)}, \quad (3.68)$$

and no flux concentration boundary conditions are

$$\partial_z c^{(1)}(z = -d^{(1)}) = \partial_z c^{(2)}(z = d^{(2)}) = 0. \quad (3.69)$$

An exact solution of this problem might be derived by Laplace transform methods (cf. Ref. [43, 77] for solutions of similar problems), which typically leads to a series expansion of the solution.

However, a simple description can be obtained by considering two semi-infinite layers, i.e. the limit of $d^{(1)} \rightarrow \infty$, $d^{(2)} \rightarrow \infty$. In this case, a solution of the two layer diffusion problem is known [51, 233] by^{III}

$$c^{(2)} = \frac{1}{1 + H^{-1} D^{-0.5}} \left[1 + H^{-1} D^{-0.5} \cdot \operatorname{erf} \left(\frac{z}{2\sqrt{tD^{(2)}}} \right) \right] c_0, \quad (3.70)$$

$$c^{(1)} = \frac{1}{H + D^{-0.5}} \left[1 - \operatorname{erf} \left(\frac{-z}{2\sqrt{tD^{(1)}}} \right) \right] c_0, \quad (3.71)$$

$$\text{with } D = D^{(2)} / D^{(1)}. \quad (3.72)$$

Note that concentration only depends on the vertical coordinate z and time t .

These functions may approximate the solution for finite heights $d^{(1)}, d^{(2)}$ for early times, when the mixing has propagated only a small distance compared to the full layer height. In

^{III}Note that the errorfunction erf yields value $\operatorname{erf}(0) = 0$ and $\operatorname{erf}(\pm\infty) = \pm 1$; the complementary errorfunction is defined as $\operatorname{erfc}(x) = 1 - \operatorname{erf}(x)$

order to estimate an upper time limit for a valid approximation, we consider how positions of constant concentration develop over time. Therewith, the upper time limit is found by requiring that a small change from the initial concentration value be still in the proximity of the interface. If the system is in such a state, it is in a *deep layer regime*.

Formally, consider a given concentration \mathcal{C} (should only deviate slightly from the initial concentration c_0) and time t : the position $z = -\delta_c$ for which $c^{(1)}(z = -\delta_c, t) = \mathcal{C}$ is $\delta_c = K2\sqrt{\hat{t}D^{(1)}}$ with a constant K depending on the special choice of \mathcal{C} [cf. Eq. (3.71)]. Note that we assumed a faster diffusion in layer (1), $D^{(1)} > D^{(2)}$. The unknown constant K is calculated by the inverse of the complementary errorfunction

$$K = \operatorname{erfc}^{-1} [\mathcal{C}/c_0 (H + D^{-0.5})]. \quad (3.73)$$

Finally, the time such that this perturbations \mathcal{C} has not travelled more than a distance of $d^{(1)}/\alpha$ from the interface is

$$t < \left(\frac{d^{(1)}}{\alpha 2K} \right)^2 \frac{1}{D^{(1)}}. \quad (3.74)$$

Transport from layer (2) to layer (1) in viscous units: The transport from the upper layer (2) to the lower layer (1) can also be expressed in viscous units. Quantities in viscous units are related by

$$c^{(i)} = \hat{c}^{(i)} c_0, \quad z = \hat{z}L, \quad t = \hat{t}(L^{(1)})^2/\nu^{(1)}, \quad (3.75)$$

see also Sec. 3.1.2. Carrying out this replacement from dimensional to viscous quantities in Eqs. (3.70,3.71) yields

$$\hat{c}^{(1)} = \frac{1}{H + \frac{1}{D^{0.5}}} \left[1 - \operatorname{erf} \left(\frac{-\hat{z}}{2\sqrt{\hat{t}/Sc^{(1)}}} \right) \right], \quad (3.76)$$

$$\hat{c}^{(2)} = \frac{1}{1 + \frac{1}{HD^{0.5}}} \left[1 + \frac{1}{HD^{0.5}} \cdot \operatorname{erf} \left(\frac{\hat{z}}{2\sqrt{\hat{t}D/Sc^{(1)}}} \right) \right]. \quad (3.77)$$

The mol per interfacial area that are transferred from one phase to another at time t is given by

$$\int_{[0, -\infty]} \hat{c}^{(1)}(\hat{z}, \hat{t}) d\hat{z} = \frac{2\sqrt{\frac{\hat{t}}{Sc^{(1)}}}}{(H + 1/D^{0.5})\sqrt{\pi}} \quad (3.78)$$

The interfacial concentration gradient is given by

$$\partial_z \hat{c}^{(1)}(\hat{z} = 0, \hat{t}) = \frac{D^{0.5}}{(1 + HD^{0.5})\sqrt{\hat{t}\pi/Sc^{(1)}}}. \quad (3.79)$$

Transport from layer (1) to layer (2) in viscous units: In preparation for future applications, the diffusion from the lower layer (1) to the upper layer(2) is written out in viscous units.

Carrying out the replacement from dimensional to viscous quantities in Eqs. (3.70, 3.71) and accounting for the changed transport direction yields

$$\hat{c}^{(1)} = \frac{1}{1 + D^{0.5}H} \left[1 + D^{0.5}H \operatorname{erf} \left(\frac{-\hat{z}}{2\sqrt{\hat{t}/Sc^{(1)}}} \right) \right], \quad (3.80)$$

$$\hat{c}^{(2)} = \frac{H}{1 + D^{0.5}H} \left[1 - \operatorname{erf} \left(\frac{\hat{z}}{2\sqrt{D\hat{t}/Sc^{(1)}}} \right) \right]. \quad (3.81)$$

Furthermore, the concentration gradient at the interface reads

$$\partial_{\hat{z}}\hat{c}^{(1)}(\hat{z} = 0, \hat{t}) = \frac{D^{0.5}H}{(1 + D^{0.5}H)\sqrt{\pi\hat{t}/Sc^{(1)}}}. \quad (3.82)$$

Exemplary calculations: To show an application of the developed formulas, a specific example is discussed next. In Ch. 7, the transport of isopropanol is studied. The relevant material properties are $Sc^{(1)}=1348$, $H=1.6$, $D=0.082$. Therefore, we apply relation (3.74) (now adapted to viscous units and the changed direction of transfer) and compare it to the numerical solution (see Ch.4 for numerical method) of the finite model. Therefore, take $C = 0.99c_0$ and $\alpha = 2$ for instance. Since layer (1) has higher diffusivity, analysis is focused there. Firstly, we calculate the auxiliary constant: $K = 1.52$. Therewith, the maximum time for which $\delta_c < 0.5d^{(1)}$ holds is

$$\hat{t} < \left(\frac{1}{2\alpha K} \right)^2 Sc^{(1)} \approx 36.56, \quad (3.83)$$

where Eq. (3.74) has been applied and transformed to viscous units.

Fig. 3.1(a) displays the relative error of the infinite model approximating the finite case in terms of the concentration gradient at the interface

$$e = \frac{\partial_z c_{\infty}^{(1)}(z = 0) - \partial_z c_{finite}^{(1)}(z = 0)}{\partial_z c_{finite}^{(1)}(z = 0)}. \quad (3.84)$$

Observe that, in this case, the relative error is lower than 10^{-4} for $t < 150$ and that the finite case is overestimated by the infinite one. So, the time calculated with Eq. (3.83) served as a conservative estimate for applicability of the infinite layer model. Additionally, Fig. 3.1 (b) shows the mean concentration in layer (2) normalized with the concentration in global equilibrium $c_{eq}^{(2)} = H/(H + 1)$ as function of time. Note that at $t > 10000$ more than 95% of the potential solute has been transported across the interface. In fact, the diffusive time scales of layers are $Sc^{(1)} = 1348$ and $Sc^{(1)}D=16438$.

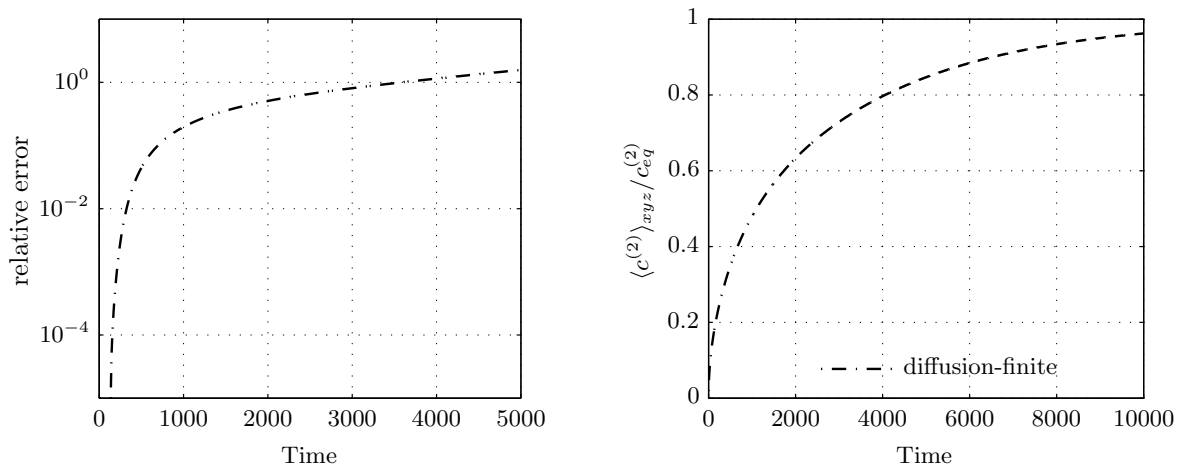


Figure 3.1: Diffusion of solute from layer (1) to (2) in viscous units and $Sc^{(1)}=1348$, $H=1.6$, $D=0.082$: (a) error of the infinite layer model according to Eq. (3.84), (b) averaged concentration in the finite model normalized by global equilibrium value.

3.4 Neutral linear stability for the pure Marangoni case

As discussed in Sec. 3.3, the PM with the ideal/unperturbed initial condition,

$$\mathbf{u}^{(1)} = \mathbf{u}^{(2)} = 0, \quad (3.85)$$

$$c^{(1)} = 1, c^{(2)} = 0 \quad (3.86)$$

permits a simple, quiescent solution for which solute is transported by pure diffusion only. In experiments, convection is though observed. Commonly, this is theoretically accounted for by the uncertainty of the initial states, i.e. a perturbation to the *ideal* initial state. In the following section, we derive the marginal (also called neutral) stability threshold for a system of two semi-infinite layers without Rayleigh effect ($Ra = 0$) and for stationary (non-oscillatory) perturbations. This is done for two concentration profiles:

(1) We start with the common linear profiles, used by Sterling & Scriven [219] in Sec. 3.4.1. The calculations will reproduce their central result for the PM. Thus, it leads to an exact and closed-form expression for the condition of marginal stability. This is in contrast to most other problem settings, where the solutions demands a numerical treatment, especially when Rayleigh and Marangoni effect are included in parallel – even for the single layer problem, cf. classical work of Nield [165].

(2) We will replace the often studied linear concentration profiles by the more appropriate nonlinear, time-dependent profiles in Sec. 3.4.2. In order to still obtain a closed-form stability threshold, the time evolution of the basic state is treated as decoupled (frozen in time) from the time evolution of the perturbations. A discussion of this stability results is postponed to the subsequent Sec. 3.5, where we combine these analytical results with an exemplary solution of the full equations.

Generally, the issue of stability in the two-layer setup has been studied thoroughly by former authors with different physical effects included, see [50, 164] for an overview. In fact,

stability results for two finite layers with linear basic profiles were performed in: Ref. [217](deformable interface), Ref. [96](with Rayleigh effect included) and [184] (deformable interface and also oscillatory modes). Recently, also time-dependent and nonlinear basic states received some interest. For this see the paper of Sun [222] and references therein, which however mostly rely on a "Biot boundary condition" for the solute transport at the interface, since they are tailored to a liquid/gas interface.

One study of a nonlinear basic state in the full two-layer setup has been performed by Gross&Hixon [83]. However, they used different initial and boundary condition, i.e. initially zero concentrations in both layers with a fixed concentration at the boundaries. There are also linear stability analysis that included the effects of adsorbed surfactants [39, 214] and heat of solution [173, 215, 216].

For the stability analysis, we will work in diffusive units $T_{diff} = (L^{(1)})^2/D^{(1)}$, L , $P_{diff} = \frac{\rho_{ref}^{(1)}(D^{(1)})^{(2)}}{L^2}$, $C = c_0$, while keeping the unit for length L unspecified. Perturbations are represented by normal modes [45]

$$u_z^{(j)}(x, y, z, t) = w^{(j)}(z) \exp(ik_x x + ik_y y + \sigma t), \quad (3.87)$$

$$c^{(j)}(x, y, z, t) = \theta^{(j)}(z) \exp(ik_x x + ik_y y + \sigma t) + C^{(j)}(z, t). \quad (3.88)$$

The profiles $C^{(i)}(z, t)$ are the basic state (solving the PM in the quiescent case). Quantities k_x, k_y are arbitrary wavenumbers with $k = \sqrt{k_x^2 + k_y^2}$ being their magnitude; and σ is the generally complex growth rate (although later it is assumed as real valued).

We restrict us to high Schmidt numbers and zero buoyancy $Ra = 0$. In this case, the perturbations are governed by the time-independent Stokes equations, i.e. Eqs. (3.55), (3.56), which are further simplified by taking twice the curl. This yields

$$0 = (d_z^2 - k^2)^2 w^{(1)}, \quad (3.89)$$

$$0 = (d_z^2 - k^2)^2 w^{(2)}. \quad (3.90)$$

The derivative with respect to the z-coordinate in the "profile functions" [$w^{(j)}(z), \theta^{(j)}(z), C^{(j)}(z, t)$] is denoted by d_z . Including the perturbation ansatz in Eqs. (3.57), (3.58) and afterwards linearizing around perturbations yields

$$\sigma \theta^{(1)} = -w^{(1)} d_z C^{(1)}(z, t) + (d_z^2 - k^2) \theta^{(1)}, \quad (3.91)$$

$$\sigma \theta^{(1)} = -w^{(2)} d_z C^{(2)}(z, t) + D(d_z^2 - k^2) \theta^{(2)}. \quad (3.92)$$

Note that the exponential ansatz in time is only formally admissible if the basic state $C^{(j)}$ does not depend on time. Nevertheless, the basic states are used with time "as a parameter"; thus, it is assumed that the basic state is frozen in time compared to the time evolution of the perturbations.

The matching condition for the perturbations at $z = 0$ read

$$H\theta^{(1)} - \theta^{(2)} = d_z(\theta^{(1)} - D\theta^{(2)}) = 0, \quad (3.93)$$

$$\mu d_z^2 w^{(2)} - d_z^2 w^{(1)} = -Ma k^2 \theta^{(1)}, \quad (3.94)$$

$$w^{(1)} = w^{(2)} = 0, \quad d_z w^{(1)} = d_z w^{(2)}. \quad (3.95)$$

In the present section, the Marangoni number is understood with the unspecified length scale L , thus $Ma = \frac{c_0 \alpha_c \sigma_{ref} L}{\rho^{(1)} \nu^{(1)} D^{(1)}}$. The velocity perturbation equations (3.89),(3.90) permit a

general solution by

$$w^{(i)}(z) = a^{(i)} \exp(-kz) + b^{(i)} \exp(kz) + c^{(i)} z \exp(-kz) + d^{(i)} z \exp(kz) \quad (3.96)$$

with eight constants depending on the boundary and matching conditions, thus in turn on wavenumber k and time of the basic state t . In the next sections, we will specify boundary conditions and the basic profiles $C^{(i)}(z, t)$.

3.4.1 Steady basic state

The finite system is approximated by two semi-infinite layers. Thus, boundary conditions alter to the assumptions that dependent variables are bounded at infinity or even decay to zero, i.e.

$$\begin{aligned} w^{(1)}(z \rightarrow -\infty) &\rightarrow 0, \quad w^{(2)}(z \rightarrow +\infty) \rightarrow 0, \\ \theta^{(1)}(z \rightarrow -\infty) &\rightarrow 0, \quad \theta^{(2)}(z \rightarrow +\infty) \rightarrow 0. \end{aligned} \quad (3.97)$$

By means of these condition and the continuity of velocities Eq. (3.95), the free parameters in the general solution of vertical velocities Eq. (3.96) are determined and incorporated into the solution:

$$w^{(1)}(z) = Kz \exp(kz) \text{ and } w^{(2)}(z) = Kz \exp(-kz), \quad (3.98)$$

where all eight constants were reduced to one free constant K .

The basic concentration profiles $C^{(i)}(z, t)$ are assumed linear with slope m in layer (1). They read

$$\partial_z C^{(1)} = m \text{ and with regard to Eq.(3.45) } \partial_z C^{(2)} = mD^{-1}. \quad (3.99)$$

This together with the derived velocity disturbances is plugged into the equations for concentration perturbations [Eqs. (3.92)-(3.92)]. Taking $\sigma = 0$ yields

$$Kz \exp(kz)m = (d_z^2 - k^2)\theta^{(1)}, \quad (3.100)$$

$$Kz \exp(-kz)mD^{-1} = D(d_z^2 - k^2)\theta^{(2)}. \quad (3.101)$$

These Eqs. (3.100),(3.101) are solved by

$$\theta^{(1)}(z) = e^{kz}C_1 + \frac{(-z + kz^2)Km e^{kz}}{4k^2}, \quad (3.102)$$

$$(3.103)$$

$$\theta^{(2)}(z) = e^{-kz}C_2 + \frac{(-z - kz^2)Kme^{-kz}}{4k^2D^2}. \quad (3.104)$$

Here, the terms unbounded for $z \rightarrow \pm\infty$ are disregarded right away, resulting to two free constants C_1, C_2 . As a next step, the Henry condition (3.93) relates the free constants by $C_2 = C_1H$. The continuity of mass fluxes (3.93) gives: $C_1 = Km(-1 + D)/(4Dk^3(DH + 1))$. Concentration perturbations (with determined free constants) are

$$\theta^{(1)}(z) = \frac{Km(-1 + D)e^{kz}}{4k^3(DH + 1)D} + \frac{Kme^{kz}(-z + kz^2)}{4k^2}, \quad (3.105)$$

$$\theta^{(2)}(z) = \frac{HKm(-1 + D)e^{-kz}}{4k^3(DH + 1)D} + \frac{(-z - kz^2)Kme^{-kz}}{4kD^2}. \quad (3.106)$$

In the last step, the Marangoni condition (3.94) provides the condition for marginal stability, which reads as follows

$$mMa = \frac{8k^2(1+\mu)D(DH+1)}{(-1+D)} \quad (3.107)$$

while K is canceling out due to linearity. Recall that the choice of L is arbitrary. It cancels out when we state the neutral curve with a dimensional wavenumber $\tilde{k} = k/L$ and dimensional concentration gradient $\tilde{m} = mc_0/L$

$$\frac{\tilde{m}\alpha_c\sigma_{ref}}{\rho^{(1)}\nu^{(1)}D^{(1)}} = \frac{8\tilde{k}^2(1+\mu)D(DH+1)}{(-1+D)} \quad (3.108)$$

or with the wavelength $\tilde{\lambda} = 2\pi/\tilde{k}$

$$\tilde{\lambda} = 2\pi\sqrt{\frac{\rho^{(1)}\nu^{(1)}D^{(1)}8(1+\mu)D(DH+1)}{(-1+D)\tilde{m}\alpha_c\sigma_{ref}}}. \quad (3.109)$$

Finally, the parameter range to satisfy Eq. (3.108) is discussed. Since \tilde{k} is an arbitrary positive number, only the sign of the right and left-hand side have to equate. Since most parameters are positive and appear as a simple factor, instability requires

$$\text{sign}(-1+D) = \text{sign}(\alpha_c\tilde{m}). \quad (3.110)$$

For example, when transfer is from (1) to (2) $\tilde{m} < 0$ and solute decreases tension $\alpha_c < 0$, then for instability it is required that $D > 1$; thus, layer (1) should have a lower diffusivity. By this, the onset of convection depends on: the mass-transfer direction, the solutal effect on interfacial tension and the diffusivity ratio. One may conclude that for most classes of solute $\alpha_c < 0$ holds, and by this, stationary instability appears for the transport out of the phase with lower diffusivity.

3.4.2 Non-linear basic state: frozen time analysis

In the present section, the basic state on which perturbations evolve is changed to the non-linear semi-infinite layer solution (Sec. 3.3). On this basis, the neutral curve is developed.

The basic state [for transport (1) \rightarrow (2)] from Eqs. (3.80),(3.81) is adapted to diffusive scales; it reads

$$C^{(1)} = \frac{1}{1+D^{0.5}H} \left(1 + D^{0.5}H \text{erf} \left(\frac{-z}{2\sqrt{t}} \right) \right), \quad (3.111)$$

$$C^{(2)} = \frac{H}{1+D^{0.5}H} \left(1 - \text{erf} \left(\frac{z}{2\sqrt{Dt}} \right) \right). \quad (3.112)$$

Actually, we only need the vertical derivative ^{IV},

$$\partial_z C^{(1)} = \frac{-1}{1+D^{0.5}H} \cdot \frac{D^{0.5}H}{\sqrt{\pi t}} e^{-\frac{z^2}{4t}}, \quad (3.113)$$

$$\partial_z C^{(2)} = \frac{-H}{1+D^{0.5}H} \cdot \frac{1}{\sqrt{\pi Dt}} e^{-\frac{z^2}{4Dt}}. \quad (3.114)$$

^{IV}Recall that for constant B it holds that $d_z(\text{erf}(Bz)) = 2B\exp(-B^2z^2)/\sqrt{\pi}$

These profiles are inserted into the perturbation equation (3.91),(3.92), which results to

$$Kz \exp(kz) \frac{-DH}{D^{0.5} + DH} \cdot \frac{1}{\sqrt{\pi t}} e^{-\frac{z^2}{4t}} = (d_z^2 - k^2)\theta^{(1)}, \quad (3.115)$$

$$Kz \exp(-kz) \frac{-H}{D^{0.5} + DH} \cdot \frac{1}{\sqrt{\pi t}} e^{-\frac{z^2}{4Dt}} = D(d_z^2 - k^2)\theta^{(2)}. \quad (3.116)$$

where the time t in the basic profiles is treated as a parameter; this time is "frozen". Alternatively, the perturbation would not grow exponentially, as was supposed and one is forced to proceed with other methods of hydrodynamic stability theory [195], which usually demand a numerical treatment.

Let us proceed with the following abbreviation,

$$A = \frac{HK}{D^{0.5} + DH} \cdot \frac{1}{\sqrt{\pi t}}. \quad (3.117)$$

By using Eq. (3.117), Eqs. (3.115),(3.116) simplify to

$$-ADze^{-\frac{z^2}{4t}+kz} = (d_z^2 - k^2)\theta^{(1)}, \quad (3.118)$$

$$-Aze^{-\frac{z^2}{4Dt}-kz} = D(d_z^2 - k^2)\theta^{(2)}. \quad (3.119)$$

Note that the reversed direction of transport (2)→(1), can be obtained by replacing Eq. (3.117) by

$$A^{rev} = \frac{-K}{D^{0.5} + DH} \cdot \frac{1}{\sqrt{\pi t}}. \quad (3.120)$$

Equation (3.120) is deduced by using the concentration profiles of the reversed direction Eq. (3.79).

The general solutions of Eqs. (3.118),(3.119) read as follows

$$\theta^{(1)}(z) = e^{-kz}C_1 + e^{kz}C_2 - 2ADt^{3/2}\sqrt{\pi}\operatorname{erf}\left(\frac{-z+4kt}{2\sqrt{t}}\right)e^{-kz+4k^2t} \quad (3.121)$$

$$\theta^{(2)}(z) = e^{kz}C_3 + e^{-kz}C_4 + 2A\sqrt{Dt}^{3/2}\sqrt{\pi}\operatorname{erf}\left(\frac{z+4kDt}{2\sqrt{Dt}}\right)e^{kz+4k^2Dt} \quad (3.122)$$

Now, more care has to be taken with the boundedness at infinity, i.e. condition (3.97) since two terms diverge. Nevertheless, constant C_1 and C_3 can be chosen properly, e.g.

$$C_1 = 2ADt^{3/2}\sqrt{\pi}e^{4k^2t}. \quad (3.123)$$

Consequently, perturbations are further specified by

$$\theta^{(1)}(z) = e^{kz}C_2 + 2ADt^{3/2}\sqrt{\pi}\operatorname{erfc}\left(\frac{-z+4kt}{2\sqrt{t}}\right)e^{-kz+4k^2t}, \quad (3.124)$$

$$\theta^{(2)}(z) = e^{-kz}C_4 - 2A\sqrt{Dt}^{3/2}\sqrt{\pi}\operatorname{erfc}\left(\frac{z+4kDt}{2\sqrt{Dt}}\right)e^{kz+4k^2Dt}, \quad (3.125)$$

where the complementary errorfunction is used, $\text{erfc}(x)=1-\text{erf}(x)$. Next, the Henry condition (3.93) relates C_4 as a function of C_2 by

$$C_4 = HC_2 + 2ADt^{3/2}\sqrt{\pi}\text{erfc}\left(2k\sqrt{t}\right)e^{4k^2t}H + 2A\sqrt{D}t^{3/2}\sqrt{\pi}\text{erfc}\left(2k\sqrt{Dt}\right)e^{4k^2Dt}, \quad (3.126)$$

and the continuity of mass fluxes (3.93) are used to determine C_2 as a function of physical parameters only

$$C_2 = -2 \frac{A\left(kD^2t^{3/2}\sqrt{\pi}\text{erfc}\left(2k\sqrt{t}\right)e^{4k^2t}H + 2D^{3/2}t^{3/2}\sqrt{\pi}\text{erfc}\left(2k\sqrt{Dt}\right)ke^{4k^2Dt} - Dt^{3/2}\sqrt{\pi}\text{erfc}\left(2k\sqrt{t}\right)ke^{4k^2t}\right)}{k(DH+1)}. \quad (3.127)$$

Finally, the Marangoni conditions (3.94) is applied to Eqs.(3.124),(3.125) and constants are included in order to derive the neutral curve $Ma(k, t)$:

$$Ma = \frac{-(1+\mu)(DH+1)(D^{0.5}+DH)}{2Hkt\left(e^{4k^2Dt}D^{3/2}(1-\text{erf}\left(2k\sqrt{D}\sqrt{t}\right)) - De^{4k^2t}(1-\text{Derf}\left(2k\sqrt{t}\right))\right)} \quad (3.128)$$

with the definition for A inserted. This expression is written in a more compact form by introducing the similarity variable

$$\eta = k^2t, \quad (3.129)$$

namely

$$Ma = \frac{k(1+\mu)(DH+1)(D^{0.5}+DH)}{2H\eta D \left[e^{4\eta}\text{erfc}\left(2\sqrt{\eta}\right) - e^{4\eta}D^{1/2}\text{erfc}\left(2\sqrt{\eta}D\right)\right]}. \quad (3.130)$$

Relation (3.128) can be regarded as a function for the marginal Marangoni number $Ma_m(p, k, t)$ depending on time t (at which basic state is taken), wavenumber k and the tuple of material-property ratios $p \equiv (\mu, D, H)$. As noted in the beginning, the current problem has to be independent of the chosen length unit L . This can be readily checked by introducing dimensional time $\tilde{t} = tL^2/D^{(1)}$, wavenumber $\tilde{k} = k/L$ and the similarity variable $\eta = \tilde{k}^2\tilde{t}D^{(1)}$ in Eq. (3.128) as consistency check. Consequently, from the independence of L (which is equivalent to principal of scale invariance discussed in Sec. 3.1.1) the following relation holds

$$Ma_m(p, t, k)/s = Ma_m(p, t \cdot s^2, k/s), \quad \forall s \in \mathbb{R}^+. \quad (3.131)$$

Here, the factor "s" can be interpreted as a change of the arbitrary length unit according to $L_{new} = L_{old}/s$.

This relation is useful, to determine unstable Marangoni number in time-wavenumber space from a known marginal point by a simple transformation. For instance, consider a marginal point (t^+, k^+) for a specific Marangoni number Ma^+ , then it holds that

$$Ma^+ = Ma_m(p^+, t^+, k^+). \quad (3.132)$$

From Eq. (3.131), we infer that for any $s > 1$ the point $(t^+ \cdot s^2, k^+/s)$ is the marginal point for Marangoni number of smaller modulus Ma^+/s . Thus, we can deduce that the full curve,

$$(t^+ \cdot s^2, k^+/s) \quad s > 1 \text{ with constant } p^+, Ma^+ \quad (3.133)$$

represent unstable conditions. With this, we followed standard reasoning of stability theory. Formally, one might show that for this Marangoni number Ma^+ , the growth rate σ has a positive real part.

The relation (3.128) implicitly provides a set of marginal times and wavenumbers (k_m, t_m) for a given set of physical parameters, i.e. p, Ma . To plot these pairs, (3.130) is rearranged as follows:

$$t_m = \left(\frac{(1 + \mu)(DH + 1)(D^{0.5} + DH)}{2H\sqrt{\eta}D [e^{4\eta}\text{erfc}(2\sqrt{\eta}) - e^{4\eta D}D^{1/2}\text{erfc}(2\sqrt{\eta D})]} \cdot \frac{1}{Ma} \right)^2 \quad (3.134)$$

A valuable information, we like to derived form (3.134), is the smallest time for which instability might be observed. Unfortunately, we were not able to derive the position (η_c) of the minimal time, i.e. $\partial_\eta t_m(\eta_c, p, Ma) = 0$, in a closed form expression. Therefore, it is proceeded with a specific example which treats Eq. (3.134) numerically. Nevertheless, as a further step (not developed here), Eq. (3.134) might be expanded for $\eta \rightarrow 0, \infty$.

3.5 Application of linear theory

In the current section, the just derived stability results [Eq. (3.134)] are applied to a specific system and compared to fully nonlinear simulation.

Therefore, let us choose the following ^V set of physical parameters: $D = 0.082$, $H = 1.6$, $Ma = 1.69 \cdot 10^6$, $\mu = 20.74 \cdot 0.96$, $\nu = 20.74$, $\rho = 0.96$, $Sc^{(1)} = 1348.3$, $G = 0$. The marginal times, according to (3.134), are plotted in Fig. 3.2(a) as a function of the similarity variable η . From this data the marginal curve (t_m, k_m) is derived by the definition of the similarity variable (3.129), i.e.

$$(t_m(\eta), \sqrt{t_m(\eta)/\eta}), \quad (3.135)$$

and plotted in Fig. 3.2(b). This figure shows the instable region (ruled area) with instable curves according to (3.133). The smallest marginal time – noted as critical time t_c – is approximately $t_c = 5 \cdot 10^{-8}$ with a wavenumber of $k_c = 1420$.

A general problem in the interpretation of this data is that the basic state may change significantly faster than the disturbance grows since this has been ignored by the "frozen time" assumption. Some additional evidence to judge if convection sets in is provided by defining a concentration boundary layer depth $\delta c_I^{(i)}$ and comparing it to the unstable wavenumbers by $2\pi/\delta c_I^{(i)}$. These boundary layer widths [for a transport (1) \rightarrow (2)] are defined by

$$\delta c_I^{(2)} = \frac{\langle c^{(2)} \rangle_s}{|\langle \partial_z c^{(2)} \rangle_s|} = \sqrt{Dt\pi}, \quad (3.136)$$

$$\delta c_I^{(1)} = \frac{1 - \langle c^{(1)} \rangle_s}{|\langle \partial_z c^{(1)} \rangle_s|} = \sqrt{t\pi}, \quad (3.137)$$

here the basic state (3.111),(3.112) has been inserted. Both of these length scales are included into Fig. 3.2(b) (circles and diamonds), they pierce the instable region at times that are higher than the critical time. Before that, the wavelength of growing modes is larger than the size of this boundary layers.

^VThis is motivated by the isopropanol system used in Ch. 7 with a reversed α_c however. Already used in Sec. 3.3.

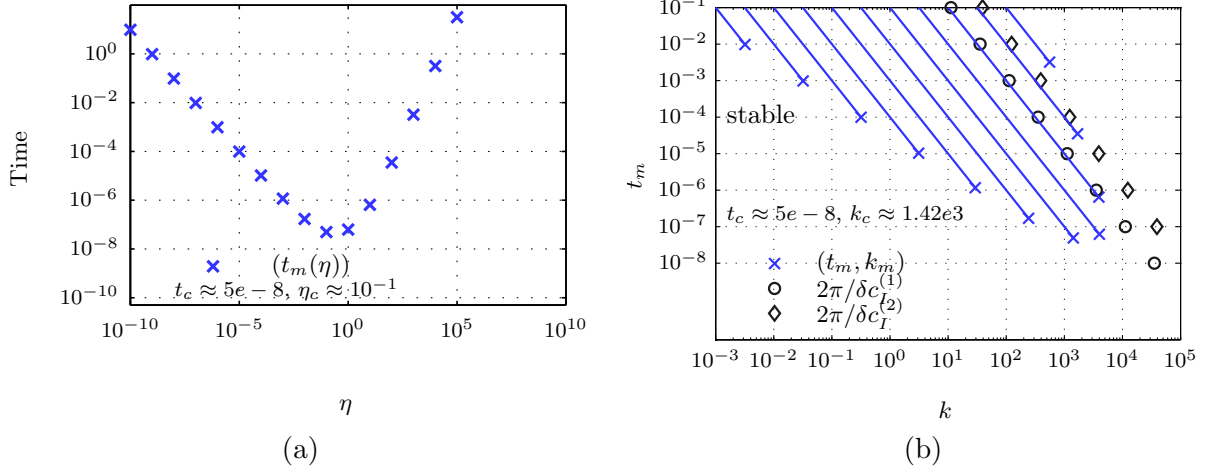


Figure 3.2: Marginal stability results for the sample system (parameters introduced in the text): (a) Marginal time versus similarity variable according to Eq. (3.134) and (b) versus wavenumber according to Eq. (3.128).

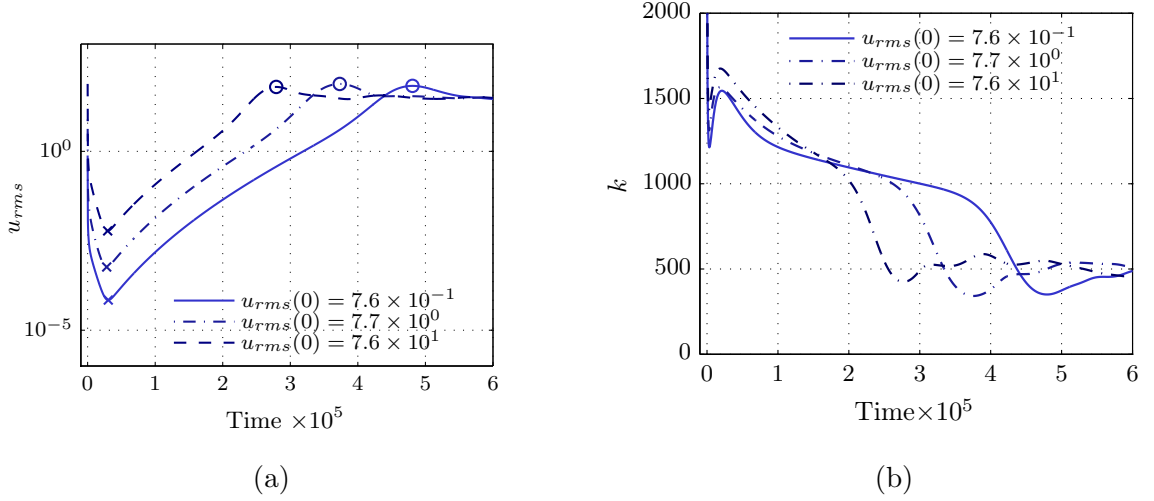


Figure 3.3: Full simulation in 2D domain, material parameter are given in the text, numerical parameters are $l_x = 0.2$, $l_y \rightarrow 0$, $N_x = 1024$, $N_z^{(1)} = 128$, $N_z^{(2)} = 256$, $\delta t_{max} = 7 \cdot 10^{-10}$. (a) Shows root mean squared velocity $1/2 \left(\sqrt{\langle \mathbf{u}^{(1)} \cdot \mathbf{u}^{(1)} \rangle_{xyz}} + \sqrt{\langle \mathbf{u}^{(2)} \cdot \mathbf{u}^{(2)} \rangle_{xyz}} \right)$ with onset times (defined in the text) $t_{c1} = 3.05 \cdot 10^{-6}$, $2.81 \cdot 10^{-6}$, $2.97 \cdot 10^{-6}$ and $t_{c3} = 4.81 \cdot 10^{-5}$, $3.73 \cdot 10^{-5}$, $2.79 \cdot 10^{-5}$ – in the order of increasing initial amplitude, respectively. (b) Characteristic wavenumber according to Eq. (3.143) by means of interfacial concentration.

These predictions from linear stability analysis are now compared to full simulations of the PM in a 2D domain for three different cases. Each case is initialized with a random velocity field (resembling white noise), where each case has a different initial amplitude and velocity fields are uncorrelated between the various simulations. The general approach for setting the initial conditions is noted in Ch. 5.

As far as the general situation is concerned, no canonical definition of "convection onset" and "characteristic wavenumbers" of structures is available. Thus, to define an onset of convection let us focus on the root-mean-squared (rms) velocity of both layers $u_{rms}(t)$, which seems most appropriate to us. Fig. 3.3(a) shows the results for the three simulations.

Now, different kinds of onset times can be defined. Firstly, the earliest time t_{c1} is taken for that rms velocity is growing, i.e.

$$t_{c1} = \min\{t : 0 < \frac{du_{rms}}{dt}(t)\}. \quad (3.138)$$

These times are drawn as a crosses in Fig. 3.3(a). It is approximately $t_{c1} \approx 3 \cdot 10^{-6}$ for all three, so, it changes only slightly with initial amplitude; compared to the linear prediction $t_c = 5 \cdot 10^{-8}$, it is distinctly later. However, it is in the time range when concentration boundary layer width cross the instable domian (see Fig. 3.2).

The difference in times may result from the interplay of stable modes that were damped (being introduced by initial perturbations) and some unstable modes that were growing. The time when growing modes outperform damped modes can not be predicted without the initial distribution of modes is known. Therefore the definite time t_{c1} may critically depend on the initial distribution of modes in the perturbation. Between cases, the qualitative distribution of modes (normalized amplitude per wavenumber) are supposed to be similar since they are generated by the same random variable.

Another possibility to characterize onset – clearly later in time – is the time t_{c2} when the positive growth rate has its first (local) maximum, i.e. an inflection point

$$d^2u_{rms}(t_{c2})/dt^2 = 0. \quad (3.139)$$

This location in time t_{c2} is maybe more related to an experimentally observed onset, but was observed to be not robust (in the sense that it reflects a similar "convective state" for our problem). Therefore is is not included in the figures.

A third choice is the first time (excluding $t < t_{c1}$) when rms velocity is maximal

$$t_{c3} = \min\{t : du_{rms}(t)/dt = 0 \wedge d^2u_{rms}(t)/dt^2 < 0\}. \quad (3.140)$$

These times are drawn as a circle in 3.3(a). At this time (if at all) convection is definitively observable in an experiment. It clearly decreases ($t_{c3}=4.81 \cdot 10^{-5}$, $3.73 \cdot 10^{-5}$, $2.79 \cdot 10^{-5}$) with increasing initial perturbation strength. This behavior gets obvious by observing the evolution of the rms velocity in Fig. 3.3(a). The initial net damping of modes and subsequent growth appears with a similar (between cases) exponential growth rate.

To quantify the length scales of structures, interfacial concentration $c^{(1)}(x, y, z = 0)$ is analyzed. Namely, a characteristic wavenumbers $k_{avg}(t)$ is calculated by a weighted mean of wavenumbers that uses the square of corresponding Fourier coefficients. Formally, for a generic function $Q(x, y, t)$, the discrete Fourier coefficients are computed by the values given

at the discrete points x_n, y_m

$$\hat{Q}(k_x, k_y, t) = \frac{1}{N_x N_y} \sum_{n=0}^{N_x-1} \sum_{m=0}^{N_y-1} Q(x_n, y_m, t) e^{-ik_x x_n} e^{-ik_y y_m}, \quad (3.141)$$

with the set of wavenumbers used in the numerical scheme (see Ch. 4 for details). From this amplitudes, an averaged powerspectrum $H_2(k, t)$ is calculated

$$H_2^Q(k, t) = \sum_{\sqrt{k_x^2 + k_y^2} \in [k \pm \frac{\pi}{2}]} |\hat{Q}(k_x, k_y, t)|^2, \quad (3.142)$$

and a dominant wavenumber is identified by a weighted average k_{avg} ,

$$k_{avg}^Q(t) = \frac{\sum_k H_2^Q(k, t) k}{\sum_k H_2^Q(k, t)}. \quad (3.143)$$

Fig. 3.3(a) shows the time evolution of k_{avg}^c for the three cases. Overall, the range of wavenumbers is in line with the predicted range from the linear analysis [Fig. 3.3(b)]. All three cases show a similar behavior: around t_{c1} the averaged wavenumber is slightly decreasing, while around t_{c3} (which is shifted between cases) wavenumbers drop steeply due to nonlinear effects of strong convection. After the definite onset, all three cases show similar wavenumbers.

3.6 Conclusion

Let us shortly summarize the main points of this chapter.

(1) In the first Sec. 3.1 the PM equations are nondimensionalized with different units. Under the assumption that no outer scale influences the evolution (i.e. the system consists practically of two semi-infinite layers), the mathematical problem will be invariant under a change of initial concentration if only Rayleigh or Marangoni effect is present. Consequently, changes in concentration can be accounted by a scaling of units: for the Marangoni case ($G = 0$)

$$\tilde{L} \propto c_0^{-1}, \quad \tilde{T} \propto c_0^{-2} \Rightarrow \tilde{U} \propto c_0^{+1}, \quad (3.144)$$

and for the Rayleigh case ($Ma = 0$)

$$\tilde{L} \propto c_0^{-1/3}, \quad \tilde{T} \propto c_0^{-2/3} \Rightarrow \tilde{U} \propto c_0^{+1/3}. \quad (3.145)$$

Although these relations are no novel findings^{VI}, a rigorous discussion appeared valuable to us, especially, in the view of simulations in following chapters. Nevertheless, since layer heights are generally important parameters, viscous units that measure length in multiples of the lower layer height were introduced. In this units, the essential non-dimensional parameters are identified and introduced in Tab. 3.1

(2) In Sec. 3.2, it is shown that if inertial effects can be neglected (Stokes flow) and buoyancy effects are absent ($G = 0$), the velocity field is mirror symmetric to the interface (in the

^{VI}For example, Blair&Quinn [27] noted these relations and used them to analysis the onset of convection for varied initial concentration

framework of the PM).

(3) In the case of two semi-infinite layers and zero motion $\mathbf{u} = 0$, the PM obeys a solution of closed form (Sec. 3.3). The solution for this purely diffusive transport is presented for both directions of transport. Although, this is a classical result [51], we outlined it in detail owing to its frequent application in this thesis.

(4) In Sec. 3.4, the onset of convection (for $G = 0$) is analyzed in terms of the linear stability of the pure diffusive evolution (i.e. the basic state). Classical results were reviewed, and the central finding of Sterling&Scriven [219] for marginal stability was reproduced in detail.

Based on this, we performed a novel linear stability analysis of the time-dependent, nonlinear concentration profile. The dependence of the basic state on time is regarded as decoupled from the time on which perturbations are evolving (frozen time). Under this assumption, a closed form expression Eq. (3.130) for the conditions of marginal stability has been derived. This relation shows that the basic state is stable for early times and that the range of unstable wavenumber grows with time.

Let us note that this analysis could be naturally extended by: assuming a finite systems in line with the analysis in [83] (they used a different basic state) and by relaxing the frozen in time assumption by more sophisticated non-modal methods [110, 195] of stability analysis.

(5) In Sec. 3.5, these predictions are applied to a specific system, for which a nonlinear simulation was carried out. The comparison leads to the conclusion that the predicted times (of linear analysis) might be considered as a lower bound for an observable time of onset. Furthermore, it was observed that onset time t_{c3} , crucially depends on the initial strength of perturbations. Furthermore, if one requires that the width of the concentration boundary layers being comparable to the unstable wavelength, then a better match between the linear prediction and the start of net kinetic energy growth was observed.

Chapter 4

Numerical methods

This chapter presents the numerical method used to solve the PM in viscous units, stated in Sec. 3.1.2. A pseudospectral method is employed. It has been developed for previous investigations of thermal interfacial convection by Boeck and co-workers [28–30]. Since this numerical scheme is well established, tested and only marginal changes in the main procedure were necessary; only a minimal amount of information is provided here to describe our numerical methods (see also thesis of Boeck [31] for further details). A general treatment of pseudospectral discretization methods and their application in the realm of fluid mechanics can be found in the classical book of Canuto *et al.* [42] or from Peyret [176].

For the current application, the temperature (relative to [29]) is replaced by the concentration field with its jump condition at the interface. Additionally, de-aliasing was applied for the horizontal directions, i.e. expansion coefficients related to wavenumbers k_x or k_y bigger than three fourth of their maximum absolute value were zeroed. To account for the transient features of the equilibration process, an automatic adjustment of the time-step size is included. This adjustment is included to account for the reduction of concentration difference over time, which is in contrast to the fixed forcing used in Ref. [29]

Furthermore, the increased problem size was accounted by including new output routines, which enabled a parallel input/output for full snapshots and new routines for saving visualization files in a binary format to save disk space.

The numerical scheme is programmed in the C language, and beside a few simulation done at FZ Jülich (NIC), computations were carried out at the computing center (UniRZ) of TU Ilmenau.

This chapter proceeds as follows. The momentum balance is reformulated into a pressure free formulation in Sec. 4.1. A spectral Galerkin approximation for the periodic directions and a finite difference approximation for the time are applied to the governing equations in Sec. 4.2. In this framework, the strategy to enforce boundary and matching conditions related to the vertical direction are described in Sec. 4.3.

4.1 Pressure-free formulation

This section reformulates the PM in viscous units (Sec. 3.1.2) into a pressure free formulation, using the incompressibility constraint. Since the velocity field is periodic in the x-y dimension and divergence-free ($\nabla \cdot \mathbf{u}$), it can be represented by the new scalar functions

$\phi^{(i)}(\mathbf{x}, t), \psi^{(i)}(\mathbf{x}, t), F_x^{(i)}(z, t), F_y^{(i)}(z, t), F_z^{(i)}(t)$ [196] in the form of

$$\mathbf{u}^{(i)} = \nabla \times \left[\nabla \times (\mathbf{e}_z \phi^{(i)}) \right] + \nabla \times (\mathbf{e}_z \psi^{(i)}) + F_x^{(i)} \mathbf{e}_x + F_y^{(i)} \mathbf{e}_y + F_z^{(i)} \mathbf{e}_z, \quad (4.1)$$

or in an equivalent form

$$\mathbf{u}^{(i)}(\mathbf{x}, t) = \begin{pmatrix} \partial_z \partial_x \\ \partial_z \partial_y \\ -\Delta_2 \end{pmatrix} \phi^{(i)}(\mathbf{x}, t) + \begin{pmatrix} \partial_y \\ -\partial_x \\ 0 \end{pmatrix} \psi^{(i)}(\mathbf{x}, t) + \begin{pmatrix} F_x^{(i)}(z, t) \\ F_y^{(i)}(z, t) \\ F_z^{(i)}(t) \end{pmatrix} \quad (4.2)$$

This representation is unique and $P = \nabla \times \nabla \times (\mathbf{e}_z \phi)$ is denoted as the poloidal part und $T = \nabla \times (\psi \mathbf{e}_z)$ as the toroidal part, respectively. Both yield zero when averaged over a horizontal plane [196]

$$\langle \phi^{(i)} \rangle_{xy} = \langle \psi^{(i)} \rangle_{xy} = 0, \quad (4.3)$$

thus, $F_x^{(i)}, F_y^{(i)}, F_z^{(i)}$ describe the mean velocity. Right away we can set $F_z^{(i)}$ to zero $F_z^{(i)} = 0$ since no fluid enter the solid boundaries [see Eqs. (3.43), (3.44)]. Furthermore, it is used that the scalar potentials $\phi^{(i)}, \psi^{(i)}$ are related to the vertical velocity and the vertical vorticity (with the horizontal Laplacian $\Delta_2 = \partial_x^2 + \partial_y^2$), which reads

$$u_z^{(i)} = -\Delta_2 \phi^{(i)} \quad (4.4)$$

and

$$\omega_z^{(i)} = \boldsymbol{\omega}^{(i)} \cdot \mathbf{e}_z = (\nabla \times \mathbf{u}^{(i)})_z = -\Delta_2 \psi^{(i)}. \quad (4.5)$$

In the following, the vertical velocity and the vertical vorticity are used as the primary quantities for calculations. Starting with these quantities the full velocity field is calculated by solving

$$\Delta_2 u_x^{(i)} = -\partial_x \partial_z u_z^{(i)} - \partial_y \omega_z^{(i)}, \quad (4.6)$$

$$\Delta_2 u_y^{(i)} = -\partial_y \partial_z u_z^{(i)} + \partial_x \omega_z^{(i)}. \quad (4.7)$$

These relations, derived with the help of the divergence free constraint, determine the velocity up the mean velocities $F_x^{(i)}, F_y^{(i)}$.

In the next stage, the momentum balance [(3.37),(3.39)] is formulated in terms of $u_z^{(i)}$ und $\omega_z^{(i)}$. For this, the curl is applied to the momentum balance [(3.37),(3.39)], which yields ^I

$$\partial_t \boldsymbol{\omega}^{(1)} - \nabla \times (\mathbf{u}^{(1)} \times \boldsymbol{\omega}^{(1)}) = \Delta \boldsymbol{\omega}^{(1)} + G \partial_x c^{(1)} \mathbf{e}_y - G \partial_y c^{(1)} \mathbf{e}_x, \quad (4.8)$$

$$\partial_t \boldsymbol{\omega}^{(2)} - \nabla \times (\mathbf{u}^{(2)} \times \boldsymbol{\omega}^{(2)}) = \nu \Delta \boldsymbol{\omega}^{(2)} + G \beta \partial_x c^{(2)} \mathbf{e}_y - G \beta \partial_y c^{(2)} \mathbf{e}_x. \quad (4.9)$$

Again applying the curl on these equations, we derive ^{II}

$$\partial_t \Delta u_z^{(1)} + \partial_z \nabla \cdot (\mathbf{u}^{(1)} \times \boldsymbol{\omega}^{(1)}) - \mathbf{e}_z \cdot \Delta (\mathbf{u}^{(1)} \times \boldsymbol{\omega}^{(1)}) = \Delta \Delta u_z^{(1)} - \Delta_2 c^{(1)} G, \quad (4.10)$$

$$\partial_t \Delta u_z^{(2)} + \partial_z \nabla \cdot (\mathbf{u}^{(2)} \times \boldsymbol{\omega}^{(2)}) - \mathbf{e}_z \cdot \Delta (\mathbf{u}^{(2)} \times \boldsymbol{\omega}^{(2)}) = \nu \Delta \Delta u_z^{(2)} - \Delta_2 c^{(2)} G \beta. \quad (4.11)$$

^I It is used that for any smooth tensor field A (we only treat Cartesian tensor [1, 193]) $\nabla(A \cdot A) = 2A \times (\nabla \times A) + 2A \cdot \nabla A$ holds.

^{II}Note the following useful identity $\nabla \times \nabla \times A = \nabla \nabla \cdot A - \Delta A$

The equations to determine the mean flows $F_x^{(i)}$, und $F_y^{(i)}$ are derived by averaging the momentum balance [(3.37),(3.39)] over x-y planes and including the periodicity conditions [(3.47)-(3.49)]. These equations are

$$\partial_t F_x^{(1)}(z) + d_z \langle u_x^{(1)} u_z^{(1)} \rangle_{xy} = d_z^2 F_x^{(1)}, \quad (4.12)$$

$$\partial_t F_y^{(1)}(z) + d_z \langle u_y^{(1)} u_z^{(1)} \rangle_{xy} = d_z^2 F_y^{(1)}, \quad (4.13)$$

$$\partial_t F_x^{(2)}(z) + d_z \langle u_x^{(2)} u_z^{(2)} \rangle_{xy} = \nu d_z^2 F_x^{(2)}, \quad (4.14)$$

$$\partial_t F_y^{(2)}(z) + d_z \langle u_y^{(2)} u_z^{(2)} \rangle_{xy} = \nu d_z^2 F_y^{(2)}. \quad (4.15)$$

To close the problem, boundary and matching conditions [Eqs. (3.43)-(3.46)] are adapted to the new formulation with the help of the divergence free constraint $\nabla \cdot \mathbf{u}^{(i)}$. Those conditions are

$$Hc^{(1)} - c^{(2)} = \partial_z(c^{(1)} - Dc^{(2)}) = 0, \quad (4.16)$$

$$\mu \partial_z \omega_z^{(2)} = \partial_z \omega_z^{(1)}, \quad \omega_z^{(1)} = \omega_z^{(2)}, \quad (4.17)$$

$$\mu \partial_z \partial_z u_z^{(2)} - \partial_z \partial_z u_z^{(1)} = \frac{Ma}{Sc^{(1)}} \Delta_2 c^{(1)}, \quad (4.18)$$

$$u_z^{(1)} = u_z^{(2)} = 0, \quad \partial_z u_z^{(1)} = \partial_z u_z^{(2)}, \quad (4.19)$$

$$F_x^{(1)} = F_x^{(2)}, \quad \partial_z \mu F_x^{(2)} = \partial_z F_x^{(1)}, \quad (4.20)$$

$$F_y^{(1)} = F_y^{(2)}, \quad \partial_z \mu F_y^{(2)} = \partial_z F_y^{(1)}. \quad (4.21)$$

4.2 Discretization of the governing equations

The discretization method is pseudospectral [42]. Both planar layers are treated as separate computational domains that are coupled at the interface. In each layer, the fields are expanded in truncated Fourier series in the two periodic horizontal directions x, y . The vertical direction z is expanded in Chebyshev polynomials T_p of order p , which read

$$T_p(s) = \cos[p \arccos(s)] \text{ with } s \in [-1, 1]. \quad (4.22)$$

The smallest wavenumbers for the x,y directions are $k_{x0} = 2\pi/l_x$, $k_{y0} = 2\pi/l_y$, respectively. For example, the expansion of a generic field q in the upper layer, where $(x, y, z) \in [0, l_x] \times [0, l_y] \times [0, d]$, reads

$$q^{(2)}(x, y, z, t) = \sum_{m=-N_x/2}^{N_x/2-1} \sum_{n=-N_y/2}^{N_y/2-1} \sum_{p=0}^{N_z^{(2)}} e^{imk_{x0}x + ink_{y0}y} T_p(2z/d - 1) \hat{q}^{(2);mnp}(t), \quad (4.23)$$

and in the lower layer $(x, y, z) \in [0, l_x] \times [0, l_y] \times [0, -1]$,

$$q^{(1)}(x, y, z, t) = \sum_{m=-N_x/2}^{N_x/2-1} \sum_{n=-N_y/2}^{N_y/2-1} \sum_{p=0}^{N_z^{(1)}} e^{imk_{x0}x + ink_{y0}y} T_p(2z + 1) \hat{q}^{(1);mnp}(t), \quad (4.24)$$

where i is the imaginary number. The expansion coefficients \hat{q}^{mnp} are calculated from the values at the equidistant grid points in the $x - y$ plane and the Chebyshev-Gauss-Lobatto points [42] in the z dimension, for layer (2) they are

$$\left(x_i, y_j, z_k \right) = \left(i \cdot l_x / N_x, \quad j \cdot l_y / N_y, \quad d \cdot 0.5 [1 + \cos(k\pi / N_z^{(2)})] \right), \quad (4.25)$$

with $i \in \{0, 1, \dots, N_x\}, j \in \{0, 1, \dots, N_y\}, k \in \{0, 1, \dots, N_z^{(2)}\}$. The collocation points for layer (1) are

$$(x_i, y_j, z_k) = \left(i \cdot l_x / N_x, j \cdot l_y / N_y, 0.5[\cos(k\pi / N_z^{(1)}) - 1] \right), \quad (4.26)$$

now with $k \in \{0, 1, \dots, N_z^{(1)}\}$. Furthermore, let us introduce the set of wave vectors K by

$$K = \{(m2\pi/l_x \mathbf{e}_x + n2\pi/l_y \mathbf{e}_y) \text{ for } m \in \{-N_x/2, \dots, N_x/2 - 1\}, n \in \{-N_y/2, \dots, N_y/2 - 1\}\}. \quad (4.27)$$

The discrete transform from the grid values to the "coefficient space" is first done with respect to the Fourier basis for each wavevector $\mathbf{k} \in K$ by

$$q_{\mathbf{k}}(z, t) = \hat{q}(rk_{x0}, sk_{y0}, z, t) = \frac{1}{N_x N_y} \sum_{n=0}^{N_x-1} \sum_{m=0}^{N_y-1} q(x_n, y_m, z, t) e^{-ik_{x0} r x_n} e^{-ik_{y0} s y_m}, \quad (4.28)$$

then for the Chebyshev basis, cf. [42](p. 67)

$$q_{\mathbf{k}}^p(t) = \hat{q}^{mnp} = \sum_{j=0}^{N_z} \hat{q}(mk_{x0}, nk_{y0}, z, t) \frac{2}{N_z c_j c_p} \cos\left(\frac{\pi j p}{N_z}\right), \quad (4.29)$$

where

$$c_j = \begin{cases} 2 & j = 0, N_z \\ 1 & 1 \leq j \leq N_z - 1 \end{cases}. \quad (4.30)$$

The expansion coefficients $q_{\mathbf{k}}^p$ are complex numbers; they obey $\hat{q}_{\mathbf{k}}^p = \overline{\hat{q}_{-\mathbf{k}}^p}$, where "q" means complex conjugate, since a real valued function is expanded.

Practically, the transformation between expansion coefficients and point values is done with a Fast Fourier Transformation (FFT) and a Fast Cosine Transformation, see [31, 180] for details. Parallelization uses a domain decomposition in one horizontal direction – of physical as well as coefficient space, see [31] for details. It is implemented with the message passing interface (MPI) standard. The number of grid points in each direction is a power of two because only base two FFTs are used.

In the next stage, the PM is formulated in a semi-discrete manner. Thus, for the x-y plane the projection of the residual onto the Fourier basis (Galerkin method) is required to vanish [42]. For a generic equation $Q(q) = 0$, this requirement reads

$$\int_{[0, l_x] \times [0, l_y]} [Q(q(x, y))] e^{-i(xk_x + yk_y)} dA = 0, \quad \forall \mathbf{k} \in K \quad (4.31)$$

but with the z -direction treated as continuous. A time-stepping scheme is employed that is based on an equidistant temporal discretization $t^n = t_0 + nh$ with time-step h . The linear terms are treated with the Euler backward formula, and the non-linear terms are treated explicitly with the Adams-Bashforth method [29]. Formally, for a generic transport equation with linear term L and non-linear term Q ,

$$\partial_t q(t) = L(t) + Q(t), \quad (4.32)$$

the time discretization (using $q(t^n) = q^n$) is

$$\frac{q^{n+1} - q^n}{h} = L^{n+1} + 1.5Q^n - 0.5Q^{n-1}. \quad (4.33)$$

Furthermore, a convenient abbreviation for the Adams-Bashforth formulas is used: $AB\{Q\}^n = 1.5Q^n - 0.5Q^{n-1}$.

On this basis, the semi-discrete PM by means of the momentum balance [Eqs. (4.8)-(4.15)] and the mass balance [(3.42) - (3.42)] is reformulated as follows:

$$(d_z^2 - \mathbf{k}^2 - \frac{1}{h})\omega_{z;\mathbf{k}}^{(1);n+1} = -\frac{\omega_{z;\mathbf{k}}^{(1);n}}{h} - AB\{[\mathbf{e}_z \cdot \nabla \times (\mathbf{u}^{(1)} \times \omega^{(1)})]_{\mathbf{k}}\}^n, \quad (4.34)$$

$$(d_z^2 - \mathbf{k}^2 - \frac{1}{h\nu})\omega_{z;\mathbf{k}}^{(2);n+1} = -\frac{\omega_{z;\mathbf{k}}^{(2);n}}{h\nu} - \frac{1}{\nu}AB\{[\mathbf{e}_z \cdot \nabla \times (\mathbf{u}^{(2)} \times \omega^{(2)})]_{\mathbf{k}}\}^n, \quad (4.35)$$

$$(d_z^2 - \mathbf{k}^2 - \frac{1}{h})\eta_{\mathbf{k}}^{(1);n+1} = -\frac{\eta_{\mathbf{k}}^{(1);n}}{h} + AB\{[\partial_z \nabla \cdot (\mathbf{u}^{(1)} \times \omega^{(1)}) - \mathbf{e}_z \cdot \Delta(\mathbf{u}^{(1)} \times \omega^{(1)})]_{\mathbf{k}}\}^n - AB\{\mathbf{k}^2 c_{\mathbf{k}}^{(1)} G\}^n, \quad (4.36)$$

$$(d_z^2 - \mathbf{k}^2 - \frac{1}{h\nu})\eta_{\mathbf{k}}^{(2);n+1} = -\frac{\eta_{\mathbf{k}}^{(2);n}}{\nu h} + \frac{1}{\nu}AB\{[\partial_z \nabla \cdot (\mathbf{u}^{(2)} \times \omega^{(2)}) - \mathbf{e}_z \cdot \Delta(\mathbf{u}^{(2)} \times \omega^{(2)})]_{\mathbf{k}}\}^n - \frac{1}{\nu}AB\{\mathbf{k}^2 c_{\mathbf{k}}^{(2)} G\beta\}^n, \quad (4.37)$$

$$(d_z^2 - \mathbf{k}^2)u_{z;\mathbf{k}}^{(1);n+1} = \eta_{\mathbf{k}}^{(1);n+1}, \quad (4.38)$$

$$(d_z^2 - \mathbf{k}^2)u_{z;\mathbf{k}}^{(2);n+1} = \eta_{\mathbf{k}}^{(2);n+1}, \quad (4.39)$$

$$(d_z^2 - \frac{1}{h})F_x^{(1);n+1} = -\frac{F_x^{(1);n}}{h} + AB\{\partial_z \langle u_x^{(1)} u_z^{(1)} \rangle_{xy}\}^n, \quad (4.40)$$

$$(d_z^2 - \frac{1}{h\nu})F_x^{(2);n+1} = -\frac{F_x^{(2);n}}{h\nu} + \frac{1}{\nu}AB\{\partial_z \langle u_x^{(2)} u_z^{(2)} \rangle_{xy}\}^n, \quad (4.41)$$

$$(d_z^2 - \frac{1}{h})F_y^{(1);n+1} = -\frac{F_y^{(1);n}}{h} + AB\{\partial_z \langle u_y^{(1)} u_z^{(1)} \rangle_{xy}\}^n, \quad (4.42)$$

$$(d_z^2 - \frac{1}{h\nu})F_y^{(2);n+1} = -\frac{F_y^{(2);n}}{h\nu} + \frac{1}{\nu}AB\{\partial_z \langle u_y^{(2)} u_z^{(2)} \rangle_{xy}\}^n, \quad (4.43)$$

$$(d_z^2 - \mathbf{k}^2 - \frac{Sc^{(1)}}{h})c_{\mathbf{k}}^{(1);n+1} = -\frac{c_{\mathbf{k}}^{(1);n} Sc^{(1)}}{h} + Sc^{(1)} AB\{[\mathbf{u}^{(1)} \cdot \nabla c^{(1)}]_{\mathbf{k}}\}^n, \quad (4.44)$$

$$(d_z^2 - \mathbf{k}^2 - \frac{Sc^{(1)}}{Dh})c_{\mathbf{k}}^{(2);n+1} = -\frac{c_{\mathbf{k}}^{(2);n} Sc^{(1)}}{Dh} + \frac{Sc^{(1)}}{D} AB\{[\mathbf{u}^{(2)} \cdot \nabla c^{(2)}]_{\mathbf{k}}\}^n, \quad (4.45)$$

where we have used a short notion for the Laplacian of the vertical velocity, namely

$$\Delta u_z^{(i)} = \eta^{(i)}. \quad (4.46)$$

The conditions on the top boundary (3.44) ($z = d$) are

$$F_x^{(2)} = F_y^{(2)} = \omega_{z;\mathbf{k}}^{(2)} = u_{z;\mathbf{k}}^{(2)} = d_z u_{z;\mathbf{k}}^{(2)} = d_z c_{\mathbf{k}}^{(2)} = 0, \quad (4.47)$$

and on the bottom $z = -1$ (3.43) are

$$F_x^{(1)} = F_y^{(1)} = \omega_{z;\mathbf{k}}^{(1)} = u_{z;\mathbf{k}}^{(1)} = d_z u_{z;\mathbf{k}}^{(1)} = d_z c_{\mathbf{k}}^{(1)} = 0. \quad (4.48)$$

The matching conditions [(3.45)-(3.46)] in terms of expansion coefficients at $z = 0$ are

$$Hc_{\mathbf{k}}^{(1)} - c_{\mathbf{k}}^{(2)} = d_z c_{\mathbf{k}}^{(1)} - Dd_z c_{\mathbf{k}}^{(2)} = 0, \quad (4.49)$$

$$\mu d_z \omega_{z;\mathbf{k}}^{(2)} = d_z \omega_{z;\mathbf{k}}^{(1)}, \quad \omega_{z;\mathbf{k}}^{(1)} = \omega_{z;\mathbf{k}}^{(2)}, \quad (4.50)$$

$$\mu d_z^2 u_{z;\mathbf{k}}^{(2)} - d_z^2 u_{z;\mathbf{k}}^{(1)} = -\frac{Ma}{Sc^{(1)}} \mathbf{k}^2 c_{\mathbf{k}}^{(1)}, \quad (4.51)$$

$$u_{z;\mathbf{k}}^{(1)} = u_{z;\mathbf{k}}^{(2)} = 0; \quad d_z u_{z;\mathbf{k}}^{(1)} = d_z u_{z;\mathbf{k}}^{(2)}, \quad (4.52)$$

$$F_x^{(1)} = F_x^{(2)}, \quad d_z \mu F_x^{(2)} = d_z F_x^{(1)}, \quad (4.53)$$

$$F_y^{(1)} = F_y^{(2)}, \quad d_z \mu F_y^{(2)} = d_z F_y^{(1)}. \quad (4.54)$$

4.3 Application of boundary and matching conditions

The merits (in the sense of numerical efficiency) of this formulation is that the ordinary differential Eqs. (4.34)-(4.45) decouple for each wavevector. And all of these Eqs. (4.34)-(4.45) are Helmholtz equation of the form $(d_z^2 - \lambda)q(z) = f(z)$ with λ is a constant real number, $f(z)$ a complex valued function, and $q(z)$ the unknown function. These equations are solved directly with the Chebyshev tau method [42]. The solution procedure is decoupled for the top and bottom layer by introducing auxiliary functions that enforce boundary and matching condition (known as "matrix influence method" [176]).

To achieve this decoupling the following ansatz is taken

$$\omega_{z;\mathbf{k}}^{(1)} = \omega_{z;\mathbf{k}}^{(1);p} + \alpha \omega_{z;\mathbf{k}}^{(1);a}, \quad (4.55)$$

$$\omega_{z;\mathbf{k}}^{(2)} = \omega_{z;\mathbf{k}}^{(2);p} + \beta \omega_{z;\mathbf{k}}^{(2);b}, \quad (4.56)$$

$$\eta_{\mathbf{k}}^{(1)} = \eta_{\mathbf{k}}^{(1);p} + a \eta_{\mathbf{k}}^{(1);a} + b \eta_{\mathbf{k}}^{(1);b}, \quad (4.57)$$

$$\eta_{\mathbf{k}}^{(2)} = \eta_{\mathbf{k}}^{(2);p} + d \eta_{\mathbf{k}}^{(2);d} + e \eta_{\mathbf{k}}^{(2);e}, \quad (4.58)$$

$$u_{z;\mathbf{k}}^{(1)} = u_{z;\mathbf{k}}^{(1);p} + a u_{z;\mathbf{k}}^{(1);a} + b u_{z;\mathbf{k}}^{(1);b}, \quad (4.59)$$

$$u_{z;\mathbf{k}}^{(2)} = u_{z;\mathbf{k}}^{(2);p} + d u_{z;\mathbf{k}}^{(2);d} + e u_{z;\mathbf{k}}^{(2);e}, \quad (4.60)$$

$$c_{\mathbf{k}}^{(1)} = c_{\mathbf{k}}^{(2);p} + c c_{\mathbf{k}}^{(1);c}, \quad (4.61)$$

$$c_{\mathbf{k}}^{(2)} = c_{\mathbf{k}}^{(2);p} + f c_{\mathbf{k}}^{(2);f}, \quad (4.62)$$

where for any wavevector \mathbf{k} eight real parameters ($\alpha, \beta, a, \dots, f$) – generally different – are to be calculated from the matching and boundary conditions.

The *particular functions* $q_{\mathbf{k}}^{(i);p}$ are set to obey Eqs. (4.34)-(4.45) but with a zero Dirichlet boundary condition, namely

$$q_{z;\mathbf{k}}^{(1);p}(z = -1, 0) = 0, \quad q_{z;\mathbf{k}}^{(2);p}(z = 0; d) = 0. \quad (4.63)$$

Furthermore, the remaining functions, say *auxiliary functions*, are set to obey the homogeneous problem but with nonzero boundary conditions. Formally, the auxiliary functions are

set by

$$(d_z^2 - \mathbf{k}^2 - \frac{1}{h})\omega_{z;\mathbf{k}}^{(1);a} = 0, \quad \omega_{z;\mathbf{k}}^{(1);a}(z = -1) = 0, \quad \omega_{z;\mathbf{k}}^{(1);a}(z = 0) = 1, \quad (4.64)$$

$$(d_z^2 - \mathbf{k}^2 - \frac{1}{h\nu})\omega_{z;\mathbf{k}}^{(2);b} = 0, \quad \omega_{z;\mathbf{k}}^{(2);b}(z = 0) = 1, \quad \omega_{z;\mathbf{k}}^{(2);b}(z = d) = 0, \quad (4.65)$$

$$(d_z^2 - \mathbf{k}^2 - \frac{1}{h})\eta_{\mathbf{k}}^{(1);a,b} = 0, \quad \eta^{(1);a,b}(0) = 1, \quad \eta^{(1);a}(-1) = -1, \quad \eta^{(1);b}(-1) = 1, \quad (4.66)$$

$$(d_z^2 - \mathbf{k}^2 - \frac{1}{h\nu})\eta_{\mathbf{k}}^{(2);d,e} = 0, \quad \eta^{(2);d,e}(0) = 1, \quad \eta^{(2);d}(d) = -1, \quad \eta^{(2);e}(d) = 1, \quad (4.67)$$

$$(d_z^2 - \mathbf{k}^2)u_{z;\mathbf{k}}^{(1);a,b} = \eta_{\mathbf{k}}^{(1);a,b}, \quad u_{z;\mathbf{k}}^{(1);a,b}(0, -1) = 0, \quad (4.68)$$

$$(d_z^2 - \mathbf{k}^2)u_{z;\mathbf{k}}^{(2);e,f} = \eta_{\mathbf{k}}^{(2);e,f}, \quad u_{z;\mathbf{k}}^{(2);e,f}(0, d) = 0, \quad (4.69)$$

$$(d_z^2 - \mathbf{k}^2 - \frac{Sc^{(1)}}{h})c_{\mathbf{k}}^{(1);c} = 0, \quad d_z c_{\mathbf{k}}^{(1);c}(-1) = 0, \quad d_z c_{\mathbf{k}}^{(1);c}(0) = 1, \quad (4.70)$$

$$(d_z^2 - \mathbf{k}^2 - \frac{Sc^{(1)}}{Dh})c_{\mathbf{k}}^{(2);f} = 0, \quad d_z c_{\mathbf{k}}^{(2);f}(-1) = 0, \quad d_z c_{\mathbf{k}}^{(2);f}(0) = 1. \quad (4.71)$$

At this stage, the free parameters can be calculated by employing the matching conditions (4.49)-(4.52) and no-slip conditions at the top and bottom [Eqs. (4.47)-(4.48)]. For example, the vertical vorticity and its interface normal derivative obey (at $z = 0$),

$$\alpha\omega_{z;\mathbf{k}}^{(1);a} - \beta\omega_{z;\mathbf{k}}^{(2);b} = \omega_{z;\mathbf{k}}^{(2);p} - \omega_{z;\mathbf{k}}^{(1);p}, \quad (4.72)$$

$$\alpha d_z\omega_{z;\mathbf{k}}^{(1);a} - \beta\mu d_z\omega_{z;\mathbf{k}}^{(2);b} = +\mu d_z\omega_{z;\mathbf{k}}^{(2);p} - d_z\omega_{z;\mathbf{k}}^{(1);p}, \quad (4.73)$$

consequently, parameters α and β are calculated by (at $z = 0$)

$$\alpha = \frac{(-\omega_{z;\mathbf{k}}^{(2);p} + \omega_{z;\mathbf{k}}^{(1);p})\mu d_z\omega_{z;\mathbf{k}}^{(2);b} - (-\mu d_z\omega_{z;\mathbf{k}}^{(2);p} + d_z\omega_{z;\mathbf{k}}^{(1);p})\omega_{z;\mathbf{k}}^{(2);b}}{-\omega_{z;\mathbf{k}}^{(1);a} b d_z\mu\omega_{z;\mathbf{k}}^{(2);b} + \omega_{z;\mathbf{k}}^{(2);b} d_z\omega_{z;\mathbf{k}}^{(1);a}}, \quad (4.74)$$

$$\beta = \frac{(\mu d_z\omega_{z;\mathbf{k}}^{(2);p} - d_z\omega_{z;\mathbf{k}}^{(1);p})\omega_{z;\mathbf{k}}^{(1);a} - (\omega_{z;\mathbf{k}}^{(2);p} - \omega_{z;\mathbf{k}}^{(1);p})d_z\omega_{z;\mathbf{k}}^{(1);a}}{-\omega_{z;\mathbf{k}}^{(1);a} d_z\mu\omega_{z;\mathbf{k}}^{(2);b} + \omega_{z;\mathbf{k}}^{(2);b} d_z\omega_{z;\mathbf{k}}^{(1);a}}. \quad (4.75)$$

The remaining conditions can be summarized by the following system

$$\begin{pmatrix} d_z u_{z;\mathbf{k}}^{(1);a}(-1) & d_z u_{z;\mathbf{k}}^{(1);b}(-1) & 0 & 0 & 0 & 0 \\ 0 & 0 & 0 & d_z u_{z;\mathbf{k}}^{(2);d}(d) & d_z u_{z;\mathbf{k}}^{(2);e}(d) & 0 \\ 0 & 0 & H c_{\mathbf{k}}^{(1);c}(0) & 0 & 0 & -c_{\mathbf{k}}^{(2);f}(0) \\ 0 & 0 & d_z c_{\mathbf{k}}^{(1);c}(0) & 0 & 0 & -D d_z c_{\mathbf{k}}^{(2);f}(0) \\ d_z u_{z;\mathbf{k}}^{(1);a}(0) & d_z u_{z;\mathbf{k}}^{(1);b}(0) & 0 & -d_z u_{z;\mathbf{k}}^{(2);d}(0) & -d_z u_{z;\mathbf{k}}^{(2);e}(0) & 0 \\ d_z^2 u_{z;\mathbf{k}}^{(1);a}(0) & d_z^2 u_{z;\mathbf{k}}^{(1);b}(0) & -Ma/Sc^{(1)}\mathbf{k}^2 c_{\mathbf{k}}^{(1);c}(0) & -\mu d_z^2 u_{z;\mathbf{k}}^{(2);d}(0) & -\mu d_z^2 u_{z;\mathbf{k}}^{(2);e}(0) & 0 \end{pmatrix} \cdot \begin{pmatrix} a \\ b \\ c \\ d \\ e \\ f \end{pmatrix} = \begin{pmatrix} -d_z u_{z;\mathbf{k}}^{(1);p}(-1) \\ -d_z u_{z;\mathbf{k}}^{(2);p}(d) \\ -H c_{\mathbf{k}}^{(1);p}(0) + c_{\mathbf{k}}^{(2);p}(0) \\ -d_z c_{\mathbf{k}}^{(1);p}(0) + D d_z c_{\mathbf{k}}^{(2);p}(0) \\ -d_z u_{z;\mathbf{k}}^{(1);p}(0) + d_z u_{z;\mathbf{k}}^{(2);p}(0) \\ -d_z^2 u_{z;\mathbf{k}}^{(1);p}(0) + \mu d_z^2 u_{z;\mathbf{k}}^{(2);p}(0) + Ma/Sc^{(1)}\mathbf{k}^2 c_{\mathbf{k}}^{(1);p}(0) \end{pmatrix} \quad (4.76)$$

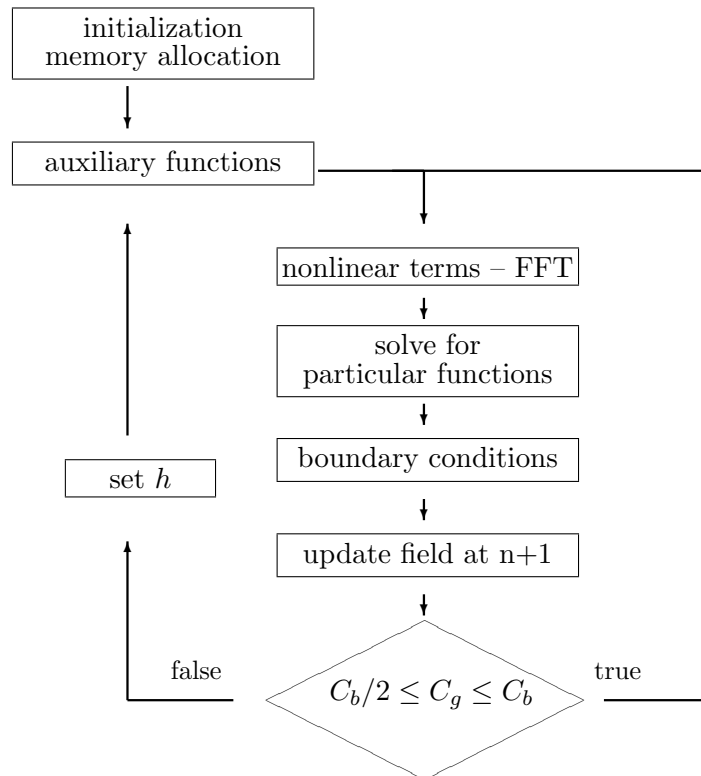


Figure 4.1: Flow chart of two layer flow solver.

4.4 Workflow

Fig.4.1 summarizes the principal numerical solution procedure. After setting initial values and allocating memory, the auxiliary functions, Eqs. (4.64)-(4.71), are calculated with a Chebyshev tau method [42], note that they do not change over time as long as the time step size h is unchanged. Then, the nonlinear terms (say at time step n) resulting from the Adams-Bashforth formula are calculated in a pseudospectral manner, i.e. by transforming from coefficient space into physical space, doing multiplication and then back to coefficient space. Specifically, these nonlinear terms are all terms with "AB" in Eqs. (4.34)-(4.45). This is the only step, which requires all MPI processes to communicate to each other, namely to perform the FFT, while the other procedure decouple in the coefficient space, say, for each wavevector \mathbf{k} . The next step is the solution of the particular functions (by Chebyshev tau-method), i.e. Eqs. (4.34)-(4.45) with boundary conditions (4.63). On this basis, parameters that enforce the matching condition are calculated according to Eqs. (4.74)-(4.76), which leads to the assembly of the new fields at time step $n+1$ according to Eqs. (4.55)-(4.62).

Due to the explicit treatment of nonlinear terms, the time stepping scheme is only conditional stable [42]. Therefore, we adjust time-step size h according to the current grid Courant-Friedrichs-Lewy (CFL) number C_g ,

$$C_g = \max \left\{ \frac{u_x h}{\Delta x}, \frac{u_y h}{\Delta y}, \frac{u_z h}{\Delta z} \right\}. \quad (4.77)$$

This number is calculated every time step by dividing the local displacement $u_\alpha h$ by the collocation grid sizes $\Delta x, \Delta y, \Delta z$. We force C_g to be smaller than a constant C_b and to be larger than $C_b/2$, i.e.

$$C_b/2 \leq C_g \leq C_b. \quad (4.78)$$

Specifically, if $C_g > C_b$ the next time step h is set such that $C_g = C_b/2$ and if $C_g < C_b/2$ the next time step h is set such that $C_g = C_b$. Additionally, we require the time step h to be smaller than δt_{max} .

Finally, whenever the time step h is changed, the auxiliary functions are recalculated. Otherwise, time marching loops starts directly without recalculations. This procedure avoids the continuous change of the time step, to save numerical cost for recalculating auxiliary functions; also the accuracy is lowered by every change in time step, since the first step is only computed with first order Euler forward formula.

Except, the concentration boundary conditions, the code was well tested for accurate implementation by Boeck *et al.* [28, 29, 31]. The changes in implementation were simply verified with the analytical solution for pure diffusion with $H = 1, D = 1$ and with an independent solver for the general case $H \neq 1, D \neq 1$ for pure diffusion.

Chapter 5

Results on Marangoni convection with stable density stratification

This chapter is dedicated to the simulation of a peculiar material system that has shown hierarchical Marangoni cell patterns [197]. As already noted in Sec. 2.4.1, we employ the ternary system made of cyclohexanol and water with butanol as transferred species. This is because of its good documentation [197, 198]. Furthermore, this chemical system appeared manageable, from the view of numerical cost, due to its high viscosity and low interfacial tension. A further advantage of this system is that we were supported by recent experimental data from Karin Schwarzenberger and Kerstin Eckert. A large part of the numerical results and the experimental data (also shown here) have been already published in joint work [111, 113, 200–202].

The present chapter is organized as follows. The material properties of the system under study, (cyclohexanol+butanol)/water, are estimated in Sec. 5.1.1, whereas the detailed procedure of estimation is shifted to the App. B.1. The physical model in viscous units is restated in Sec. 5.1.1 for a quicker reference, however already introduced in Sec. 3.1.2. Afterward, we present the numerical setup for the specific simulations. The details of the numerical method have been described in the former Ch. 4.

The large Sec. 5.2 presents the evolution of Marangoni convection in the reference simulation, focusing on the different convective structures that evolve over time. Section 5.2 is further subdivided: Sec. 5.2.1 overviews the simulated time, thereby classifying the different regimes of convection – in accordance with Linde’s concepts of basic pattern [146] – into three regimes. The properties of each regime are detailed separately: onset of convection in Sec. 5.2.2, initial ROs in Sec. 5.2.3 and hierarchical patterns of RC in Sec. 5.2.4.

Section 5.3 compares the simulated patterns with experimental results from literature [198] and recent experimental observation. For this, the experimental procedure is sketched and then the development of cell sizes is presented qualitatively as well as quantitatively. Section 5.4 discusses what is identified as the two main mechanisms of pattern formation. The role of the stable density stratification on convection is studied in Sec. 5.5 by simulations with zero buoyancy ($G = 0$) and with changed initial concentration c_0 . In Sec. 5.6, computation within a two-dimensional domain ($l_y \rightarrow 0$) are related to the reference simulation. Finally, Sec. 5.7 provides a brief discussion and conclusions of the presented data.

5.1 Cyclohexanol-water-butanol system

5.1.1 Physical modeling

Solutal Marangoni convection at the planar interface between an aqueous phase [bottom layer (1)] and a lighter organic phase [top layer (2)] is studied. These layers are the mutually saturated phases of a water-cyclohexanol ($\text{H}_2\text{O} - \text{C}_6\text{H}_{11}\text{OH}$) mixture. In this binary system, a third species 1-butanol ($\text{C}_4\text{H}_9\text{OH}$) is dissolved in the organic phase. The subsequent natural transport of butanol to the aqueous phase has shown convective patterns in experiments of E. Schwarz [197, 198].

To perform simulations, we require the material properties that appear in the paradigmatic model (Sec. 2.2). Several of these material properties have been measured by E. Schwarz, but not all of them are documented in his works. The remaining parameters were taken from literature [135] or were estimated by suitable relationships as described in App.B.1. The results of this estimation are collected in Tab. 5.1.

Based on this data, the system is of type I (Fig. 2.3) for transport out of the top layer (2) \rightarrow (1). This is because, butanol lowers density as well as interfacial tension ($\beta_c^{(i)} < 0$, $\alpha_c < 0$ cf. Tab. 5.1), and it is transported out of the phase with lower diffusivity $D^{(2)} < D^{(1)}$ and in the direction of gravitational acceleration. Consequently, a stationary Marangoni instability and a stable density stratification is expected, which was indeed concluded from the experimental studies of Schwarz [197, 198]. Also the reversed transport direction has been studied experimentally (grouped as type III according to Fig. 2.3); where the discussed eruption regime was observed [197, 198].

The transport of butanol, accompanied by Marangoni convection, is modeled by the PM in viscous scales. Although already introduced in Sec. 3.1.2, this theoretical framework is shortly restated here, since we will omit the hats at the nondimensional quantities, i.e. the replacement $\hat{q} \rightarrow q$ is implied in present chapter.

In accordance with the experiments (described later in Sec. 5.3.1), we consider two superposed immiscible, isothermal, liquid phases in a cubical computational domain with horizontal extent of $0 < x < l_x, 0 < y < l_y$. The vertical extent is $-1 \leq z \leq 0$ for the lower, water-rich phase and $0 \leq z \leq d$ for the upper, cyclohexanol-rich phase. Both phases are in contact at a plane interface $z = 0$. Initially, the system is quiescent, and the solute is solely present in the upper organic phase. This setup is sketched in Fig. 5.1.

In both layers, the momentum transport is modeled by the incompressible Navier-Stokes-Boussinesq equations and the transport of solute by an advection-diffusion equation. The dimensionless equations were derived by introducing the following units (cf. Sec. 3.1.2): The mass is measured in multiples of $\tilde{M} = \rho^{(1)}(d^{(1)})^3$, time in viscous units $\tilde{T} = (d^{(1)})^2/\nu^{(1)}$, length in multiples of the lower layer height $\tilde{L} = d^{(1)}$ and amount of substance in $\tilde{N} = c_0(d^{(1)})^3$.

The nondimensionalization yields the following equations (cf. Sec. 3.1.2), which are the

description	symbol	unit	value
molar mass butanol	M_b	g/mol	74.12
mass density H_2O sat. $C_6H_{11}OH$	$\rho_{ref}^{(1)}$	kg/m ³	$0.997 \cdot 10^3$
mass density $C_6H_{11}OH$ sat. H_2O	$\rho_{ref}^{(2)}$	kg/m ³	$0.955 \cdot 10^3$
mass density butanol	ρ_b	kg/m ³	$0.81 \cdot 10^3$
kinematic viscosity (1)	$\nu^{(1)}$	m ² /s	$1.2 \cdot 10^{-6}$
kinematic viscosity (2) with $y_b^{(2)}=0.075$	$\nu^{(2)}$	m ² /s	$20 \cdot 10^{-6}$
partition coefficient $c_{eq}^{(2)}/c_{eq}^{(1)}$	H	(mol/l)/(mol/l)	31
diffusivity solute (1)	$D^{(1)}$	m ² /s	$5 \cdot 10^{-10}$
diffusivity solute (2)	$D^{(2)}$	m ² /s	$7 \cdot 10^{-11}$
interfacial tension of the binary system	σ_{ref}	N/m	$3.4 \cdot 10^{-3}$
change in interfacial tension per mol/l of $c^{(1)}$	$\sigma_{ref}\alpha_c$	N/m/(mol/l)	$-8.77 \cdot 10^{-3}$
solubility expansion coefficient (1)	$\beta_c^{(1)}$	l/mol	-0.0172
solubility expansion coefficient (2)	$\beta_c^{(2)}$	l/mol	-0.0128
density change per solute conc. (1)	$\rho_{ref}^{(1)}\beta_c^{(1)}$	(kg/m ³)/(mol/l)	-17.11
density change per solute conc. (2)	$\rho_{ref}^{(2)}\beta_c^{(2)}$	(kg/m ³)/(mol/l)	-12.26
initial concentration for $y_b^{(2)}=0.05$	c_0	mol/l	0.55
initial concentration for $y_b^{(2)}=0.075$	c_0	mol/l	0.82
gravitational acceleration	g	m/s ²	9.81

Table 5.1: Properties of the system (cyclohexanol+butanol)/water. Phase 1 is the water-rich phase marked with upper index ⁽¹⁾ and phase 2 the organic cyclohexanol-rich phase marked with ⁽²⁾. The data sources are detailed in App. B.1. The volume concentration is denoted as $y_b^{(2)}$, this is the volume of pure butanol at standard condition divided by the volume of the mixture phase (2) with butanol dissolved.

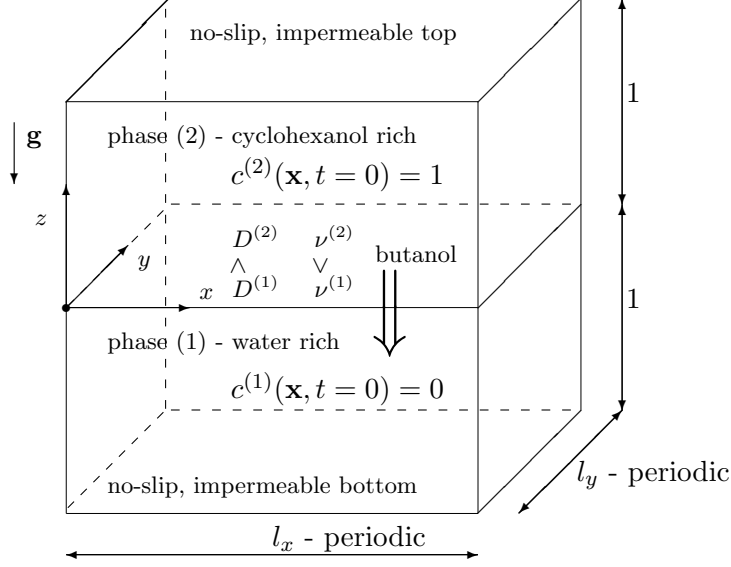


Figure 5.1: Two-layer cyclohexanol-water-butanol system in viscous units with (2) \rightarrow (1) transport. Throughout the present chapter the layer height ratio d is fixed to unity $d=1$.

basis of our numerical investigations. These are

$$\partial_t \mathbf{u}^{(1)} = -\mathbf{u}^{(1)} \cdot \nabla \mathbf{u}^{(1)} - \nabla p_d^{(1)} + \Delta \mathbf{u}^{(1)} - c^{(1)} G \mathbf{e}_z, \quad (5.1)$$

$$\nabla \cdot \mathbf{u}^{(1)} = 0, \quad (5.2)$$

$$\partial_t \mathbf{u}^{(2)} = -\mathbf{u}^{(2)} \cdot \nabla \mathbf{u}^{(2)} - \frac{1}{\rho} \nabla p_d^{(2)} + \nu \Delta \mathbf{u}^{(2)} - c^{(2)} G \beta \mathbf{e}_z, \quad (5.3)$$

$$\nabla \cdot \mathbf{u}^{(2)} = 0, \quad (5.4)$$

$$\partial_t c^{(1)} = -\mathbf{u}^{(1)} \cdot \nabla c^{(1)} + \frac{1}{S c^{(1)}} \Delta c^{(1)}, \quad (5.5)$$

$$\partial_t c^{(2)} = -\mathbf{u}^{(2)} \cdot \nabla c^{(2)} + \frac{D}{S c^{(1)}} \Delta c^{(2)}. \quad (5.6)$$

In these equations $c^{(i)} \cdot c_0$ is the molar concentration and $\mathbf{u}^{(i)} \cdot \tilde{L}/\tilde{T}$ is the dimensional velocity in phase i . According to the experimental set-up, no-slip and impermeable boundary conditions are imposed for the solid walls at the bottom and top:

$$\partial_z c^{(2)} = u_z^{(2)} = u_x^{(2)} = u_y^{(2)} = 0 \quad \text{for } z=d, \quad (5.7)$$

$$\partial_z c^{(1)} = u_z^{(1)} = u_x^{(1)} = u_y^{(1)} = 0 \quad \text{for } z=-1. \quad (5.8)$$

The matching conditions at the plane interface ($z=0$) are

$$u_x^{(1)} = u_x^{(2)}, \quad u_y^{(1)} = u_y^{(2)}, \quad u_z^{(1)} = u_z^{(2)} = 0, \quad \partial_z c^{(1)} = D \partial_z c^{(2)}, \quad H c^{(1)} = c^{(2)}, \quad (5.9)$$

$$\frac{Ma}{S c^{(1)}} \partial_x c^{(1)} = -\nu \rho \partial_z u_x^{(2)} + \partial_z u_x^{(1)}, \quad \frac{Ma}{S c^{(1)}} \partial_y c^{(1)} = -\nu \rho \partial_z u_y^{(2)} + \partial_z u_y^{(1)}. \quad (5.10)$$

dimensionless quantity	definition	value
Grashof number	$G = \frac{c_0 \beta_c^{(1)} g (d^{(1)})^3}{(\nu^{(1)})^2}$	$-7.67 \cdot 10^5$
Schmidt number aqueous phase	$Sc^{(1)} = \frac{\nu^{(1)}}{D^{(1)}}$	2400
Marangoni number	$Ma = \frac{c_0 \alpha_c \sigma_{ref} d^{(1)}}{\rho^{(1)} \nu^{(1)} D^{(1)}}$	$-2.4 \cdot 10^8$
partition coefficient	$H = c_{eq}^{(2)} / c_{eq}^{(1)}$	31
density ratio	$\rho = \frac{\rho_{ref}^{(2)}}{\rho_{ref}^{(1)}}$	0.96
kinematic viscosity ratio	$\nu = \frac{\nu^{(2)}}{\nu^{(1)}}$	16.7
diffusivity ratio	$D = \frac{D^{(2)}}{D^{(1)}}$	0.14
layer height ratio	$d = \frac{d^{(2)}}{d^{(1)}}$	1
ratio of expansion coeff.	$\beta = \frac{\beta_c^{(2)}}{\beta_c^{(1)}}$	0.75

Table 5.2: Nondimensional parameters of the reference configuration calculated with: values from Tab. 5.1, layer heights $d^{(1)} = d^{(2)} = 20 \text{ mm}$, $c_0 = 0.82 \text{ mol/l}$, i.e. 7.5 vol% butanol dissolved in the organic phase.

The arising nondimensional parameters from these governing equations are collected in Tab. 5.2 and evaluated for a *reference configuration*. The specific values result from the general material properties of Tab. 5.1 and the experimental set-up that will be introduced in Sec. 5.3.1. Namely, we were supported with recent experimental data for an initial volume concentration ^I of 7.5 vol% ($y_b^{(2)} = 0.075$) in a system with layers of 20 mm height $d^{(1)} = d^{(2)} = 20 \text{ mm}$. The dimensional initial concentration c_0 and the volume concentration are related by

$$c_0 = \frac{\rho_b y_b^{(i)}}{M_b}, \quad (5.11)$$

where M_b is the molar mass and ρ_b the density of pure butanol at standard condition.

The last step to uniquely define the problem is to set initial conditions. *Standard initial conditions* are set as follows. The velocity field is initialized ($t = 0$) with pseudorandom numbers for u_z and $(\nabla \times \mathbf{u}) \cdot \mathbf{e}_z$ that are uniformly distributed between $[0, 1 \cdot 10^{-3}]$ ^{II} at each collocation point \mathbf{x} independently

$$u_z^{(i)} = \mathcal{U}(0, 10^{-3}), \nabla \times \mathbf{u}^{(i)} \cdot \mathbf{e}_z = \mathcal{U}(0, 10^{-3}). \quad (5.12)$$

Furthermore, the yet unspecified mean flow is set to zero $F_x^{(i)}(z, t = 0) = F_y^{(i)}(z, t = 0) = 0$.

^I The volume concentration of butanol in phase (2) is denoted $y_b^{(2)}$. It is the volume of pure butanol at standard condition divided by the volume of the mixture phase (2), in which it was dissolved (including butanol)

^{II}The uniform random distribution between a, b is abbreviated as $\mathcal{U}(a, b)$

The solute is initialized with a homogeneous concentration of unity for layer (2) and zero for layer (1)

$$c^{(1)} = 0, \quad c^{(2)} = 1. \quad (5.13)$$

5.1.2 Sample configurations

Stationary Marangoni convection is studied by simulating different parameter sets. This section names simulations with a short string and relates the changes in physical parameters (relative to Tab. 5.2) and numerical parameters (e.g. $l_x, l_y, N_x, N_y, \dots$) to them.

First, simulations were carried out for our reference configuration. The corresponding *reference simulation* is named E_1_1, see Tab. 5.3. The simulation E_1_2 uses the same material parameters but is calculated on a smaller domain where it is easier to process data. Simulation E_1_3 used a peculiar small time step to especially resolve the onset of convection. Simulation E_2 realizes a decrease in initial concentration $y_b^{(2)} = 0.05$.

The name is built by the following structure: The first literal denotes a group of simulation. The second number stands for a change in material parameters in this respective group. The third number just distinguishes between different simulation and a potential change in the numerical parameters with independent realization of the initial random velocity fields. ^{III} The literal "E" denotes simulations that correspond to recent experiments with the 20mm layers.

A further group of simulations correspond to experiments of Schwarz [198] with a decrease in layer height $d^{(1)} = d^{(2)} = 15mm$. This group is denoted by (S...). Different butanol concentration were simulated, see Tab. 5.3. For the simulation with the lowest solute concentration S_3 (see Tab. 5.3) we used stronger noise to lower the onset time of convection. In particular, $u_z; (\nabla \times \mathbf{u}) \cdot \mathbf{e}_z$ is initialized with values in $[0, 1 \cdot 10^{-2}]$ and also solute is perturbed by $c^{(1)} = \mathcal{U}(0, 1 \cdot 10^{-3}), c^{(2)} = 1 + \mathcal{U}(0, 1 \cdot 10^{-3})$.

To analyze the influence of a stable density stratification, the group G... of simulations is established. Simulation G_1_1 is the counterpart of the reference simulation E_1_1 with the Grashof number is set to zero $G = 0$. In the framework of zero gravity, the influence of the domain size l_x, l_y is also probed. For G_1_1, the domain size l_x, l_y was chosen large enough so that the influence of the periodic horizontal boundaries on the pattern evolution might be neglected in the time frame considered, however, for runs G_1_2-G_1_4 we decreased l_x, l_y to demonstrate how geometric limitations influence convection patterns.

Furthermore, two-dimensional (2D) simulation were performed by setting $l_y \rightarrow 0$, which are denoted by E_1_2D, G_1_2D. The last group of simulations is denoted by "L_" with a low Marangoni number and no buoyancy. These parameters enabled us to simulate the almost full equilibration process.

The numerical resolution requirements turned out to be quite severe. For the reference simulation, a very high vertical resolution $N_z^{(1)} = 256, N_z^{(2)} = 512$ was required to capture the vertical structures near the interface properly. The horizontal resolutions (N_x, N_y) are set to resolve the fine solute structures in the horizontal directions. We verified grid convergence for selected test cases, cf. Tab. 5.4, by changing the number of expansion coefficients in the

^{III}Please, note that the last number is occasionally omitted. So for instance S_2_1 denotes the same simulation as S_2

horizontal N_x, N_y and vertical direction $N_z^{(1)}, N_z^{(2)}$. Furthermore, we changed the maximum time step δt_{max} and the bound for the grid CFL number C_b .

To provide comparability, all test simulations are based on exactly the same initial conditions. For that purposes, the standard random initial conditions are generated for the case of lowest resolution, i.e. N_0. The resulting fields are then used as an input for N_0–N_15. We checked two necessary properties: the numerical stability and the smoothness of the shadowgraph image $s(x, y)$ [see Eq. (5.15)] as shown in the last two columns of Tab. 5.4. Possibly appearing shortwave oscillations (last column) are characteristic for insufficient spatial resolution.

Those simulations that satisfy the requirements of numerical stability and absence of visible oscillations differ only marginally in the relevant field quantities, cf. Fig. 5.2(a) where two simulations are plotted simultaneously. However, for post processing purposes, e.g. in the reference simulation E_1_1 (Tab. 5.3), we used a finer grid size than the marginal grid size of N_3 (Tab. 5.4). Note that if the maximum time step is set too large – case N_9 – the initial perturbation are damped stronger such that convection is not triggered. The validity of the numerical method is also proven by the comparison with the experimental data.

The reference simulation E_1_1 consumed approximately 650 GB main memory. On 512 processors, it took $1.24 \cdot 10^5$ core hours for the simulation to be advanced until $t = 2.07$ with 17800 time steps. The size of these time steps is governed by the CFL restriction given in Eq. (4.77) except before the onset of convection.

5.2 Marangoni convection in the reference configuration

In this section, the evolution of Marangoni convection in the reference configuration is presented. The first subsection 5.2.1 outlines the general development over the simulate time range. The following subsections chronologically examine the typical flow regimes more closely: convection onset in Sec. 5.2.2, initial relaxation oscillations (RO) in Sec. 5.2.3 and hierarchical convection cells in Sec. 5.2.4.

5.2.1 Overview

To give an overview of the temporal evolution of the Marangoni convection, Figs. 5.2(a,b,c) depict the root-mean-square velocities $u_{rms}^{(i)}, u_{rms}^{(s)}$ in the bulk and at the interface, respectively

$$u_{rms}^{(i)}(t) = \sqrt{\langle \mathbf{u}^{(i)} \cdot \mathbf{u}^{(i)} \rangle_{xyz}}, \quad u_{rms}^{(s)}(t) = \sqrt{\langle \mathbf{u} \cdot \mathbf{u} \rangle_s}. \quad (5.14)$$

They are obtained by averaging over the entire layer $\langle \rangle_{xyz}$ and over the interface $\langle \rangle_s$. Fig. 5.2(d) shows the amount of solute transferred to the lower layer normalized with the global equilibrium value in the bottom layer $c_{eq}^{(1)} = 1/(H + 1)$. In parallel, Figs. 5.3–5.4 show synthetic shadowgraph images ^{IV}

$$s(x, y) = \int_{[-1, d]} (\partial_x^2 + \partial_y^2) c(\mathbf{x}, t) dz \quad (5.15)$$

^{IV}Please note that the legends in the synthetic shadowgraph images denote the negative value of $s(x, y)$, thus $(-s(x, y))$, which is indicated in the figure captions. This has "historical" reasons, as we changed the definition of s at some point and we wanted to have a uniform definition throughout this work.

#	$y_b^{(2)}$	C_b	δt_{max}	$l_x(N_x)$	$N_z^{(1)}$	$N_z^{(2)}$	varied phys. parameter
E_1_1	0.075	$3 \cdot 10^{-1}$	$5 \cdot 10^{-4}$	0.5(2048)	256	512	$Ma = -2.4 \cdot 10^8$; $G = -7.67 \cdot 10^5$
E_1_2	0.075	$1 \cdot 10^{-1}$	$1 \cdot 10^{-4}$	0.15(1024)	256	512	$Ma = -2.4 \cdot 10^8$; $G = -7.67 \cdot 10^5$
E_1_3	0.075	$3 \cdot 10^{-1}$	$1 \cdot 10^{-7}$	0.2(1024)	256	512	$Ma = -2.4 \cdot 10^8$; $G = -7.67 \cdot 10^5$
E_2	0.05	$3 \cdot 10^{-1}$	$1 \cdot 10^{-4}$	0.8(2048)	256	256	$Ma = -1.6 \cdot 10^8$; $G = -5.11 \cdot 10^5$
E_1_2D	0.075	$3 \cdot 10^{-1}$	$5 \cdot 10^{-4}$	0.5(2048)	256	512	$Ma = -2.4 \cdot 10^8$; $G = -7.67 \cdot 10^5$ $l_y = 0$
S_1	0.1	$3 \cdot 10^{-1}$	$1 \cdot 10^{-4}$	0.15(1024)	256	512	$Ma = -2.4 \cdot 10^8$; $G = -4.13 \cdot 10^5$;
S_2	0.05	$3 \cdot 10^{-1}$	$1 \cdot 10^{-4}$	0.3(1024)	256	256	$Ma = -1.2 \cdot 10^8$; $G = -2.16 \cdot 10^5$
S_3	0.025	$3 \cdot 10^{-1}$	$1 \cdot 10^{-4}$	0.4(1024)	256	256	$Ma = -6.0 \cdot 10^7$; $G = -1.08 \cdot 10^5$
D_1	-	$3 \cdot 10^{-1}$	$1 \cdot 10^{-4}$	-	256	512	$Ma = 0$; $G=0$
G_1_1	0.075	$3 \cdot 10^{-1}$	$1 \cdot 10^{-4}$	0.5(2048)	256	512	$Ma = -2.4 \cdot 10^8$; $G=0$
G_1_2	0.075	$3 \cdot 10^{-1}$	$1 \cdot 10^{-4}$	0.1(512)	256	512	$Ma = -2.4 \cdot 10^8$; $G=0$
G_1_3	0.075	$3 \cdot 10^{-1}$	$1 \cdot 10^{-4}$	0.05(256)	256	512	$Ma = -2.4 \cdot 10^8$; $G=0$
G_1_4	0.075	$3 \cdot 10^{-1}$	$1 \cdot 10^{-4}$	0.01(128)	256	512	$Ma = -2.4 \cdot 10^8$; $G=0$
G_1_2D	0.075	$3 \cdot 10^{-1}$	$1 \cdot 10^{-4}$	0.5(2048)	256	512	$Ma = -2.4 \cdot 10^8$; $G=0$ $l_y = 0$
L_1	-	$2 \cdot 10^{-1}$	$5 \cdot 10^{-2}$	4(1024)	128	128	$Ma = -1.2 \cdot 10^7$; $G=0$
L_2	-	$2 \cdot 10^{-1}$	$1 \cdot 10^{-1}$	8(1024)	64	128	$Ma = -0.6 \cdot 10^7$; $G=0$

Table 5.3: Parameters for different simulation runs. The names are constructed as follows: we use E for simulations related to recent experiments, S for those related to experiments of Schwarz [198], G's are without buoyancy, D is a simulation with pure diffusion and the L's denote simulation with low Marangoni number and without buoyancy. Parameters not given here are collected in Tab. 5.2. The computational domain has a square horizontal cross-section ($l_x = l_y$, $N_x = N_y$) except simulations E_1_2D, G_1_2D with $l_y = 0$.

#	C_b	δt_{max}	$l_x(N_x)$	$l_y(N_y)$	$N_z^{(1)}$	$N_z^{(2)}$	num. stability	vis. oscill.
N_0	0.3	5e-4	0.3(256)	0.3(256)	64	64	unstable	-
N_1	0.3	5e-4	0.3(256)	0.3(256)	512	256	unstable	-
N_2	0.3	5e-4	0.3(512)	0.3(512)	512	256	stable	yes
N_3	0.3	5e-4	0.3(1024)	0.3(1024)	512	256	stable	no
N_4	0.3	5e-4	0.3(2048)	0.3(2048)	512	256	stable	no
N_5	0.3	5e-4	0.3(1024)	0.3(1024)	64	64	unstable	-
N_6	0.3	5e-4	0.3(1024)	0.3(1024)	128	128	unstable	-
N_7	0.3	5e-4	0.3(1024)	0.3(1024)	256	256	stable	no
N_3	0.3	5e-4	0.3(1024)	0.3(1024)	512	256	stable	no
N_8	0.3	5e-4	0.3(1024)	0.3(1024)	512	512	stable	no
N_9	0.3	1e-2	0.3(1024)	0.3(1024)	512	256	stable/no convection	-
N_10	0.3	1e-3	0.3(1024)	0.3(1024)	512	256	stable	no
N_3	0.3	5e-4	0.3(1024)	0.3(1024)	512	256	stable	no
N_11	0.3	1e-4	0.3(1024)	0.3(1024)	512	256	stable	no
N_12	0.3	5e-5	0.3(1024)	0.3(1024)	512	256	stable	no
N_13	0.1	5e-4	0.3(1024)	0.3(1024)	512	256	stable	no
N_3	0.3	5e-4	0.3(1024)	0.3(1024)	512	256	stable	no
N_14	0.6	5e-4	0.3(1024)	0.3(1024)	512	256	stable	no
N_15	1	5e-4	0.3(1024)	0.3(1024)	512	256	stable	early phase

Table 5.4: Overview of test simulations with exactly the same initial conditions but changed numerical parameters. For these test simulations, we use the numerical parameters from the reference configuration, cf. Tab. 5.2.

at selected times, obtained from the reference simulation E.1.1 and E.1.2. This quantity is employed to enable a direct comparison with experimental shadowgraph images, see details in Sec. 5.3.

For the present physical configuration, $s(x, y)$ basically displays the horizontal solute distribution near the interface (due to highest horizontal solute gradients there) preferentially for the top layer. Bright regions ($s(x, y) > 0$) in the synthetic shadowgraph images can be considered as locations with a gain in solute by horizontal diffusion, which is mostly equal to a low concentration and hence high surface tension. This interpretation is simply deduced by comparing the definition (5.15) with the diffusion equation for the solute. Furthermore, the following correlations were observed: (bright region) \leftrightarrow (flow from the interface to the bulk, high interfacial tension) and (dark regions) \leftrightarrow (flow from the bulk to the interface, low interfacial tension). Note that the specific grayscale is not generic. It depends on the specific experimental configuration. At present, the grayscale is simply adapted to the experimental data.

On comparing the shadowgraphs from Figs. 5.3-5.4 with the time history in Fig. 5.2, the evolution is divided into two main phases, see Fig. 5.2(a). The rapid phase *I* is called *initial spreading*, which encompasses two short sub-phases. The first subphase *Ia* is that of *exponential growth*, detailed in Fig. 5.2(b) by using logarithmic scales. After a maximum in interfacial velocity, the second subphase *Ib* – named *saturation* – sets in. Phase *Ib* is terminated after approaching the inflection point at $t=0.07$, cf. Figs. 5.2(a,b). Thereafter, the long phase *II*, named *hierarchy formation and coarsening*, starts by substructuring of the cells in Fig. 5.3(c) and continues with only minor changes in $u_{rms}^{(i)}$ and $u_{rms}^{(s)}$.

Fig. 5.3(a) shows phase *Ia* with a spotted pattern of small cells, being nuclei for a vivid spreading of cells. According to Linde’s classification [146](see Sec. 2.4.1), these growing structures are called (initial) relaxation oscillations – ROs.

The next subphase *Ib* saturation [Fig. 5.3(b)] shows strongly growing cells and cells that are either squeezed or incorporated by the stronger advective motion of their neighbors. Due to the balance of equally strong neighbors, the extensive spreading motion comes to a halt with a maximum in cell sizes. The cell borders orient in mostly straight lines and thus build a polygonal pattern.

Phase II, termed *hierarchy formation and coarsening*, is initiated by the breakdown of the initial ROs, where the biggest cells (e.g. in the region marked with a square in Fig. 5.3) split into a network of smaller polygonal, more persistent cells.

In Fig. 5.4(a-d), the more vigorous cells grow and develop an internal substructure of smaller Marangoni cells. In line with [146], we term these polygonal patterns with substructure *Marangoni roll cells of second order* RC-IIs. The enclosed cellular substructures and the individual cells without substructure are called *Marangoni roll cells of first order*, RC-Is [146]. They constitute the lowest level of the hierarchy. In the early stage, presented in Fig. 5.4(a), an unambiguous assignment of the individual cells to a hierarchy order is hardly possible due to the continuous evolution of length scales. However, from Fig. 5.4(b) to (d) the beginning spatial hierarchy formation is clearly discernible because the RC-IIs steadily increase in size and the separation of scales between RC-Is and RC-IIs grows.

Another type of pattern, in contrast to the closed polygonal RC-Is, is observed in Fig. 5.4(b-d). Particularly in those RC-IIs that are about to shrink and disappear, e.g. white **A** mark in Fig. 5.4(b), arrays of aligned, straight solute fronts are visible. According to its wavelike

appearance, this pattern is referred to as *relaxation oscillation waves* - ROWs [146], see also Fig. 2.4. This pattern is not that persistent and appears favored in host RC-II that have a distinctly elongated geometry.

In the late Fig. 5.4(d) the periodicity length of the domain becomes of the same order as the RC-IIs and consequently influences their behavior. In this view, no numerical resources are invested to progress this simulation further. At this time, only approximately 4% of the maximum transferable amount of solute was transferred, see Fig. 5.2(d). In the following sections, we will describe the observed structures in depth.

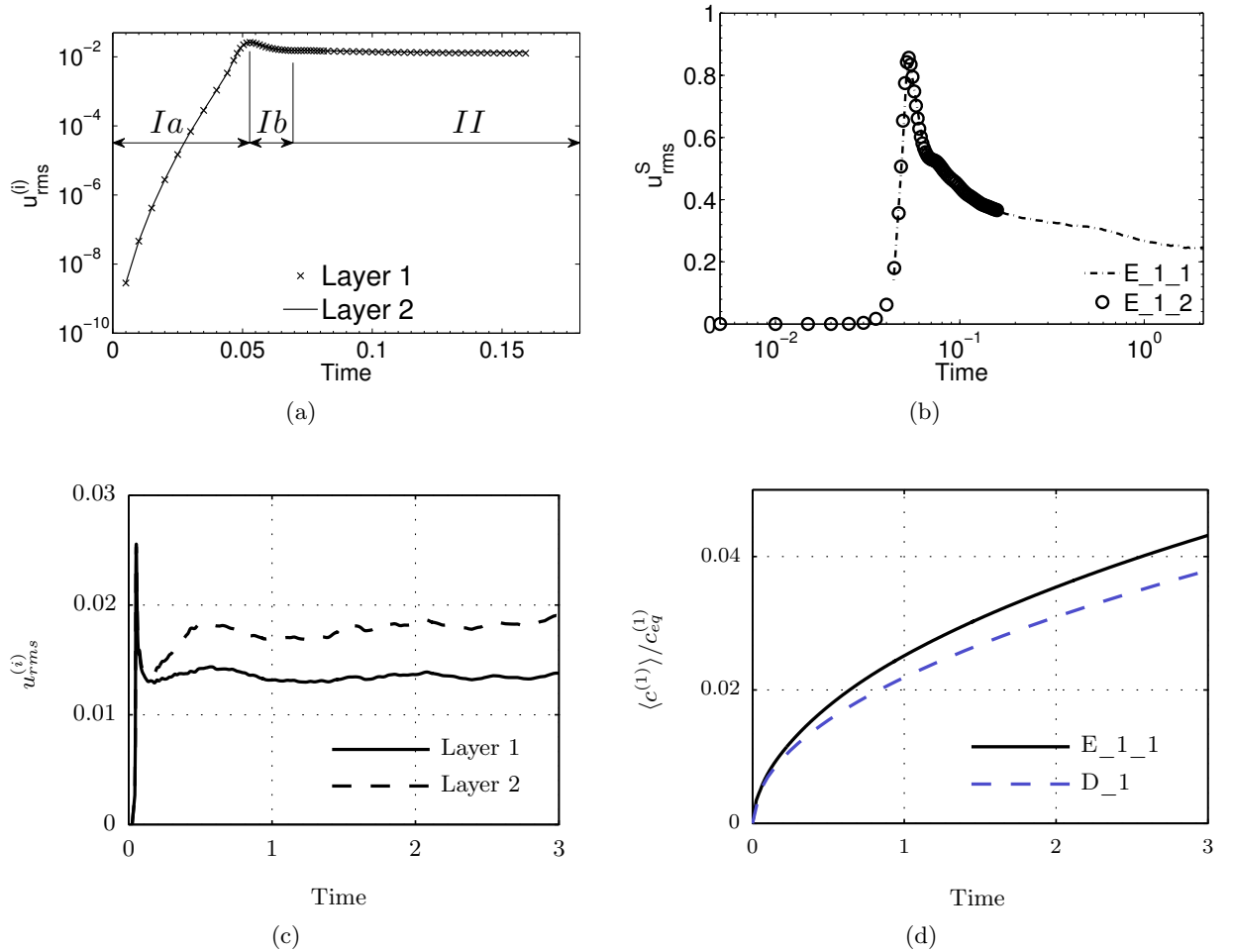


Figure 5.2: Overview of convection in the reference configuration: (a) Root-mean-squared velocity in the bulk for simulation $E_{1.2}$ performed with a higher temporal resolution than $E_{1.1}$, (b) rms velocity at the interface for both simulations $E_{1.1}, E_{1.2}$ (no visible difference), (c) rms velocity for the reference simulation $E_{1.1}$. The global maximum of $u_{rms}^{(i)}$ and $u_{rms}^{(s)}$ is around $t=0.053$. (d) Averaged solute concentration in the bottom layer normalized by global equilibrium value.

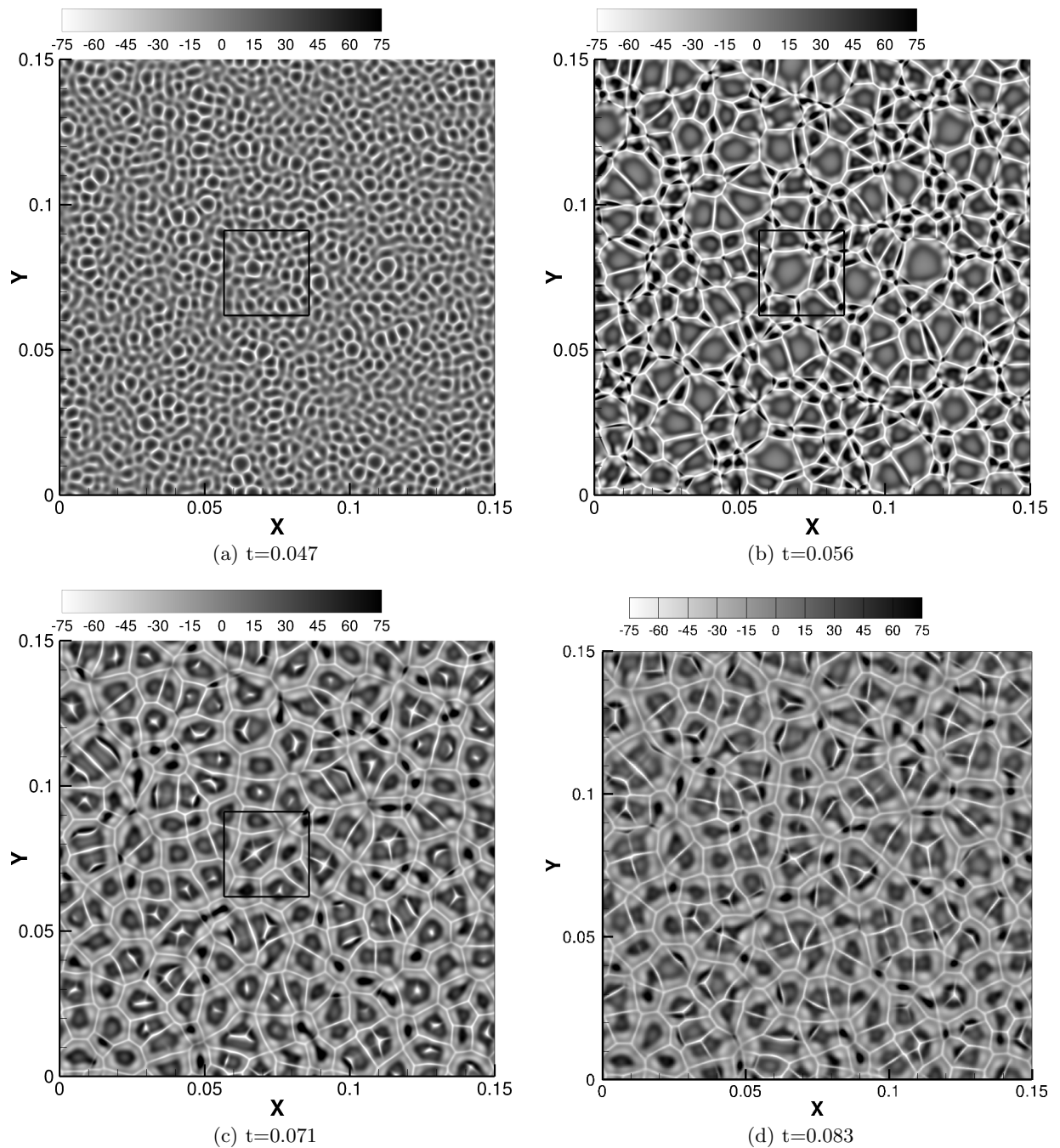


Figure 5.3: Synthetic shadowgraph images ($-s(x, y)$) show the pattern formation at start-up of interfacial convection: (a) the end of phase *Ia*—exponential growth, (b) phase *Ib* with initial RO mark the saturation of perturbation growth, (c,d) transition to phase *II* by breakdown of initial RO. All subfigures show simulation E.1.2. The black boxes depict details that are illustrated more precisely later in Figs. 5.7, 5.8.

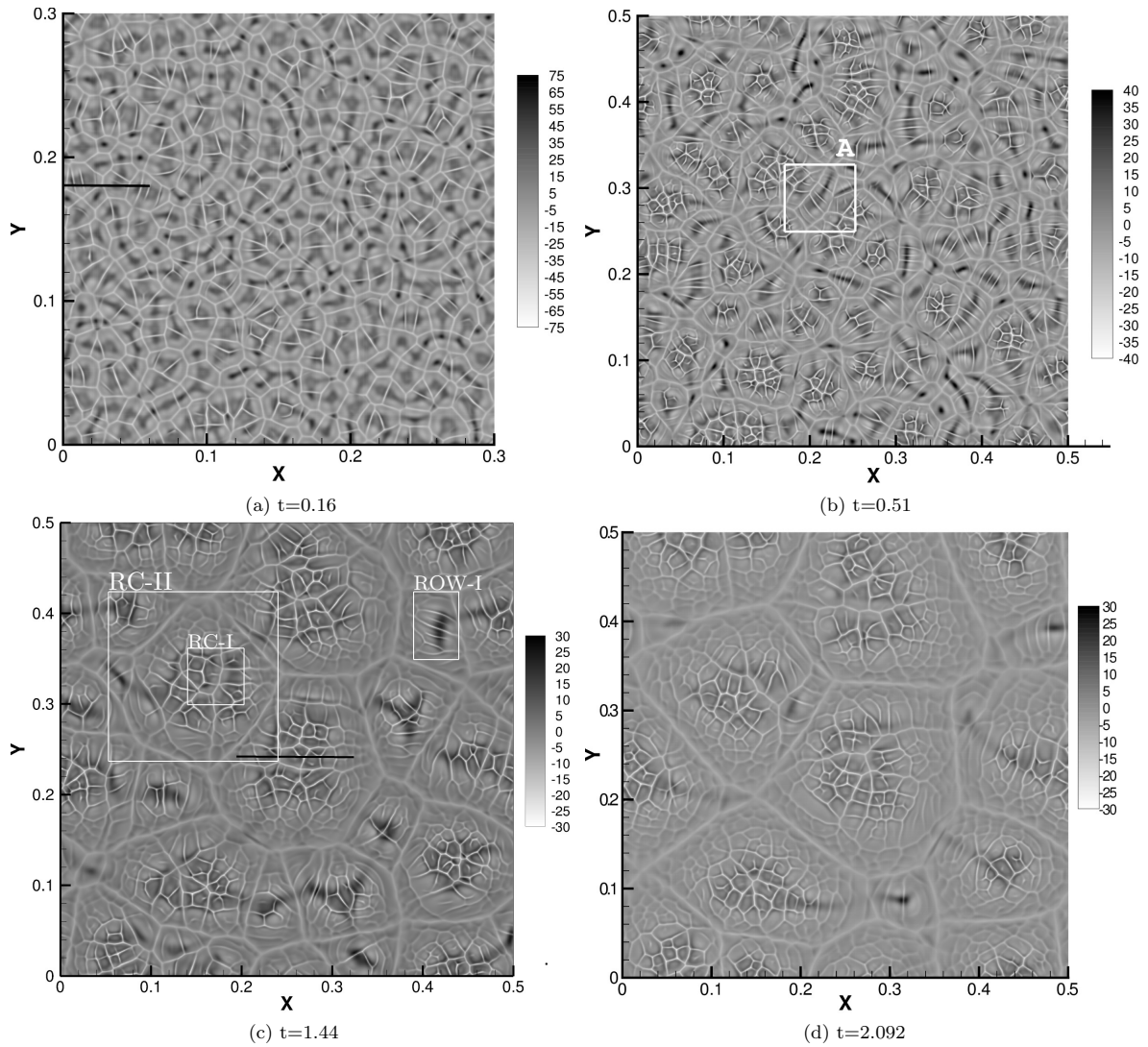


Figure 5.4: Synthetic shadowgraph images ($-s(x, y)$) in phase *II* – formation of substructures and coarsening of interfacial convection – in simulation E_1.1. The black lines in (a) and (c) mark the vertical cuts shown in Fig. 5.10(b), Fig. 5.11(b), respectively. Note the change in the domain size from (a) to (b) and also the adaption of the grayscale.

5.2.2 States of convection: onset

After simulations started, the initial perturbations [see velocity u_{rms} in Fig. 5.5(a)] get damped and consequently the solute distribution evolved mainly under the action of pure diffusion. Profiles of solute concentrations as a function of the vertical coordinate z – evolving under pure diffusion – are plotted in Fig. 5.6, showing the small mixing layers near the interface.

According to the "frozen time" linear stability analysis of Sec. 3.4.2, the first time t_m a sinusoidal perturbation with wavenumber k is predicted to grow is

$$t_m = Sc^{(1)} \left(\frac{(1 + \mu)(DH + 1)(D^{-0.5} + H)}{2\sqrt{\eta} [e^{4\eta D} \operatorname{erfc}(2\sqrt{\eta D}) D^{1/2} - e^{4\eta} \operatorname{erfc}(2\sqrt{\eta})]} \cdot \frac{1}{Ma} \right)^2 \quad (5.16)$$

with similarity variable

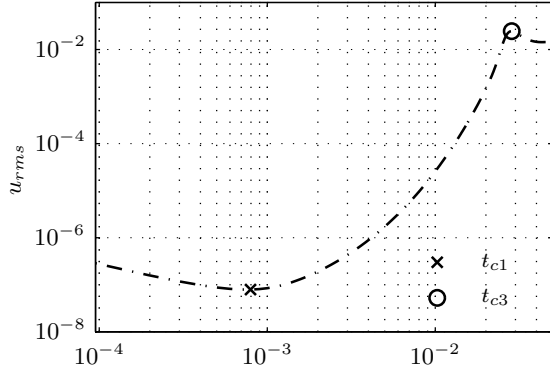
$$\eta = k^2 t_m / Sc^{(1)}. \quad (5.17)$$

This formula (5.16) is derived in the same way as Eq. (3.134), but with utilizing Eq. (3.120) owing to a changed in transport direction as well as a change from diffusive to viscous units.

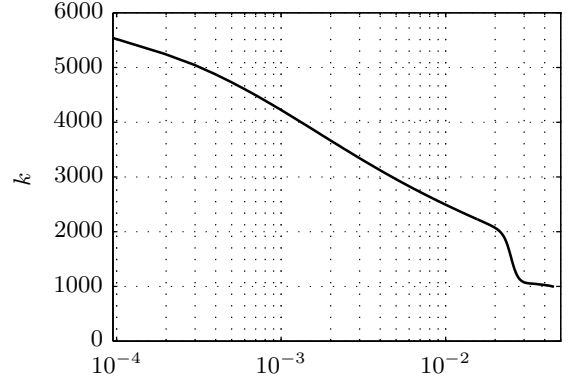
Fig. 5.5 shows these pairs of (t_m, η) in (c) and (t_m, k) in (d) in accordance with Eq. (5.16). The first time when linear theory predicts a growing mode is at $t_c \approx 1.4 \cdot 10^{-5}$, $k_c \approx 4.2 \times 10^3$, which is distinctly earlier than the first net growth in velocity $t_{c1} = 8.0 \cdot 10^{-4}$ [Fig. 5.5(a) based on simulation E_1.3] (see Sec. 3.5 for definition of times t_{c1}, t_{c3}). Fig. 5.5(b) shows the dominate wavenumber of the interfacial concentration (see Eq. 3.143) decreasing over time; observe the sharp bend around $t=0.02$ when strong convection set in; the linear prediction k_c passably represent the dominant mode at t_{c1} .

Also note that in simulation E_1.3, the peak in velocity (Fig. 5.5(a), $t_{c3} = 0.029$) appeared earlier than in the reference simulation (maximum around $t \approx 0.05$), although they started from a similar velocity amplitude $u_{rms}(t = 0) \approx 5.5 \cdot 10^{-4}$. This behavior is attributed to the numerical error in the first few time steps, which let the velocity amplitude drop stronger for the reference simulation as it is calculated with a larger time step, cf. Tab. 5.3. However, the subsequent process of pattern formation is observed as generic and independent of initial velocity perturbation.

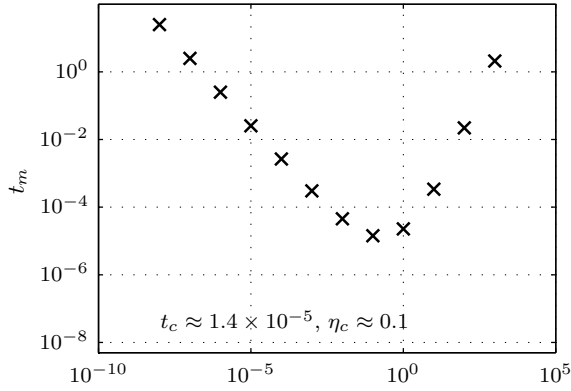
In addition to the instability domain of linear theory [Fig. 5.5(d) ruled area], also the boundary layer width $\delta c_I^{(i)}$ (of the the semi-infinite solution analogue to Eqs. (3.136),(3.137) are included. They pierce the marginal boundary around $t \approx 10^{-3}$, $k \approx 5000$. Before this time the boundary layer width is smaller (in terms of wavelength) than the smallest instable modes. This time when boundary layer is comparable to the instable mode is in better agreement with the simulated onset time t_{c1} .



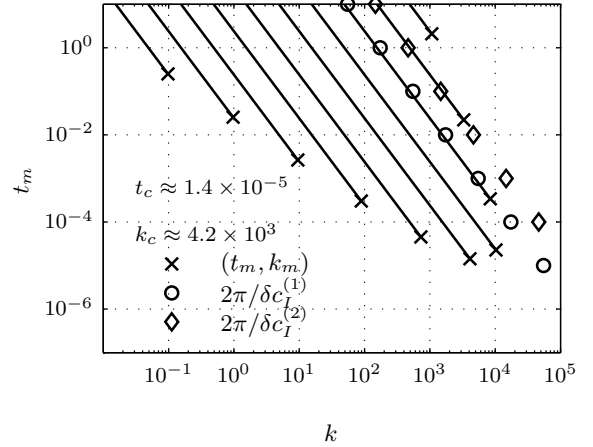
(a)



(b)



(c)



(d)

Figure 5.5: Onset of convection in simulation E_1.3: (a) Root-mean-squared velocity and (b) mean wave number of interfacial concentration [according to Eq. (3.143)]. Derived onset times (see Sec. 3.5 for definition) from simulation E_1.3 are $t_{c1} = 8 \cdot 10^{-4}$, $t_{c3} = 0.029$. (c) Marginal stability threshold according to Eq. (5.16) with time versus the similarity variable and marginal wavenumber versus time (d) with boundary layer widths $\delta c_I^{(i)}$, Eq. (3.137) adapted to viscous units.

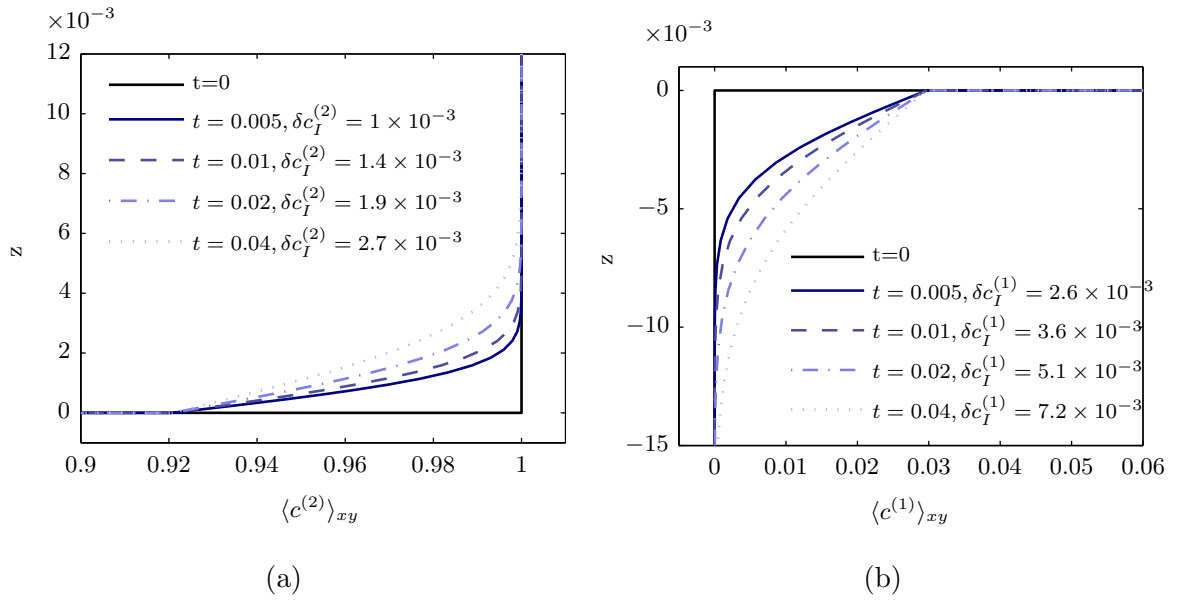


Figure 5.6: Initial pure diffusive evolution of concentration profiles (simulation D.1) in top layer (a) and bottom layer (b) with noted boundary layer width $\delta c_I^{(2)} = \sqrt{Dt\pi}/Sc^{(1)}$, $\delta c_I^{(1)} = \sqrt{t\pi}/Sc^{(1)}$, see Eq. (3.136) (does not change with the transport direction).

5.2.3 States of convection: growth and saturation of initial ROs

Growth of initial ROs

The unsteady *initial ROs* [Fig. 5.3(a,b)] arose in phase I after the onset of instability. Their self-energizing mechanism was driven by the inflow of solute-rich fluid in the center and the outflow of depleted fluid at the periphery. The ROs were heterogeneously distributed; some cells were amplified more rapidly than others. Such a dominant cell is detailed next.

Figs. 5.7 and 5.8 focus on the spreading of the initial ROs and highlight: (1) The primary instability of the pure diffusive evolution where cells still have a common length scale [Fig. 5.7(a)]. (2) Amplification and the ensuing growth of the most intense RO by a spreading motion [Fig. 5.7(b)]. (3) A polygonal network is what remains from the nonlinear competition of spreading ROs [Fig. 5.8(a)].

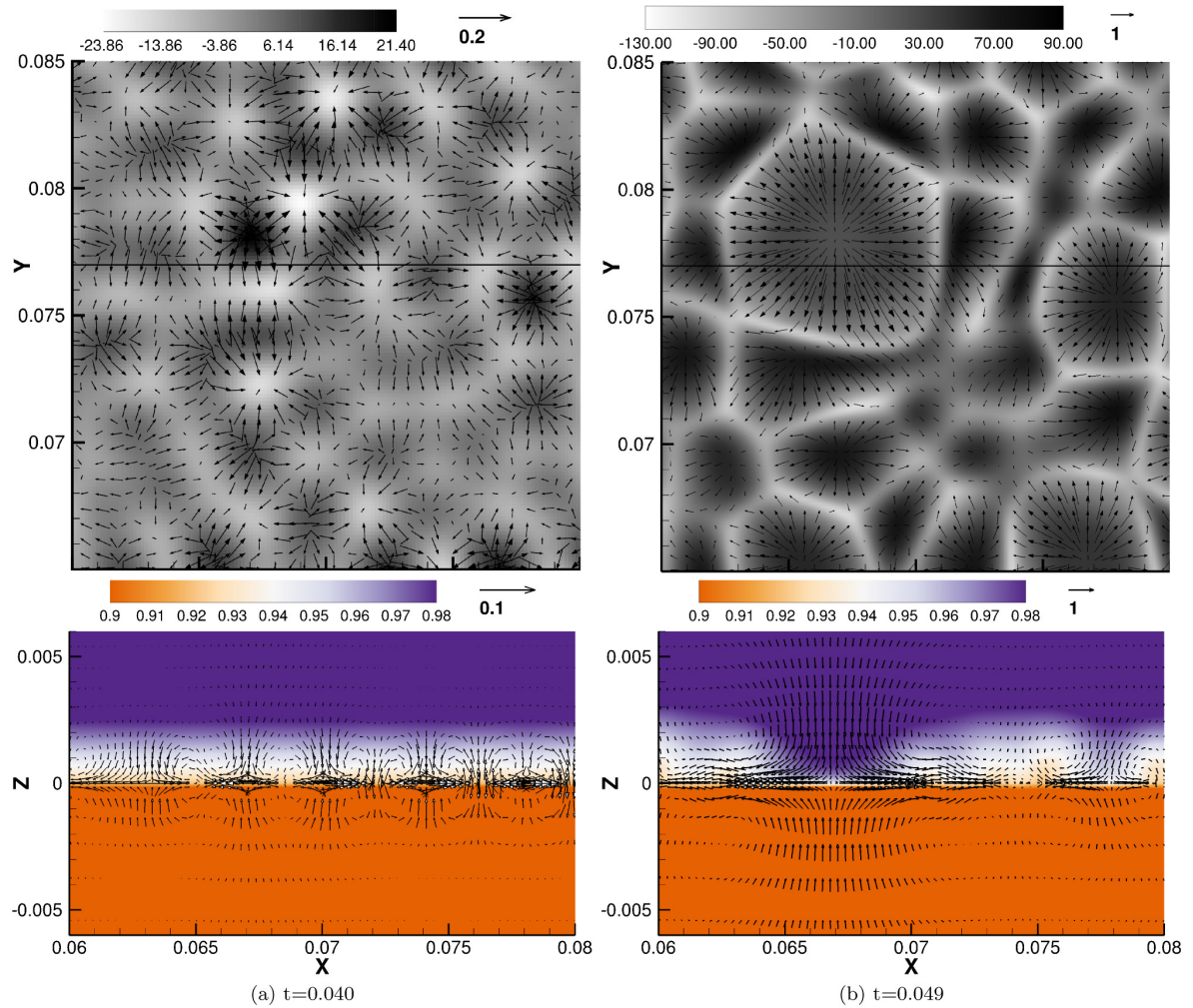


Figure 5.7: Growth of the initial ROs. Synthetic shadowgraph pictures $(-s(x,y))$ in the upper row and the corresponding concentration distributions $c^{(1)}H$ and $c^{(2)}$ at $y=0.077$ in the lower row, both with the corresponding velocity field. The synthetic shadowgraph pictures are a detail of the simulation $E_{1.2}$ marked by a black square in Fig. 5.3.

Breakdown of initial ROs

At the stage of Fig. 5.8(a), the largest cells developed an inner region with a fairly constant interfacial concentration distribution together with a large stagnation point in its center. This situation lead to a *substructuring* in Fig. 5.8(b) at $x=0.067$ and $y=0.077$. The shape of these newly created convection cells is governed by the spatial structure of the hosting cell, that is the position of the inner stagnant zone and the distance to the hosting cell boundaries.

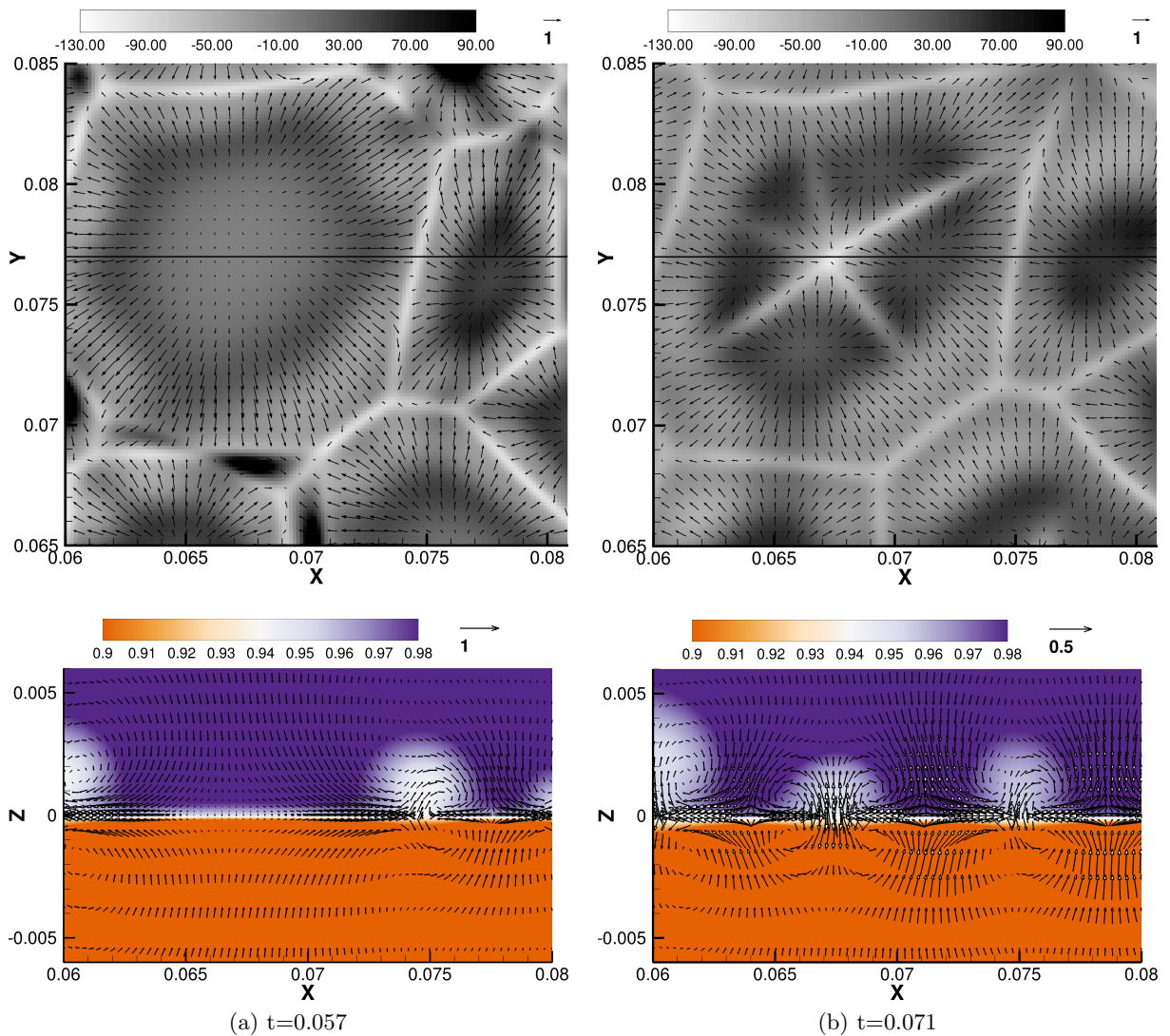


Figure 5.8: Splitting of a large RO into RC-Is. Synthetic shadowgraph pictures ($-s(x, y)$) in the upper and concentration distributions $c^{(1)}H$ and $c^{(2)}$ at $y=0.077$ in the lower row, both with the corresponding velocity field. The synthetic shadowgraph pictures are a detail of the simulation $E_{1.2}$ marked by a black square in Fig. 5.3.

5.2.4 States of convection: hierarchical patterns

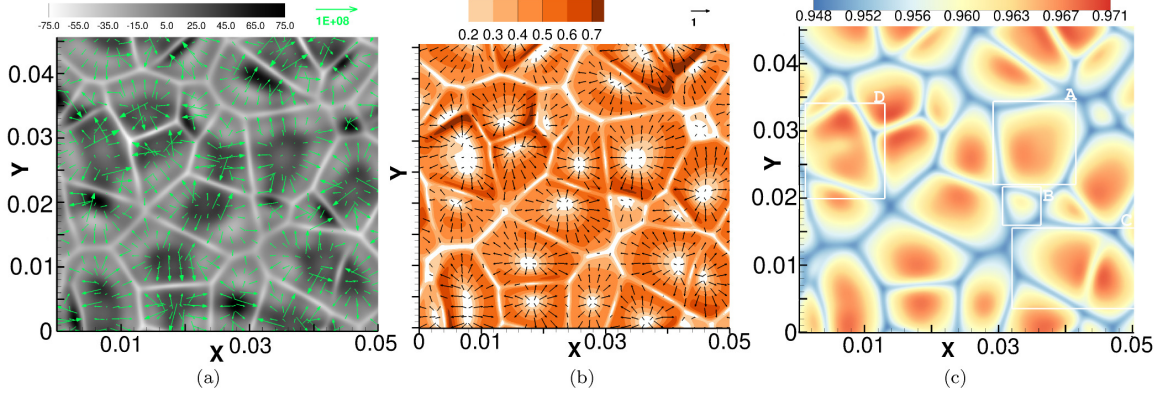


Figure 5.9: Polygonal network of mainly first order cells (RC-Is) at $t=0.10$ (E_1_1). (a) Synthetic shadowgraph image ($-s(x,y)$) with \mathbf{t}_{Ma} , (b) velocity magnitude $|\mathbf{u}|(z=0)$ with velocity vectors at the interface and (c) concentration at the interface $c^{(2)}(z=0)$ with marks A-D used in the text.

After the spreading of ROs, the interface was occupied by Marangoni roll cells without substructure RC-I. The *RC-Is pattern* is characterized in Fig. 5.9 by: (a) the shadowgraph with interfacial force (as arrows)

$$\mathbf{t}_{Ma} = \nabla_s c^{(1)} Ma, \quad (5.18)$$

(b) the velocity magnitude and (c) the interfacial concentration $c^{(2)}(=Hc^{(1)})$.

At this early stage of phase II, the neighboring RCs form a polygonal network, featuring high local Marangoni stresses towards the bright, solute poor boundaries in (a). The stresses are still synchronized with the velocity in (b), i.e. no large-scale advection has developed yet. Fig. 5.9 also reveals characteristic features of the pattern dynamics. Firstly, large cells grow at the expense of the small ones, e.g. a large cell marked with **A** in Fig. 5.9(c) expands in the negative y -direction, thereby incorporating the weak (= white) small cell **B**. Second, the splitting of large cells by *elongated solute fronts* is observed at **C**. Furthermore, new solute fronts can develop out of large stagnant inflow zones, as visible at **D**.

Fig. 5.10 shows horizontally averaged concentration (a) and velocity (c) profiles for subsequent times together with a 2D concentration and velocity field (b) at $t = 0.16$ and $y = 0.18$. The velocity field of the 3D polygonal cells appear as a double vortex in this 2D cut.

The *concentration profiles* in Fig. 5.10(a) correspond to characteristic states of run E_1_1, namely (i) the state of emerging initial ROs at $t=0.047$, cf. Fig. 5.3(a), (ii) a polygonal network of RC-Is at $t=0.163$, cf. Fig. 5.4(a), where some of the cells already begin to develop irregular small substructures, and (iii) large RC-II at $t=1.436$, cf. Fig. 5.4(c). Note that the profiles are the horizontal averages over the whole x - y plane. The curves with light gray (or green in color) plus signs (+) depict a purely diffusive evolution, i.e. starting with ideal initial conditions without noise. The individual data points in the 1D profiles correspond to the collocation points in the z -direction.

In both layers, the initially thin concentration boundary layers grow with time as the mass transfer proceeds and the individual convection cells increase in size. The mean interface

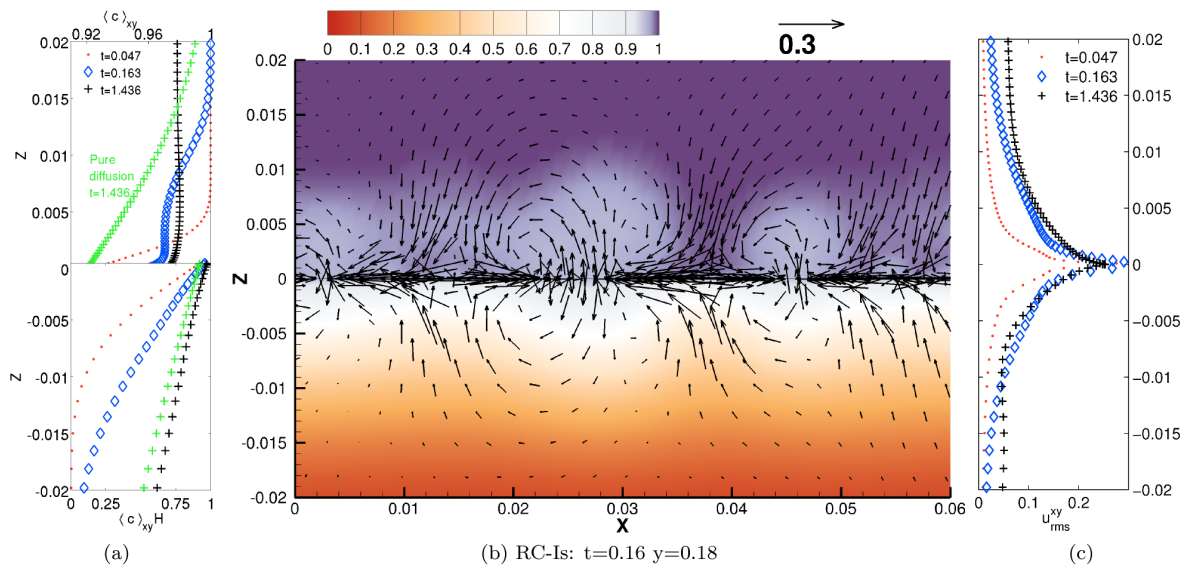


Figure 5.10: Marangoni roll cells in simulation E_1_1 : Horizontally averaged concentration (a) and rms velocity profiles (c) together with a vertical cross section through a *network of RC-Is* at $t=0.163$ for $y=0.18$ in (b). This cut is along the black line in Fig. 5.4(a). The color shows the concentration distribution in the upper layer $c^{(2)}$ and the scaled concentration in the lower layer $c^{(1)}H$. Vectors for velocity are plotted on a coarse grid to emphasize the large-scale flow. The individual markers in the profiles (a) and (c) represent the collocation points. Note that solid walls are at $z = \pm 1$.

concentration rises, and the bottom layer is progressively saturated with solute. In the top layer, the bulk concentration is necessarily lowered.

Furthermore, the graphs illustrate the influence of the diffusivity ratio on the concentration profiles. Due to the distinctly higher diffusivity in the bottom layer ($D^{(2)}/D^{(1)} = 0.14$), Marangoni convection affects the shape of the concentration profiles less pronounced there, but additional convection intensifies mixing of solute, cf. green (+)-curve for pure diffusion and black (+)-curve with convection at $z < 0$ in Fig. 5.10(a).

Additional profiles and a concentration distribution are plotted in Fig. 5.11 for a larger z -range at $t = 1.436$. In the upper phase ($z > 0$) in Fig. 5.10(a) and 5.11(a) the concentration profiles ($t = 0.163$, $t = 1.436$) have two characteristic gradients separated by turning points. The first gradient near the interface is formed by the combined action of small-scale flow of RC-Is, large-scale advection by RC-IIIs and the diffusive transport near the interface. The second gradient connects the *mixed fluid* near the interface with almost unchanged bulk fluid. This situation is visualized by the vertical cross section of the RC-Is pattern in Fig. 5.10(b) and the large-scale RC-II in Fig. 5.11(b). In both of these 2D concentration distributions, the mixed fluid appears in light gray. Mixing extends up to $z \approx 0.01$ for $t = 0.163$ [Fig. 5.10(a)] and $z \approx 0.04$ for $t = 1.436$ [Fig. 5.11(a)] in the top layer.

The cross-section in Fig. 5.11(b) explains the local maximum in the concentration profile of Fig. 5.11(a) at $z \approx 0.005$, which results from the general flow structure of the RC-IIIs in this system. The jet-like inflow in the center carries solute-rich fluid from the deeper bulk regions towards the interface, where the flow is diverted parallel to the interface. The fluid depleted of butanol, however, accumulates in the rather flat vortices at the cell boundaries

with a local minimum of concentration at $z \approx 0.02$.

The *velocity profiles*

$$u_{rms}^{xy}(z) = \sqrt{\langle \mathbf{u} \cdot \mathbf{u} \rangle_{xy}} \quad (5.19)$$

for the same states as the concentration profiles are shown in Figs. 5.10(c) and 5.11(c). In line with the concentration profiles, the zone influenced by interfacial convection grows in time. For late times, the rms velocity reaches a weak local maximum in the bottom layer at $z \approx -0.015$ [Fig. 5.11(c)]. This maximum can be assigned to the flow of the large RC-II-vortex in Fig. 5.11(b).

The shape of the presented velocity profile with the global maximum at the interface and the local maximum of the RC-II vortex qualitatively agrees with measured velocity profiles of substructured Marangoni cells in a Hele-Shaw geometry [199].

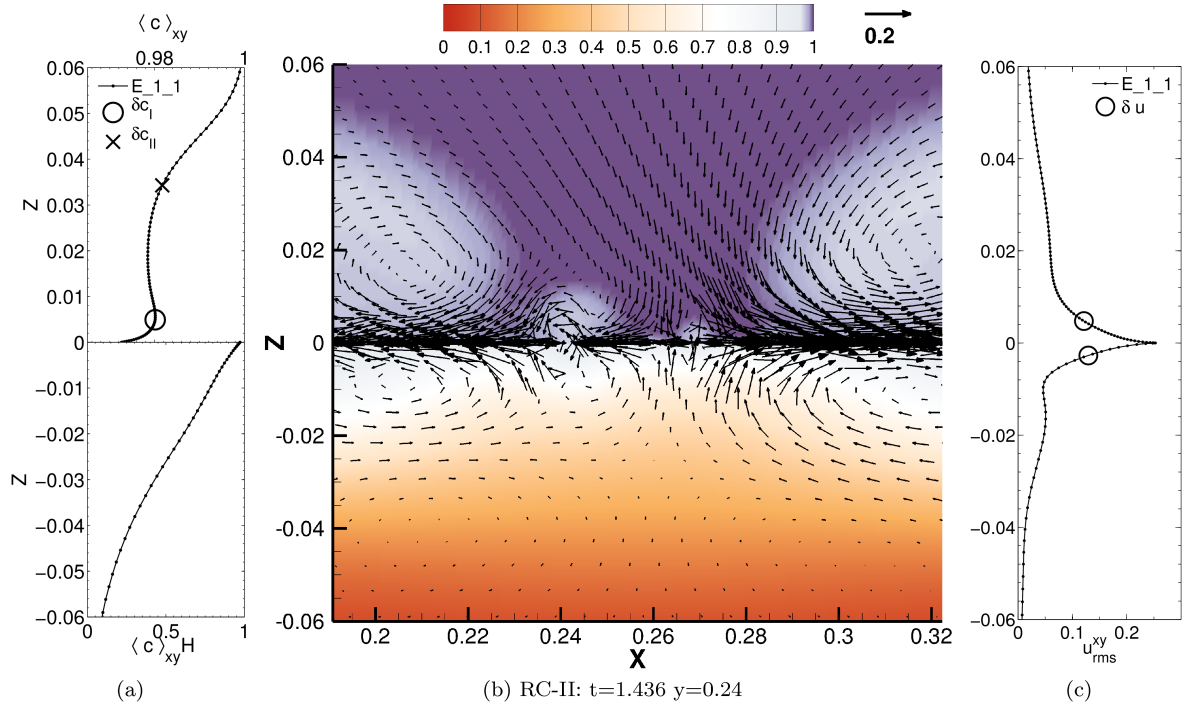


Figure 5.11: Marangoni roll cells in simulation E_1_1 : Horizontally averaged concentration (a) and rms velocity profiles (c) together with a vertical cross section of a *RC-II* with a substructure of smaller *RC-Is* at $t=1.436$ for $y=0.24$ in (b), so along the black line in Fig. 5.4(c). The color depicts the concentration distribution in the upper layer $c^{(2)}$ and the scaled concentration in the lower layer $c^{(1)}H$. Vectors for velocity are plotted on a much coarser grid than used in the simulation rendering the large-scale flow. The individual markers in the profiles (a) and (c) represent the collocation points. The size of the domain presented is roughly tripled relative to Fig. 5.10. Additional locations $\delta c_I, \delta c_{II}, \delta u$ represent length scales introduced in Sec. 5.4.2.

The potential mirror symmetry of the flow (for Stokes flow with $G = 0$), discussed in Sec. 3.2, was increasingly broken with advancing time. This asymmetry of the velocity is seen by

the difference between rms velocities of individual layers [Fig. 5.2(c)] and the just discussed profiles. The velocity distribution in Fig. 5.11(b-c) reaches further into the upper organic bulk phase.

We expect the asymmetry is due to the action of buoyancy arising in the course of mass transfer. The confinement of roll cell motion to the proximity of the interface is more pronounced in the lower aqueous phase. This asymmetry could be owing to the higher solutal expansion coefficient there $\beta = 0.75$ but is maybe also impacted by the higher diffusivity in the bottom layer. Other potential reasons for the asymmetry are inertial effects. However, in our units the Reynolds number is calculated by the velocity times a length $Re = ul$. Since the velocity at the interface is usually lower than one and every arising length scale is also lower than one, so $Re \ll 1$. Buoyancy effects are further studied in Sec. 5.5.

Finally, the vertical cut through the RC-II in Fig. 5.11 is supplemented with the planar view in Fig. 5.12. It combines the synthetic shadowgraph image with stress vectors in (a) and the velocity amplitude with velocity vectors in (b). The velocity field at the interface is primarily governed by the large-scale flow of the RC-II; secondary the RC-I substructure modulates this flow. The individual small RC-I's can be identified in both the distribution of the local Marangoni stresses (a) and the velocity magnitude of the central cells (b).

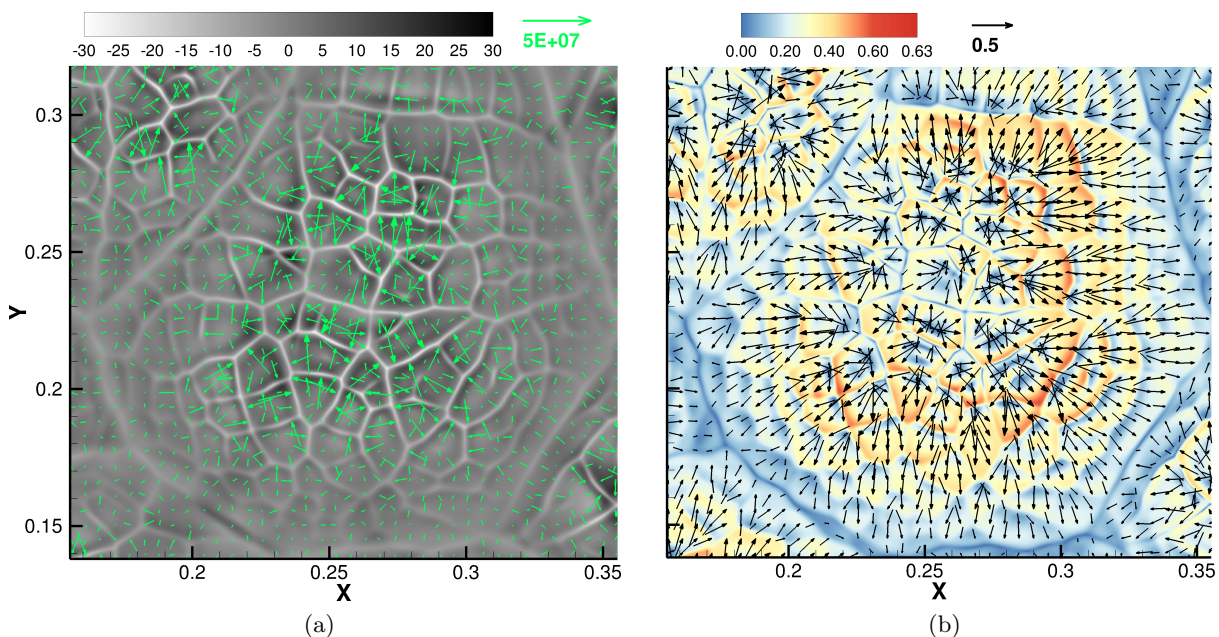


Figure 5.12: Fully developed RC-II (E_1_1): (a) Synthetic shadowgraph image ($-s(x,y)$) with \mathbf{t}_{Ma} , (b) velocity magnitude $|\mathbf{u}|(z = 0)$ with velocity vectors at the interface, both at $t=1.436$.

5.3 Comparison of simulations with experiments

The present section compares the performed simulations with experimental observation. We will use data from two independent experimental studies: Results from the thesis of Schwarz [198] and recent experimental data from Schwarzenberger and Eckert [111]. Before the comparison, the experimental procedure is presented in Sec. 5.3.1 according to Ref. [111].

Thereafter, a qualitative (Sec. 5.3.2) and quantitative (Secs. 5.3.3-5.3.5) comparison is performed.

5.3.1 Experimental procedure

This section briefly quotes the experimental procedure from Schwarzenberger & Eckert [111]. Cyclohexanol and water were mutually presaturated by gently stirring the superposed fluids each with the same volume for at least 24 hours. After separation of both phases, the desired solution of butanol in the cyclohexanol-rich phase with a molar concentration of c_0 was prepared and stirred well to distribute the solute homogeneously in the organic phase.

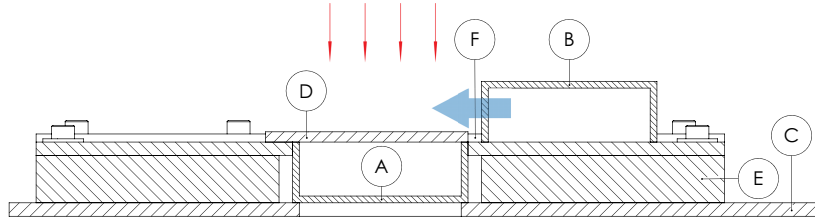


Figure 5.13: Experimental setup to superimpose the two phases. Image reproduced from [111].

The prepared phases were then filled in a glass cuvette (A),(B) (see Fig. 5.13) with an inner size of $L \times W \times H = 60 \text{ mm} \times 60 \text{ mm} \times 20 \text{ mm}$. As indicated by the horizontal block arrow both phases were joined by sliding cuvette B over A. After this procedure of superposition (referred as layering), the whole apparatus was introduced into the shadowgraph optics (beam path sketched by the vertical arrows).

The experimental shadowgraph images $s_{exp}(x, y)$ result from the deflection of light that is caused by the dependence of the refractive index on solute concentration. The experimental images were mimicked in the simulations by averaging the horizontal Laplacian of the solute concentration distribution over both layers [160] as already introduced in Eq. 5.15.

Thus, the synthetic shadowgraph images $s(x, y)$ permits a visual comparison of the emerging structures with the experiments. However, note that the *experimental* shadowgraph records were affected by potential deflections at the deformed interface and general nonlinearities in ray propagation and detection, in addition to the basic model Eq.(5.15).

A similar experimental setup was used by Linde & Schwarz [197, 198], but with a cuvette height $H=15\text{mm}$. Schwarz [198] described three experiments – with the current material system – that differ in the initial butanol concentration, i.e. $y_b = 0.025, 0.05, 0.1$. The corresponding numerical parameters were already presented in Tab. 5.3 under the group "S...". He showed several consecutive images of pattern formation for $y = 0.05$ and $y = 0.1$ and measured the RC-I sizes. This data will be discussed in the following sections.

Furthermore, in experiments of Schwarzenberger & Eckert, a larger field of view allowed to monitor the growth of the higher-order patterns, which cannot be extracted from the data of Schwarz. This was done for two initial concentration $y = 0.05, y = 0.075$. In this way, the multi-scale properties of the interfacial convection were substantiated. However, the images of Schwarz [198] were recorded with a higher magnification, i.e. they are suitable for an exact visual comparison with the high-resolution simulations. Whereas in the recent experiments, the smallest structures were not fully resolved.

5.3.2 Qualitative comparison

Sec. 5.2.1 showed the emerging Marangoni patterns in their temporal succession for the reference simulation. These images are compared versus two experimental images from the thesis of Schwarz [198] in Fig. 5.14. Although this experiments corresponds to parameters S_1 of Tab. 5.3, it differs from E_1-1 only by a slightly lower Grashof number $G = -4.35 \cdot 10^5$, which has only marginal influence on pattern formation, cf. Sec. 5.5. For this reason, no additional images from simulation S_1 are shown. Additional experimental images are shown in Fig. 5.15 from recent experiment [111] that correspond to reference parameters.

Generally, a remarkably good agreement, regarding the visual nature and the overall development of the structures is found between experimental images ^V and our simulations. Two main differences might be noted.

Firstly, the first phase I with initial RO is not covered with images or verbally by Schwarz. The earliest image that Schwarz showed is for a pattern of RC-I without substructure, Fig.12 in [198]. However, Linde noted such a phase of initial spreading in his review [146]. Recent experiments [111] failed to resolve these very small cells.

A second and clearer difference is that experimental pattern formation appeared accelerated relative to simulations. This acceleration is in two respects: the onset of convection as well as the consecutive speed of hierarchy formation. This becomes apparent when Schwarz's images are compared to the simulated images (Fig. 5.4 versus Fig. 5.14) and with recent experiments (Fig. 5.15).

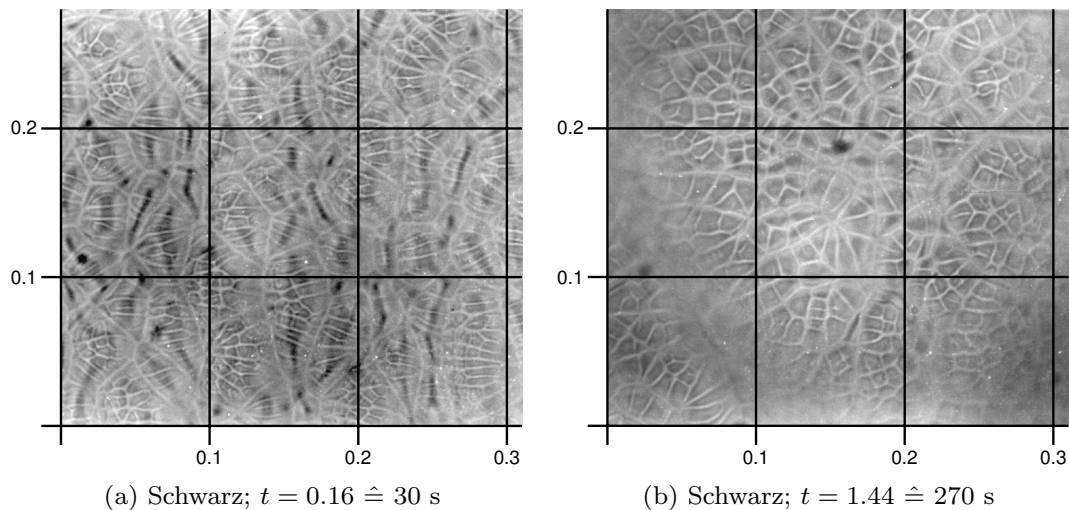


Figure 5.14: Coarsening phase of interfacial convection: experimental shadowgraph records of Schwarz [198]. The grid lines were inserted afterwards.

5.3.3 Horizontal size of RC-Is

The first-order Marangoni cells RC-Is are the basic modules of the solutal Marangoni pattern. Schwarz [198] measured their averaged diameter as a function of time. This circumstance calls for a unique and robust method to identify individual RC-Is from simulations automatically.

^VThis also applies to the additional images from Schwarz [198] not shown here and to his verbal description.

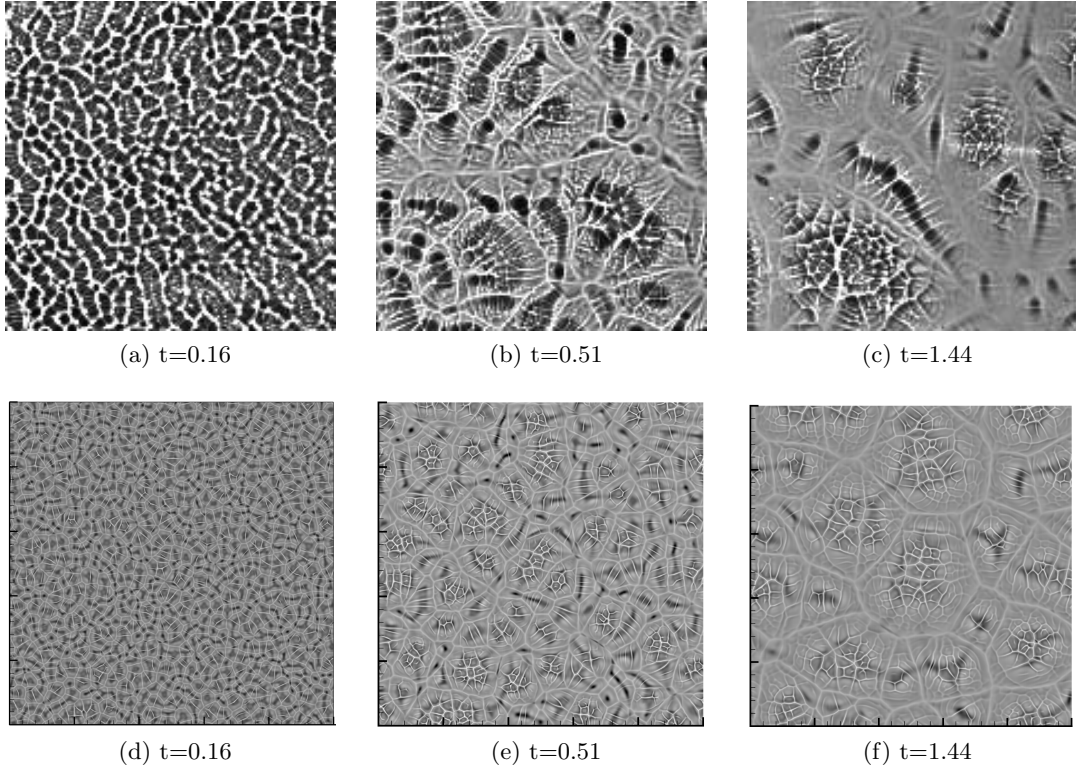


Figure 5.15: Growing size of RC-IIs: (a,b,c) In the experimental shadowgraph images (window of approx. 0.5×0.5) corresponding to the physical parameters of the reference simulation E_1_1 and (d,e,f) simulated pattern $(-s(x, y))$ in domain of 0.5×0.5 in (cf. Fig 5.4). Experiments from Schwarzenberger & Eckert reproduced from [111].

We identify individual RC-I by dividing the interfacial area into two parts, one with a negative and one with a positive vertical velocity gradient $\partial_z u_z(z = 0)$. Note that $\partial_z u_z$ is continuous at the interface, so we do not mark the phase. This definition accounts for the source of convection, i.e. the Marangoni stresses between the inflow region ($\partial_z u_z < 0$, low interfacial tension) and the outflow region ($\partial_z u_z > 0$, high interfacial tension). Specifically, we produce a binary distribution $I_0(\partial_z u_z)(x, y)$ of white $I_0(\partial_z u_z)(x, y) = 1$ for $\partial_z u_z > 0$ (outflow) and black $I_0(\partial_z u_z)(x, y) = 0$ for $\partial_z u_z \leq 0$ (inflow). An example of such a binarized image is shown in Fig. 5.16.

A conspicuous feature in Fig. 5.16 is the general bounding of the black inflow regions by the white outflow regions. These connected black subareas are identified as individual cells. The characteristic horizontal length scale, λ_{RC-I} , of the RC-Is is calculated from the individual cell areas A_j as the mean of the circular diameters

$$\lambda_{RC-I} = \frac{1}{N_c} \sum_{j=1}^{N_c} \sqrt{A_j 4/\pi}, \quad (5.20)$$

where N_c denotes the total number of cells. Details of the image processing are described in App. E.

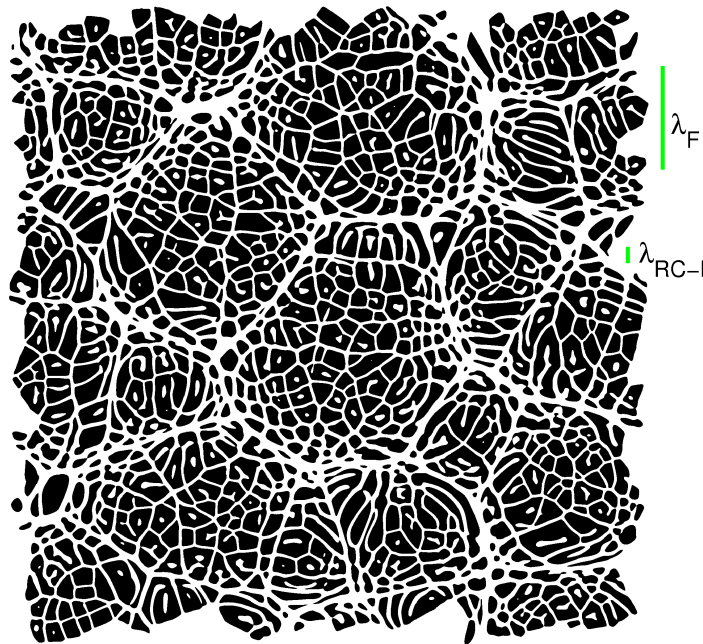


Figure 5.16: Vertical velocity gradient in binary representation $I_0(\partial_z u_z(z = 0, t = 1.44))$ of $E_{1.1}$ together with calculated length scales (λ_F , λ_{RC-I}).

The mean diameter of the RC-Is for the reference simulation $E_{1.1}$ is presented in Fig. 5.17(a). The diameter grows until it reaches a fairly constant value of $\lambda_{RC-I} \approx 0.013$, which agrees well with the corresponding measurement of Schwarz [198] (circles), see his Fig. 56. The end of the RC-Is growth phase coincides with the occurrence of the RC-IIs.

For a further comparison of the RC-I sizes, we have performed simulations corresponding to experiments of Schwarz [198] with lower butanol concentrations $y_b^{(2)} = 0.025$ (S.3) and $y_b^{(2)} = 0.05$ (S.2), cf. Tab. 5.3.

The size of RC-Is increased with lowered butanol concentration, which is reflected both in the experiment [198] and simulation when considering Figs. 5.17(a,b). Note that simulation S.3 had to be conducted with stronger initial perturbations to better match better the onset time of interfacial convection according to the experiments for this low butanol concentration. However, even under these conditions, the simulation S.3 shows a significantly retarded growth phase in Fig. 5.17(b). The simulation and the experiment agree better for $y_b^{(2)} = 0.05$.

According to our analysis in Sec. 3.1.1, we tried to account for the concentration change by the rescaling of time and length scales in Fig 5.17(c),(d). The rescaling is done by the relative Marangoni number $Ma_r = Ma / -2.4 \cdot 10^8$. Fig. 5.17(c) shows an effectively identical behavior of the RC-I sizes for different concentrations, especially in the early stage. ^{VI}

Rescaling is also applied to the data of Schwarz in Fig. 5.17(d). The differences between the early evolution of experiments are larger, although diameters for large times approximately show the assumed scaling. These differences might be explained by changes in material properties (e.g. diffusivities, viscosities, Henry coefficient) with concentration or the superposition procedure for creating the initial state.

^{VI}The deviation of S.3 is due to increased initial perturbations.

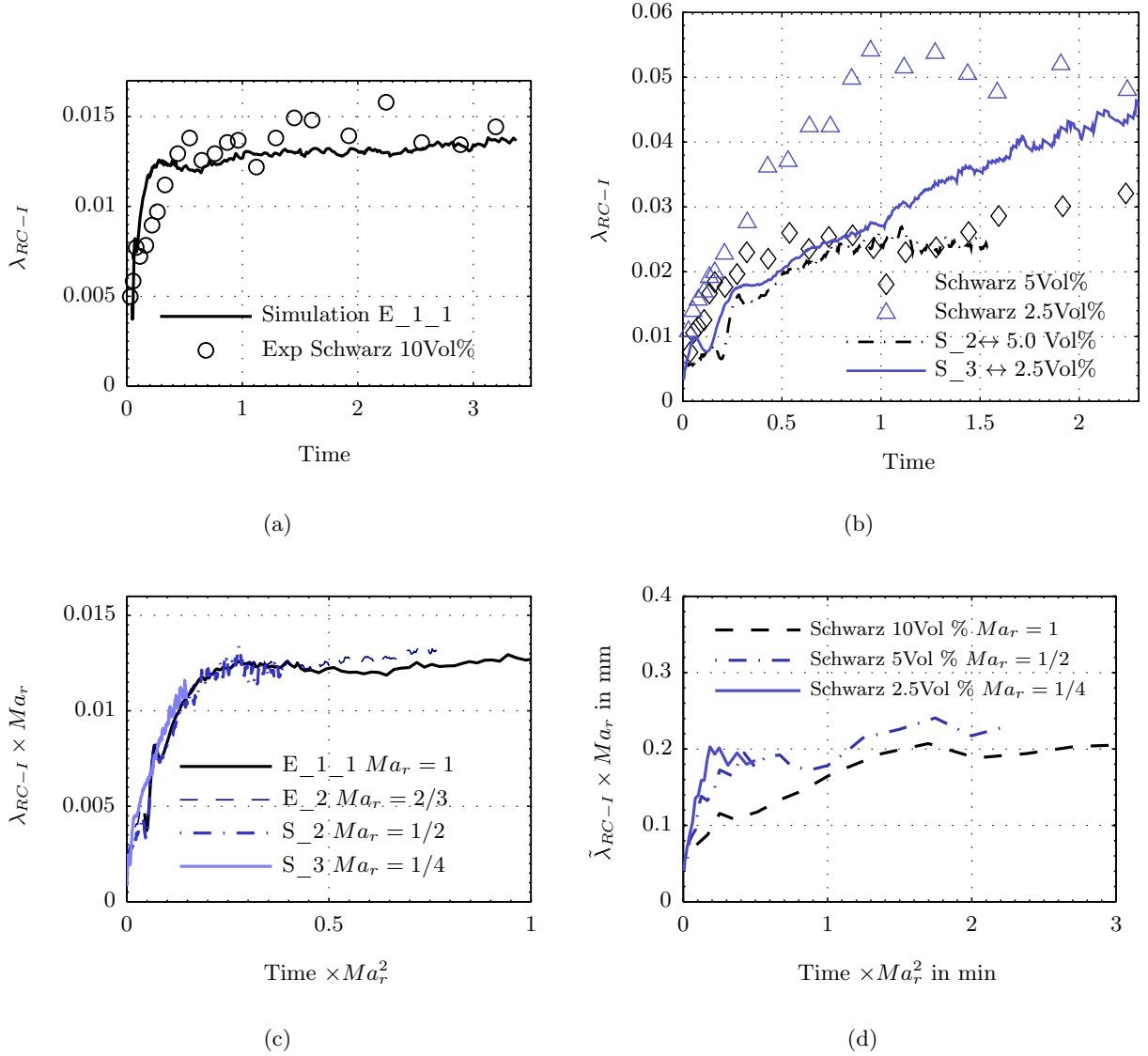


Figure 5.17: Sizes of RC-Is in the simulation and experiments of Schwarz [198]: (a) Mean circular diameter λ_{RC-I} of the RC-Is from image analysis of simulation $E_{1.1}$ and measurements of the mean RC-Is size by Schwarz (see Fig.56 in [198]). (b) Mean circular diameter λ_{RC-I} of the RC-Is of two simulations (S.3-1, S.2.1), cf. Tab. 5.3 and corresponding measurements of Schwarz [198], (c) mean circular diameters λ_{RC-I} from the simulations scaled with relative Marangoni number, (d) experimental data from Schwarz [198] rescaled but in *dimensional* representation.

5.3.4 Horizontal size of RC-IIs

After the RC-Is growth phase, the hierarchy formation towards the RC-IIs regime was the prevailing process, i.e. the difference in the length scales of the RC-IIs compared to the RC-Is rose in time. This difference is reflected in the synthetic shadowgraph pictures in Fig. 5.4 as well as in the experimental ones in Fig. 5.15.

The mean RC-IIs size was quantified by the dominant Fourier modes in the shadowgraph image and denoted as λ_F (with the subscript F for Fourier). The calculation is explained in App. E cf. Eq. (E.1). Please note that we applied a rather non-standard definition for λ_F to extract a length scale from experimental as well as simulated images that indeed represent RC-II sizes in agreement with the visual impression. This is because the power spectrum of $s(x, y)$ peaks for wavenumbers that are related to the width of cell boundaries, which is not the desired length and also not accurately resolved in the experimental images.

The quantity λ_F reflects the RC-IIs size after $t=0.3$ (E_1.1) when the RC-II regime started to dominate. The same evaluation procedure was carried out for the experimental shadowgraph records, cf. Fig. 5.15. Experiments with a lower concentration of solute (corresponding to E_2.1) merely produced a poor signal-to-noise ratio due to the low contrast of the shadowgraph images; so, they were not used.

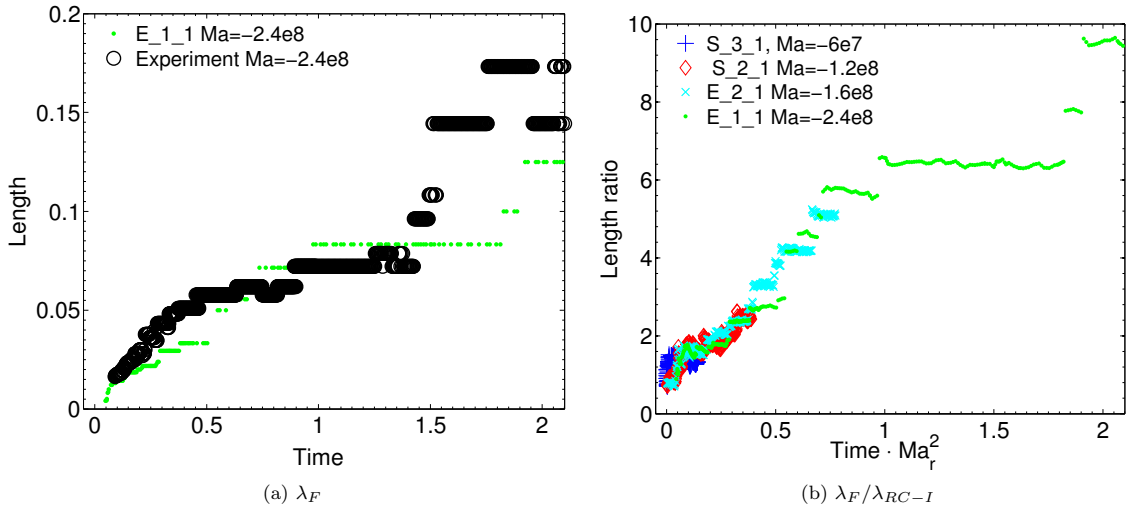


Figure 5.18: Length scales of RC-IIs from experiment [111] and simulation: (a) Evolution of λ_F from the radially averaged spectrum of $s(x, y)$ in the reference configuration, (b) ratio of λ_F and the RC-Is size λ_F/λ_{RC-I} for the simulations with rescaled time. The discrete nature originates from averaging the spectrum around wavelength l_x/i for $i \in (1, 2, 3, \dots, N_x/2)$.

The growth of λ_F is shown in Fig. 5.18(a). It agrees between the simulations (dots) and the observations from the reference experiment (black circles). However, as already noticed in the progression of the RC-Is sizes in Fig. 5.17(b), the experimental length scales exceed the ones from the simulations. This is in line with the visual impression from Fig. 5.15.

Fig. 5.18(b) illustrates the degree of hierarchy formation, which is manifested in the ratio of λ_F to the formerly calculated RC-Is size λ_{RC-I} . This length ratio λ_F/λ_{RC-I} is related to the number of subcells in a RC-II and increases with time.

5.3.5 Optical flow

In this section, a third method to compare the simulated with the experimental data is presented. On the basis of shadowgraph records, it is also possible to obtain information on the flow field of the RC-II. This is done by calculating the optical flow field \mathbf{u}_{of} [12] from two consecutive shadowgraph images. However, as the quantity (\mathbf{u}_{of}) is not identical to any direct physical quantity, the interpretation of the optical flow requires special care. In the following we will relate this optical flow with the interfacial velocity.

A standard commercial particle image velocimetry (PIV) tool "PivView" [241] was used to calculate an optical flow \mathbf{u}_{of} . Basically, the PIV method partitions the image into interrogation regions. Then, it calculates a displacement of these interrogation regions between successive images such that the cross-correlation functions between displaced [239] interrogation regions is maximized. These optimal displacements are afterwards divided by the time between images to yield the *optical flow*.^{VII}

Fig. 5.19 shows such an optical flow from an experiment with the reference parameters (E.1.1). The root mean squared value of the optical flow is $\sqrt{\langle(\mathbf{u}'_{of})^2\rangle_{xy}} = 0.2226$, where the mean flow has been subtracted as it is substantial $\langle\mathbf{u}_{of}\rangle = -0.42\mathbf{e}_x + 0.0531\mathbf{e}_y$. This is probably caused by the interaction of the curved interface near the cuvette walls.

The same procedure is applied to the simulated synthetic shadowgraph distribution and displayed in Fig. 5.20(b) for a similar state of pattern formation than shown in the experimental image. For comparison, the interfacial velocity is plotted beside in Fig. 5.20(a). In fact, both flow fields from Fig. 5.20 agree to a large extent for the hierarchical RC-II. A quantitative comparison, however, reveals that the optical flow underestimates the actual velocity at the interface: The mean interfacial velocity is $u_{rms}^{(s)} = \sqrt{\langle(\mathbf{u}(z=0))^2\rangle_{xy}} = 0.2516$ and the mean optical flow is $\sqrt{\langle(\mathbf{u}'_{of})^2\rangle_{xy}} = 0.1363$, both calculated for the state in Fig. 5.20. Furthermore, the experimental optical flow is twice as high as the simulated one (0.2226/0.1363), although a similar pattern is picked from the experiment.

From the purely theoretical point of view, one reason for the general underestimation of interfacial velocity by the optical flow is the spatial averaging, which is inherent in PIV method. Namely, the cross-correlation is determined for discrete image subdomains of finite width. The impact of spatial averaging was estimated by downsampling interfacial velocity and thereafter calculating the mean.

In detail, the data is given at the gridpoints (x_i, y_j) for $i \in \{0, 1, \dots, N_x - 1\}, j \in \{0, 1, \dots, N_y - 1\}$

$$x_i = il_x/N_x, \quad y_j = jl_y/N_y \quad (5.21)$$

For downsampling, we defined a square of edge length $l_x N_s / (N_x)$ (with $N_s < N_x$) in which the velocity is averaged and then assigned to the center of these squares. We call N_s the sub-sampling factor and reduce the resolution by covering the full area by these disjoint squares. The outcome of downsampling and afterwards averaging the velocity is shown in Fig. 5.22(a). As expected the rms velocity drops with increasing N_s .

A second reason why the optical flow underestimated interfacial flow is that the flow induced by the smallest structures cannot be detected, since they do not transport a detectable

^{VII}For comprehensive theoretical understanding this procedure is a bit unsatisfactory since the exact algorithm is only partly laid out to the public. However, this method is widely used in experimental fluid mechanics so we will proceed. The data of optical flow calculations is provided to us by Karin Schwabenberger.

optical inhomogeneity. This effect is visualized in Fig. 5.21 for the early state of mass transfer, where the pronounced hierarchical patterns have not developed yet and mainly RC-I exist. In this case, optical flow and interfacial velocity distinctly deviate. Flow is only detected in regions where RC-IIs begin to form. Hence, the mean magnitude of the optical flow is very small $\langle |\mathbf{u}'_{of}| \rangle = 0.0355$ compared to the mean magnitude of the interfacial velocity $\langle |\mathbf{u}| \rangle = 0.3338$, see also Fig. 5.22(b) for the impact of subsampling .

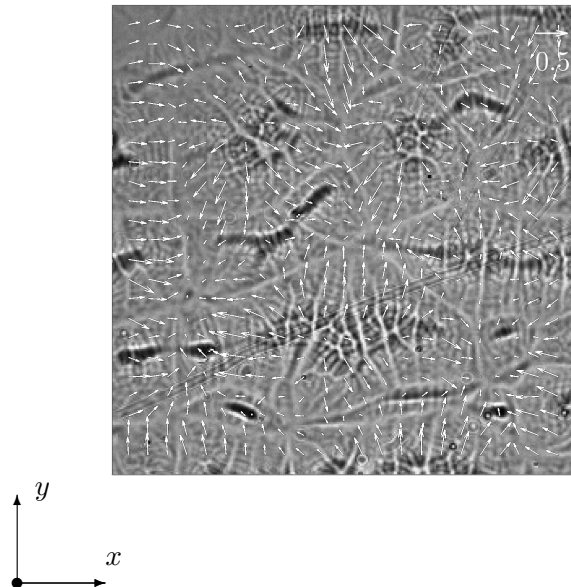


Figure 5.19: Experimental pattern of RC-II with optical flow field. A window of 0.5×0.5 (corresponding to $1 \text{ cm} \times 1 \text{ cm}$) is shown. $\langle u_x \rangle = -0.42$, $\langle u_y \rangle = 0.0531$. We plot $\mathbf{u}'_{of} = \mathbf{u}_{of} - \langle \mathbf{u}_{of} \rangle_{xy}$. The averaged velocity is $\langle |\mathbf{u}'_{of}| \rangle = 0.2021$, $\sqrt{\langle (\mathbf{u}'_{of})^2 \rangle} = 0.2226$. Image reproduced from Ref. [200].

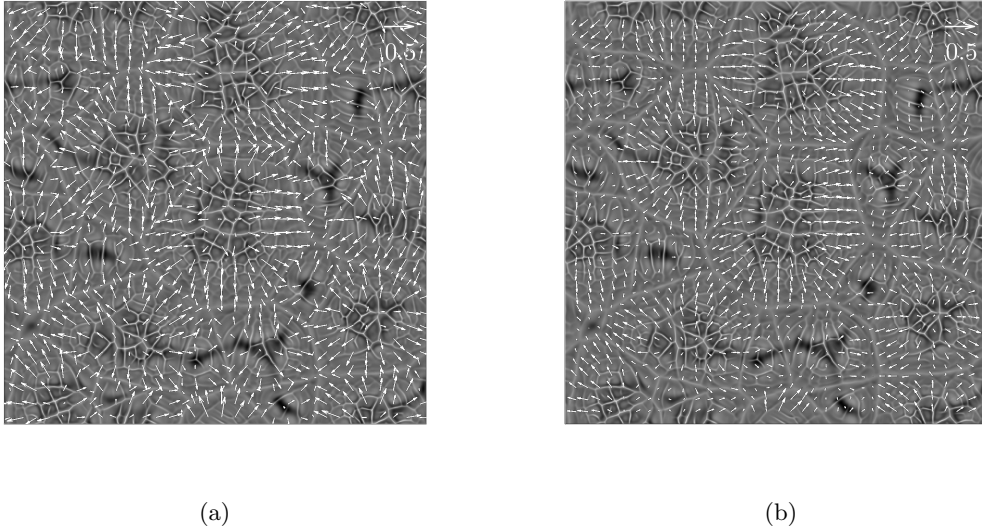


Figure 5.20: (a) Interfacial velocity and optical flow (b) for a pattern of RC-II at $t = 1.5$ (simulation E_1.1). The interfacial velocity in (a) is plotted on a coarse grid, i.e. averaged over 64×64 points. The domain size is 0.5×0.5 . Mean flow is very small $\langle \mathbf{u}(z=0) \rangle_{xy} = 2.1 \cdot 10^{-5} \mathbf{e}_x + 1.57 \cdot 10^{-5} \mathbf{e}_y$. Averaged velocity is $\langle |\mathbf{u}| \rangle = 0.2303$, $\sqrt{\langle (\mathbf{u})^2 \rangle} = 0.2516$ and averaged optical flow is $\langle |\mathbf{u}_{of}| \rangle = 0.1228$, $\sqrt{\langle (\mathbf{u}_{of})^2 \rangle_{xy}} = 0.1363$.

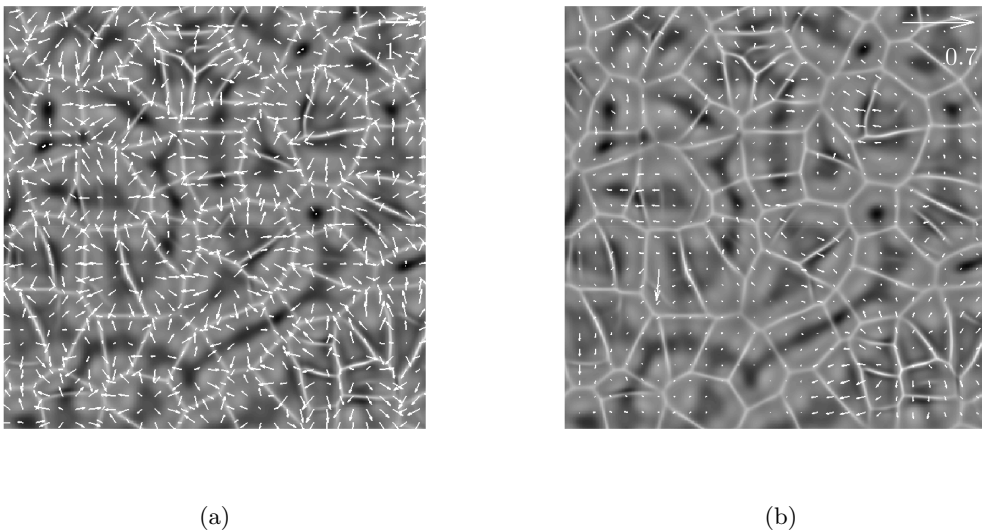


Figure 5.21: (a) Interfacial velocity and optical flow (b) for a pattern of mainly RC-I at $t = 0.2$ (simulation E_1.1). The interfacial velocity in (a) is plotted on a coarse grid, i.e. averaged over 16×16 collocation points. The size of the shown domain is 0.125×0.125 .

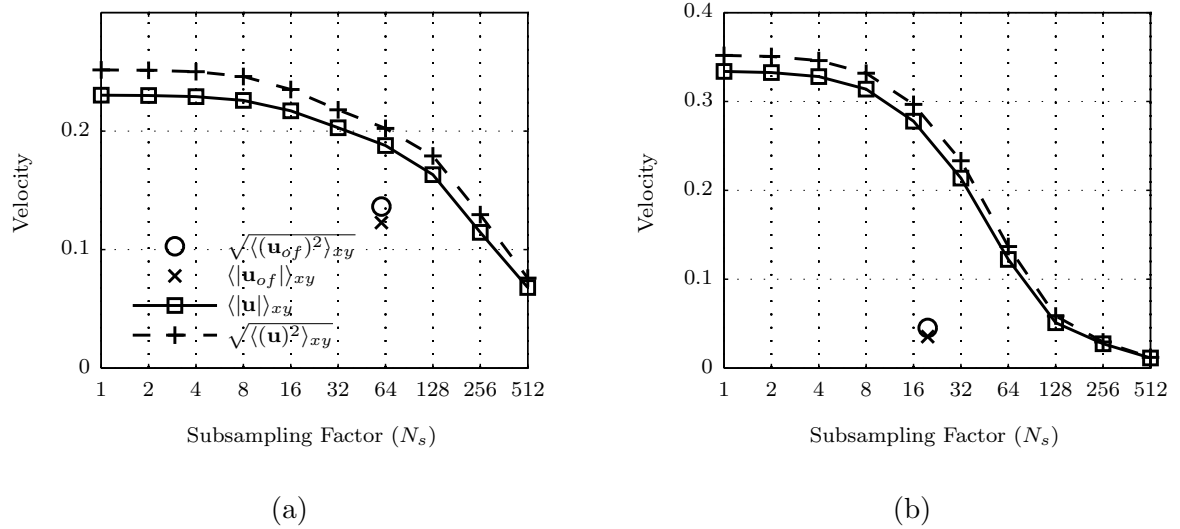


Figure 5.22: Averaged interfacial velocity and optical flow for $t=1.5$ (a) and $t=0.188$ (b) in simulation E_1_1. Interfacial velocity is shown for different subsampling factors N_s , whereas for N_s is the size of the interrogation window for PIV method.

5.4 Discussion: mechanism of multiscale structures

Section 5.2 illustrated the main evolution and generic structures of solutal Marangoni in a regime of *deep layer* convection, where convection is restricted to the proximity of the interface and the largest structures are smaller than the periodicity length. This was done until $t \approx 1.5$ for simulation E_1_1. In this framework, the question of how structures change and transform locally is addressed in the following.

To classify the pattern evolution, we identified two main mechanisms: The *coarsening* of convection patterns and their subdivision by a *local instability* at the inflow regions. The two mechanisms are present in both the very early phase and in the later evolution. In the following subsections, both mechanisms are discussed on the basis of a hierarchical cellular pattern.

5.4.1 Coarsening of hierarchical pattern: general properties

We expect that coarsening is caused by the continuing equilibration of concentration differences between the phases. Therefore, cells with large vertical dimensions are favored as they are more efficient at transporting solute over a mixed layer of width δc_{II} . The growth of individual cells leads to a growing velocity penetration depth δu , which in turn causes an increase in the horizontal length scales as both quantities are coupled by the cellular flow structure. The horizontal length scales λ_{RC-I} and λ_F have been determined in Sec. 5.3. In the following, we further describe these interactions by displaying additional data from the reference simulation. The noted vertical length scales $(\delta u, \delta c_{II})$ are calculated in the next Sec. 5.4.2.

The coarsening and substructuring of individual cells continues after the vigorous initial phase, and the most efficient cells keep expanding to compensate the growing mixing zone in the organic phase, illustrated in Fig. 5.23 by a sequence of shadowgraph images together with corresponding cross sections at $y=0.24$.

In Fig. 5.23(b), the inflow zones – i.e. where fluid streams towards the interface – of two major RC-IIs are visible in the center ($x=0.25$) and at the right-hand side ($x=0.46$) as dark zones in the upper organic phase (violet color). At $x=0.165$, a weak inflow zone of a fading RC-II can be observed. It is incorporated by its neighbors in Fig. 5.23(c,d). Finally, in Fig. 5.23(e,f), the inflow zones of two remaining large RC-IIs are visible in the center and at the left and right margin (due to the periodicity of the displayed image section in the x -direction) separated by the outflow with white, plume-shaped depletion zones. Contrary to Fig. 5.23(b), where these depletion zones are modulated by different smaller RC-IIIs, they now appear as continuous white regions.

Figs. 5.23(b,d,f) illustrate that a characteristic feature of the RC-IIIs is their slow evolution based on the history of these depleted zones. Fig. 5.24 depicts the topography of these zones at $t=1.44$ by the isosurface of concentration $c^{(2)} = 0.98$ in the organic phase. The large, bulky depletion zones are interconnected and bound the individual inflow regions. At the inflow regions, the fine RC-Is that are created by the local instability can be observed because the high concentration of the bulk phase is carried to the interface.

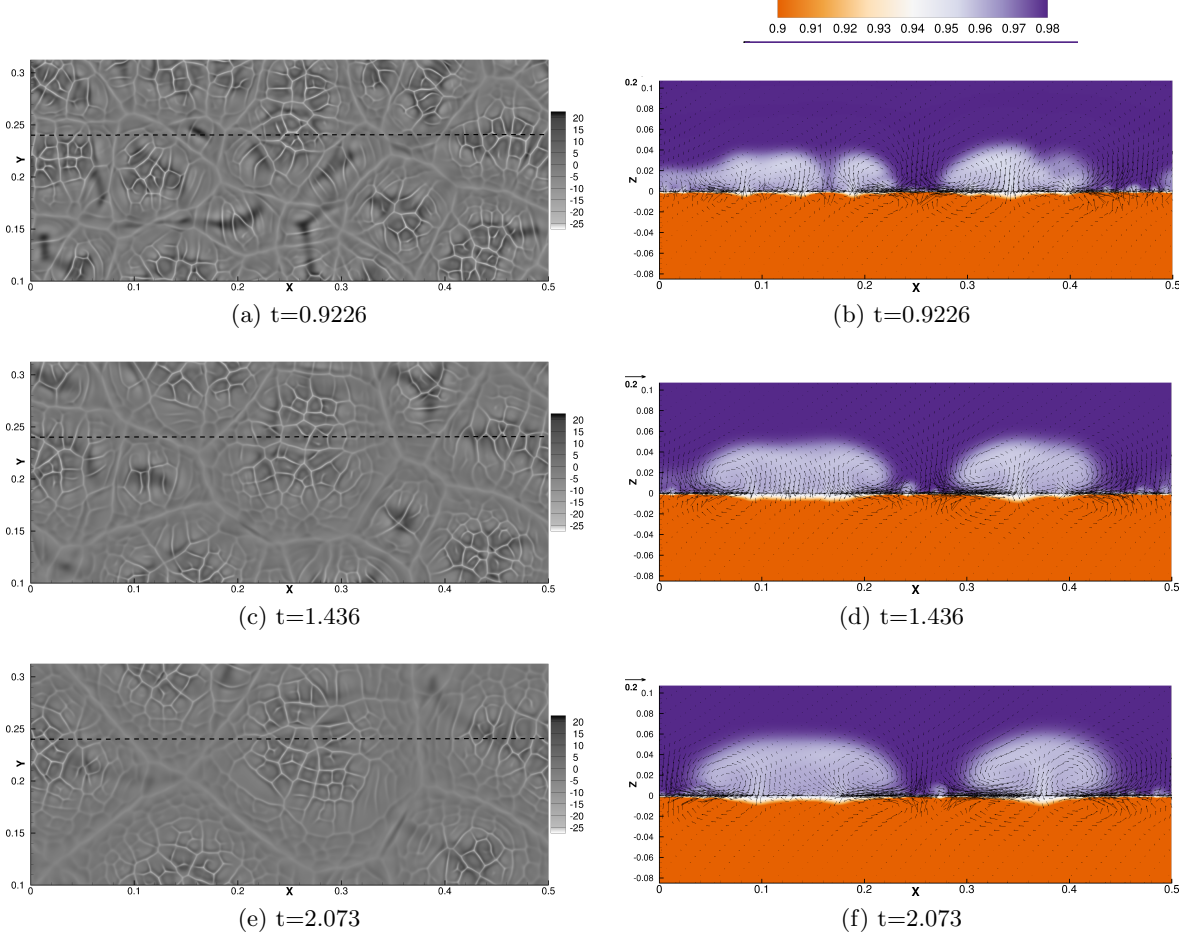


Figure 5.23: RC-IIs development for E_1.1.1.: Synthetic shadowgraph pictures $(-s(x, y))$ on the left and concentration distributions $c^{(1)}H$ and $c^{(2)}$ along the black dashed line at $y=0.24$ on the right hand side with the velocity field.

5.4.2 Coarsening of hierarchical pattern: vertical length scales

In line with the former discussion, the solute concentration can be characterized by two length scales: the boundary layer width $\delta c_I^{(i)}$ —already introduced to analyze the onset of convection—and the larger mixing-zone width $\delta c_{II}^{(2)}$,

$$\delta c_I^{(2)} = \frac{1 - \langle c^{(2)} \rangle_s}{|\langle \partial_z c^{(2)} \rangle_s|}, \quad \delta c_{II}^{(2)} = \frac{1 - \langle c^{(2)} \rangle_{\Omega^{(2)}}}{1 - \langle c^{(2)} \rangle_s}, \quad (5.22)$$

We only discuss the upper phase concerning concentration since division of scales is stronger there.

The highest numerical requirements for spatial resolution are set by the boundary layer width $\delta c_I^{(2)}$. Its temporal behavior is shown in Fig. 5.25(a) for four different initial concentrations of butanol. At the beginning, its evolution is governed by pure diffusion, and it grows as \sqrt{t} . The onset time of Marangoni convection is given by the local maximum in Fig. 5.25(a). At this instant of time, $\delta c_I^{(2)}$ drops due to the strong advection of the initial ROs. The sub-

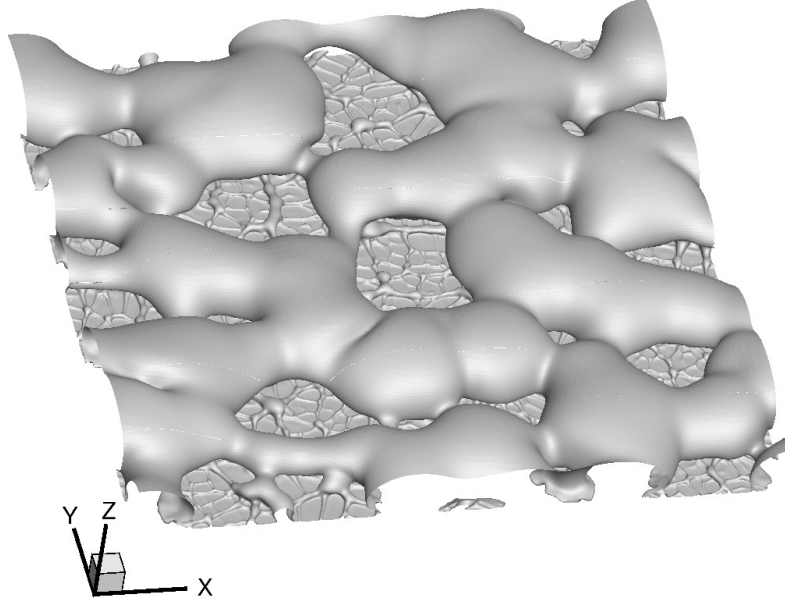


Figure 5.24: Isosurface of concentration at $c^{(2)} = 0.98$ in the upper layer for $t = 1.44$, $E_{1.1}$.

sequent growth of $\delta c_I^{(2)}$ is associated with the general reduction of concentration difference across the layers.

The mixing-zone width corresponds to a virtual layer of height $\delta c_{II}^{(2)}$, base areas $l_x \times l_y$, a concentration of $1 - \langle c^{(2)} \rangle_s$ (i.e. the difference to the initial concentration) and that contains the transported amount of solute $(1 - \langle c^{(2)} \rangle_{\Omega^{(2)}})l_x l_y$. The growth of $\delta c_{II}^{(2)}$ is therefore accelerated by the convective motion compared to the case of pure diffusion, cf. Fig. 5.25(b).

Similar to the mixing zone width $\delta c_{II}^{(2)}$, we define a vertical velocity penetration depth $\delta u^{(i)}$ by the ratio

$$\delta u^{(i)} = \frac{\langle \mathbf{u}^{(i)} \cdot \mathbf{u}^{(i)} \rangle_{xyz}}{\langle \mathbf{u}^{(i)} \cdot \mathbf{u}^{(i)} \rangle_s}. \quad (5.23)$$

The penetration depth of velocity, see Figs. 5.26(a) follows the coarsening trend in time just as the formerly introduced scales λ_{RC-I} , λ_F , $\delta c_I^{(2)}$, $\delta c_{II}^{(2)}$.

With this length $\delta u^{(2)}$ and the interfacial rms velocity, a Reynolds number $Re^{(2)}$ for the top layer is defined by

$$Re^{(2)} = \delta u^{(2)} \sqrt{\langle \mathbf{u} \cdot \mathbf{u} \rangle_s} \nu^{-1} = \frac{\langle \mathbf{u} \cdot \mathbf{u} \rangle_{\Omega^{(2)}}}{\nu \sqrt{\langle \mathbf{u} \cdot \mathbf{u} \rangle_s}}. \quad (5.24)$$

This definition uses the length scale of characteristic structures. Therefore, Re estimates the common ratio of advective to viscous momentum transport. Fig. 5.26(b) shows that $Re^{(2)}$ is clearly below unity, hence momentum transport is mainly due to viscous diffusion. Furthermore, the mass transport mechanisms can be characterized by the Peclet number $Pe^{(2)} = Re^{(2)} Sc^{(2)} = Re^{(2)} \cdot 2.86 \cdot 10^5$, which takes values around 10^1 in the upper phase and around unity in the lower phase (because $Pe^{(1)} = Sc^{(1)} \delta u^{(1)} \sqrt{\langle \mathbf{u} \cdot \mathbf{u} \rangle_s}$). Thus mass transport of butanol is dominated by advection despite small Re , particularly in the upper phase on account of the low diffusivity there.

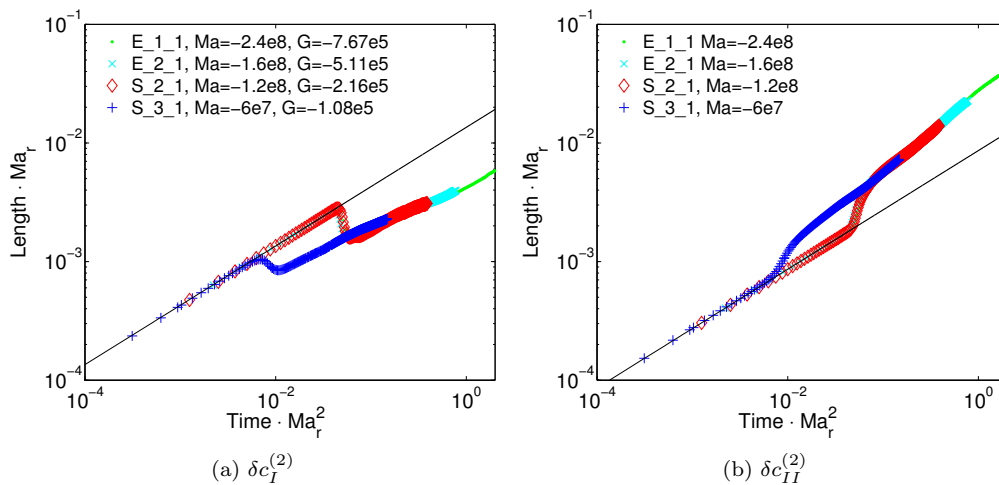


Figure 5.25: Temporal evolution of (a) concentration boundary layer and (b) mixing zone for four different simulations, cf. Tab. 5.3. The thin solid line represents the analytical solution of the diffusion problem in two semi-infinite layers (Sec. 3.3).

5.4.3 Substructuring of hierarchical pattern

The second mechanism is the *local instability* that leads to a subdivision of the inflow regions. It appears clearly visible during the creation of new solute fronts in the shadowgraph images. It limits the maximum size of RC-Is since the probability of splitting seems to increase with the size of a contiguous inflow region and with the local concentration gradient.

The generation and drift of substructures are shown in Fig. 5.27. This image sequence is taken from the center of the large RC-II in the middle of Fig. 5.23, while the time range is located in between Fig. 5.23(a) and (c). The mean drift of the substructure cells is directed from the center to the left and right margins of the images. In Fig. 5.27(a), large inflow zones with a stagnant velocity are visible at **A** and **B**. Subsequently, they split into two smaller cells. The bright cell boundaries that divide the freshly generated substructure cells become visible in the shadowgraph images (b) and (c).

Comparable to the breakdown of the initial ROs (Fig. 5.8), the local instabilities appeared in the growing inflow zones. We expect that this instability to be governed by the high vertical concentration gradients there. As a result, small length scales are produced in the inflow zones that are subsequently advected by the large-scale flow throughout the RC-IIs. This process of small length scale production competes with coarsening and may, therefore, explain the plateau phase in the λ_{RC-I} evolution from $t \approx 0.3$ on, cf. Fig. 5.17.

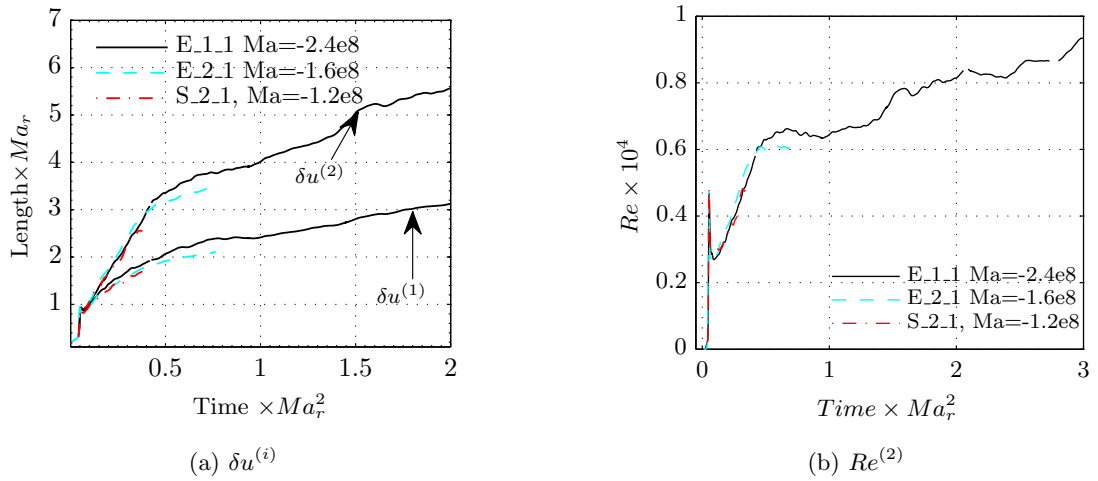


Figure 5.26: Temporal evolution of (a) velocity penetration depth $\delta u^{(i)}$ Eq. (5.23) and of (b) Reynolds number in the top layer $Re^{(2)}$ according to Eq. (5.24).

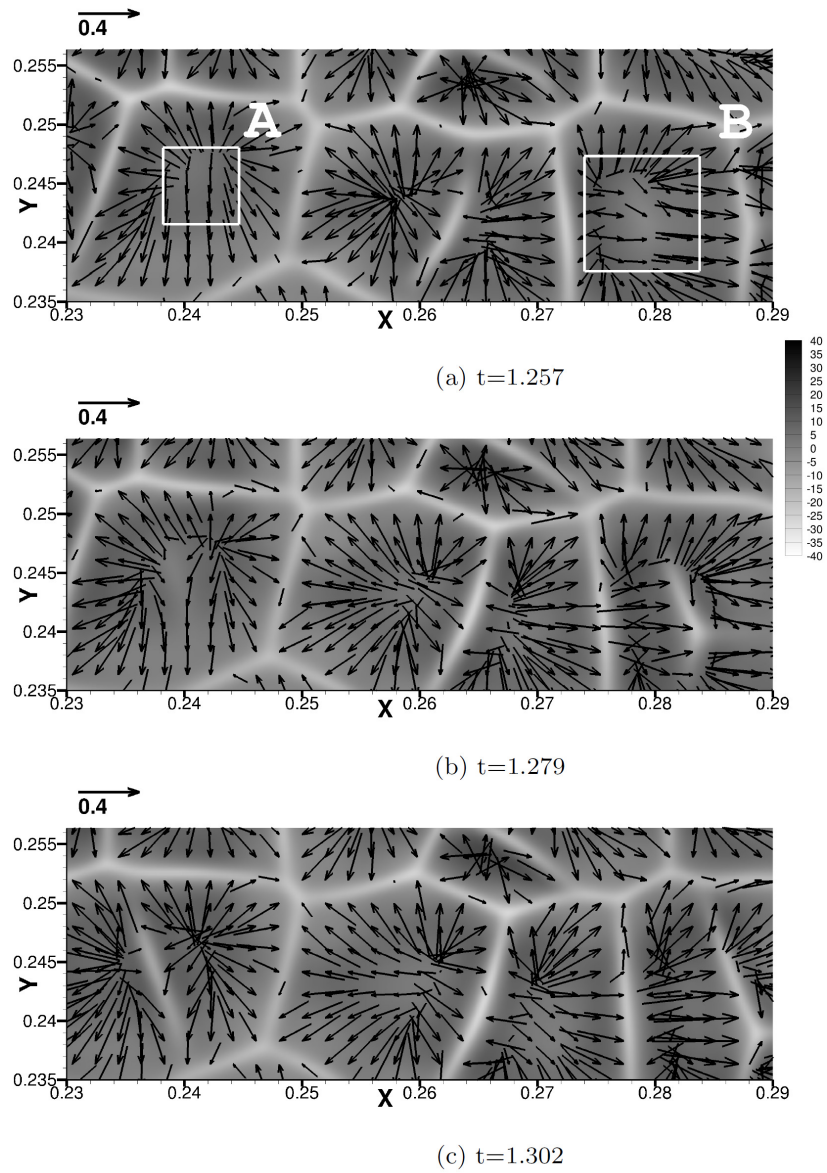


Figure 5.27: Drift and creation of substructures in shadowgraph images ($-s(x, y)$) from the reference simulation $E_{1.1}$ with the corresponding velocity field at consecutive times.

5.5 Role of gravity and geometrical constraints

This section is dedicated to further parametric studies. Parameter space is obviously quite large, and yet the experimental parameters used were such that we could not afford a sufficiently large interface (l_x, l_x) to study the process of pattern coarsening beyond $t \approx 3$, since largest cell were comparable to the interface size (l_x, l_y) . Of course, one has to pick configurations that are of distinct theoretical and practical importance. Therefore, we investigate further the role of scale invariance under a change of Ma noted in Sec. 3.1.1 and already applied in the former sections. This is done by a selective variation of the prerequisites for scale invariance – i.e. geometrical limitations and buoyancy influence. The principle of scale invariance is important with regard to two aspects: the change of initial concentration (and thereby Ma) is simple to apply in experiments and the impact of concentration variations (thus Ma) on mass transfer rates is important for industrial extraction processes.

Density stratification, which grows with advancing equilibration, is analyzed by performing an additional simulation without gravity influence G_1.1, but otherwise the same parameters as in the reference simulation E_1.1. Furthermore, with simulations G_1.2–G_1.4 (see Tab.5.3), it is demonstrated how reduction of periodicity lengths l_x, l_y change patterns and mass transfer. Finally, two simulations L_1, L_2 are presented, having lower Marangoni numbers and also vanishing Grashof number $G = 0$. These simulations capture the full equilibration process, thereby probing the vertical constraints set by the layer heights.

5.5.1 Impact of density stratification

The impact of density stratification on mass transfer of will be characterized by two quantities: (1) The transient Sherwood number

$$Sh(t) = \frac{\langle \partial_z c^{(1)}(t, z = 0, x, y) \rangle_{xy}}{\partial_z c_{diff}^{(1)}(t, z = 0)}, \quad (5.25)$$

which relates the actual mass flux to the one from the pure diffusive solution D_1. Note that $\partial_z c_{diff}^{(1)}$ is obviously also time dependent. (2) The enhancement factor

$$R = \frac{\langle c^{(1)} \rangle_{xyz}}{\langle c_{diff}^{(1)} \rangle_{xyz}} \quad (5.26)$$

represents the actual amount of transported solute normalized by the one from the purely diffusive solution.

The difference in Sh due to the presence ($G \neq 0$) or absence ($G = 0$) of a stabilizing density stratification is shown in Fig. 5.29(a). It compares the reference simulation E_1.1 with its counterpart with zero Grashof number G_1.1. Both show a steep increase in Sh at the onset of interfacial convection. In the phase of hierarchy formation ($t > 0.1$), Sh was growing further in the zero Grashof number case (G_1.1) but leveled off for the reference simulation. The same behavior is reflected in the enhancement factor R in Fig. 5.29(c).

A further difference is seen in the rms-velocity for the separate layers [Fig. 5.29(b)]. For $G = 0$, the velocity in both layers is almost identical (blue lines no visible difference), which is in line with the symmetry properties of the Stokes equations for $G = 0$, cf. Sec. 3.2. A bit unexpected is that the upper layer (2) velocity is lower for $G = 0$ than for $G = -7.7 \cdot 10^5$.

This situation might be caused by a difference in flow structure. For instance, RC-IIs have smaller horizontal extent for $G=0$: see Fig. 5.28(b) and compare to Fig. 5.4(d).

The simulation G_1_1 shows the same key properties in terms of pattern formation as described for the reference simulation. Additional shadowgraph images of simulation G_1_1 are collected in Fig. D.1 in App. D.1.

In former Sec. 5.3, different initial concentration were simulated. In the presence of gravity, *lower* solute concentrations yield *higher* Morton numbers $Mo = (|G|(Sc^{(1)})^3)/(|Ma|^3)$, see legend of Fig. 5.29(d). We introduced the Morton number in Sec. 3.1.1, where we discussed the scaling of equations without external length scale. There we showed that in the deep layer regime (i.e. when the system appears as practically semi-infinite) Mo should be used to measure the impact of buoyancy.

In this view, Fig. 5.29(d) shows the increased deviation from G_1_1 with increased Morton number as well as with increased rescaled time.

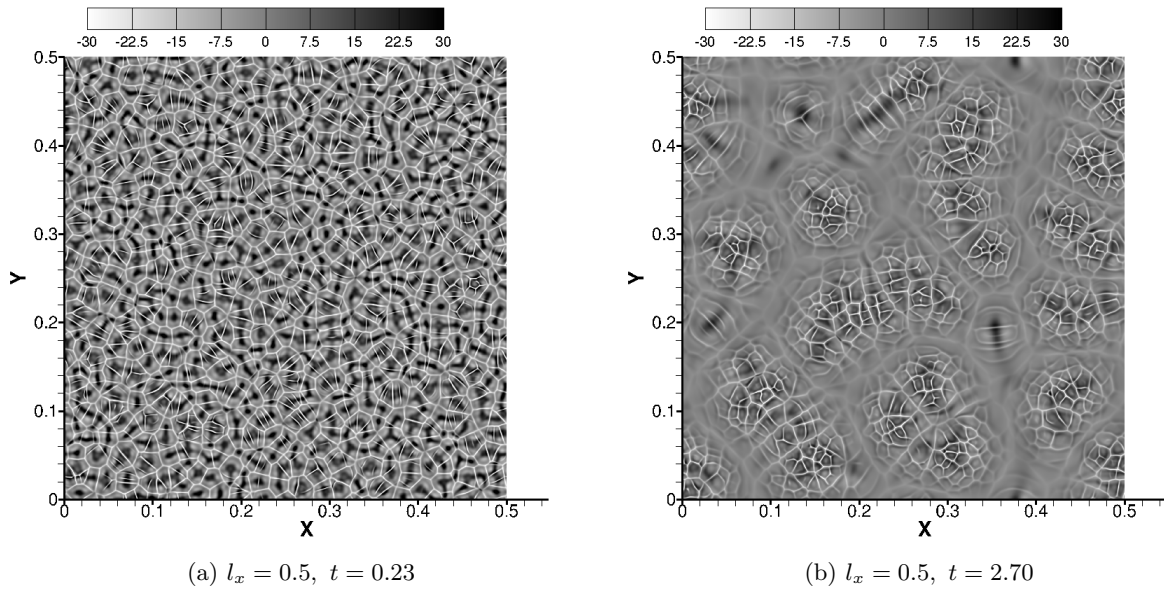


Figure 5.28: Computed shadowgraph images showing the pattern formation for a domain size of $l_x, l_y = 0.5$ in G_1_1.

·
·

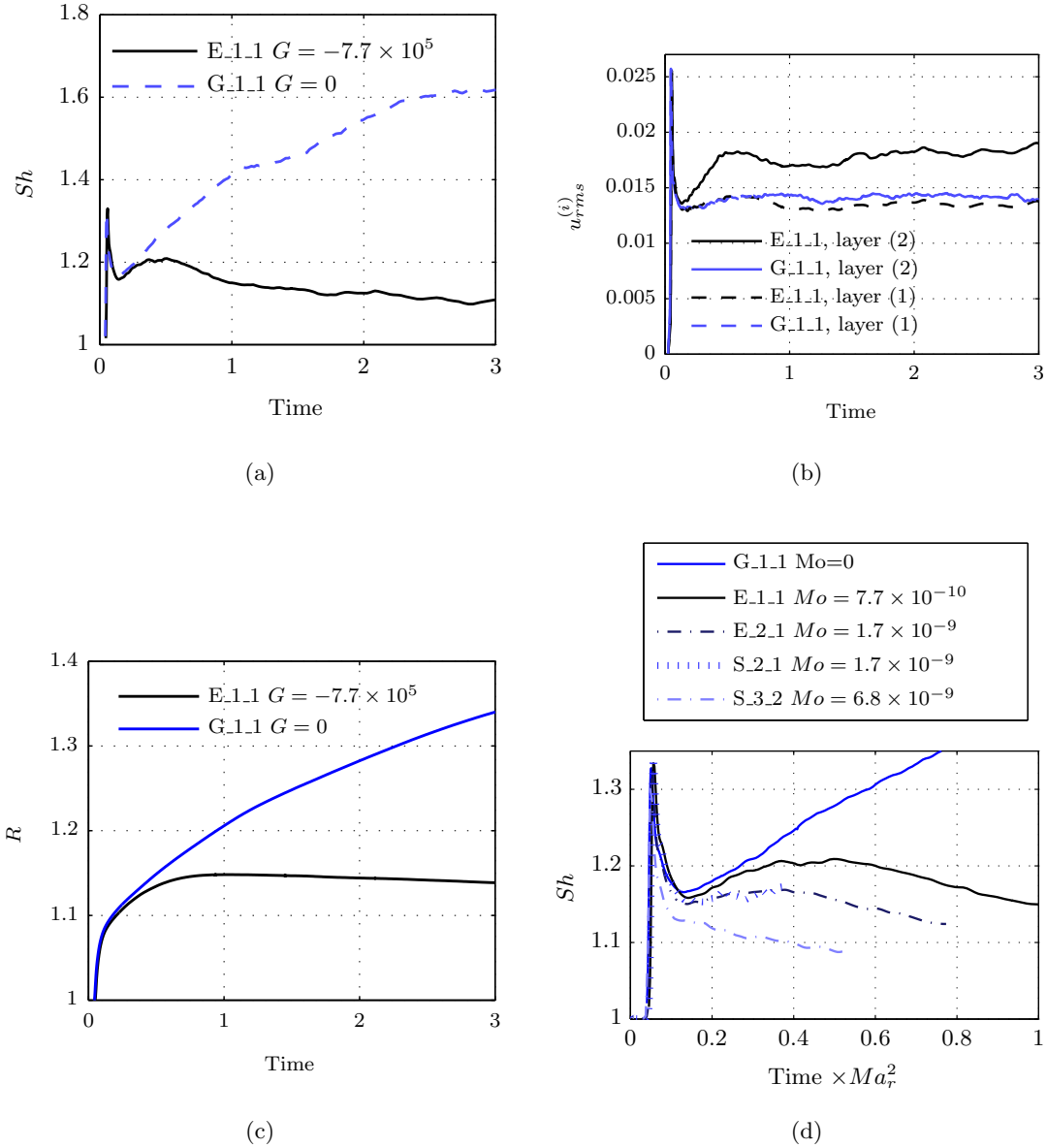


Figure 5.29: Impact of density stratification: (a) Sherwood number Sh for simulation E_1.1 and G_1.1 both with $Ma=-2.4 \cdot 10^8$, (b) rms velocity in each layer for E_1.1 and G_1.1, (c) enhancement factor R for simulation E_1.1 and G_1.1 and (d) Sh for different Morton numbers and rescaled time with $Ma_r = Ma / -2.4 \cdot 10^8$.

5.5.2 Impact of geometrical constraints

We imposed limitations on the coarsening of flow patterns in horizontal direction by reducing the lateral dimensions $l_x = l_y$, but fixing the other parameters (cf. Tab. 5.3 simulation G_1.2, G_1.3, G_1.4). Figure 5.30(a) shows that Sh decreased with decreasing domain size.

This plot is substantiated by snapshots of the pattern evolution in the small domain of $l_x = l_y = 0.05$ (Fig. 5.31). At $t \approx 0.2$, the Sh -curve for $l_x = 0.05$ still followed that of the largest domain size $l_x = 0.5$. It distinctly deviates for $t > 0.4$. Correspondingly, the pattern in Fig. 5.31(b) shows one large cell with substructures. For $t > 1.5$ the Sherwood number levels off, the flow pattern consists of a single square cell with (at $t=2$) a circular substructure.

We found that when the ratio of domain size normalized with the concentration boundary layer width (calculated for the pure diffusion case)

$$l_x / \delta c_I^{(1)} = l_x \left(\sqrt{\frac{t\pi}{Sc^{(1)}}} \right)^{-1} \quad (5.27)$$

was smaller than three [see Fig. 5.30(b), dashed cyan line], a clear deviations from the Sh curve of $l_x = 0.5$ appeared.

Another notable feature is the extent of fluctuations in the Sherwood number evolution [Fig. 5.30(a)]. As the curve for $l_x = 0.5$ results from averaging over a large number of cells, structural changes give rise to only a slight modulation. Accordingly, fluctuations are more pronounced for the smaller domain sizes.

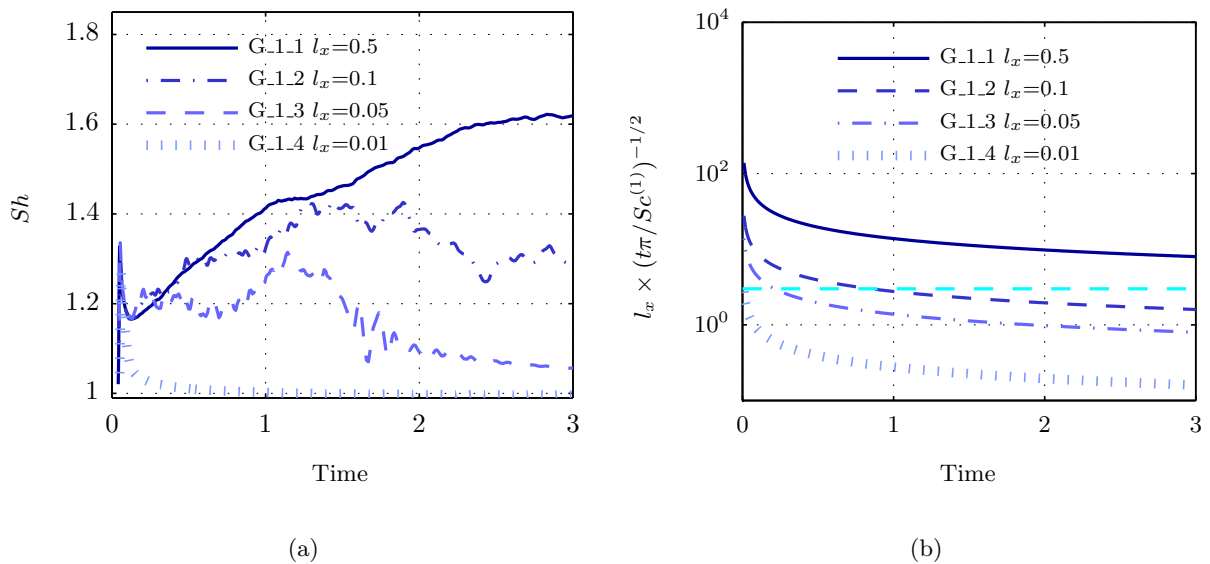


Figure 5.30: Mass transfer in reduced domain sizes: (a) Progression of Sherwood number and (b) comparison of domain size to boundary layer width for pure diffusion with horizontal dashed line at a value of three.

Finally, we present the impact of vertical confinement. Therefore two simulation with low Marangoni number and $G = 0$ are performed: L_1 ($Ma=-1.2 \cdot 10^7$) and L_2 ($Ma=-0.6 \cdot 10^7$). This could be realized in an experiment by reducing layer heights to 1 mm or 0.5 mm with

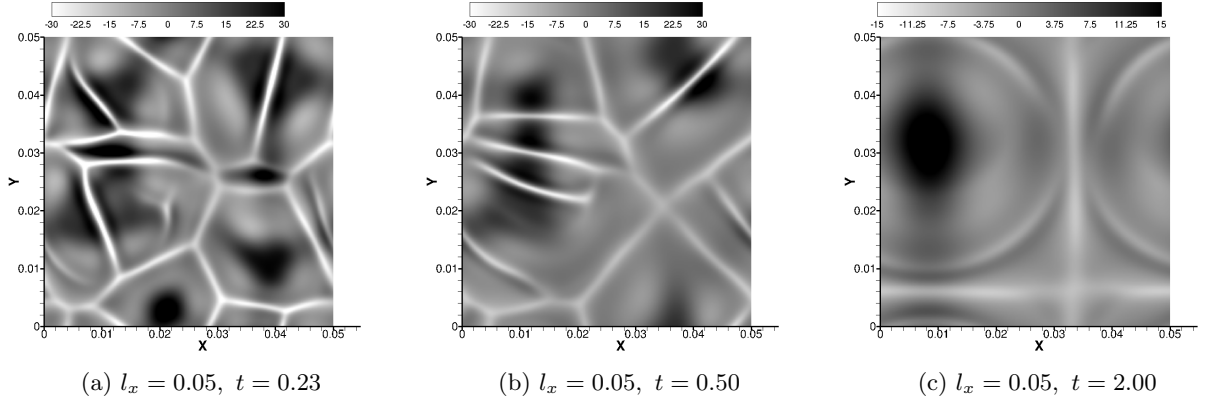


Figure 5.31: Computed shadowgraph images showing the pattern formation for a domain size of $l_x = 0.05$ in G_1.3.

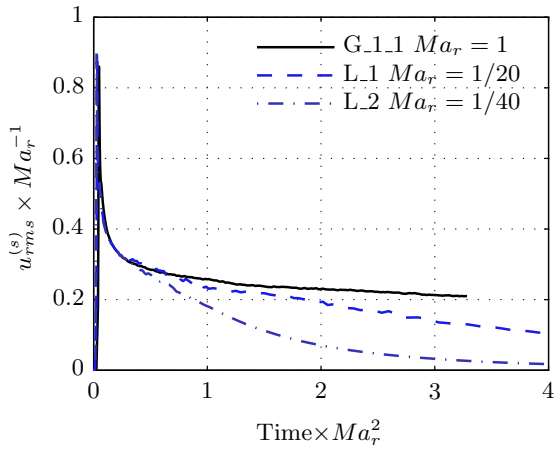
7.5Vol% butanol. ^{VIII} In Fig. 5.32(a), the interfacial velocity is presented for these simulations and G_1.1 ($Ma = -2.4 \cdot 10^8$). In these plots, quantities are rescaled according to the principle of scale invariance. Initially, scaled velocities match since convection is not influenced by the finite vertical size.

Simulations clearly deviated from deep layer regime (G_1.1) when one half of the solute passed the interface, i.e. $\langle c^{(1)} \rangle / c_{eq}^{(1)} > 0.5$, see Fig. 5.32(b). Scaling of the averaged concentration is not applied in Fig. 5.32(b) to show the meaningful absolute value but it is applied in (c). There, the deviations from the deep layer regimes get obvious. Note that the mean concentration scales as $\langle c^{(1)} \rangle (t \cdot Ma_r^{-2}) \propto Ma_r^{-1}$ in the deep layer regime.

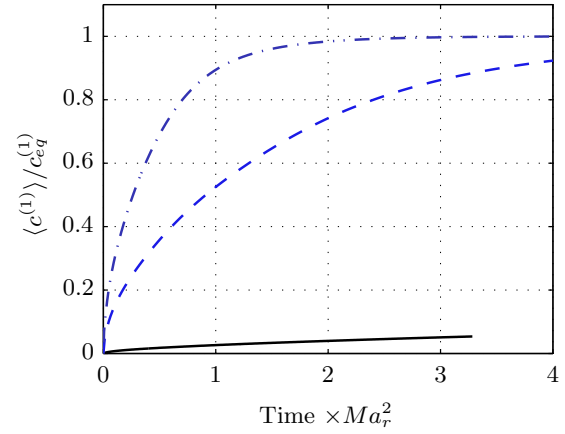
Figure 5.33 shows the development of patterns for L_1. As expected from the former graph, until $t \cdot Ma_r^2 = 0.6$ they followed the generic evolution of G_1.1 qualitatively. However, when RC-IIs were reaching a characteristic size of unity – that is the layer height – the finite vertical size impacts pattern formation. As a final stage, a pattern of RC-I appears with a characteristic size of twice a layer height [Fig. 5.33(d)].

Simulations L_1, L_2 showed that if lateral confinement and buoyant influences are excluded, the change in Marangoni number could be accounted for by a simple scale transformation from a generic simulation until approximately one-half of the solute has been transferred and the size of the largest convection cell is not more than unity. However, we would be careful to extrapolate our results to even smaller Marangoni numbers, i.e. when even initial cells are not distinctly smaller than a length of unity.

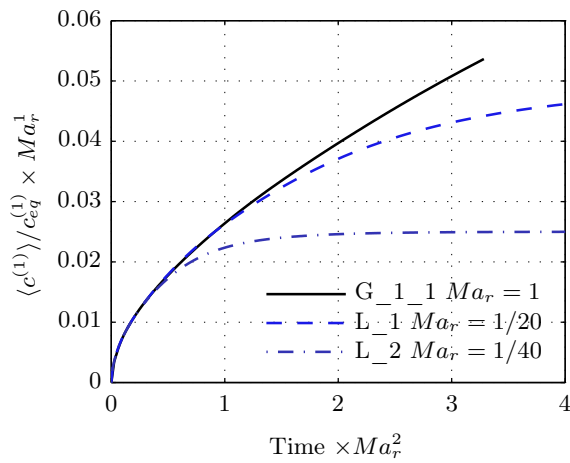
^{VIII}Of course this reduction could be also enforced by lowering c_0 . However, this leads to a dramatic reduction in sensitivity of the shadowgraph method since the dimensional horizontal Laplacian of concentration is expected to scale like $\hat{\Delta}_2 \tilde{c} \propto c_0^3$.



(a)



(b)



(c)

Figure 5.32: Simulation with full equilibration L-1, L-2 compared to G-1-1: (a) interfacial velocity against time and (b) mean concentration in the lower layer partly scaled, (c) mean concentration in the lower layer scaled.

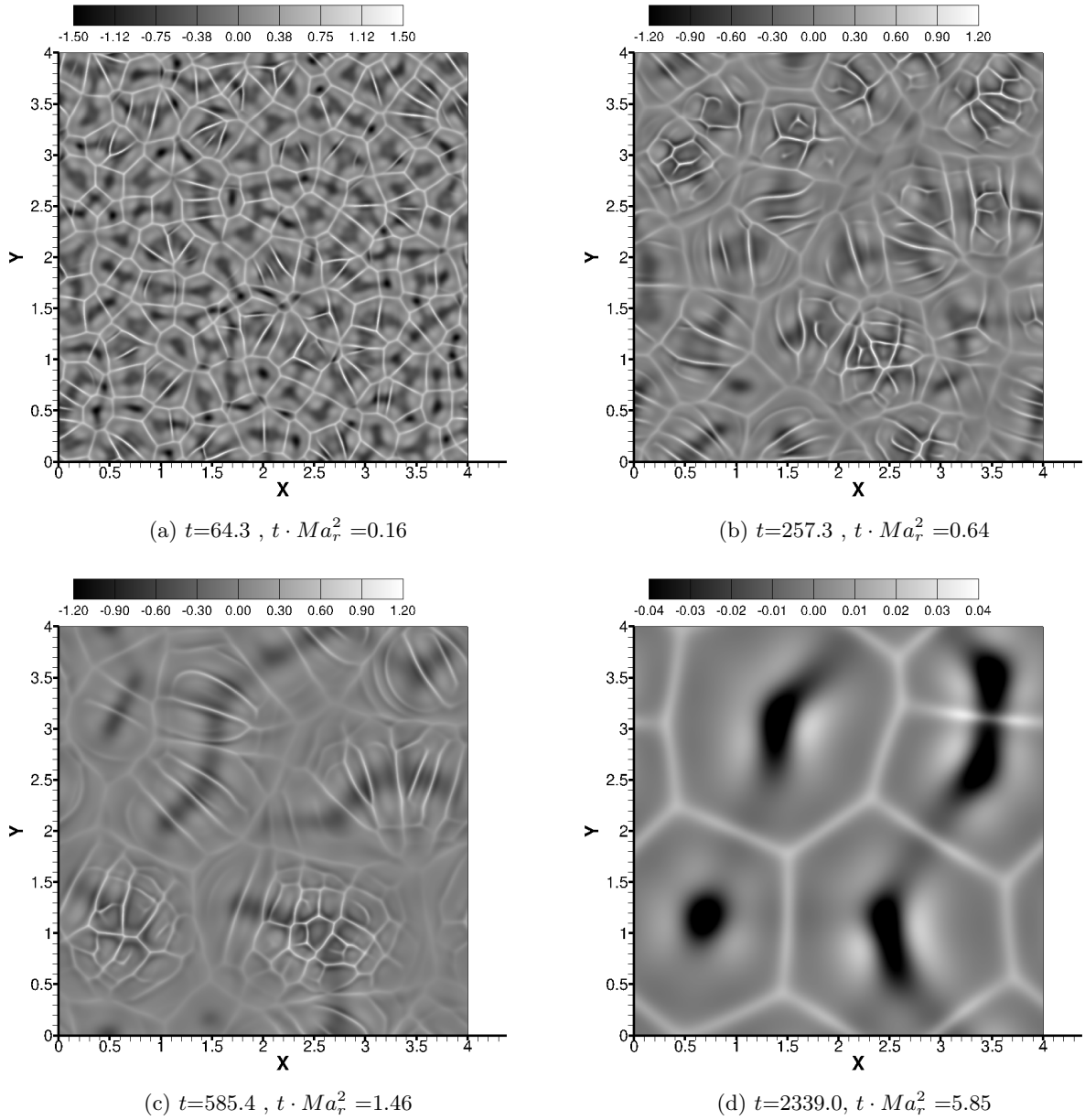


Figure 5.33: Computed shadowgraph images showing the pattern formation in simulation L_1, the relative Marangoni number Ma_r is $1/20$.

5.6 Two-dimensional geometry

A common strategy to reduce computational cost is to disregard one of the three spatial dimensions. This strategy is also applied to our reference configuration by disregarding the dependence on the y dimension for all fields and setting $\mathbf{u}_y = 0$. This section compares 3D (E.1.1, G.1.1) and 2D simulations (E.1.2D, G.1.2D), which we think is of general interest due to the convenience of solving a 2D model and extrapolating to three dimensions. The reduction of governing equations is straightforward. These 2D equations are equal to Hele-Shaw model equations introduced in the next Ch. 6 with zero wall friction ($\gamma = 0$).

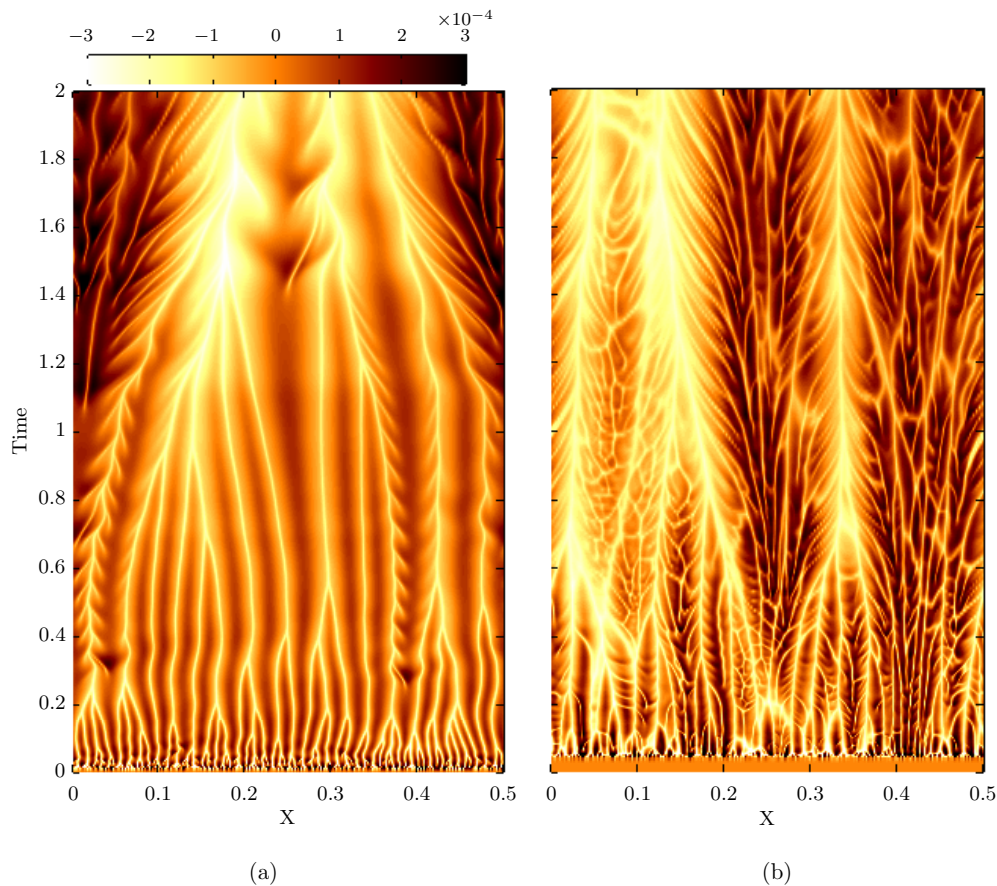


Figure 5.34: Temporal evolution of concentration variation at the interface: (a) $c^{(1)}(x, z = 0, t) - \langle c^{(1)}(x, z = 0, t) \rangle_x$ for the 2D simulation E.1.2D, (b) $c^{(1)}(x, y = 0.25, z = 0, t) - \langle c^{(1)}(x, y = 0.25, z, t) \rangle_x$ for a horizontal line $y = 0.25$ of the 3D simulation E.1.1.

Figure 5.34 shows two space-time plots of the concentration variation at the interface $c^{(1)}(x, t) - \langle c^{(1)}(x, t) \rangle_x$: one for the 2D simulation in (a) and one for the 3D simulation in (b). In the 3D case, the concentration variation is taken along a fixed value of the y -position ($y = 0.25$). In Fig. 5.34, dark colors (equal to high concentrations, therefore low interfacial tension) mainly correspond to inflow regions. Whereas, bright colors mark outflow regions (low concentration). Small-scale modulations indicate substructure RC-Is, which are advected by the RC-II. For both models, the coarsening and substructuring are well visible. However, some differences between the 2D and 3D case are observed:

(1) The instability sets in earlier for the 2D simulation in Fig. 5.34(a), which is simply a result of decreasing the first time step size to 10^{-10} .

(2) The additional dimension in the 3D simulation affects the appearance of substructure cells. At locations with considerable flow in y-direction (i.e. out-of-plane), the substructures manifest as closed cellular structures in Fig. 5.34(b) in the $t - x$ plane and so the impression of finer structures in the 3D case is created.

In order to quantify this, the size of RC-I is again measured. Though now, a procedure slightly adapted (relative to the procedure in Sec. 5.3.3) to the 2D simulation is used. The calculation of characteristic size λ of the RC-I follows the same procedure as described in Sec. 5.3.3 except the last step after individual cells (N_c in number) are identified. Now instead measuring the area of every cell, λ is set to the edge length of supposed square cells that fill the complete area $l_x \times l_y$

$$\lambda = \sqrt{\frac{l_x \times l_y}{N_c}}. \quad (5.28)$$

In the 2D case, the mean interval length is used

$$\lambda = \frac{l_x}{N_c}. \quad (5.29)$$

This RC-I size λ is plotted in Fig. 5.35(a) for 2D and 3D and each for $G = 0, -7.7 \cdot 10^5$. Due to the higher variance in time for the 2D system, the ensemble average over three independent runs is plotted in Fig. 5.35(a). For all cases, λ grows until it reaches a fairly constant value. For nonzero Grashof number $G = -7.7 \cdot 10^5$, the 2D simulations had larger cells. On the other hand for zero Grashofnumber $G = 0$, the difference between 2D and 3D was less pronounced. For both 2D and 3D simulations, $G=0$ showed smaller λ than $G = -7.7 \cdot 10^5$.

(3) The enhancement of mass transfer is depicted in Fig. 5.35(b). For the 2D simulations, R is plotted separately for the three different runs (dashed curves). After the initial phase, the 3D simulation yields higher values in R .

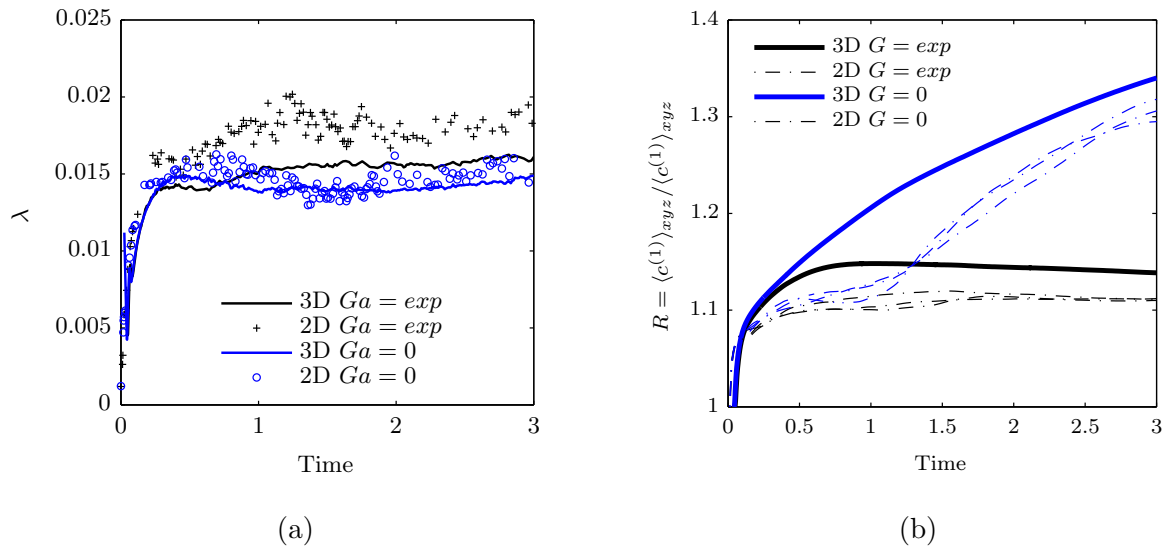


Figure 5.35: Comparison between the 2D simulation and the 3D simulation: Temporal evolution of (a) the cell size λ [Eqs. (5.28),(5.29)], (b) the enhancement factor R . In (a), we averaged over three simulations for the 2D case.

5.7 Discussion and conclusion

Motivated by a long history of experimental observations of complex and transient patterns in solutal Marangoni convection [142, 146, 166, 198], a numerical study has been performed to clarify the open questions (M_1 - M_4) stated in Sec. 2.4.1, which are explicitly answered in the following.

(M_1) Reproduction of experimental patterns: Simulations based on the PM indeed resembled the experimentally observed hierarchical patterns in most aspect. However, only a statistical reproduction of experiments was possible due to the nonlinear, transient and chaotic character of convection patterns. In this way, we have shown that the nonlinear evolution towards a multiscale flow pattern is primary not the result of any other physical effect (e.g. adsorption of contaminants or interactions with interfacial deformations).

Main differences between experiments and simulation were found owing to: the problematic reproduction of the experimental layering procedure, the limited size of the numerical domain (due to computational resources), the disregard of lateral walls by the periodicity conditions, uncertainty in material properties, but also a lack of the resolution of experimental images affected the quality of comparison.

(M_2) Basic structures according to Linde’s hypotheses: Indeed, the proposed scheme of Linde *et al.* [146] has been found as a sound basis to describe the simulated structures. The simulated chemical system has covered all three basic structures RC, RO, ROW (Fig. 2.4) that Linde proposed in his first hypothesis L_1 . His second hypothesis L_2 has been confirmed by observing a hierarchical pattern. The observation of higher order patterns requires an increased numerical effort, whereas some geometric order between the RC-II might be already claimed for the simulations presented (see Fig. D.1).

Linde’s third hypothesis L_3 also holds since we have found that the RCs-II are driven by an integral (disregarding the modulation of the RC-I) concentration difference between the cell center and its margin. Linde’s fourth hypothesis L_4 , i.e. a potential decay and reamplification of convective regimes, has not been confirmed. This is however in line with the experimental observation in the sample system; so, another chemical system might be studied to simulate this aspect in future. Possibly, such a cyclic behavior might be partly caused by buoyant effects, which would imply a correction of Linde’s fourth hypothesis. Further recommendations can be found in Ch. 8.

Two mechanisms that control the formation of hierarchical patterns have been identified, namely *coarsening* and *local instability*. It has been revealed that the largest cells RC-II grow in parallel with the layer of mixed fluid near the interface (coarsening). Furthermore, the RC-II cause a critical distribution of solute near the interface that is susceptible to a continuous creation of smaller Marangoni cells (local instability). In this view, we expect that the number of hierarchy levels indeed increases with the Marangoni number as described by Linde [146], since coarsening sets the largest size independent of Ma , but smallest cells are further scaled down with increasing Ma .

The transition between basic structures of RC and ROW is observed as fluent. The ROW structure appeared as a substructure of those RC-II that had a distinguished dimension (i.e. like elongated rolls), where the local instability produces substructures with a preferential orientation (e.g. perpendicular to the distinguished dimension of the hosting cell). In this

view, the questions on the appearance of ROW (when disregarding the crucial effect of coarsening in time) might be of a similar type as the questions whether rolls or cell are selected depending on the governing parameters, which was studied in thermal convection [44, 66].

An analogy to the *local instability* mechanism might be drawn to Bénard-Marangoni convection with silicone oil in containers with small aspect ratio [115, 156]. Namely, we have seen that the boundaries of hosting cell (RC-II) consist of solute poor fluid (at the interface) with the flow directed away from the interface, which is similar to the conditions at the container walls [115, 156]. In both configurations, the respective number of smaller structures arranges according to the available space. However, in contrast to rigid walls, the boundaries of the hosting cells move so that the generated structures are not stationary in our case. Also, local instability might be related to dynamical regimes in Bénard-Marangoni convection for high Prandtl numbers, e.g. pulsating and splitting cells were found in a recent simulation of Medale&Cerisier [157].

Another connection to established works on interfacial tension driven flow is to consider an isolated large cell (RC-II) that produces horizontal gradients of interfacial tension and its velocity field. Such situations of horizontal concentration or temperature gradients have been classically studied by instability analysis of Smith&Davis [56, 218], known as hydrothermal instabilities. However, the base states that they considered (i.e. a return flow or a linear flow) deviates too much from the flow state of a RC-II to make a reasonable comparison.

(M₃) Comparison of simulations with experiments: The manual cell-size measurements of Schwarz for cells without substructure (RC-I) based on shadowgraph images have been related to simulated cell sizes. The simulated cell sizes have been calculated with an automatic method based on the gradient of vertical velocity at the interface. Generally, simulations have shown a good qualitative agreement with experiments. However, simulations appeared retarded relative to the experimental data; differences were especially present in low concentration. These differences might be partly explained by the uncertainty of material properties as well as a variation of transport parameters with the concentration of butanol.

Recent experiments focused on observing the largest structures, which were measured by a Fourier method based on the shadowgraph images for both experiment and simulation. A similar conclusion is drawn, i.e. experiments appeared accelerated (structures were larger for equal times). The quality of experimental observations might be improved by observing the large scale but also resolving the small scale structures, completely. It should be also attempted to improve the method of comparing shadowgraph images, e.g. based on geometrical methods [228], which might be less affected by optical artifacts.

A third quantitative comparison has been done in terms of the optical flow of the shadowgraph images. The optical flow has been found to be a capable method to analyze substructured patterns since substructures serve as tracers that are advected by the hosting cell. The comparison between simulations and experiments has revealed similar findings as both other methods before. Namely, a reasonable qualitative agreement with the flow structures was observed, but optical flow in experiments was two times as high as the simulated value.

(M₄) Influence of governing parameters and further predictions: The influence of physical parameters on the development has been studied in several respects. Mainly the role of scale invariance (see Sec. 3.1.1) has been examined, and we have reported the respective deviations from the generic development (simulation G.1.1).

In this framework, the role of the stabilizing-density stratification has been studied by simulating different Morton number $Mo = (|G|(Sc^{(1)})^3)/(|Ma|^3)$. As expected from theoretical considerations, a non-zero Morton number prohibits the application of the scale transformation, and it leads to a reduction of mass transfer. This effect on mass transfer is already known from experimental observation of Berg& Morig [20, 191].

A second observation has been the matching of cases via scale transformation gets worse as time increases, which could be explained when considering that the influence of gravitational work increases with the characteristic length scales of stratification.

Moreover, we excluded buoyancy ($Mo=0$) and considered a geometrical confinement of convection. For both lateral confinement (decreasing l_x, l_y) and vertical confinement (low Ma and high times), there was a departure from the generic development, when convection cells reached the typical outer length (l_y, l_x or unity for vertical confinement). This departure manifested itself by a lower rate of mass transfer. For the cases with vertical confinement (low Ma), mass transfer could be described by a scale transformation until approximately one-half of possible solute was transferred through the interface. The effect of geometrical confinement also occurs for droplet geometries where it is particularly obvious.

Chapter 6

Marangoni convection in a HS cell

In the present chapter, the cyclohexanol+butanol/water system is further studied inside a Hele-Shaw cell. In a Hele-Shaw setup, the fluids are enclosed between two parallel plates that are sufficiently close together such that the fluid motion becomes mainly two-dimensional. The Hele-Shaw (HS) cell is a versatile experimental and numerical configuration in chemical engineering studies of biphasic systems [8,37,40,65,68,80,88,116], e.g. to investigate transport processes at liquid interfaces. It provides simplified access to the vertical structures by optical methods such as shadowgraphy, interferometry and particle image velocimetry. By varying the orientation of the HS cell, it is possible to reveal information about the influence of gravity [64,141,199,208].

Also from the viewpoint of theoretical modeling, the HS setup is advantageous since it may be described by a two-dimensional (2D) model based on gap-averaged equations [37], which significantly saves computational cost compared to full three-dimensional (3D) simulations. A similar motivation underlies studies that assume a pure 2D model without the influence of wall friction [26,206]. Despite this interest, a detailed one-to-one comparison of experimental observations to numerical simulations of solutal Marangoni convection in the HS setup is still lacking.

The aim of the present chapter is to study Marangoni convection in the HS geometry with the same material as in the three-dimensional setup (Ch. 5). There the *horizontal* structure of the simulated hierarchical Marangoni roll cells compared well to our own and to independent experiments. Now, by using a HS cell instead of the 3D setup, we are able to compare numerical results to experimental measurements that observe the *vertical* structure of the emerging Marangoni roll cells. Four cases are considered using 0.5 mm and 1 mm gap width and a vertical and horizontal orientation of the HS cell. On this basis, we discuss the applicability of the 2D gap-averaged model by comparing structures and measured heights of Marangoni cells from simulations and experiments.

The following chapter reproduces the authors publication [112] with only small changes, where experimental and numerical results have already been published in a joint work.

It is divided into four main sections. Sec. 6.1 presents the experimental setup and the corresponding theoretical model. The comparison of experimental and numerical results are consecutively presented in Sec. 6.2 for the four different cases. A rough analytic estimation is given in Sec. 6.3 for the parasitic density convection in the horizontally oriented HS cell. A concluding discussion in Sec. 6.4 interprets deviations of the experiment from the model.

6.1 Methods

6.1.1 Experiments

In this section, the experimental setup of Schwarzenberger & Eckert is introduced. They performed a mass transfer of 1-butanol from an upper cyclohexanol-rich layer (2) to a lower water-rich layer (1). The preparation of phases proceeds as described in Sec. 5.3.1. Now it is exclusively focused on an initial concentration of $c_0 = 0.82$ mol/l, identical to the reference configuration in the former chapter.

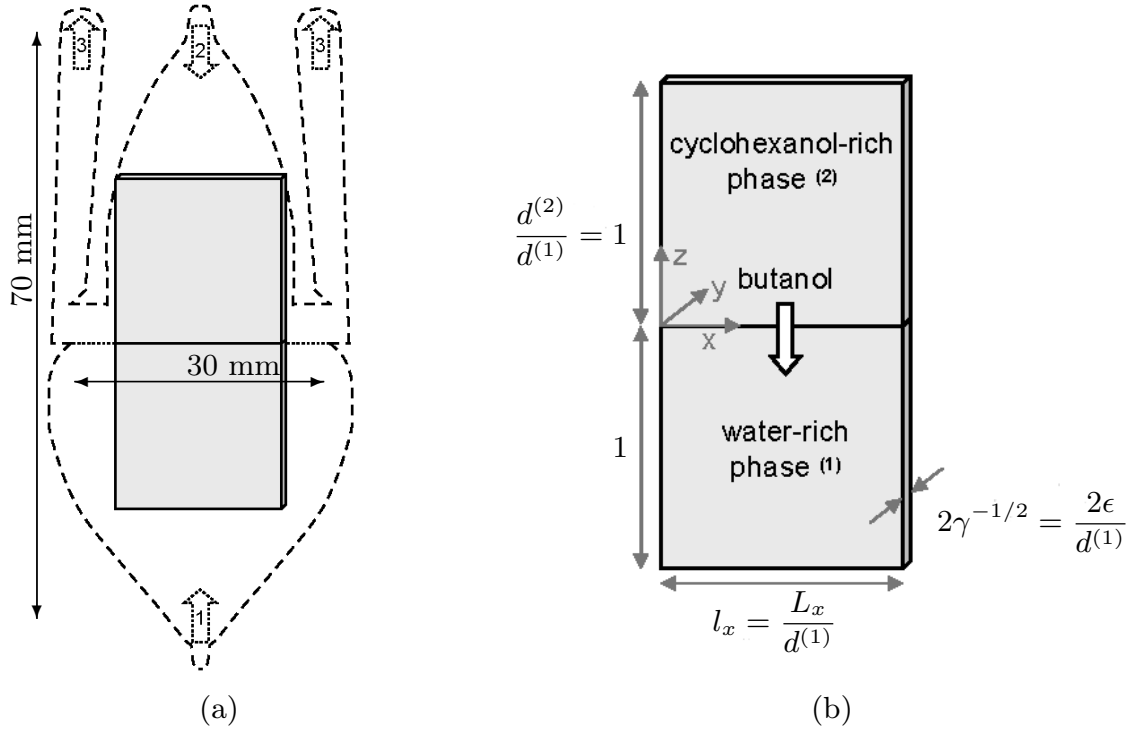


Figure 6.1: Hele-Shaw (HS) geometry: experimental setup (a) from Schwarzenberger & Eckert [112] with gray inset of numerical domain; detailed numerical domain (b) in viscous units (scaled by lower layer height $d^{(1)} = 20$ mm).

To obtain the HS configuration, the phases were placed in a narrow gap between two glass plates. Fig. 6.1 sketches the experimental HS setup (a) and the computational domain (b), which is drawn as a gray inset in (a) for comparison. A spacer made of polytetrafluoroethylene (PTFE) foil, whose inner contour is shown as a dashed line in Fig. 6.1(a), acted as a container for the liquids. The gap width 2ϵ , see Fig. 6.1(b), was set by the thickness of the foil: a thickness of 0.5 mm and 1 mm was used. The width of the interface, marked by a dotted line and horizontal arrow in Fig. 6.1(a), amounts to 30 mm.

For the analysis of the experimental data (Sec. 6.2) only the central 20 mm of the interface are considered. This is done to disregard boundary effects that arise in the vicinity of the pinning edges and near the outflow channels. In the simulations, we use these 20 mm as the horizontal domain size L_x , see Fig. 6.1(b). According to former simulations, layer heights are set to $d^{(1)} = d^{(2)} = 20$ mm. In the experimental HS cell, the height of the liquid layers (approx. 35 mm) was larger. However, since Marangoni convection was restricted to a small

zone near the interface, this difference is expected to be negligible.

The shape of the PTFE foil was optimized to provide a robust filling procedure for different two-phase systems [209]. The numbered arrows in Fig. 6.1(a) mark relevant stages of this filling procedure. In step 1, the aqueous phase is injected in the lower half of the container until its surface is pinned at the lateral edges of the PTFE foil. During the filling of the organic phase in the second half of the container (step 2), the HS cell has to be placed in a horizontal position, i.e. the acceleration due to gravity is $\mathbf{g} = g\mathbf{e}_y$ (Fig. 6.1). When the organic phase contacts the aqueous surface, the interface (dotted line) is established quickly via spreading of the organic phase. Finally in step 3, the exhaust channels are filled to avoid side effects of the air-liquid interface. The duration of the last step involves a compromise between an uncontrolled mass transfer during slow filling and an increased interfacial deformation for rapid filling. This rather delicate filling procedure was due to the interfacial tension of the system cyclohexanol/water ($\sigma_{ref} = 3.4 \times 10^{-3}$ N/m), which is low when compared to the alkane/water systems mostly used in this HS cell design [64, 65, 68, 199, 208, 209].

To vary gravity influence, the HS cell can either remain horizontally ($\mathbf{g} = g\mathbf{e}_y$) or it is tilted to a vertical position ($\mathbf{g} = -g\mathbf{e}_z$, Fig. 6.1) immediately after filling.

The concave meniscus^I (wrt the aqueous phase) that is formed across the plates is characterized by its height $\tilde{\omega}$ given by the wall-parallel distance of the triple line to the apex (the lowest point) of the meniscus. It was measured at both plate distances of $2\epsilon = 0.5$ mm (1 mm) and is $\tilde{\omega} = 0.094$ mm (0.180 mm). The corresponding contact angle (with respect to the aqueous layer) is estimated to $\theta \approx 50^\circ$. This calculation assumes a circular interface as the corresponding Bond number is below unity.

Pattern evolution in the course of the experiment were visualized by a shadowgraph optics operating in transmission (TSO, Germany). Additionally, particle image velocimetry (PIV) measurements were conducted in the vertically oriented HS cell for two different gap widths (0.5 and 1 mm).

6.1.2 Theoretical Hele-Shaw model

The mass transfer process is simulated on the basis of the PM in viscous units (cf. Sec. 3.1.2). However to account for the effects of the plates, the model is adapted by a common gap-averaging procedure [32, 37, 38, 80], which assumes a *parabolic flow* profile, *no solute variation* along the y -direction and a plane undeformable interface.

A new nondimensional parameter appears, i.e. the ratio of the squared layer height to the half plate distance $\gamma = \frac{(d^{(1)})^2}{\epsilon^2} = 6400$ ($2\epsilon = 0.5$ mm), 1600 ($2\epsilon = 1$ mm), cf. Fig. 6.1(b). By this definition, the nondimensional plate distance is $2\gamma^{-1/2} = 0.025$ (thin), 0.05 (thick). As introduced in Sec. 6.1.1 and illustrated by Fig. 6.1(b), the fluid is located in a box $(x, y, z) \in [0, l_x] \times [-\gamma^{-1/2}, \gamma^{-1/2}] \times [-1, 1]$ composed of layer⁽¹⁾ for $z < 0$ and layer⁽²⁾ for $z > 0$.

For the modeling, we follow the formulation of Ref. [37] by averaging over the gap. Specifically, the following two assumptions are applied. First, the velocity field $\mathbf{u}^{(i)}(x, y, z, t)$ in layer⁽ⁱ⁾ is assumed two-dimensional ($u_y^{(i)} = 0$) with a parabolic dependence (see Eq. (1) in

^IThe interface position might be described by a height function $z = \xi(x, y)$. In these terms, "concave" means $\partial_y^2 \xi(x, y) \geq 0$ and the measured meniscus height (being effectively constant over x) is $\tilde{\omega} = \max_y(\xi(x, y)) - \min_y(\xi(x, y))$, cf. Fig. 6.9. In our theoretical model $\xi(x, y) = 0$.

Ref. [37]) on y , i.e.

$$\mathbf{u}^{(i)}(x, y, z) = \frac{3}{2}(1 - y^2\gamma)(v_x^{(i)}(x, z)\mathbf{e}_x + v_z^{(i)}(x, z)\mathbf{e}_z). \quad (6.1)$$

In what follows, we are concerned with velocity fields that are gap-averaged over y and denoted by $\mathbf{v}^{(i)}(x, z, t) = \langle \mathbf{u}^{(i)} \rangle_y$. The second assumption is that solute concentration is constant across the gap, i.e. it does not depend on the y -coordinate: $c^{(i)} = c^{(i)}(x, z, t)$.

With these assumptions, the governing equations that were presented in Sec. 3.1.2 simplify to the two-dimensional *HS model*, which reads

$$\partial_t \mathbf{v}^{(1)} = -\frac{6}{5}\mathbf{v}^{(1)} \cdot \nabla \mathbf{v}^{(1)} - \nabla p_d^{(1)} + \Delta \mathbf{v}^{(1)} - c^{(1)}G\mathbf{e}_z - 3\gamma\mathbf{v}^{(1)}, \quad (6.2)$$

$$\partial_t \mathbf{v}^{(2)} = -\frac{6}{5}\mathbf{v}^{(2)} \cdot \nabla \mathbf{v}^{(2)} - \frac{1}{\rho}\nabla p_d^{(2)} + \nu\Delta \mathbf{v}^{(2)} - c^{(2)}G\beta\mathbf{e}_z - 3\gamma\nu\mathbf{v}^{(2)}, \quad (6.3)$$

$$\nabla \cdot \mathbf{v}^{(1)} = 0, \quad \nabla \cdot \mathbf{v}^{(2)} = 0, \quad (6.4)$$

$$\partial_t c^{(1)} = -\mathbf{v}^{(1)} \cdot \nabla c^{(1)} + \frac{1}{Sc^{(1)}}\Delta c^{(1)}, \quad \partial_t c^{(2)} = -\mathbf{v}^{(2)} \cdot \nabla c^{(2)} + \frac{D}{Sc^{(1)}}\Delta c^{(2)}. \quad (6.5)$$

The values of non-dimensional parameters are summarized in Table 6.1. Note that these coincide with the reference configuration, except that γ appears as a new parameter. Bottom ($z = -1$) and top ($z = 1$) boundaries are considered as impermeable solid walls

$$\partial_z c^{(2)} = v_z^{(2)} = v_x^{(2)} = 0 \quad \text{for } z = 1, \quad \partial_z c^{(1)} = v_z^{(1)} = v_x^{(1)} = 0 \quad \text{for } z = -1. \quad (6.6)$$

At the plane interface ($z = 0$), the solute mass fluxes and velocities are continuous, bulk concentrations are in equilibrium and tangential stresses are related to interfacial tension gradients:

$$\partial_z c^{(1)} = D\partial_z c^{(2)}, \quad v_x^{(1)} = v_x^{(2)}, \quad v_z^{(1)} = v_z^{(2)} = 0, \quad (6.7)$$

$$Hc^{(1)} = c^{(2)}, \quad \frac{Ma}{Sc^{(1)}}\partial_x c^{(1)} = -\mu\partial_z v_x^{(2)} + \partial_z v_x^{(1)}. \quad (6.8)$$

The x -direction is periodic, so velocity $\mathbf{v}^{(i)}$ and concentrations $c^{(i)}$ obey $f(x + l_x, z, t) = f(x, z, t)$, where the horizontal length is set to unity $l_x = 1$. Initially, butanol is only present in layer⁽²⁾, i.e. $c^{(1)}(x, z, t = 0) = 0$, $c^{(2)}(x, z, t = 0) = 1$. Furthermore, velocity is zero except for a small amount of noise added to the vertical velocity in order to trigger Marangoni instability as described in Sec. 5.1.1.

The resolution was $N_x = 2048$ and $N_z^{(1)} = N_z^{(2)} = 256$. The additional damping with prefactor 3γ in Eq. (6.2) is well known from Darcy's law. It is discretized implicitly in time. Our implementation was validated by simulating a case presented in [38] for pure density convection (results not shown here). Reasonable agreement was found regarding the pattern characteristics and the evolution of length scales.

6.1.3 Discussion of the Hele-Shaw model

After the introduction of our theoretical model, we give a short review on the modeling of flows in a HS-cell and show the problems which are inherent to our assumptions. Generally, the gap-averaged model is clearly restricted to a physical situation where viscous and diffusive perturbations equilibrate sufficiently fast across the gap on a comparable time scale. Apart

Description	Symbol	Value
Schmidt number aqueous phase	$Sc^{(1)} = \frac{\nu^{(1)}}{D^{(1)}}$	2400
Marangoni number	$Ma = \frac{c_0 \alpha_c \sigma_{ref} d^{(1)}}{\rho^{(1)} \nu^{(1)} D^{(1)}}$	-2.4×10^8
Grashof number	$G = \frac{c_0 \beta_c^{(1)} g (d^{(1)})^3}{(\nu^{(1)})^2}$	-7.67×10^5 (vertical) or 0 (horizontal)
partition coefficient	$H = c_{eq}^{(2)} / c_{eq}^{(1)}$	31
density ratio	$\rho = \frac{\rho_{ref}^{(2)}}{\rho_{ref}^{(1)}}$	0.96
kinematic viscosity ratio	$\nu = \frac{\nu^{(2)}}{\nu^{(1)}}$	16.7
diffusivity ratio	$D = \frac{D^{(2)}}{D^{(1)}}$	0.14
ratio of expansion coefficients	$\beta = \frac{\beta_c^{(2)}}{\beta_c^{(1)}}$	0.75
layer height to thickness squared	$\gamma = \frac{(d^{(1)})^2}{\epsilon^2}$	6400(thin), 1600(thick)

Table 6.1: Basic parameters for HS simulation in the cyclohexanol + 7.5 vol% butanol \rightarrow water system. The acceleration due to gravity is $g = 9.81 \text{ m/s}^2$. Both layer heights are set to $d^{(1)} = d^{(2)} = 20 \text{ mm}$, material properties can be found in Tab. 5.2

from the deviations caused by 3D flow effects and interfacial deformations (will be discussed in Sec. 6.4), which mainly have an effect in the vicinity of the interface, the *bulk flow* HS model might as well be a source of discrepancies between experiment and simulation. Former works have proposed certain model corrections for the bulk. However, they have typically focused either on the momentum or on the species balance but not on both.

Momentum transport: The assumption of a parabolic profile in the Navier-Stokes equation may be violated due to gradients in density, viscosity, or geometrical effects. Ruyer-Quil [190] derived a gap-averaged equation as a first order correction to the parabolic profile. He found inertial terms with other prefactors: $\frac{6}{5}\partial_t \mathbf{v}^{(1)} + \frac{54}{35}\mathbf{v}^{(1)} \cdot \nabla \mathbf{v}^{(1)} = -\nabla p - 3\gamma \mathbf{v}^{(1)}$. Another approach is pursued by Zeng et al. [245], who started with the steady Stokes equation in three dimensions and solved different examples including a density-driven case and a case with viscosity gradients. It is concluded there that the viscous term (the so-called Brinkmann correction) should carry a prefactor $\beta = 12/\pi^2$, which yields $0 = -\nabla p - 3\gamma \mathbf{v}^{(1)} + \beta \Delta \mathbf{v}^{(1)}$. A later work [98] adopted this approach with modifications of β .

In the Stokes limit for interfacial-tension driven flows, however, Boos et al. [32] and Gallaire et al. [75] discussed and showed the good quality of the parabolic assumption, i.e. $\beta = 1$. By examining the Rayleigh-Taylor instability, Martin et al. [155] compared Ruyer-Quil's model (with additional second order correction $6/5\Delta \mathbf{v}^{(1)}$) to the one we introduced, i.e. Eqs. (6.2) and (6.3). In summary, they recommended the model we are using.

As a final remark on the momentum balance, let us note that when inertia is small compared to viscous forces (Reynolds number $Re \ll 1$), the Brinkman equation [32] can be used instead of Eqs. (6.2) and (6.3), i.e. the terms $\partial_t \mathbf{v}^{(i)} + \frac{6}{5}\mathbf{v}^{(i)} \cdot \nabla \mathbf{v}^{(i)}$ are omitted in these equations. Actually, by estimating Re a posteriori from the typical velocity and size of the convection cells in Fig. 6.7, it can be shown that $Re \ll 1$ applies for our system. Consequently, neglecting inertial terms in the momentum balance is possible. However, for other Marangoni-unstable systems this may not be the case. Therefore, we adopt the more general model.

Species transport: The second assumption is the quasi instantaneous equilibration of the concentration field across the gap. It demands that the diffusion time $\tau_d = \epsilon^2/D^{(i)}$ is much lower than the characteristic time for advection $\tau_a = \epsilon/\tilde{U}$. The "cross-gap" Peclet number $Pe = \tau_d/\tau_a = \tilde{U}\epsilon/D^{(i)}$ is evaluated with the experimentally measured velocity $\tilde{U} \approx 10 \mu\text{m/s}$ (see Fig. 6.7). In the case of the thin cell ($\epsilon = 0.25 \text{ mm}$), the Peclet number in the lower (upper) layer is $Pe = 5$ (35.7) and for the thicker cell ($\epsilon = 0.5 \text{ mm}$) it is $Pe = 10$ (71.4).

Clearly, this leads to the effect of Taylor dispersion [224], i.e. solute in the middle of the gap is transported faster than in the vicinity of the plates. Taylor and later Aris [7] showed for a simpler geometrical configuration that this process could be accounted for by transport with the mean velocity and an additional dispersion term. Recently, the dispersion effect for *unidirectional* flows has been incorporated in density-driven flows [98, 130].

For *non-unidirectional* flows, we are concerned within this study, Zimmermann *et al.* [248] proposed a model based on the analysis of Horne *et al.* [92] that which Zimmerman *et al.* and Petitjeans *et al.* [175] used to study miscible displacement in the Hele-Shaw setup. To the best of our knowledge, this is the most reasonable two-dimensional model that includes the effect of Taylor dispersion. Zimmermann *et al.* cast the effect of Taylor dispersion into an anisotropic and velocity-dependent diffusivity tensor \mathbf{D} . The new transport equation for solute in layer

⁽ⁱ⁾ then reads (for dimensional quantities that have a nondimensional counterpart we add a tilde)

$$\partial_{\tilde{t}}\tilde{c}^{(i)} + \tilde{\mathbf{v}}^{(i)} \cdot \tilde{\nabla}\tilde{c}^{(i)} = \tilde{\nabla} \cdot (\mathbf{D}^{(i)} \cdot \tilde{\nabla}\tilde{c}^{(i)}). \quad (6.9)$$

The dispersion tensor is given as follows:

$$\mathbf{D}^{(i)} = D^{(i)}\mathbf{I} + \frac{2\epsilon^2}{105D^{(i)}}\tilde{\mathbf{v}}^{(i)} \otimes \tilde{\mathbf{v}}^{(i)}, \quad (6.10)$$

where \mathbf{I} is the unity tensor. This formulation leads to an enhanced diffusion in flow direction while there is only molecular diffusion orthogonal to the flow. Since this model is just a heuristic extension of the analysis of Horne *et al.* [92], the validity of this approach is not assured, especially near the interface where the dispersion effect should increase the transport of solute in the center of the HS cell.

Nevertheless, to roughly estimate the influence of Taylor dispersion, we applied this model for the case of the thin and vertically oriented cell. The simulations with the dispersion model only *marginally* departed from our standard model without dispersion. After an initial phase ($t < 1$) for which the dispersion model evolves faster, the difference in the cell height η (introduced in the following section) amounted to the typical variance between all simulation runs, i.e. distinctly below 10% relative deviation. In view of these small differences and the weak rigorous foundation of the dispersion correction, we decided to work with the formulation described in Sec. 6.1.2.

6.2 Results

Based on the HS model, we study butanol transport from the top⁽²⁾ to the bottom⁽¹⁾ layer that causes Marangoni convection. We consider four cases that differ in the plate distance $2\epsilon = 0.5$ mm (*thin*), 1 mm (*thick*) and in the orientation of the cell, i.e. *vertical* or *horizontal*.

6.2.1 *Thin and vertically oriented Hele-Shaw cell*

The convective structures in experiment and simulation have the closest resemblance in the thin cell ($2\epsilon = 0.5$ mm) and for vertical orientation. A sequence of experimental and corresponding numerical shadowgraph images $s(x, z)$ [160]

$$s(x, z) = (\partial_x^2 + \partial_z^2)c(x, z, t) \quad (6.11)$$

is given in Fig. 6.2. The maximum and minimum of the numerical gray scale, see Fig. 6.2(b), is adapted to the experimental images (a) at one time and remains unchanged thereafter.

A conspicuous feature is the region of *mixed fluid* (poor in solute, i.e. butanol). It is bordered by a slightly darker rim to fluid rich in solute at the top and by the interface at the bottom. As dark colors mainly correspond to negative values $s(x, z, t) < 0$, see Eq. 6.11, they could be interpreted as a loss of solute (here to the mixed fluid) by molecular diffusion. The dark rim is bent to the interface at the *inflow regions*, which is illustrated by white circles with "A" mark in Fig. 6.2(c,d), where butanol-rich fluid from the bulk flows to the interface. Apparently, the horizontal size of the roll cells (distance from inflow to inflow) is larger in experiments, but the trend for *coarsening*, i.e. a general growth of length scales in time, is seen both in experiment and simulation. Between the inflow regions, the *outflow regions* (where fluid is diverted into the bulk) are well resolved in simulations by small bright spikes,

e.g. detailed in Fig. 6.2(f) by white "B" mark. In the experimental images, the outflow regions are not visible. Moreover, the interface between both layers appears thicker in the experiment due to the deflection of light at the curved meniscus.

A quantitative comparison is carried out by measuring the roll-cell height η marked by the distance between the horizontal lines in the shadowgraph images of Fig. 6.2. The experimental cell height was extracted at the outflow points of the roll cells x_{out} illustrated with a vertical line in Fig. 6.2(a). It was measured as the distance from the lower edge of the concave meniscus to the local minimum (darkest gray shade) of $s(x = x_{out}, z > 0)$ in the organic phase. This procedure was performed manually since the experimental images are perturbed by optical inhomogeneities. A mean value over all cells is plotted in Fig. 6.3 (black crosses) together with the standard deviation as error bars.

For the cell height data, only experiments with the least pronounced interfacial deformations (also shown in Figs. 6.2, 6.4, 6.5) were evaluated. These experiments required a quite slow filling of the HS cell, lasting approx. 0.4 viscous time units. The starting point $t = 0$ is defined as the average between the moment of phase contact and the end of the filling procedure with a related temporal uncertainty of $t \pm 0.2$ (viscous time units).

The simulated cell height η (full lines in Fig. 6.3) was determined similarly but in a fully automated way: the synthetic shadowgraph distribution was averaged along the x-direction $\langle s(x, z) \rangle_x$ and searched for the local minimum with highest vertical distance to the interface, formally,

$$\eta = \max\{z : \partial_z \langle s(x, z) \rangle_x = 0\}. \quad (6.12)$$

As expected, the coarsening of roll cells according to Fig. 6.2 is also reflected in the calculated cell height (Fig. 6.3) for both experiment and simulation. Experimental heights exceed simulated ones by approximately 0.025 length units, which is considerable compared to the meniscus height $\omega = \tilde{\omega}/d^{(1)} = 0.0047$ or the gap size $2\gamma^{-1/2} = 0.025$. Furthermore, η was simulated for purely diffusive transport ($Ma = 0$, blue dashed line in Fig. 6.3). It turns out that already for the small gap size the deviations of the experimental data are of the same order of magnitude as the accelerating effect of interfacial convection in the simulations. However, it is in line with former simulations (Ch. 5) that height and horizontal dimension of experimental cells increase simultaneously (readily visible in Fig. 6.2), since both scales are coupled by the coarsening mechanism.

6.2.2 *Thin and horizontally oriented Hele-Shaw cell*

The transport of butanol leads to a stabilizing density stratification in both phases for vertical orientation as the *mixed fluid* (adjacent to the interface) becomes denser in the upper organic and lighter in the lower aqueous phase. Sec. 5.5 already showed that this density stratification retards mass transfer when compared to no variation in density. The influence of gravity was studied experimentally by leaving the HS cell in a horizontal position after filling and numerically by zeroing the Grashof number, $G = 0$. Figs. 6.3 and 6.4 show that the growth of cell height is increased when density stratification by solute transport is excluded. As for vertical orientation, the experiment appears distinctly accelerated when compared with the simulation, but the main flow structures appear identical.

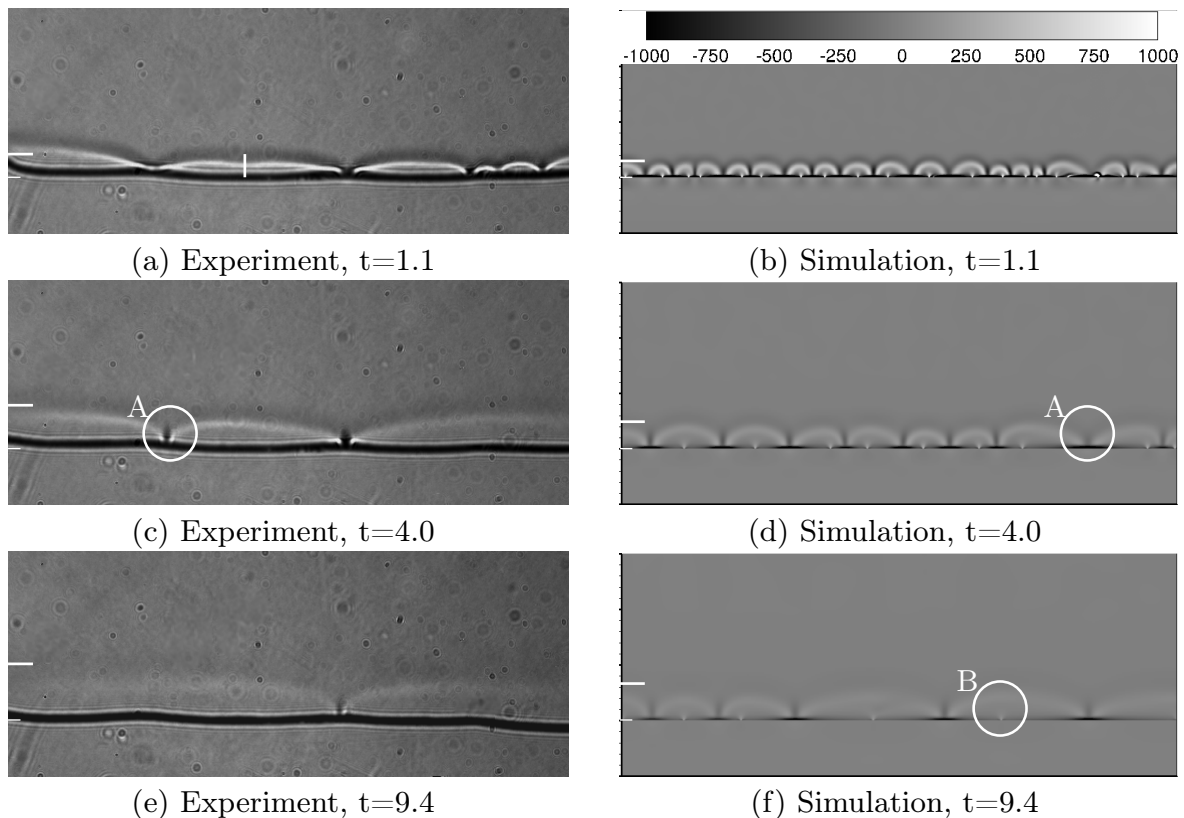


Figure 6.2: *Thin, vertical HS cell*: shadowgraph images for experiment with $2\epsilon = 0.5$ mm, corresponding to $\gamma = 6400$ in the simulation (right column). All figures show the same domain with horizontal extent of one length unit $l_x = 1$ (20 mm) and vertical extent of 0.4 length units with 0.3 in the upper phase and 0.1 in the lower phase (20 mm x 8 mm). The grayscale for simulations is fixed and given in (b). The vertical distance between the white lines illustrates the derived cell heights η , cf. Fig. 6.3. White circles with mark *A* (c),(d) illustrate what is called an inflow region, the white circle with *B* in (f) marks an outflow region. Experimental images were provided by Schwarzenberger & Eckert.

6.2.3 *Thick and vertically oriented Hele-Shaw cell*

Next the impact of a doubled plate distance $2\epsilon = 1$ mm is studied. Notice the shadowgraph images for vertical orientation in Fig. 6.5: in the experimental image (a) the dark boundary of the mixed fluid is still well visible but the clear horizontal division into individual roll cells has disappeared. A second remarkable observation is the appearance of a hierarchical pattern of small and large roll cells in the simulation, cf. Fig. 6.5(b). In the experimental image (a) small substructures – observed in simulation – are only faintly visible by a dim horizontal modulation near the interface. This lacking agreement might be due to the shadowing effect of the curved meniscus. The corresponding cell heights were again calculated (Fig. 6.6, blue circles exp): they increased relative to the thin cell (black crosses exp, again plotted for direct comparison). Remarkably, cell heights were of similar magnitude as the plate distance $2\gamma^{-1/2} = 0.05$ (meniscus height is $\omega = \tilde{\omega}/d^{(1)} = 0.009$), i.e. three-dimensional flow effects have to be expected.

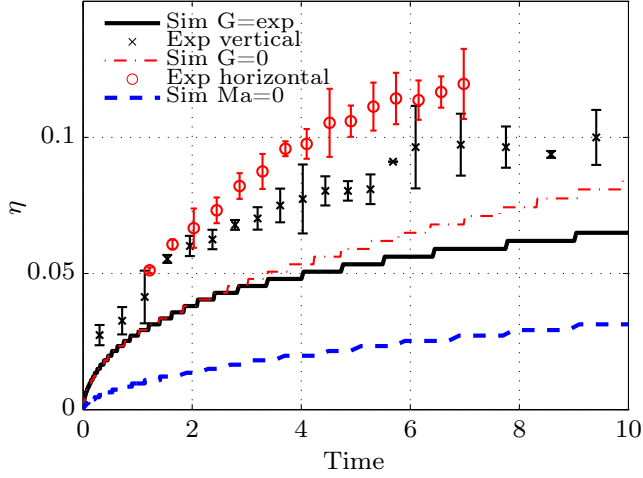


Figure 6.3: *Thin HS geometry* with varied orientation: cell height η of the Marangoni cells versus time for experiment with $2\epsilon = 0.5$ mm and corresponding simulation with $\gamma = 6400$. Experimental data were provided by Schwarzenberger & Eckert.

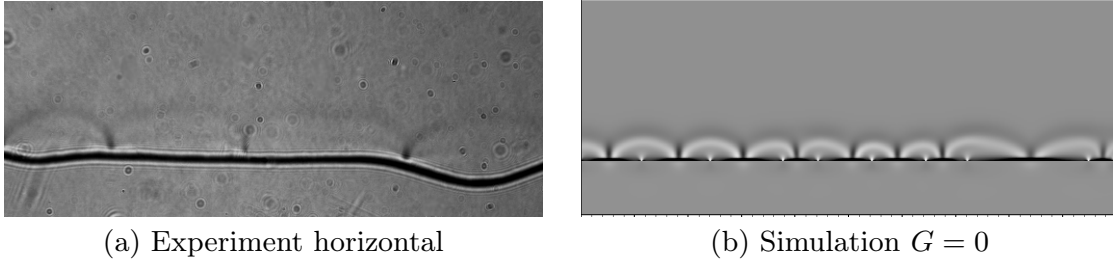


Figure 6.4: *Thin, horizontal HS cell*: shadowgraph images at $t=4.0$ for (a) experiment with $2\epsilon = 0.5$ mm and (b) simulation with $G = 0$, $\gamma = 6400$. Experimental images were provided by Schwarzenberger & Eckert.

Likewise, the cell heights increases in the simulations for the large plate distance, see blue dashed line in Fig. 6.6(a). However, the distinct deviations to the experimental data remained, see blue circles and blue dashed line in Fig. 6.6(a).

Fig. 6.7 displays an experimental (upper row) and a numerical (lower row) velocity field in the top fluid layer for both plate distances and vertical orientation. In general, these velocity fields confirm and augment the two main findings, derived so far from the shadowgraph images. First, Marangoni convection in the experiments operated on larger length scales and at higher velocities but has the same flow topology as in the simulations. Second, increased plate distance led to an intensified flow.

6.2.4 *Thick and horizontally oriented Hele-Shaw cell*

In the case of a thick HS cell ($2\epsilon = 1$ mm, $\gamma = 1600$) with horizontal orientation ($G = 0$), the simulation shows an intensified flow [Fig. 6.6(b) and 6.8(b)], i.e. smaller substructures and increased η compared to the vertical orientation. However, the corresponding experiment

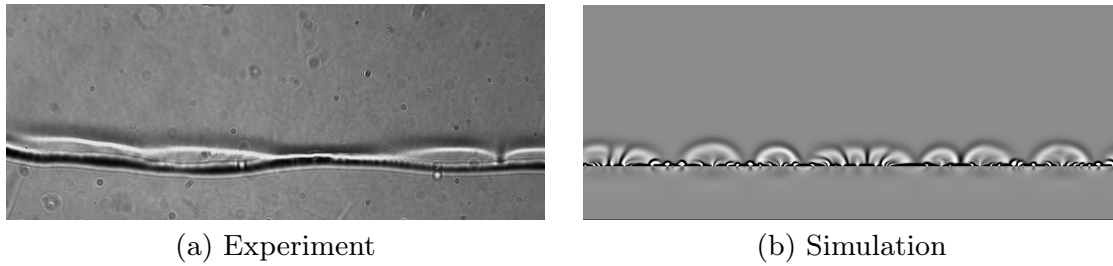


Figure 6.5: *Thick, vertical HS cell*: shadowgraph images at $t=1.1$ for (a) experiment with $2\epsilon = 1$ mm and (b) simulation with $\gamma = 1600$. Experimental images were provided by Schwarzenberger & Eckert.

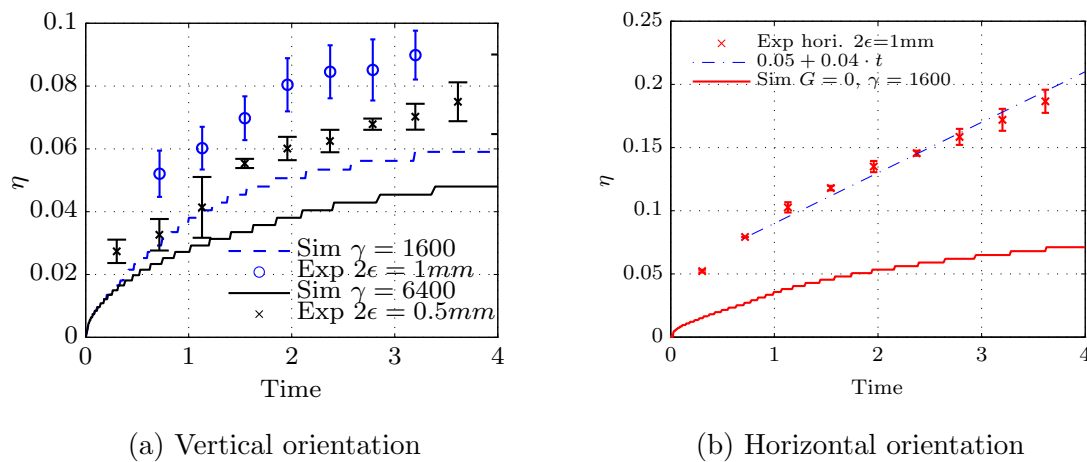


Figure 6.6: HS cell with varied gap size and varied orientation: (a) cell height for vertical orientation and both plate distances (experiment with $2\epsilon = 0.5$ mm, 1 mm and simulation with $\gamma = 6400$, $\gamma = 1600$); data for thin cell previously shown in Fig. 6.3 is repeated for direct comparison. (b) cell height for horizontal orientation with thick gap size (experiment with $2\epsilon = 1$ mm and simulation with $G = 0$, $\gamma = 1600$). The dashed line is plotted to guide the eye. Experimental data were provided by Schwarzenberger & Eckert.

differs clearly in the observed flow structures, cf. Fig. 6.8(a): a *solute front* (see "C" mark) emerged which is almost equidistant to the interface along with a regular horizontal modulation adjacent to the interface. The solute front moved away from the interface. Its position is measured analogously to the cell height and plotted in Fig. 6.6(b). A probable cause of the different appearances is the interference of Marangoni convection with a buoyancy-driven flow as discussed in Sec. 6.3.

6.3 Density convection in horizontal orientation

This section suggests an explanation for the solute front that is observed in the thick and horizontal cell, cf. Fig. 6.8(a). For this, let us consider layer (2) when the HS cell is filled and mass transfer has started (see Fig. 6.9 for illustration): Dense mixed fluid (adjacent to the interface) lies next to lighter unmixed fluid situated further away from the interface (dark

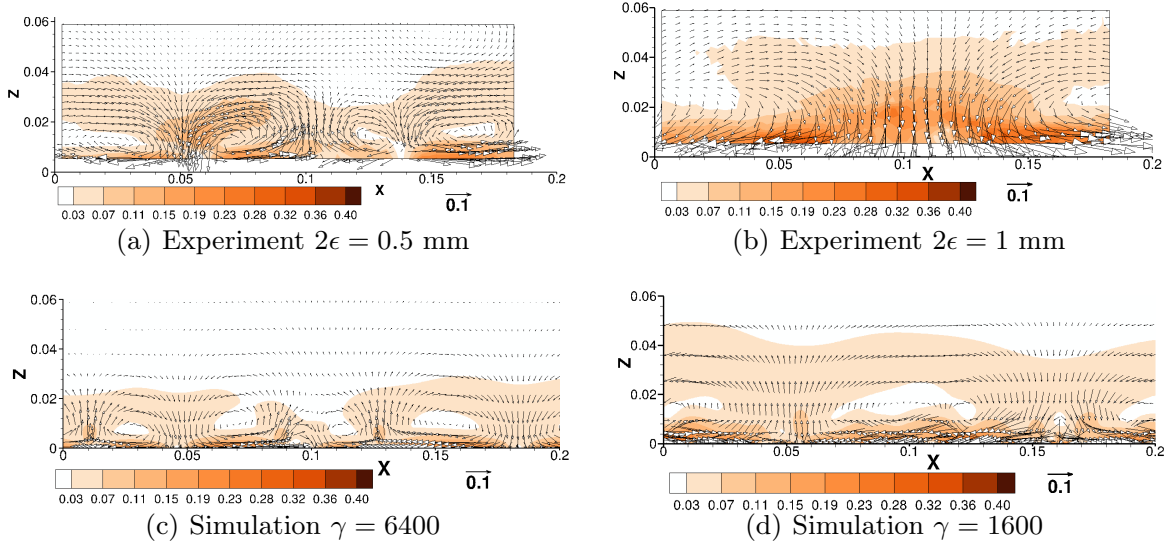


Figure 6.7: *Vertical HS cell* with varied gap size: experimental (PIV) and simulated velocity ($\mathbf{v}^{(2)}$) fields at $t=1.6$. The color illustrates the amplitude of velocity. Note that the velocity scale is $\nu^{(1)}/d^{(1)} = 60 \mu\text{m/s}$. Experimental images were provided by Schwarzenberger & Eckert.

color in Fig. 6.9).

Since gravity (\mathbf{g}) acts perpendicular (in $-\mathbf{e}_y$ -direction for horizontal orientation) to the density gradient, a flow ($u_y \neq 0$) is inevitably established due to the horizontal pressure gradient $\partial_z p$. The present 2D model is not able to capture such a flow across the gap, but we discuss how its amplitude can roughly be estimated by the so-called Hadley flow (cf. [126] p. 80).

This Hadley flow is pictured as follows: Consider a fluid layer infinitely extended in z -direction $-\infty < \tilde{z} < +\infty$ which is bounded in \tilde{y} direction by solid walls at $\tilde{y} = \epsilon, -\epsilon$ with a constant solute gradient $\partial_{\tilde{z}} \tilde{c}$ of magnitude $\Delta \tilde{c}/\delta l$. This well-known problem has a time-independent solution [126]. The dimensional velocity \tilde{U} established in the z -direction with material properties of layer (2) reads

$$\tilde{U}(\tilde{y}) = -\frac{g\beta_c^{(2)}(2\epsilon)^3}{\nu^{(2)}6} \frac{\Delta \tilde{c}}{\delta l} \left[\left(\frac{\tilde{y}}{2\epsilon} \right)^3 - \frac{\tilde{y}}{2\epsilon} \frac{1}{4} \right]. \quad (6.13)$$

In order to apply this simple model to the experimental situation, we estimate the solute difference $\Delta \tilde{c}$ in phase (2) by the difference between the initial concentration c_0 and the concentration at the interface for a semi-infinite system undergoing only pure diffusion [51], i.e. $\Delta \tilde{c} = c_0 - c_0/(1 + H^{-1}D^{-0.5}) \approx 0.0794c_0$. The selection of an appropriate length δl on which concentration gradients exist is a delicate task as our flow is not infinitely extended. For simplicity, we assume a distance of $\delta l = 0.1d^{(1)}$, which is approximately the vertical extent of the convective structures (a more sophisticated approach can be found in [171]). Finally, a characteristic nondimensional velocity U is taken at $\tilde{y} = \epsilon/2$ (with material parameters tabulated in Table 6.1). For 0.5 mm (1 mm) plate distance this amounts to $U=0.0033$ ($U=0.027$).

Consequently, a buoyancy-driven convection explains the appearance of a solute front for the thick and horizontal cell in Fig. 6.8(a). This interpretation is supported by three facts.

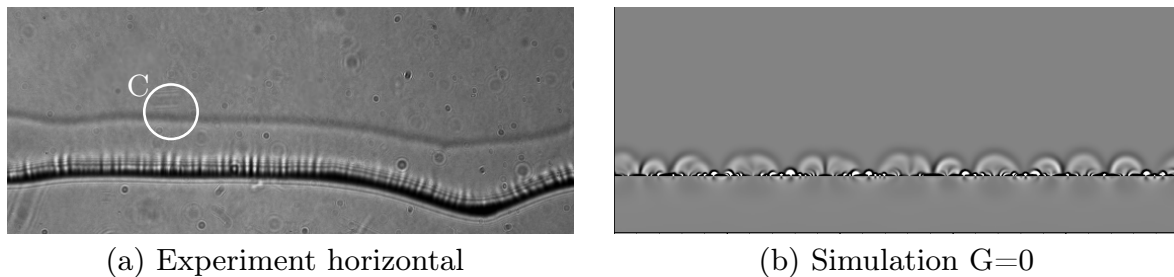


Figure 6.8: *Thick, horizontal HS cell*: shadowgraph images at $t=1.1$ for (a) experiment with $2\epsilon = 1$ mm and (b) simulation with $G = 0$, $\gamma = 1600$. White circle with C mark (a) illustrates the solute front observed in experiment. Experimental images were provided by Schwarzenberger & Eckert.

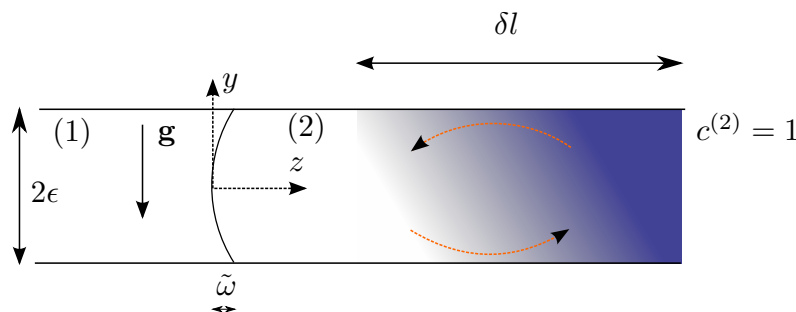


Figure 6.9: Sketch of horizontal HS cell to illustrate density-gradient driven convection.

First, the estimated value $U=0.027$ is of similar order as the measured speed of ≈ 0.04 , corresponding to the dashed line in Fig. 6.6(b). Second, no solute front is visible in the thin cell, which is in line with the small velocity ($U=0.0033$) predicted. Third, the propagation of the solute front in the thick cell bears a strong resemblance with that of an $A+B \rightarrow C$ reaction front [68, 208] for which the buoyancy-driven origin was clearly proved in [68]. Moreover, in interference with the buoyant convection, the fine Marangoni-driven solute structures at the interface seem to be drawn towards the solute front as visible in Fig. 6.8(a). These flow characteristics were also observed in a similar setup of chemo-Marangoni convection (Fig. 6a in [68]).

6.4 Discussion and conclusion

The major findings of this chapter are summarized as follows:

(1) Thin, vertical HS cell: Marangoni roll cells without internal substructure developed. The experimental flow structures were qualitatively well represented by the simulated Marangoni roll cells.

(2) Thick, vertical HS cell: The reduced wall friction caused an increased mass transfer and more substructures. In experiments, cell height growth was also enhanced with increased gap width, but the substructures were only faintly visible.

(3) Thin, horizontal HS cell: In simulations with zero Grashof number, the suppression of stabilizing density stratification led to an increased mass transfer. This enhanced cell height growth was also observed in the experiment.

(4) Thick, horizontal HS cell: In the experiment, a propagating solute front appeared, which is not explained by our gap-averaged model.

(5) In general, experiments appeared accelerated in time compared to simulations, which is in line with former observation in Sec. 5.3.

Besides the uncertainty of material properties, the observed differences can be explained by the limitations of the 2D model and the experimental filling procedure. The most obvious limitations are *3D flow effects*, i.e. a variation of concentration across the gap and deviations from the parabolic velocity profile. In detail, three features that lead to 3D effects might be noted. Firstly, the Marangoni roll cells that occur in the simulations are smaller than the gap size. By this, it is expected that Marangoni roll cells are also amplified across the gap ($\partial_y c \neq 0$). Secondly, the circular meniscus^{II} might lead to flow from the three phase contact line to the meniscus apex, since the meniscus apex reaches further into the water-rich phase. Thus, higher interfacial tension owing to a lower concentration is aspected there. Thirdly, for horizontal orientation, a density instability is induced, which leads to a buoyancy-driven flow across the gap ($u_y \neq 0$). Although its impact is not that obvious for the small gap width, a certain influence of this additional transport mechanism on the pattern growth can be assumed here as well.

Besides the 3D flow effects, deviations from the assumed plane interface are another source of discrepancies between experimental and numerical results. Apart from the circular meniscus, the position of the interface $\xi(x, y)$ also changes in lateral direction ($\partial_x \xi(x, y) \neq 0$) as a result of the filling procedure. This imposes a higher concentration at parts reaching deeper into the delivering phase. Furthermore, the interfacial area increases by 10-15 % due to interfacial deformations (circular meniscus and lateral undulation).

Despite the limitations of our theoretical and experimental approach, the qualitative agreement of our results for the vertical orientation and the small gap width show promising options for a quantitative analysis of solutal Marangoni convection. However, we can also conclude that the HS model is expected to be more precise for systems where large Marangoni cells without substructure develop, e.g. in [65], since 3D flow effects will be less pronounced in that case. These limitations also concern 2D simulations without the influence of wall friction.

A further option to check the applicability of the 2D model to an experiment might be deduced from the scale invariance noted in Sec. 3.1.1. A change in the initial concentration c_0 is equivalent to the change of length $L \sim c_0^{-1}$ and timescale $T \sim c_0^{-2}$. The HS model includes an additional outer length, i.e. the plate distance 2ϵ , which also needs to be scaled $2\epsilon \sim c_0^{-1}$. For instance, by doubling the plate distance and halving the concentration in an experiment, the pattern could remain unchanged if the 2D model is applicable. However, note that the requirement of negligible interfacial deformations still holds for this comparison.

^{II}The interface position $z = \xi(x, y)$ has a circular shape for fixed x .

Chapter 7

Results on Rayleigh-Marangoni convection

7.1 Introduction

In line with studies on Marangoni driven roll-cell convection in Ch. 5, the present chapter is once again motivated by former experimental works and their still pending detailed theoretical reproduction. In Sec. 2.4.2, it was shown that convective structures, named eruptions, were reported in situations when Rayleigh convection is expected (see type III system of Fig. 2.3). Along the lines of Ch.5, this issue is studied for a specific mass-transfer system for which experimental results are reported in literature [197,198] and furthermore detailed experimental data has been provided to us by K. Schwarzenberger (currently unpublished).

We consider the ternary system cyclohexanol/water+isopropanol undergoing an equilibration of the composition. Specifically, a cyclohexanol-rich phase is placed over a denser water-rich phase – both are mutually saturated and initial taken as ideally quiescent (identical to Ch. 5). But as a driving force for convection, *isopropanol* is dissolved in the aqueous layer, which then spreads into the organic phase.

This system is stable with respect to the stationary Marangoni instability (cf. Sec. 3.4.1) since isopropanol lowers the interfacial tension and diffuses much faster in the aqueous phase. This change from butanol to isopropanol is primarily because of the quality of experimental observations: Isopropanol dissolves much better in the aqueous phase [$(H = 1.6 = c_{eq}^{(2)}/c_{eq}^{(1)})$] than butanol ($H = 31$)] and therewith improves the quality of shadowgraph images.

The following sections are organized as follows. The different cases studied numerically are introduced in Sec. 7.2. Section 7.3 reports on the evolution of convection in a *reference configuration*. It is subdivided in: the early development of convection including the appearance of eruptions (Sec. 7.3.1), details on the onset of convection (Sec. 7.3.2) and the long term evolution, i.e. when the convection regime only marginally changes (Sec. 7.3.3).

A comparison to experimental data is performed in Sec. 7.4: Especially, we compare typical patterns, observed by shadowgraphy, and explain their formation by the visualization of numerical results (Sec. 7.4.1). Section 7.4.2 compares the optical flow calculated from the experimental and numerical shadowgraph images.

Section 7.5 presents numerical results with varied parameters. We undertook three studies: (1) The initial concentration of isopropanol is changed (relative to the reference configuration)

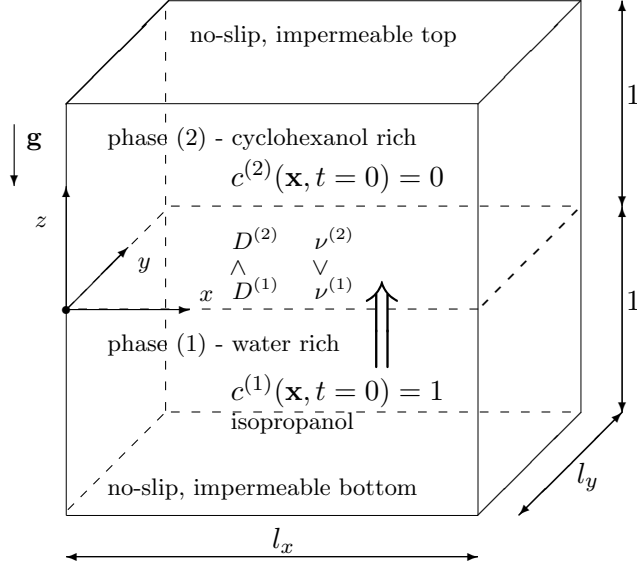


Figure 7.1: Two layer system in viscous units. Transport of isopropanol in direction (1) \rightarrow (2).

with the resulting impact on temporal evolution is studied (Sec. 7.5.1). (2) The evolution of pure Rayleigh convection is presented (Sec. 7.5.2), i.e. with $Ma=0$ but otherwise keeping parameters of the reference configuration. (3) The impact on mass transfer rates is shown for a *two dimensional* system (Sec. 7.5.3). Finally, Sec. 7.6 provides a discussion of results and Sec. 7.7 outlines our conclusions.

7.2 Sample configurations

Fluid motion and mass transport are modeled by the PM introduced in Sec. 3.1.2 and restated in the presently used form (without hats for nondimensional quantities) in Sec. 5.1.1. According to a change in transfer direction, i.e. (1) \rightarrow (2), the dimensionless initial conditions are changed and read as follows

$$c^{(1)}(t=0, x, y, z) = 1, \quad c^{(2)}(t=0, x, y, z) = 0. \quad (7.1)$$

Figure 7.1 shows a sketch of the computational domain. The velocity field is again initialized ($t=0$) with random numbers for u_z ; $(\nabla \times \mathbf{u}) \cdot \mathbf{e}_z$, which are uniformly distributed in the interval $[0, 10^{-3}]$, and zero mean flow.

The aim of our theoretical study is to explain the observations in mass-transfer experiments. Besides a few results that are reported by Schwarz [197, 198] (few single images), using a cuvette of $d^{(1)} = d^{(2)} = 15\text{mm}$; we were provided with detailed experimental results from Schwarzenberger performed in the experimental setup that is already described in Sec. 5.3.1 ($d^{(1)} = d^{(2)} = 20\text{mm}$).

In contrast to the water/cyclohexanol+1-butanol system that was discussed in Sec. 5.1.1, the transferred solute (butanol) is replaced by isopropanol (equivalently called 2-propanol).

The experimental preparation of the water+isopropanol / cyclohexanol system proceeds similar to the butanol system: First, the phases of a water and cyclohexanol ($C_6H_{11}OH$) mixture are separated – so both binary phases are in equilibrium due to mutual saturation. Secondly, isopropanol (C_3H_8O), which lowers interfacial tension as well as density, is dissolved in the aqueous phase. Note that this leads to the desired regime, i.e. a density lowering substance is transported against gravitational acceleration and out of the phase with higher diffusivity. The detailed estimation of material properties is given in App. B.2

Experimental data (shadowgraph images) are provided to us for initial volumetric concentration of 2.5vol% and 5vol%, which correspond to molar concentration of $c_0 = 0.32, 0.65$ mol/l, respectively. Experiments were performed in two geometries: (1) screening experiments in a low cuvette $d^{(1)} = 5mm$ [related simulations are denoted by RM_2a (2.5vol%) and RM_3a (5vol%)] and (2) the tall cuvette $d^{(1)} = 20mm$ described in Sec. 5.3.1 [simulation denoted as RM_2at (2.5vol%) and RM_3at (5vol%)]. For each concentration (and additional 1vol%), we give the physical parameters in Tab. 7.1 (low cuvette) and Tab. 7.2 (tall cuvette). An overview of the different simulations is given in Tab. 7.3.

For the detailed presentation of evolving convection, we shall focus on the RM_2a case, as it requires less numerical effort (versus the tall cuvette case) for both the simulation and the post-processing. In the following we will call this the *reference configuration*, i.e. the low cuvette with initially 2.5vol% dissolved isopropanol.

However, for a one-to-one comparison, experiment versus simulation, the RM_2at case is mainly employed since experiments in the tall cuvette are more suitable to the PM than in the lower one. This is because, in the low cuvette layering was performed by a tilting procedure of a previously filled single cuvette, as sketched in Fig. 7.2. Nevertheless, optical flow calculation from the shadowgraph images in both experimental devices will be presented.

Additional parameters studies were performed: (1) Convection is observed for the Marangoni effect turned off ($Ma=0$), noted as the RM_2b case in Tab. 7.3. (2) Similar to the procedure in Ch. 5, the onset of convection is studied by changing the initial strength of velocity perturbation in simulations RM_2a_onset and RM_2b_onset. (3) The computational domain is reduced to a two-dimensional one by neglecting variations in the y-dimension, referred as cases RM_2a_2d and RM_2b_2d.

dimensionless quantity	definition	value
Grashof number	$G = \frac{c_0 \beta_c^{(1)} g (d^{(1)})^3}{(\nu^{(1)})^2}$	$(-1.15, -2.83, -5.76) \times 10^3$
Rayleigh number	$Ra^{(1)} = GSc^{(1)} = \frac{c_0 \beta_c^{(1)} g (d^{(1)})^3}{\nu^{(1)} D^{(1)}}$	$(-1.55, -3.82, -7.76) \times 10^6$
Schmidt number aqueous phase	$Sc^{(1)} = \frac{\nu^{(1)}}{D^{(1)}}$	1348
Schmidt number organic phase	$Sc^{(2)} = \frac{\nu^{(2)}}{D^{(2)}}$	$3.41 \cdot 10^5$
Marangoni number	$Ma = \frac{c_0 \alpha_c \sigma_{ref} d^{(1)}}{\rho^{(1)} \nu^{(1)} D^{(1)}}$	$(-0.69, -1.69, -3.44) \cdot 10^6$
partition coefficient	$H = \frac{c_{eq}^{(2)}}{c_{eq}^{(1)}}$	1.6
density ratio	$\rho = \frac{\rho_{ref}^{(2)}}{\rho_{ref}^{(1)}}$	0.96
kinematic viscosity ratio	$\nu = \frac{\nu^{(2)}}{\nu^{(1)}}$	20.74
diffusivity ratio	$D = \frac{D^{(2)}}{D^{(1)}}$	0.082
layer height ratio	$d = \frac{d^{(2)}}{d^{(1)}}$	1.
compressibility ratio	$\beta = \frac{\beta_c^{(2)}}{\beta_c^{(1)}}$	0.92
intrinsic mass	$M_{vis} = (d^{(1)})^3 \rho_{ref}^{(1)}$	$1.24 \cdot 10^{-4} \text{kg}$
intrinsic length scale	$L_{vis} = d^{(1)}$	5 mm
intrinsic time scale	$T_{vis} = \frac{d^{(1)} \cdot d^{(1)}}{\nu^{(1)}}$	20.833 s
intrinsic velocity scale	$V_{vis} = \frac{\nu^{(1)}}{d^{(1)}}$	$0.24 \cdot 10^{-3} \text{m/s}$

Table 7.1: Nondimensional parameters for the isopropanol system in the low cuvette calculated with values from material properties (Tab. B.1), layer heights $d^{(1)} = d^{(2)} = 5 \text{ mm}$, and concentrations $c_0 = 0.13, 0.32, 0.65 \text{ mol/l}$, corresponding to volumetric concentration of 1vol%, 2.5%, 5%, respectively.

name	definition	value
Grashof number	$G = \frac{c_0 \beta_c^{(1)} g (d^{(1)})^3}{(\nu^{(1)})^2}$	$(-0.74, -1.81, -3.68) \times 10^5$
Rayleigh number	$Ra^{(1)} = GSc^{(1)} = \frac{c_0 \beta_c^{(1)} g (d^{(1)})^3}{\nu^{(1)} D^{(1)}}$	$(1.00, 2.44, 4.96) \times 10^8$
Schmidt number aqueous phase	$Sc^{(1)} = \frac{\nu^{(1)}}{D^{(1)}}$	1348
Schmidt number organic phase	$Sc^{(2)} = \frac{\nu^{(2)}}{D^{(2)}}$	3.41×10^5
Marangoni number	$Ma = \frac{c_0 \alpha_c \sigma_{ref} d^{(1)}}{\rho^{(1)} \nu^{(1)} D^{(1)}}$	$(-0.28 -0.68 -1.38) \times 10^7$
partition coefficient	$H = c_{eq}^{(2)} / c_{eq}^{(1)}$	1.6
density ratio	$\rho = \frac{\rho_{ref}^{(2)}}{\rho_{ref}^{(1)}}$	0.96
kinematic viscosity ratio	$\nu = \frac{\nu^{(2)}}{\nu^{(1)}}$	20.74
diffusivity ratio	$D = \frac{D^{(2)}}{D^{(1)}}$	0.082
layer height ratio	$d = \frac{d^{(2)}}{d^{(1)}}$	1
compressibility ratio	$\beta = \frac{\beta_c^{(2)}}{\beta_c^{(1)}}$	0.92
intrinsic mass	$M_{vis} = (d^{(1)})^3 \rho_{ref}^{(1)}$	$8 \times 10^{-3} kg$
intrinsic length scale	$L_{vis} = d^{(1)}$	20mm
intrinsic time scale	$T_{vis} = \frac{d^{(1)} \times d^{(1)}}{\nu^{(1)}}$	333.33s
intrinsic velocity scale	$V_{vis} = \frac{\nu^{(1)}}{d^{(1)}}$	$6 \times 10^{-5} m/s$

Table 7.2: Nondimensional parameters for the isopropanol system in the tall cuvettes with values from Tab. B.1 and layer heights $d^{(1)} = d^{(2)} = 20 \text{ mm}$. The concentrations used are $c_0 = 0.13, 0.32, 0.65 \text{ mol/l}$, corresponding to volumetric concentration of 1vol%, 2.5%, 5%, respectively.

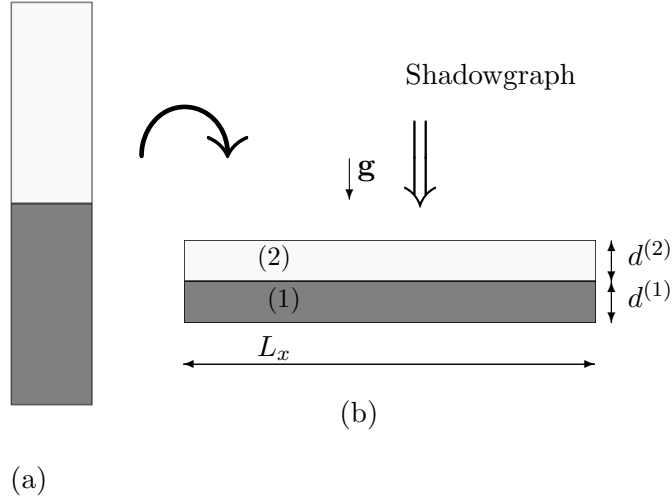


Figure 7.2: Sketch showing the low-cuvette experimental geometry: (a) Vertical position for the filling. (b) Horizontal position for the observation of mass transfer. The dimensions are $d^{(1)} = d^{(2)} = 5\text{mm}$ and $L_x = 50\text{mm}$ with a square base area thus $L_y = 50\text{mm}$ (not drawn).

#	δt_{max}	$l_x(N_x)$	$l_y(N_y)$	$N_z^{(1)}$	$N_z^{(2)}$	phys parameter
RM_1a	5e-2	5(1024)	5(1024)	128	256	$G = -1.15 \times 10^3$, $Ma = -0.69 \times 10^6$
RM_2a	5e-2	3(1024)	3(1024)	128	256	$G = -2.83 \times 10^3$, $Ma = -1.69 \times 10^6$
RM_2b	5e-2	3(1024)	3(1024)	128	256	$G = -2.83 \times 10^3$, $Ma = 0$
RM_2at	1e-3	0.75(1024)	0.75(1024)	256	512	$G = -1.81 \times 10^5$, $Ma = -0.68 \times 10^7$
RM_3a	5e-3	2(1024)	2(1024)	128	256	$G = -5.76 \times 10^3$, $Ma = -3.44 \times 10^6$
RM_2a_onset	5e-2	3(1024)	3(1024)	128	256	$G = -2.83 \times 10^3$, $Ma = -1.69 \times 10^6$
RM_2b_onset	5e-2	3(1024)	3(1024)	128	256	$G = -2.83 \times 10^3$, $Ma = 0$
RM_2a2d	5e-2	3(1024)	1e-6(2)	128	256	$G = -2.83 \times 10^3$, $Ma = -1.69 \times 10^6$
RM_2b2d	5e-2	3(1024)	1e-6(2)	128	256	$G = -2.83 \times 10^3$, $Ma = 0$
RM_diff	1e-4	-	-	128	256	$G = 0$ $Ma = 0$

Table 7.3: Numerical parameter for different Rayleigh-Marangoni runs, with $C_b = 0.2$. Parameters that are not listed are unchanged and can be found in Tab. 7.1.

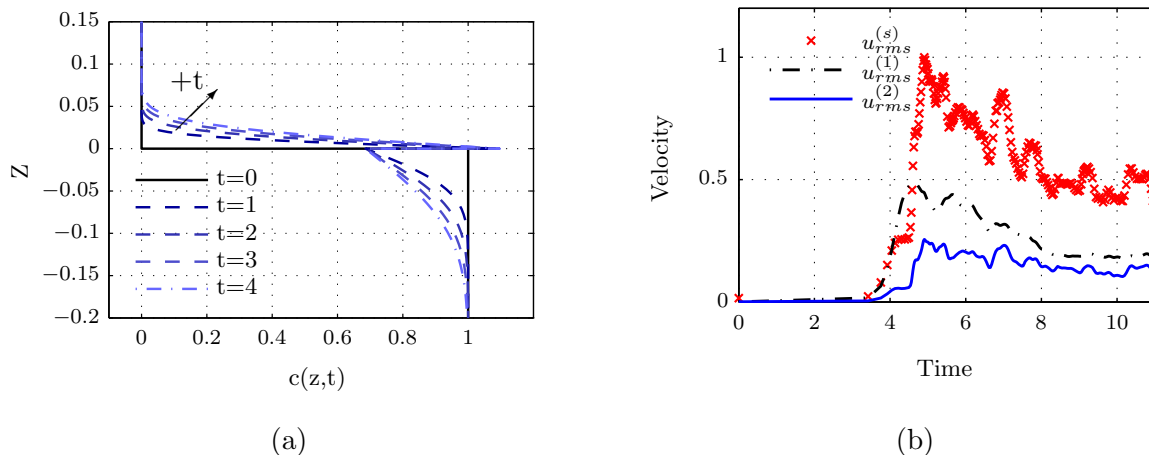


Figure 7.3: Onset of convection in the reference configuration: (a) Concentration profiles for pure diffusion, i.e. $G=Ma=0$, from numerics (RM_diff), (b) rms velocities.

7.3 Rayleigh-Marangoni convection in the reference configuration

7.3.1 Early phase of convection

Based on the numerical data of simulation run RM_2a, the present section reports on the onset and the subsequent basic structures of convection.

The simulation was started with an initial homogeneous solute distribution in the bottom ($c^{(1)} = 1$), no solute in top layer (2) and slightly perturbed velocity field ($u_{rms}(t=0) = 7.2 \times 10^{-4}$). This initial disturbance is dissipated firstly (cf. Sec. 7.3.2 for further details). Consequently, before onset of noticeable convection (i.e. for $t < 3.5$), the transport of solute was mainly driven by pure diffusion [see rms velocities in Fig. 7.3(b)].

Thus, the solute concentration evolves as a function of time and the vertical coordinate $c^{(i)} = c^{(i)}(z, t)$ only, within a very good approximation. Fig. 7.3(a) shows the temporal succession of solute profiles for pure diffusion ($\mathbf{u} = 0$): A lighter fluid layer above the interface and a denser layer under the interface develops since density decreases with solute ($G^{(1)} < 0$, $\beta > 0$). This density configuration is susceptible to a Rayleigh instability [182] (also noted as Rayleigh-Taylor or Rayleigh-Bénard instability) [45]). This means that fluid motion may be triggered due to the fact that lifting of lighter fluid and sinking of denser fluid could lower potential energy globally.

Fig. 7.3(b) depicts an increasing velocity for a time around $t \approx 3.5$ [first in layer (1)]. To visualize the onset of convection, the distribution of solute and velocity arrows are displayed in a vertical plane of $y = 0$ for five time instances in Fig. 7.4. In a first stage, the unstable layer of mixed fluid gathered in rather regular portions, which tended to sink in the bottom layer and rise in the top layer [Fig. 7.4(b) $t=3.93$]. The influence of surface tension becomes apparent by inspecting the related space-time plot of interfacial concentration [Fig. 7.4(a)]. Therefore, consider location $x = 1.5$, $t = 3.93$ [at (b) line]. Here fluid departs from the interface due to the Rayleigh effect. At the same time, interfacial concentration is slightly lower here (compared to a neighborhood of $x = 1.5$) which means a local maximum of surface ten-

sion. Hence, interfacial forces were *supporting* the Rayleigh effect at $t=3.93$. This particular situation is potentially related to the asymmetry of the velocity amplitude between layers, i.e. convection dominates in the *bottom* layer. Fig. 7.3(b) also reflects this, namely $u_{rms}^{(1)} > u_{rms}^{(2)}$. As an explanation for this relation, note the lower viscosity ($\nu^{(1)} < \nu^{(2)}$) and higher density impact $\beta^{(1)} > \beta^{(2)}$ in the bottom layer.

The next stage in the development of convection is central to our present work, because interfacial tension, now, influences the dynamics essentially. A unique convective structure, called *eruption* [123] appears. Therefore, observe at $x=1.5$, $t=4.56$ [Fig. 7.4(a), (c) line)], how concentration rises, forming a cone of high concentration in the $x-t$ plane that is open to the future. In the vertical cuts, the inflow of fluid from the bulk to the interface is seen at $x=1.5$ [Fig. 7.4(c)]. It appears as if portions of enriched fluid that accumulated (by the Rayleigh convection) above the interface are drawn back to the interface by the Marangoni effect. For this, see also next time $t=4.69$ [Fig. 7.4(d)], revealing the strong growth in velocity and the spreading of solute portions. The onset of eruptions, around $t=4.5$, also manifests in the rise of interfacial velocity $u_{rms}^{(s)}$ in Fig. 7.3(b).

The subsequent Figs. 7.4(e,f) show that the system dynamics get rather chaotic, but can be characterized by three features: (1) frequent emission of solutal plumes in the bottom layer, (2) the presence of erratic and continuous interfacial motion (eruptions), (3) formation of larger portions of enriched fluid in the top layer that slowly rise.

In order to visualize the three stages of convection onset: "*diffusion* \rightarrow *Rayleigh instability* \rightarrow *eruptions*" by means of their fully three-dimensional characteristics, isosurfaces of concentration are drawn in Fig. 7.5 at the relevant times. Let us note two observations: (1) Rayleigh instability occurred in polygonal planforms that were disrupted by the eruptions. (2) Sinking plumes were much faster than rising ones and were only marginally influenced by the eruptions.

In the next Sec. 7.3.2, time of onset is quantified, especially regarding its dependence on initial disturbance amplitude. Further aspects of the long-term evolution of convection are presented in Sec. 7.3.3.

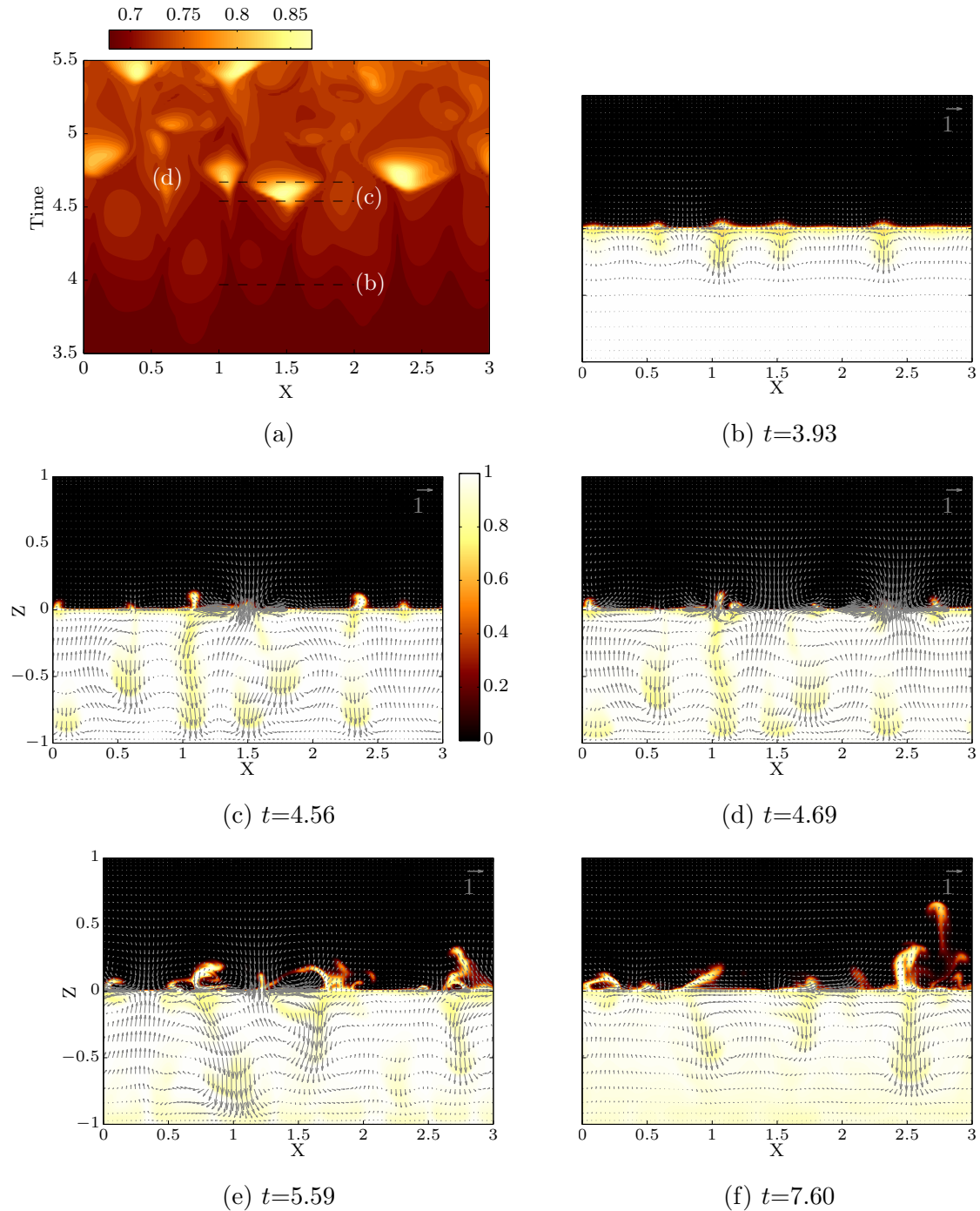


Figure 7.4: Onset of convection for simulation RM_2a: (a) Space-time plot of interfacial concentration $c^{(1)}(x, y = 0, z = 0, t)$ and (b-f) concentration and velocity field at a plane $y = 0$ for increasing times.

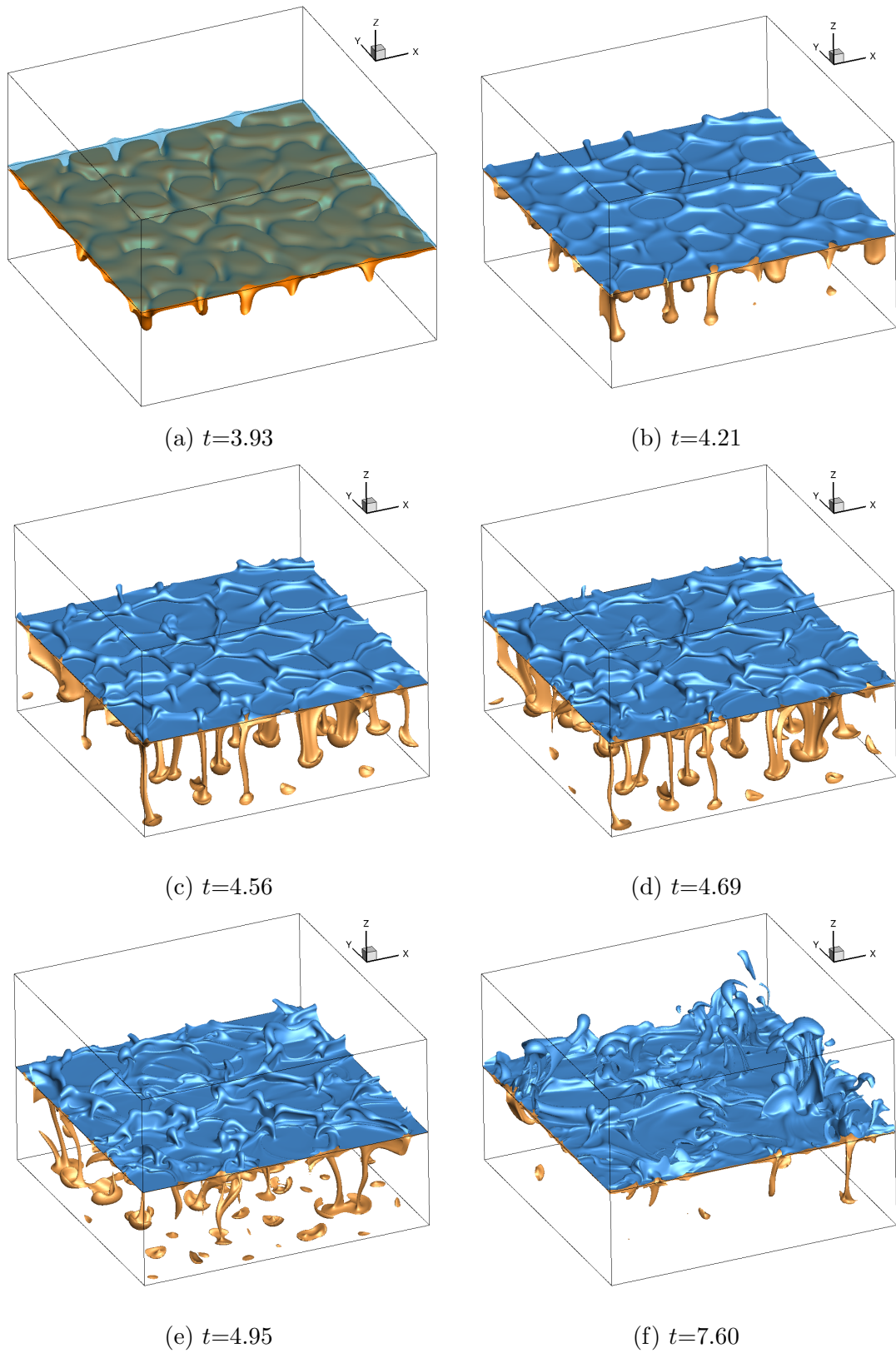


Figure 7.5: Onset of convection in RM.2a simulation: isosurfaces of concentration $c^{(1)}=0.85$ (bottom layer), $c^{(2)}=0.45$ (top layer), time instances partly correspond to Fig. 7.4.

7.3.2 Onset time and onset wavenumbers

In the current section, the instability of the primary diffusive evolution is studied by additional simulations (RM_2a_onset, see Tab. 7.3). Material parameters were kept constant relative to simulation RM_2a, but the initial velocity perturbations were varied in strength while keeping the initial homogeneous concentration. This choice of initial perturbations might be in line with a hypothetical experiment, whereby homogenization of each layer seems feasible, but not with a simultaneous quiescent state when homogeneous phases are brought into contact.

The present analysis proceeds along the same lines as our study in Sec. 3.5. Namely, to quantify the onset of convection, the averaged rms velocity of both layers $u_{rms}(t)$ is considered. Figure 7.6(a) shows its development for four simulations with different initial amplitudes (velocity fields are uncorrelated between different simulations). Furthermore, length scales of structures are quantified by analyzing interfacial concentration $c^{(1)}(x, y, z = 0)$ and the synthetic shadowgraph images $s(x, y)$ by their Fourier spectrum: Wavelengths λ_c [Fig. 7.6(b)], λ_s [Fig. 7.6(c)] are defined by their weighted means $\lambda_c = 2\pi/k_{avg}^{c(x,y,z=0)}$, $\lambda_s = 2\pi/k_{avg}^{s(x,y)}$ according to Eq. 3.143. We shall use λ_c favorably since derived from a primary quantity. Therefore, it is more comparable with the common modal, linear stability analysis from literature.

In line with former procedures (Sec. 3.5), two representative times are extracted from each rms velocity curve [Fig. 7.6(a)], i.e. t_{c1} (crosses) for the first net growth and t_{c3} (circles) when rms-velocity is maximal.

The times t_{c1} are correlated with the initial amplitude (see caption of Fig. 7.6 for specific values of t_{c1}). We suspect that in a real system or at least in a very well prepared experiment, the time t_{c1} is hardly detected as its amplitude is very low.

The time of maximal motion (t_{c3}) decreased with an increase in initial amplitude. The influence of the initial amplitude on t_{c3} (cf. Fig. 7.6) is roughly described by fitting data to a logarithmic dependence, namely $t_{c3} = 4.18 - 0.17 \ln(u_{rms}(0))$ ¹. Such behavior would be exactly observed for a purely exponential growth with equal exponential growth rates but starting from different amplitudes.

The derived mean wavelengths λ_c, λ_s show only a marginal dependency on the initial amplitudes [Fig. 7.6(b,c)]. Here the analysis of the interfacial concentration λ_c better reflects the actual size of convective structure, namely, initial polygonal cells with characteristic size around 0.5 (cf. isosurfaces in Fig. 7.5 or shadowgraph images in the appendix Fig. D.3). The analysis of shadowgraph images (λ_s) only shortly reflects the size of convection cells. Especially, when eruption set in (around t_{c3}), the spectrum is shifted to smaller features.

Several authors [48,101,107,222] have experimentally and theoretically (mainly with linear stability methods) tried to measure and predict times for convection onset. Our nonlinear simulations can be viewed as a methodical connection between classical linear methods and experiment since we exactly have control over the physical effects involved, which is not the case when analyzing an experimental situation. This issue is discussed in Sec. 7.6.1, where results of the linear stability analysis from Kim and coworkers [107] are related to the present findings.

¹This should not be extrapolated to higher onset amplitudes than simulated

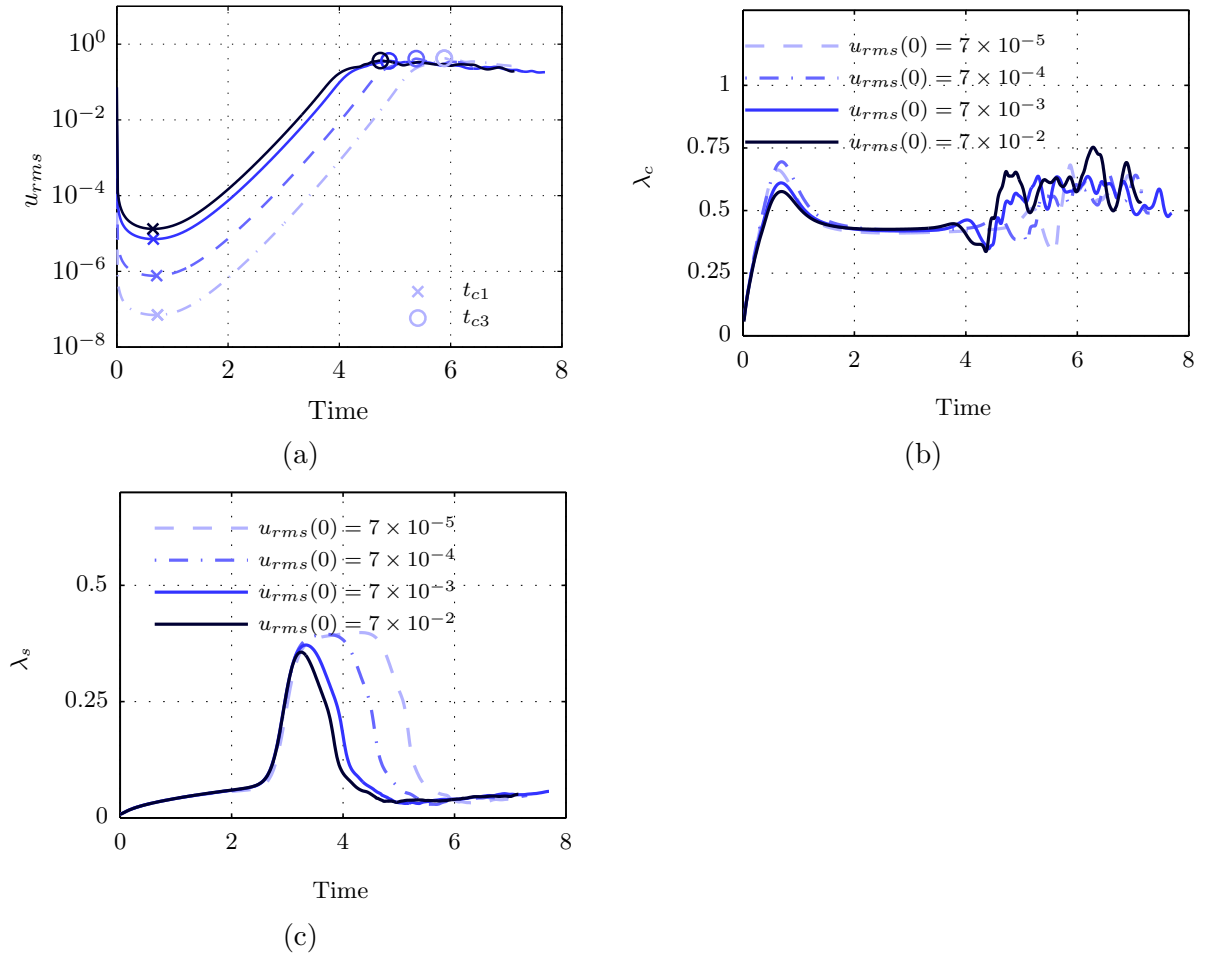


Figure 7.6: Onset of convection in RM.2a-onset: (a) rms velocity $u_{rms}(t)$ with derived onset times $t_{c1}=0.73, 0.72, 0.66, 0.65$ and $t_{c3} = 5.89, 5.38, 4.89, 4.74$ in order of increasing initial amplitude; (b) weighted mean averaged wavenumber of interfacial concentration [Eq. (3.143)]; (c) weighted mean averaged wavenumber of synthetic shadowgraph [Eq. (3.143)].

7.3.3 Long term evolution

The present section outlines further details on the development of convection in the reference configuration. After the onset of convection, solutal plumes and eruptions kept on supporting fluid motion. This equilibration process is simulated up to $t \approx 60$, when one-third of the solute was transferred [cf. Fig. 7.7(a)]. Nevertheless, some results for very late times (i.e. when 90% of the potential mass is transferred) are reported from the two-dimensional simulation in Sec. 7.5.3.

After onset of convection, the velocity and the solute flux show a global maximum at $t=5$ ($\approx t_{c3}$) see Fig. 7.7(b,c). Subsequently, the system evolves chaotically, but with a clear trend in a decline of convective motion [see rms velocity Fig. 7.7(c)], surely correlated with the decline in concentration difference between layers [see Fig. 7.7(a)]. Accordingly, the mass flux [Fig. 7.7(b)] and the rate of work done on the system Fig. 7.7(d) decrease with time as well. Note that the work performed by interfacial forces ω_s is distinctly higher than the work due to gravitation ω_g .^{II}

The presentation of isosurfaces of concentration is continued from Fig. 7.5 in Fig. 7.8 to visualize the transport of solute. These isosurfaces are supported by horizontally averaged profiles from velocity and concentration in Fig 7.9. Particular features from both figures are noted next:

The vertical [Fig. 7.9(a)] and horizontal [Fig. 7.9(c)] variation of concentration is smaller in the bottom layer – readily explained by the higher diffusivity $D = D^{(2)}/D^{(1)} = 0.082$ there. This is also reflected by the isosurfaces, namely, it is difficult to visualize sinking fluid portions [in layer (1)] by a fixed concentration value over time (Fig. 7.8) – e.g. at $t=58$ concentration is completely below $c^{(1)} = 0.85$.

In the top layer, mixing was rather poor. Concentration profiles are even inverted ($\partial_z c^{(2)} > 0$ for some z), because of the high concentration of ascending solutal plumes. Their concentration is higher than the global equilibrium value $c_{eq}^{(2)} = 0.65$.^{III}

The velocity profiles [Fig. 7.9(b)] in the bottom layer with a local maximum around the mid height ($z \approx -0.3$) indicate the prevalence of convection cells with a typical size of the whole layer. However, in the top layer, velocity monotonically decreased with distance from the interface. The peak at the interface can be assigned to the Marangoni convection, the velocity field is directly influenced around $|z| < \approx 0.1$. Moreover, by inspection of velocity profiles, the Reynolds number might be calculated using the layer heights and the rms-velocity, i.e. $Re^{(1)} = u_{rms}^{(1)}$, $Re^{(2)} = u_{rms}^{(2)}/\nu$. This shows that fluid motion is still in a Stokes flow regime, similar to the case of stationary Marangoni convection in Ch. 5.

The profiles of $\langle u_z c \rangle_{xy}$ [Fig. 7.9(d)] illustrate the distribution of work done by gravity on the system (see Eq. C.10). Generally, these profiles show (especially their variation) the nature of sinking and rising fluid in discrete portions (solutal plumes). The higher variation in the top layer, might be interrelated to the horizontal variance of concentration [Fig. 7.9(c)], i.e. coherent plumes have a higher concentration contrast in the top layer.

^{II}The rate of work done on the fluid is almost equal to the viscous dissipation ϵ since temporal changes in kinetic energy are negligible in the energy balance, see Eqs. (C.12),(C.11).

^{III}This indicates that a "paradox" late state might be possible (for deeper layers), for which the net mass flux reverses its direction due to accumulation of solute with over-equilibrium concentration $c^{(2)} > c_{eq}^{(2)}$ in the top.

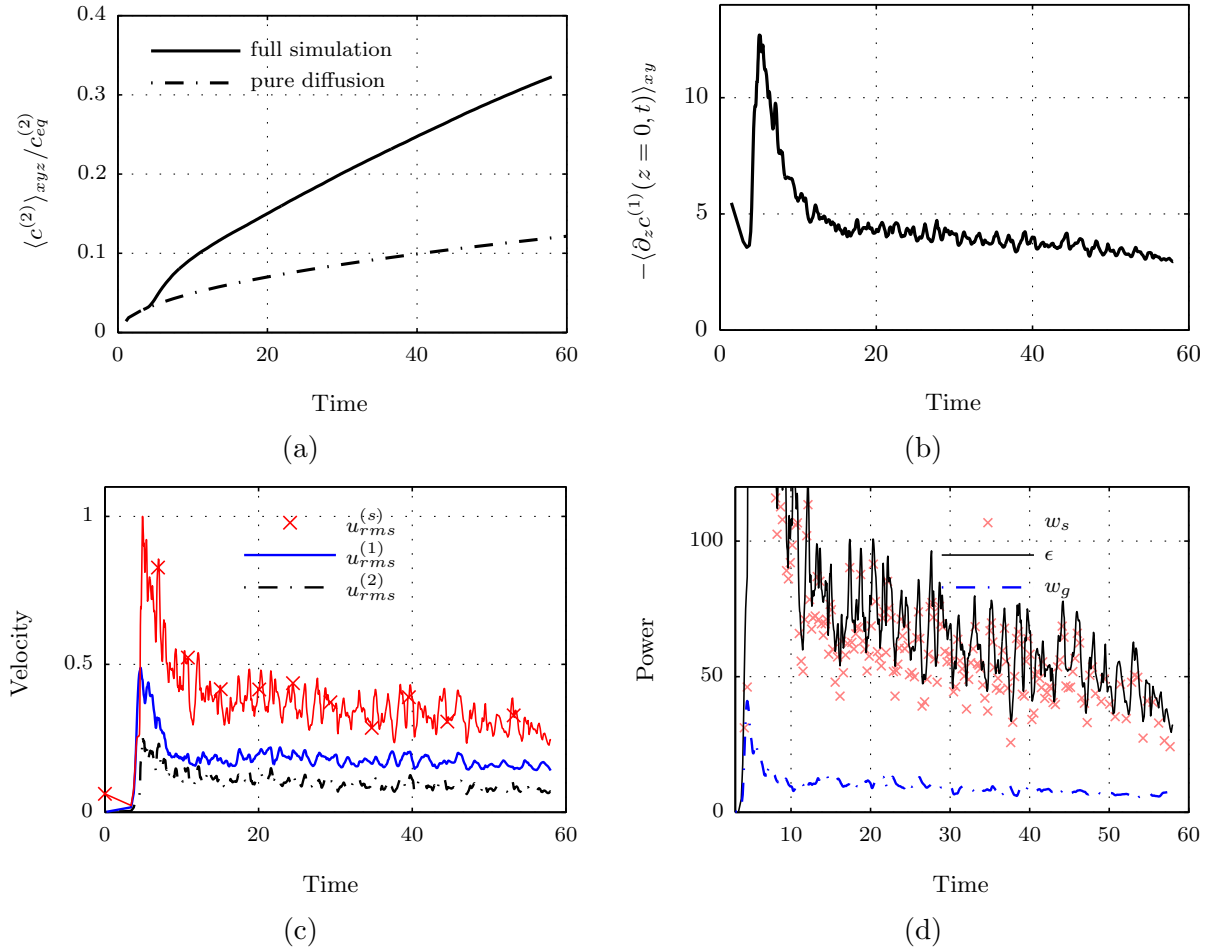


Figure 7.7: Simulation RM.2a scalar properties over time: (a) integral top layer concentration normalized by the final concentration $c_{eq}^{(2)}=0.615$ (b) vertical concentration gradient at the interface (c) root mean squared velocity (d) kinetic energy budget with viscous dissipation ϵ , rate of work due to gravity w_g and interfacial forces w_s (see Eq. C.10)

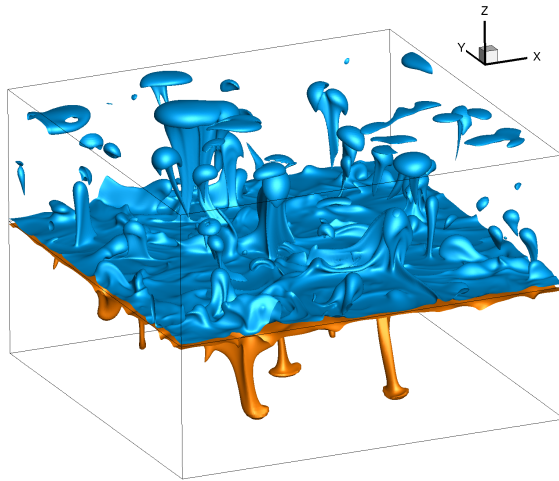
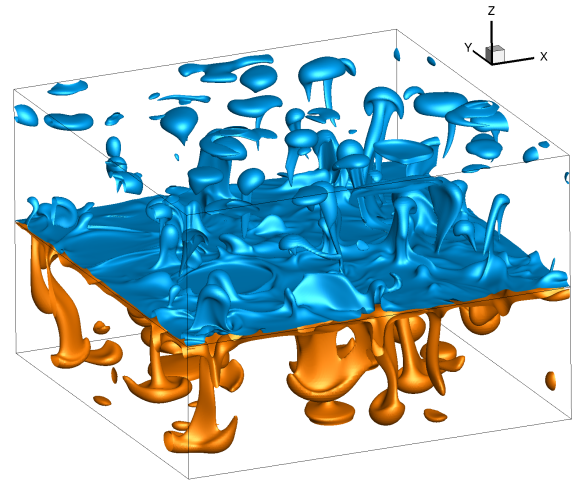
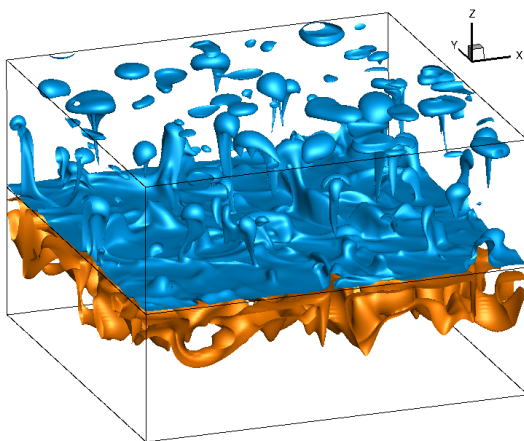
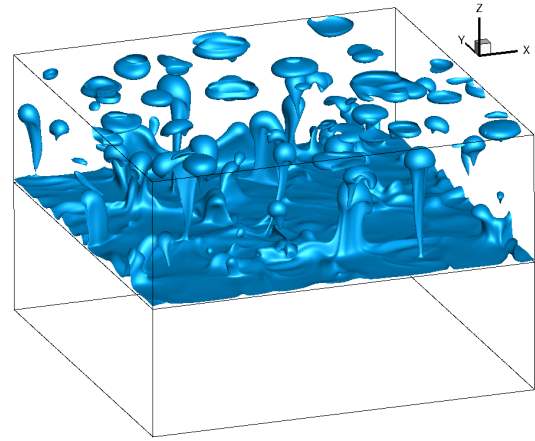
(c) $t=14.98$ (d) $t=30.27$ (c) $t=45.02$ (d) $t=58.00$

Figure 7.8: Simulation RM_2a concentration isosurfaces $c^{(1)} = 0.85$, $c^{(2)} = 0.45$ for four consecutive times.

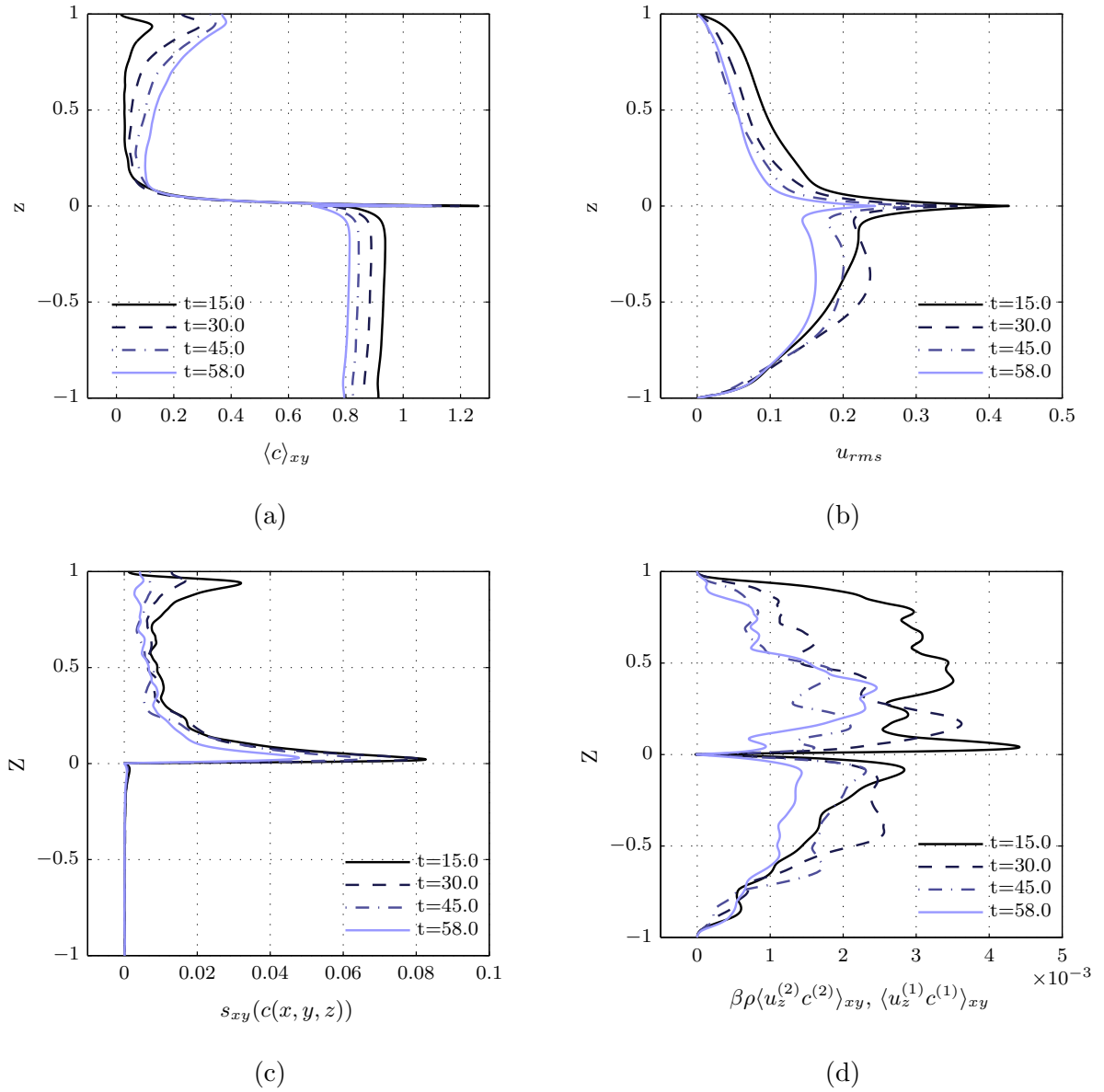


Figure 7.9: Simulation RM_2a vertical profiles of horizontally averaged: (a) concentration, (b) rms-velocity, (c) standard deviation of concentration in $x - y$ planes and (d) velocity times concentration [related to the work done by gravity see Eq. (C.11)].

7.4 Comparison to experiments

This section compares a mass-transfer experiment (by *K. Schwarzenberger, personal communication*) to our simulations. This comparison is based on the tall cuvette configuration (simulation RM_2at), since there, the initial conditions and the geometry are better suited to our paradigmatic model.

Although, we introduced non-dimensional equations based on the layer height – now $d^{(1)} = d^{(2)} = 20\text{mm}$ – in this section we depart from this agreement. Namely, we will stick to $L_{vis} = 5\text{mm}$ as a length scale, consequently time scale and velocity scale are $\tilde{T} = 20.8\bar{3}\text{s}$, $\tilde{U} = 240\mu\text{ m/s}$, respectively. By this, the results of simulation RM_2at [Tab. 7.3] are scaled accordingly, i.e. nondimensional lengths were multiplied by 4, the time by 4^2 and the velocity by 4^{-1} ; also, dimensional quantities are given partly. This is done to get a better comparability to former and following sections since the effect of the increased layer heights affected dynamics (in dimensional terms) only marginally.

The experiments were carried out by the procedure described in Sec. 5.3.1. The *start* of the mass-transfer experiment ($t_{exp} = 0$) is regarded as the time when both phases come into contact for the first time. The subsequent sliding of both layers against each other took one time units (20.6s).

Fig. 7.10 shows the early phase of convection onset. At $t=4.79$ (simulation) a polygonal pattern due to Rayleigh instability has established – quite similar to the pattern observed in simulation RM_2a (Fig. D.3). In the experiment ($t_{exp}=1.29$) a similar pattern is found, although not in such a polygonal order. Times between experiment and simulations were matched by adding 3.5 time units ($\approx 72.9\text{s}$) to the experimental time, i.e. $t=t_{exp}+3.5$ in Fig. 7.10. This particular time difference was motivated by comparing the optical flow of shadowgraph images (Fig. 7.13) – this will be commented on later. Insofar, the experiment appears advanced with respect to the simulation. A reason for this might be the numerical initial conditions (low level of random noise) that give only a poor description of the experimental layering procedure.

The following two subsection compare typical patterns arising in the shadowgraph images (Sec. 7.4.1), and a quantitative comparison is carried out between the characteristic velocities in the simulated and the experimental shadowgraph (Sec. 7.4.2).

7.4.1 Typical patterns

In the following, we describe and compare characteristic structures seen in the experimental and simulated shadowgraph images. To identify structures reliably, we examined the full time-resolved data since motion and interaction among structures is especially characteristic. Our observations of different structures is listed below:

- **A – Transferred solute at interface** (Fig. 7.10): The transferred solute accumulated in connected outflow zones in the top layer – observed as a stripy pattern at the boundary of convection cells. In the simulation, the convection cells formed a polygonal pattern at the onset of convection. After that, images became more disordered.
- **B – Downwelling plume** (Fig. 7.10): The plumes in the bottom layer were only visible during the first strong Rayleigh instability. They were not observed in the ex-

periment (low contrast). They showed a poor lateral ($x - y$) movement and disappeared with time while growing in radius.

- **C – Eruptions** (Fig. 7.10) were well observed in experiment and simulation due to fast radial growth of an initial nearly circular but later deflected schlieren, see further details in Fig. 7.12.
- **D – Distorted cell boundaries** (Fig. 7.11): Mixed fluid portions in the top layer were deformed by eruptions with tendency to rise from the interface. These portions of solute show: a strong visibility, lateral movement due to eruptions and a long life time.
- **E1 – Upwelling plumes in the bulk** (Fig. 7.11): Their visibility was correlated with the amount of jointly upwelling solute. The visible circumferences kept almost constant in time while rising, unless they approached the top region, see **E2**. Plumes were well observed in experiment due to long life time, i.e. the time between departure from interfacial region and the arrival at the top. They could be exhibited by observing a time averaged shadowgraph image, formally $s_E = \langle s(x, y, t) - \langle s(x, y, t) \rangle_{xy} \rangle_{a < t < b}$.
- **E2 – Upwelling plumes approaching top** (Fig. 7.11): The corresponding circular patterns grew accelerated, no mechanical interaction with structures near the interface (**A,C,D**) was observed.

In addition to the described structures, some experimental features are not reproduced numerically. Firstly, observe the thick stripes aligned with the x -axis (Fig. 7.10) in the experimental images. They were present right after the layering procedure and changed only very slowly. Furthermore, experimental shadowgraph image appeared more crowded with structures.

Dynamics of eruptions

In the present paragraph, a single eruption for both experiment and simulation is monitored. Therefore, consecutive shadowgraph images including interfacial velocity (simulations) or the optical flow (experiment) are plotted in Fig. 7.12. Thereby, the details of this striking convective structure are examined.

For analyzing the experimental shadowgraph image a standard commercial particle image velocimetry (PIV) tool was used "PivView" [241] to calculate an optical flow \mathbf{u}_{of} . Basically, PIV method partitions the image into interrogation regions. Then it calculates a displacement of interrogation regions between successive images such that a cross-correlation functions between displaced [239] interrogations regions is maximized. These optimal displacements are afterward divided by the time between images to yield the *optical flow* \mathbf{u}_{of} .^{IV}

For Fig. 7.12, an exemplary eruption was picked from the experiment and the simulation, each for three consecutive time instances. In general, eruptions proceed in a common sequence, which is accounted in Fig. 7.12 by the selection of time instances.

First ($\tau = 0$), there is the *initialization*, where solute-rich fluid (in the upper phase) that gathered near the interface is abruptly transported towards to the interface (cf. Sec. 7.3.1).

^{IV}For a comprehensive theoretical understanding this procedure is a bit unsatisfactory since the exact algorithm is only partly laid out to the public. However, this method is widely used in experimental fluid mechanics, so, we will proceed.

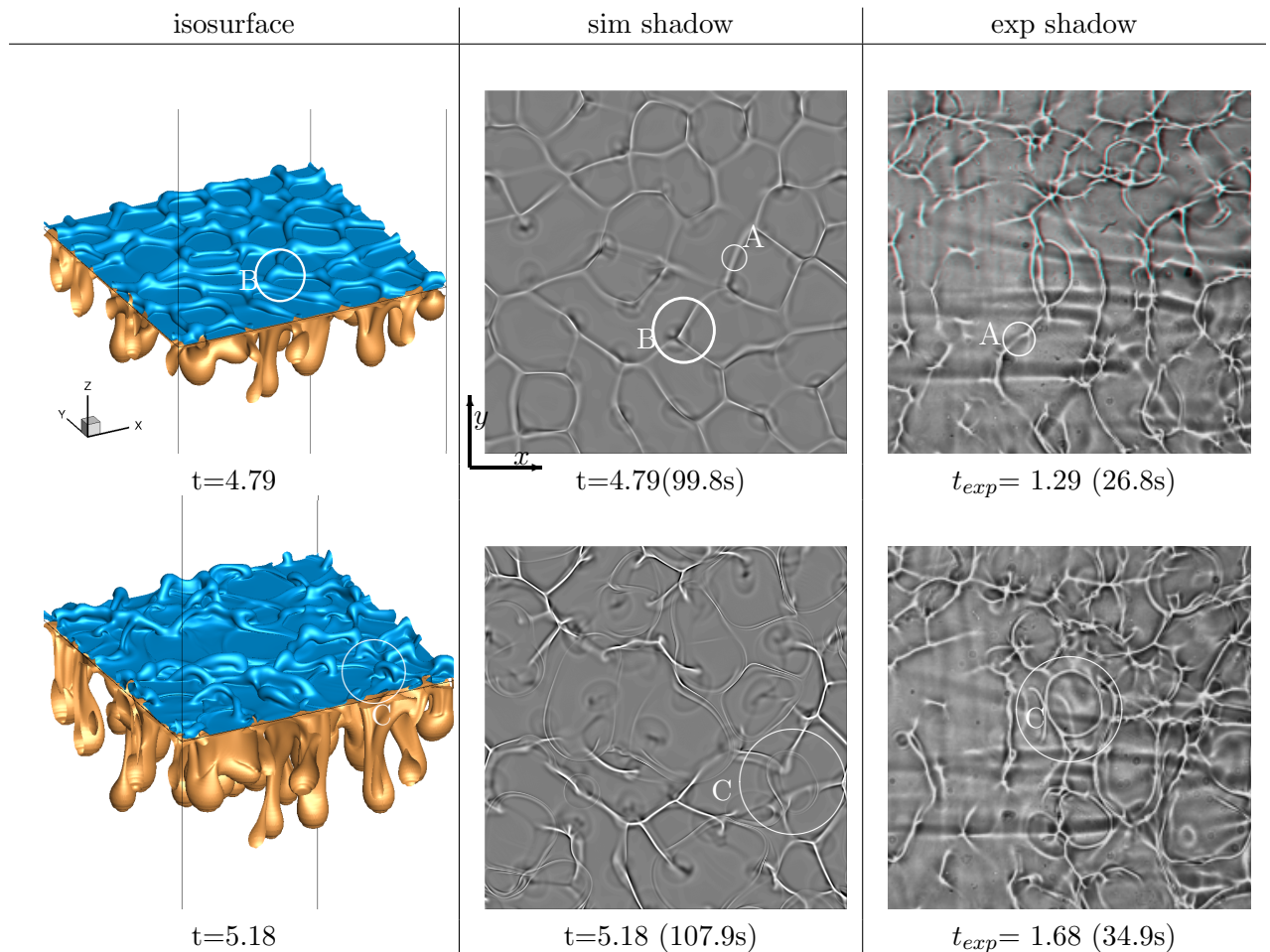


Figure 7.10: Simulated (RM_2at) and experimental pattern (received from *K. Schwarzenberger, personal communication*) for tall cuvette and 2.5vol% initial isopropanol: (left) simulated isosurface $c^{(1)} = 0.97$ $c^{(2)} = 0.2$ in a box of $3(15\text{mm}) \times 3(15\text{mm}) \times 8(40\text{mm})$; (center) synthetic shadowgraph image $s(x,y)$ in a domain of $3(15\text{mm}) \times 3(15\text{mm})$; (right) experimental shadowgraph image from a detail of $15\text{mm} \times 15\text{mm}$. White circles facilitate the interpretations in the text. In this view, the upper phase was combined by sliding it from left to right.

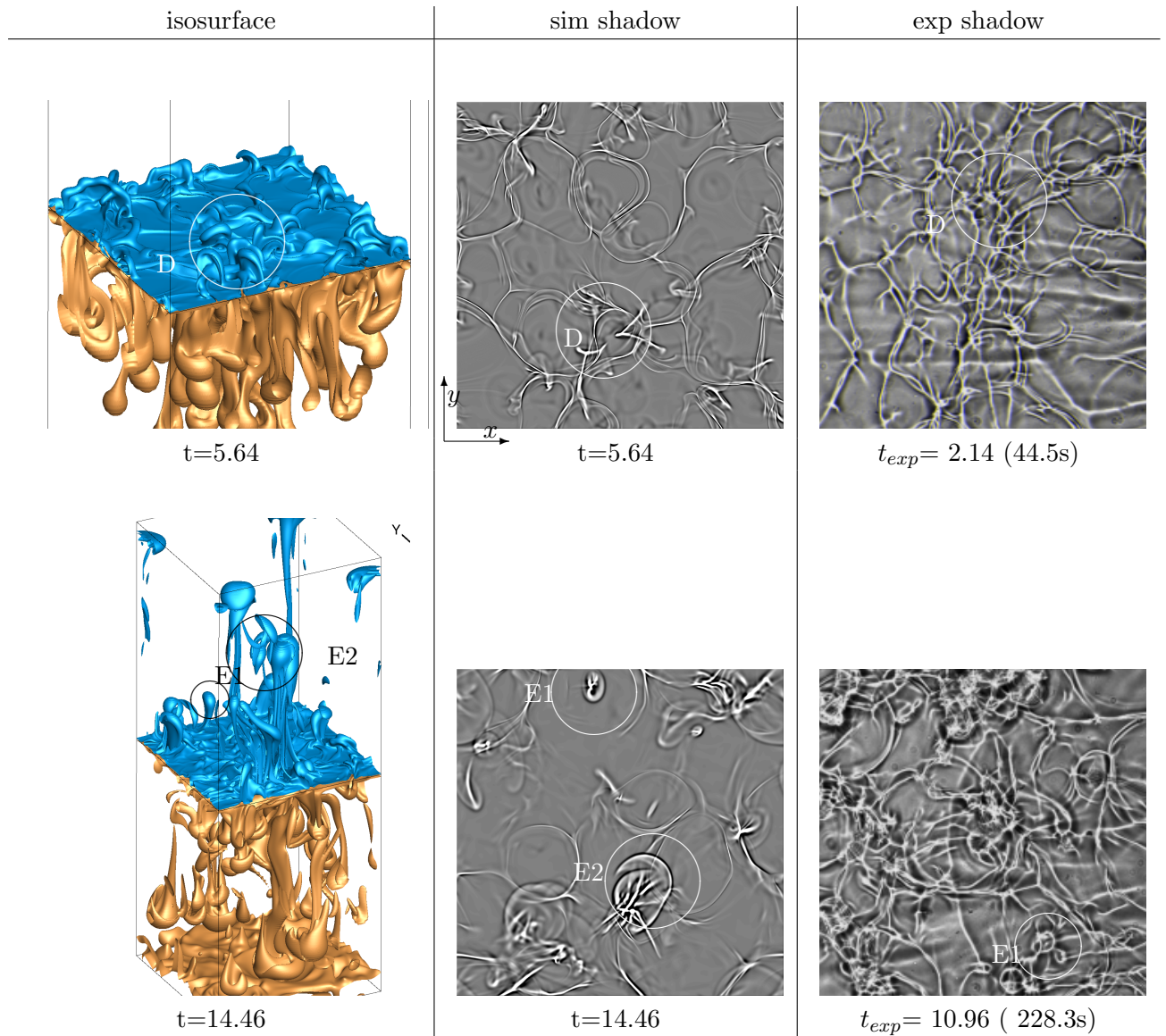


Figure 7.11: Simulated (RM.2at) and experimental pattern (*K. Schwarzenberger, personal communication*) for tall cuvette and 2.5vol% initial isopropanol: (left) simulated isosurface $c^{(1)} = 0.97$ $c^{(2)} = 0.2$ in a box of $3(15\text{mm}) \times 3(15\text{mm}) \times 8(40\text{mm})$; (center) synthetic shadowgraph images $s(x,y)$ in domain of $3(15\text{mm}) \times 3(15\text{mm})$; (right) experimental shadowgraph image from a detail of $15\text{mm} \times 15\text{mm}$. White circles facilitate the interpretations in the text.

For this, concentrate at position marked with the with circle an A letter. This flow towards the interface is seen by the diverging radial motion in both images.

Secondly ($\tau = 0.07$), the spreading of solute accelerates and adopts a state of *maximum speed*. Such a state is seen in Fig. 7.12 at $\tau = 0.07$ in the experiment as well as in the simulation.

Thirdly ($\tau = 0.07$), the eruptions *decay*, i.e. the spreading of solute declines by interfering with the neighboring structures.

7.4.2 Quantitative comparison - optical flow

In the following paragraph, we apply the optical flow method in order to determine a characteristic velocity as function of time.^V The optical flow of shadowgraph images \mathbf{u}_{of} is determined in the middle of the cuvette for a square of $15\text{mm} \times 15\text{mm}$, as in Fig. 7.11. Afterwards the established velocity field is averaged over the domain to get a characteristic velocity at time t , namely $\bar{u}_{of}(t) = \sqrt{\langle \mathbf{u}_{of}^2(x, y, t) \rangle_{xy}}$. Simulations are also represented by applying this method to the synthetic shadowgraph images $s(x, y)$ but also characterized by the interfacial velocity $u_{rms}^{(s)}(t) = \sqrt{\langle \mathbf{u}^2(x, y, z = 0, t) \rangle_{xy}}$

Fig. 7.13 depicts the optical flows and interfacial velocities as functions of time. The data from the tall cuvette (RM.2at) is plotted together in Fig. 7.13(a). To match the onset of convection between experiment and simulation, an offset time $\Delta t = 3.5$ was added to the experimental time $t_{exp} + 3.5$. Note that $t_{exp} = 0$ corresponds to the first contact of phases. All three velocity curves show the same characteristic behavior: vigorous onset with subsequent decline of motion, which is in line with Sec. 7.3.

The experimental flow appears accelerated, approximately twice when compared with the simulated optical flow. Furthermore, optical flow and interfacial velocity (of the simulation) seem to be well correlated, but interfacial velocity was roughly twice as high as the simulated optical flow.

A similar behavior was observed in the low cuvette Fig. 7.13(b). Two independent experiments are displayed. Note that in the low cuvette, the layering procedure was changed: it is done by tilting the cuvette around 90 degrees, cf. Fig. 7.2; here start of tilting is defined as $t_{exp} = 0$. To match the onset of convection in this setup, $\Delta t = 4$ was added to the experimental time.

^V This method is already applied in Sec. 5.3.5 to study Marangoni cell convection.

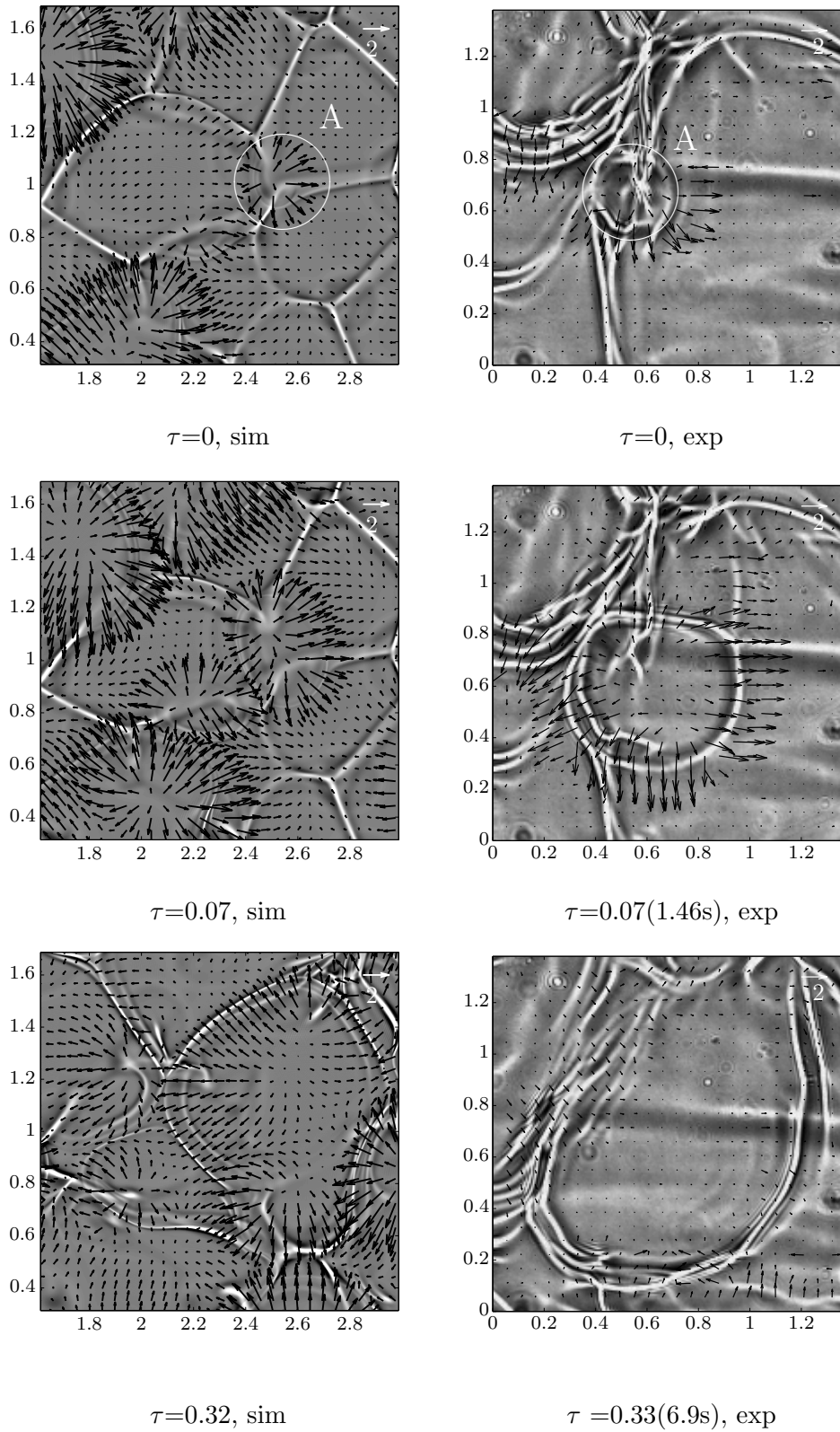


Figure 7.12: Development of eruption: (left) Shadowgraph images for RM_2at with interfacial velocity $\mathbf{u}(x, y, z = 0, t)$ and (right) optical flow \mathbf{u}_{of} (experiments, provided by *K. Schwarzenberger, personal communication*). Both simulated and experimental image have dimension of 1.37×1.37 (6.9mm \times 6.9mm). The simulated images (left) start at $t=5.08$ ($\tau = 0$) and the experimental at $t_{exp}=5.55$ (115.6.s), thus, τ refers to the relative time which is matched.

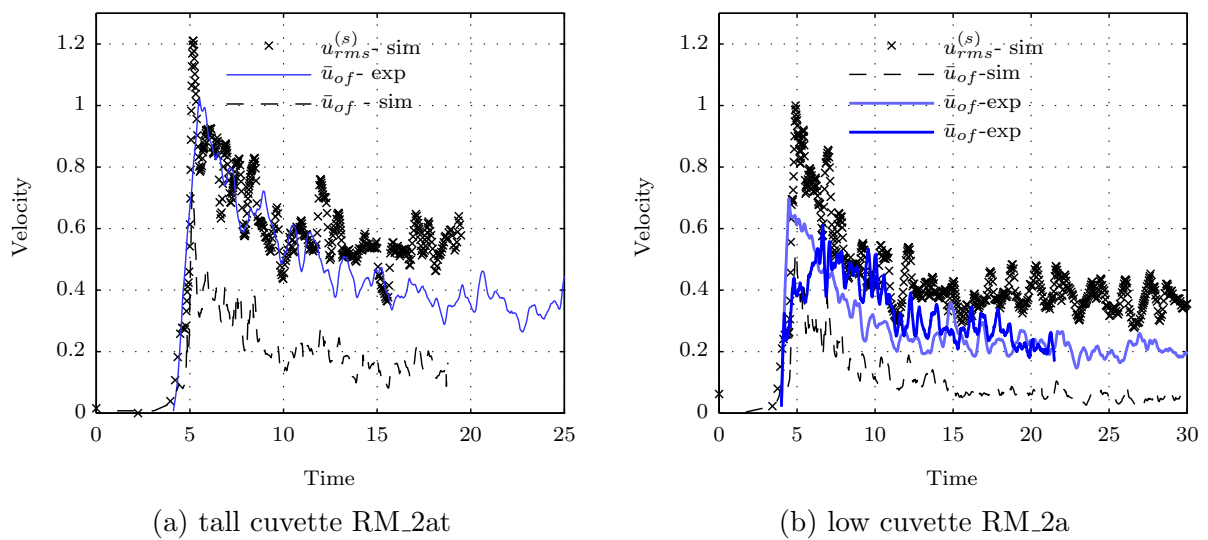


Figure 7.13: Comparison of optical flow from simulations and experiments as well as the interfacial velocity from the simulations: (a) tall cuvette (RM_2at) with offset time $\Delta t=3.5$, (b) low cuvette (RM_2a) with $\Delta t=4$. So "Time" refers to "Time" = t for the simulation and "Time" = $t_{exp} + \Delta t$ for the experiments. Velocity and time is nondimensionalized by $T_{vis} = 20.83s$, $U_{vis} = 0.24$ mm/s, respectively. Optical flow data is provided by *K. Schwarzenberger, personal communication*.

7.5 Parametric study

7.5.1 Variation of concentration

The present section studies the impact of the initial concentration on the development of convection. The so far studied case RM_2a (2.5vol%) is supplemented by simulations related to 1vol% (RM_1a) and 5vol% (RM_3a). In terms of the numerical parameter, this amounts to a change of Grashof and Marangoni number (see Tab. 7.3). However, the relative strength between Marangoni and Rayleigh effect is constant in terms of the dynamic Bond number [$Bo_d = Sc^{(1)}G/Ma$] which is $Bo_d = 2.25$.

Before presenting the numerical data, we like to recall our remarks of Sec. 3.1. Namely, that the PM obeys a scale invariance, if either the Marangoni or the Rayleigh effect are excluded and no outer scale (like layer heights) impacts the dynamics. For the reference configuration, it has been shown (Sec. 7.2) that initially Rayleigh convection evolved from an unstable density stratification localized near the interface (see Fig. 7.3). In this view, we try to account for concentration changes by the noted scaling; this scaling for length, time and velocity units reads

$$L \propto c_0^{-1/3}, T \propto c_0^{-2/3} \rightarrow U \propto c_0^{1/3}. \quad (7.2)$$

Of course, in the view of yet presented data, such scaling fails owing to the violation of its premises: the impact of Marangoni convection (eruptions) and the complete coverage of bulk volumes by solutal plumes. Nevertheless, we will see that especially time can be reasonably scaled. For scaling, the relative Grashof number G_r is employed. It is the actual Grashof number normalized by the one for the reference configuration $G_r = G / 2.83 \times 10^3 \in \{0.4, 1, 2\}$.

Fig. 7.14 combines several integral quantities over time. In (a), the top layer mean concentration without scaling depicts that mass transport is enhanced with growing initial concentration, which seems natural since forces are increased. When the naive Rayleigh scaling in a deep layer regime is applied, i.e. $\langle c^{(2)} \rangle_{xyz} (\tau G_r^{-2/3}) \propto G_r^{-1/3}$, see (b), onset times perfectly match but the mass transfer is distinctly underestimated, which is certainly caused by the Marangoni effect.

In the second row of Fig. 7.14(c,d), characteristic velocities are depicted; they increase with initial concentration. Here we applied the Rayleigh scaling for time, which lets the onsets of convection nicely fall to the same scaled time. However, for the actual value of velocity measures, a power law behavior is suggested by simply fitting to the data: for the rms velocity $u_{rms} (\tau G_r^{-2/3}) \propto G_r^1$ and the interfacial velocity $u_{rms}^{(s)} (\tau G_r^{-2/3}) \propto G_r^{1.2}$.^{VI}

In the last row of Fig. 7.14(e,f), the averaged concentration gradient at the interface (e) and the enhancement factor (f) are plotted. Again, a power law scaling is proposed by roughly fitting the data. In the present context of transport (1) \rightarrow (2), the enhancement factor relates the actual top layer mean concentration with the one for pure diffusion, formally

$$R = \frac{\langle c^{(2)} \rangle_{xyz}}{\langle c_{diff}^{(2)} \rangle_{xyz}} \quad (7.3)$$

We refrain from introducing a mass transfer coefficient (or Sherwood number) based on the concentration difference between layers – as often done in such a context – since this would

^{VI}Note that the prediction for a deep layer (cf. Sec. 3.1) with pure Marangoni is $u_{rms}^{(s)} (\tau G_r^{-2}) \propto G_r^1$. For pure Rayleigh it is $u_{rms}^{(s)} (\tau G_r^{-2/3}) \propto G_r^{1/3}$.

anticipate that the actual mass flux does not depend on the detailed distribution of solute in the system, but rather on a single number, i.e. a concentration difference, which seem not the case when the poorly mixed top layer is regarded. However, we could still define a Sherwood number as in Ch. 5 by relating the actual mass flux versus the one for pure diffusion.

Qualitatively, the development of convection proceeded similar for the three cases, i.e. as presented for the reference case in Sec. 7.3. However, we expect that if the initial concentration is further reduced, the vertical size of buoyant structures is more restricted by the finite layer size and so dynamics may also qualitatively change.

7.5.2 Pure Rayleigh convection

This section presents simulations without Marangoni effect (RM.2b see Tab. 7.3), i.e. setting $Ma = 0$, noted as Rayleigh convection (RC), but otherwise keeping parameters from RM.2a.

Fig. 7.15 shows four integral quantities developing over time derived from the RC simulation. The evolution is divided by the marked events visible in the interfacial concentration gradient [Fig. 7.15(a)]: (I) Onset of Rayleigh convection in the bottom layer with peak around $t \approx 6$; (II) Onset of Rayleigh convection in top layer $t \approx 13$; (III) Anticipated half-life time of mass transfer (not simulated so far). This interpretation of a "staggered" (first bottom then top) onset is supported by isosurfaces of concentration in Fig. 7.16. Let us comment on further observation in the form of the list below.

- Onset in the RC case appears a little later, which is further discussed in Sec. 7.6.1.
- For RC, there is a synchronized emission of plumes in the top layer at onset [Fig. 7.16(b)], which is disturbed by eruptions for RMC.
- For RC, velocity is distinctly larger in the bottom than in the top layer, and velocity does not peak at the interface, cf. Fig. 7.15(b) versus Fig. 7.9(b).
- The energy balance for RC [Fig. 7.15(c)] is augmented with the hypothetical interfacial power ω_s (using Ma from RM.2a). It would support RC until $t \approx 7$, but afterwards, when convection in the top layer started, interfacial forces would act against RC.
- The Marangoni effect increased mass transfer, see Fig. 7.15(d).
- For RC, structures appeared more persistent in time, i.e. mainly fragmented roll cells that slowly change their orientation and emit solutal plumes were observed. These structures can be observed in the isosurfaces (Fig. 7.16) and the synthetic shadowgraph images (Fig. 7.17).

This comparison again documents the outstanding role of the Marangoni effect.

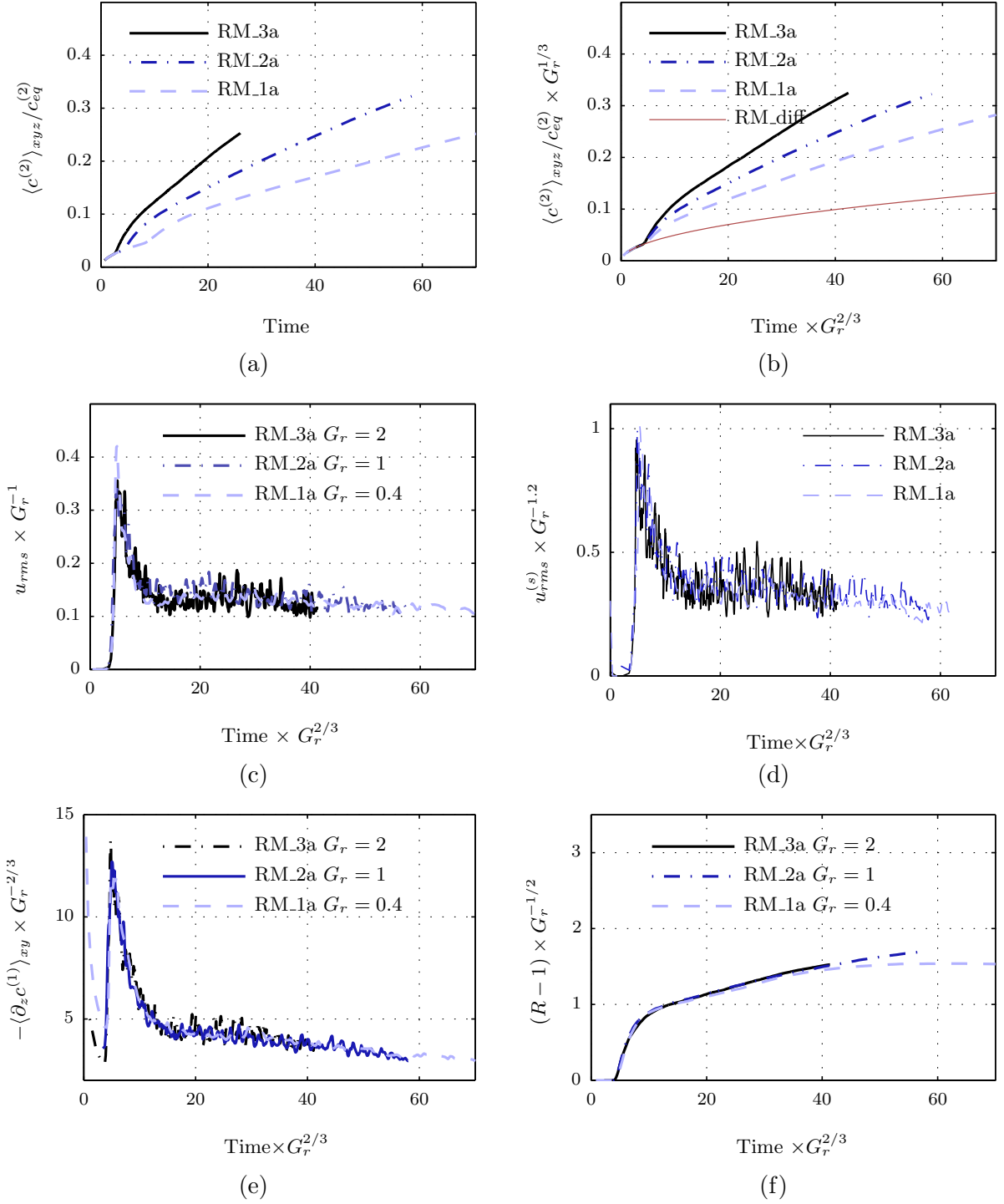


Figure 7.14: Comparison of simulations with changed initial concentration, thus we fix $Bo_d = Ra^{(1)}/Ma = 2.25$: (a) unscaled averaged concentration in the top layer normalized with global equilibrium value, (b) scaled concentration in the top layer normalized with global equilibrium value, (c) scaled rms velocity, (d) scaled interfacial velocity, (e) scaled interfacial concentration gradient of the bottom layer, (f) scaled enhancement factor Eq.(7.3).

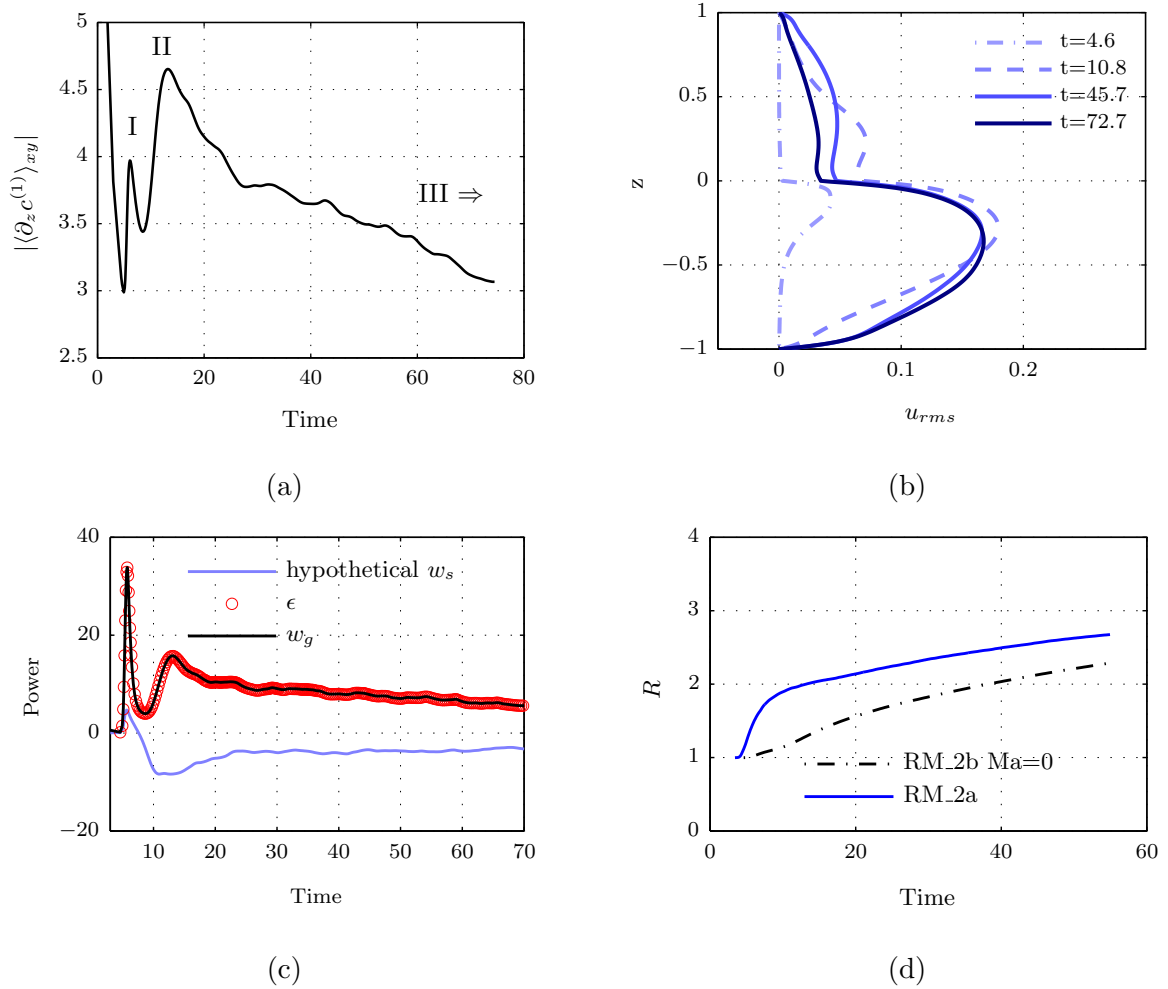


Figure 7.15: Pure Rayleigh convection RM.2b: (a) interfacial concentration gradient with marked events noted in the text; (b) rms velocity profiles for four different times that approximately correspond to isosurfaces in Fig. 7.16; (c) energy budget according to Eq. (C.10) while setting $\text{Ma} = -1.69 \times 10^6$ artificially, (d) enhancement factor according to Eq. (7.3) comparing RC and RMC case.

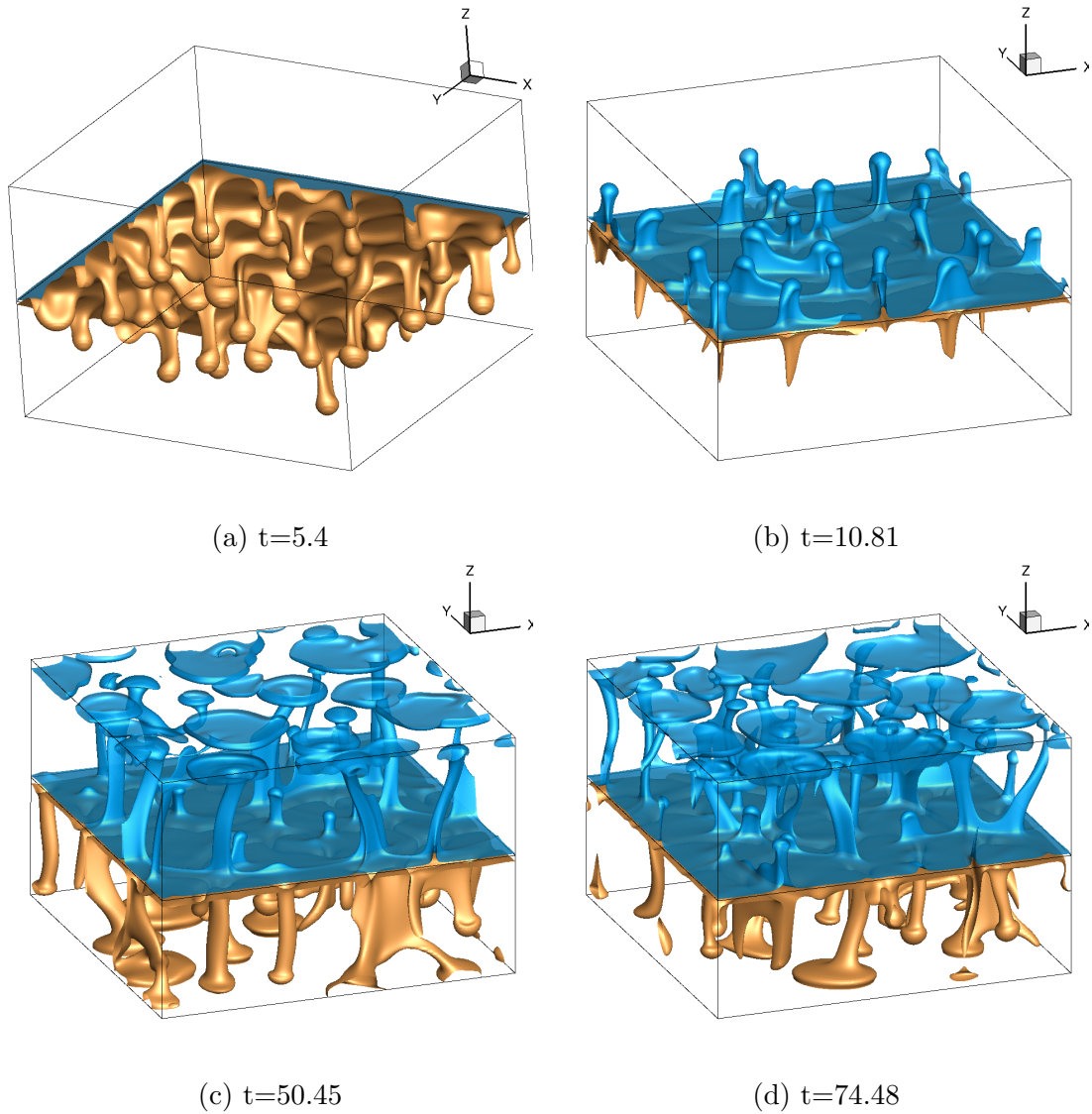


Figure 7.16: Pure Rayleigh convection RM_2b: isosurfaces of concentration $c^{(2)} = 0.45$ fixed over time and $c^{(1)} = 0.9$ (a,b), $c^{(1)} = 0.83$ (c), $c^{(1)} = 0.77$ (d).

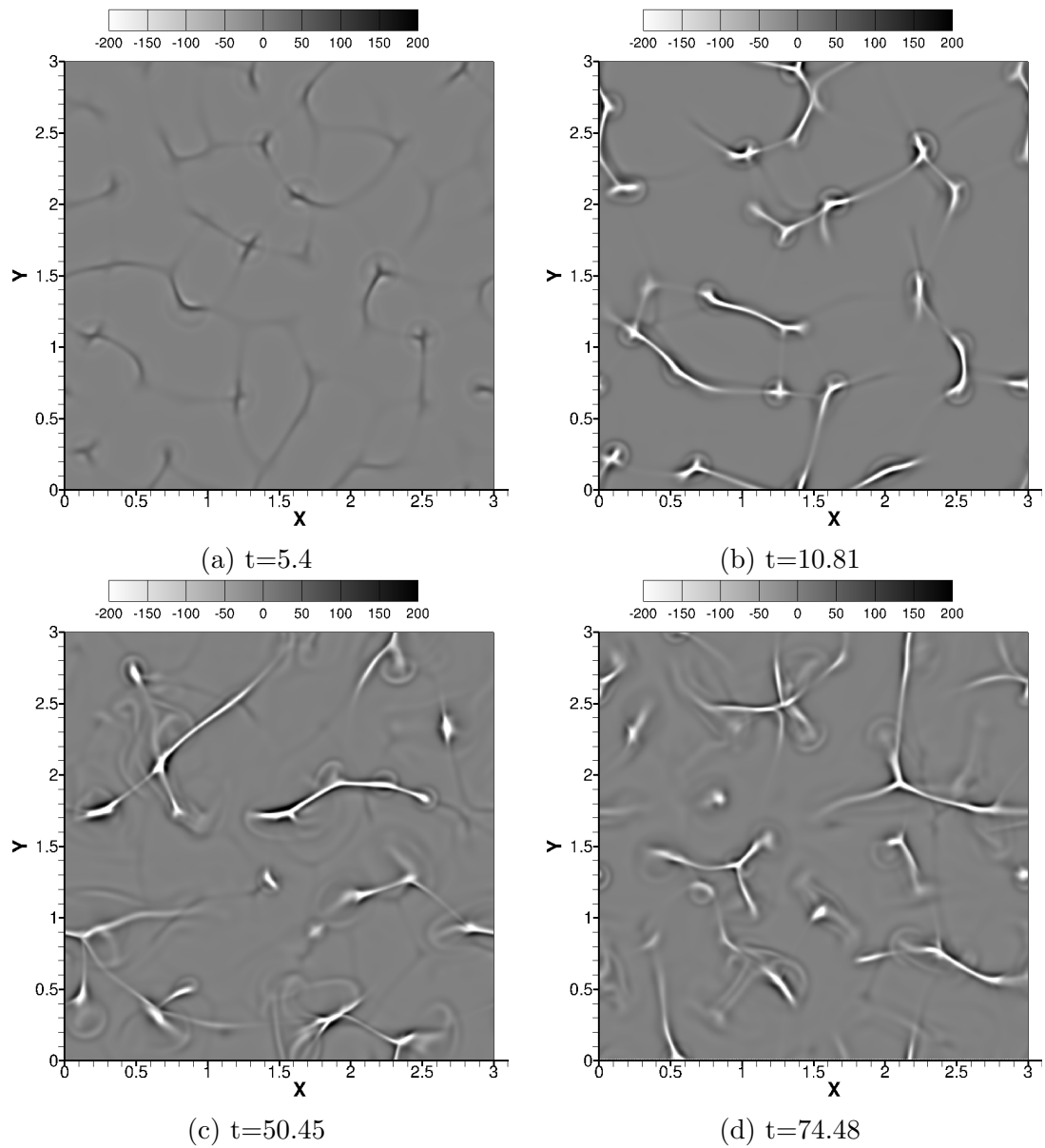


Figure 7.17: Pure Rayleigh convection RM.2b: synthetic shadowgraph images $0.5s(x, y)$ (sic) [Eq. (5.15)] for four consecutive times.

7.5.3 Two-dimensional simulations

As a last class of simulations, any variation in the y-dimension was disregarded by 2D simulations, namely RM_2a2d, RM_3a_2d (RMC) and RM_2b2d (RC), cf. Tab. 7.3.

Figure 7.18(a,b) compares the development of RMC in 2D and 3D. The velocity was higher (on average) in the 2D than in the 3D case [Fig. 7.18(a)]. In the early course, the transport of mass proceeded faster in 3D, i.e. until $t \approx 15(RM_2a)$ $t \approx 30(RM_2a)$. Afterwards, mass transport was faster in the 2D configuration [Fig. 7.18(b)].

The disregard of one dimension allowed us to simulate a much larger time range of equilibration owing to huge savings in computing resources. Fig. 7.18(c) shows the mean concentration normalized with the final equilibrium value for the RC and RMC case. Two interesting features might be noted: (1) For a long time span, mass transport proceeded faster in the RMC, namely up to $t \approx 500$. Moreover, half of solute is transferred at $t \approx 100$ (RM_2a2d) and $t \approx 140$ (RM_2b2d). (2) But after $t \approx 500$, less solute was transported in the RMC case. In this context, the viscous dissipations are plotted in Fig. 7.18(d). Note the decreasing difference between RC and RMC with time. Consequently, it seems that the damping of Rayleigh convection by the Marangoni effect – as monitored in Fig. 7.15(c) by negative hypothetical interfacial work – outperforms the increased mixing via eruptions in the late stage.

7.6 Discussion

During the presentation of results, several interpretations and potential connections have been already given. The present section will discuss some of the results more in detail in three subsections: the onset of convection, the features of eruption, and the deviation between experiment and simulation.

7.6.1 Onset of convection

In the earlier Sec. 7.3.2, the onset of convection (RM_2a_onset) has been characterized in terms of onset time and typical length scales. The current section relates these finding with the predictions of Kim *et al.* [107].

Kim *et al.* described the transport of a solute from a semi-infinite liquid layer into a gaseous phase with fixed interfacial concentration. They treated the instability due to the Rayleigh effect (i.e. without Marangoni effect) and proposed a critical time τ_{on} for which convection is expected to appear and a related wavelength λ_{on} (by means of a linear stability method). By applying their findings to the bottom layer, we find that

$$\tau_{on} = a \left(\frac{-GD^{1/2}H}{(1 + D^{1/2}H)\sqrt{Sc^{(1)}}} \right)^{(-2/3)}, \quad (7.4)$$

$$\lambda_{on} = \frac{2\pi}{b} \left(\frac{-Ra^{(1)}D^{1/2}H}{1 + D^{1/2}H} \right)^{(-1/3)}. \quad (7.5)$$

The parameters a, b depend on the whether a free slip interface ($a=4.21$ $b=0.149$) or a rigid boundary ($a=7.38$ $b=0.195$) is assumed; the constant concentration at the interface was approximated by the prediction of the pure diffusion problem, cf. Eq.(3.80). For the present system the rigid case seems more suitable, because of the high viscosity in the top layer. The

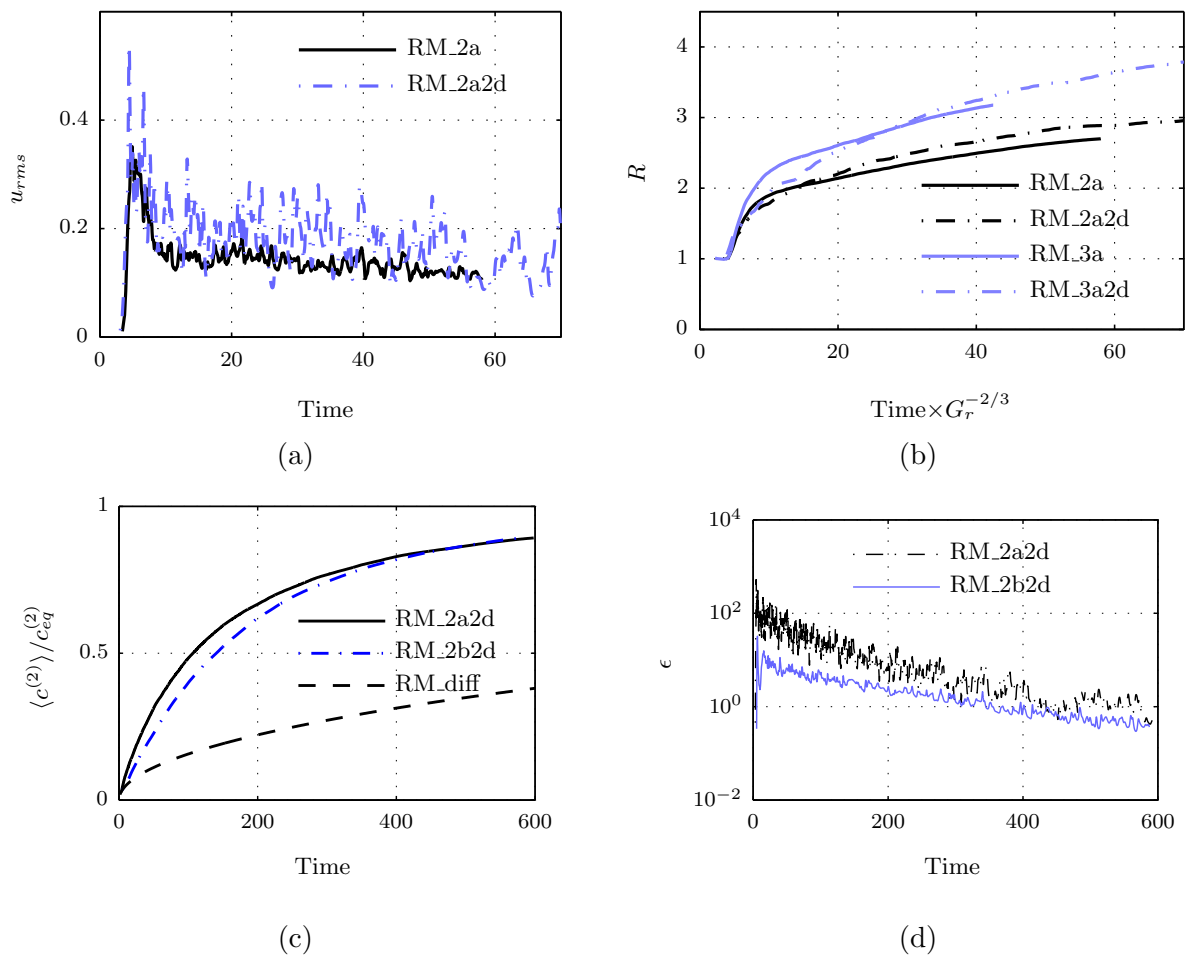


Figure 7.18: Comparison of two and three-dimensional simulations: (a) rms velocity , (b) enhancement factor, (c) normalized, averaged concentration in the top layer, (d) viscous dissipation ϵ .

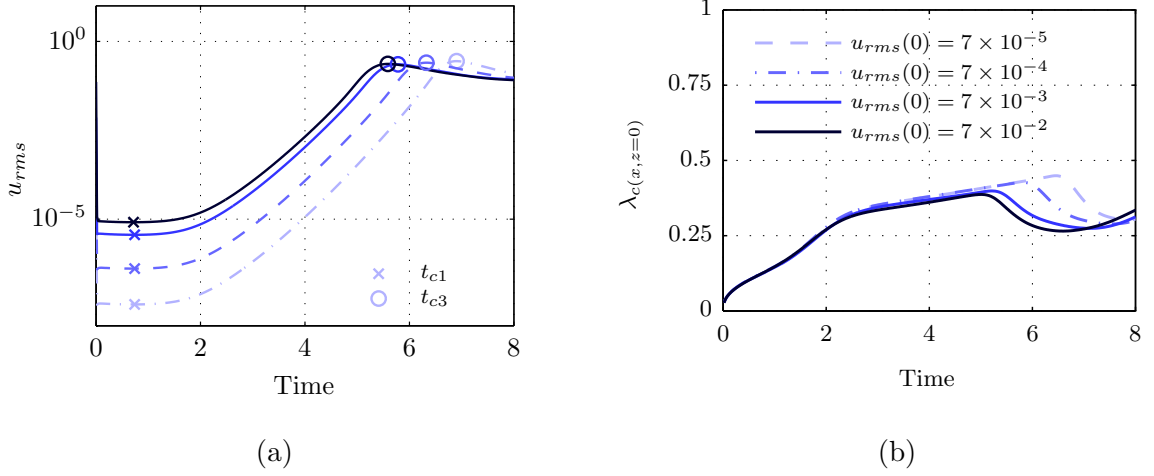


Figure 7.19: Onset of convection for RM_2b_onset: (a) rms velocity over time with derived onset times $t_{c1}=0.74, 0.74, 0.74, 0.72$ and $t_{c3}=6.90, 6.32, 5.78, 5.59$.

nondimensional time and length for case RM_2b is $\tau_{on} = 0.88(0.50)$ $\lambda_{on}=0.30(0.40)$ with rigid (free) interface condition.

This prediction fits reasonably well to the onset times measured in the RM_2a configuration (cf. Fig. 7.6). There it has been found that the first net growth is around $t_{c1} \approx 0.7$ with related wavelength $\lambda \approx 0.4$. Our choice to compare analytical predictions with the first net growth t_{c1} seems natural to us since predictions of Kim *et al.* are based on a linear analysis. Although the analysis of Kim *et al.* does not account for the presence of the top layer neither in the momentum balance nor the mass balance, it seems to give a reasonable prediction.

The impact of the Marangoni effect is further examined by simulations in line with the procedure applied in Sec. 7.3.2, but now for the case of pure RC (RM_2b_onset). Once again, the rms velocity and the dominant mode of interfacial concentration are monitored for different initial amplitudes of velocity (Fig. 7.19). For RC, the first net growth of velocity is observed at a similar time $t_{c1} \approx 0.7$ than in the RMC (a bit later). In the RC case, times (t_{c1}) dependent less on the initial amplitudes. However, the peak in velocity $t_{c3} \approx 6$ was monitored roughly one time unit later, possibly explained by the absence of the early supporting effect of Marangoni convection [see Fig. 7.15(c) positive interfacial work].

Kim and coworkers [107] pointed out that their predicted onset time τ_{on} should be multiplied by a *fitting factor* of 4 to reflect a measurable onset time in an experiment. Indeed, in the view of our data, we can certainly conclude that the instability at t_{c1} is hardly detectable in an experiment due to simple lack of sensitivity of typical measurement devices. However, without further knowledge of the initial state and the specific experimental method that defines the onset of convection, any time between t_{c1} and t_{c3} could be the outcome of an experiment, which would lead to a potential fitting factor between 1 and 9 for the present configuration (instead of exactly 4). Thus, for the author, it seems only possible to predict the first time for the "observation" of convection in a range of fitting factors, unless the specific non-linear effects of an experiment (initial state, detection) are taken into account.

7.6.2 Mechanism of eruptions

This section explains the different interactions between transport processes that are responsible for eruptions.

In previous sections, the appearance of eruptions was documented for our reference configuration (Sec. 7.3.1) and the experimental setup (Sec. 7.4.1). In Fig. 7.20, the mechanism leading to this kind of structure are outlined via two steps:

(1) Fig. 7.20(a) "build up" sketches Rayleigh convection with the departure of mixed fluid in the bottom layer. In Fig. 7.21, we monitored a situation as sketched in the Fig. 7.20 with profiles of the concentration field and the vertical velocity field at the center of an eruption. The "build up" corresponds to profiles at $t=3.97, 4.22$. Here, a relative low concentration is seen under the interface and a thick solute rich sheet above the interface.

(2) Fig. 7.20(b) "burst" shows the action of the Marangoni effect acting on the solute distribution, which corresponds to profiles of Fig. 7.21 at times $t=4.56, 4.69$. See also vertical cuts with concentration in Fig. D.2 from the appendix.

In this view, eruptions might be also regarded as a kind of oscillation due to the "sign" change in the velocity and the surface tension gradient, thus a change from Rayleigh to the Marangoni effect. However, the oscillation shown here are certainly more involved than those predicted from a linear stability analysis [50, 164] of a steady conduction state since the cause for the spreading is the peculiar distribution of transferred solute, which is a result of the Rayleigh instability. So is it unclear and should be examined in further studies, if eruptions could be predicted by stability methods.

From the presented data, one is not able to predict under which circumstances eruption are to be expected or when eruption have a peculiar effect on Rayleigh convection, except earlier classification of types in Fig. 2.3. However, the probability of eruptions seems to increase with growing Schmidt number and low dynamic Bond number $Bo_d = Ra/Ma$ since these are peculiar properties of the solutal setup compared to the thermal one, for which the author is not aware of such eruption regime [100, 164]. The comprehensive experimental data of Schwarz (see Tab. 1 in [198]) outlines that in most liquid/liquid mass transfer system of type III eruptions appear. Also, note that a similar coupling between Rayleigh and Marangoni convection at dissolving drops has been experimentally observed by Agle et al. [2–4], but is not yet fully understood. They tuned the Marangoni effect by including different surfactants into the continuous phase.

7.6.3 Reproduction of experiments

In Sec. 7.4, we attempted to reproduce specific experiments. Our main findings were that structures could be qualitatively reproduced, but simulated velocities appeared clearly smaller than in experiment. We like to note three main reasons for this deviation:

(1) *Physico-chemical modeling*: The uncertainty of material properties (see Sec. B.2), especially the estimation of diffusivities introduces an error to the calculation. Also note that the dependence on the interfacial tension $\sigma_{ref}\alpha_c$ may include a large error since it relies on the measurements of Schwarz. The specific surface tension difference employed for calculating material properties was only 0.2 mN/m (see Eq. B.12) and Schwarz noted [198] a sensitivity of his measurement device of 0.1mN/m. So without taking into account the several other uncertain parameters, a relative error of 50% for Ma or even more has to be expected.

Moreover, an impact on the deviation is inherent to the model since transport properties

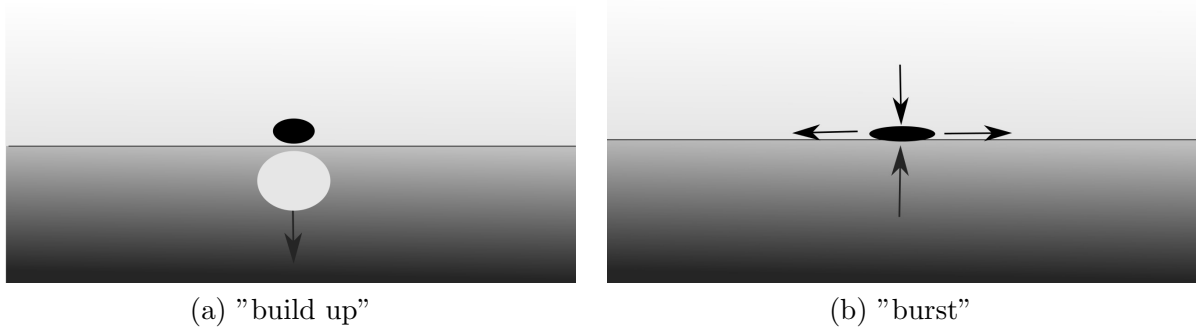


Figure 7.20: Sketch to explain the nature of eruptions: Dark color represents high concentration of a solute that lowers density and interfacial tension: (a) Rayleigh convection in both layers, bottom layer fluid is more mobile with sinking dense fluid. (b) Fluid portion poor in solute has departed from the interface, but solute-rich fluid (black ellipse) is still localized near the interface to trigger Marangoni convection.

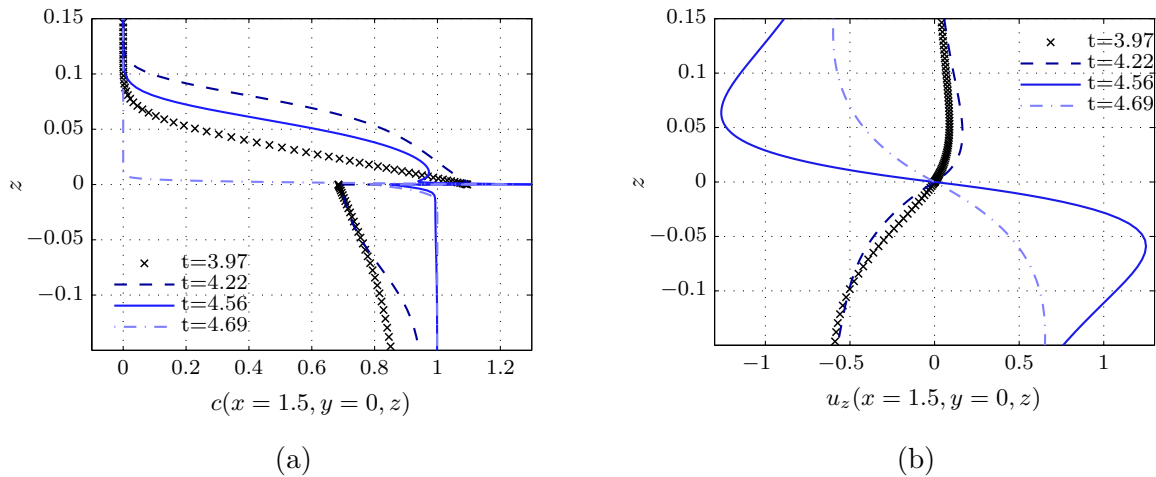


Figure 7.21: Simulation RM_2a, development of eruptions depicted by: (a) Concentration profiles and (b) vertical velocity profiles at $x=1.5, y=0$. Interfacial concentration evolves as $c^{(1)}(x = 1.5, y = 0, z = 0, t) = 0.685, 0.693, 0.849, 0.787$ in order of increasing time.

(as $\nu^{(i)}, D^{(i)}$) depend on the composition of phases in general. Such uncertainties could be resolved by including dependencies into the physical model. In turn, this would require using other material systems that are better known (e.g. toluol-water-acetone [81,161]) or additional measurements on the current system were required.

However, when such compositional effects are included, then one may also model the full composition, i.e. including additionally a transport equation for water or cyclohexanol, which in general requires to account for the cross effects in diffusion between species [225]. Consequently, one may account for the changes in partition equilibrium [192] and the variation of phase volumes, which would demand to solve for a moving interface.

The experimental setup is composed of two finite sized cuvettes, whereas we have solved a model with periodic boundary conditions. Generally, the solid boundaries could be included into the physical model with different levels of physical – and consequently – mathematical complexity, but then also, the dynamics near the boundary should be observed experimentally. For instance, the wetting properties [211] of the cuvette walls had to be controlled or the actual geometry of the three phase contact line needs to be known from experimental observation (it could be pinned at the edges of both cuvettes). Already Berg&Morig [20] noted that the meniscus formed at the solid boundary is able to trigger buoyant convection.

Another physical effect neglected in the present model is the heat of solution, which certainly takes place in the current system. For instance Perez de Ortiz & Sawistowski [174] observed that the partially miscible system of water and cyclohexanol shows a heat-of-solution-driven Marangoni instability, when water is transported to the organic as well as when cyclohexanol is transported to the aqueous phase. Certainly, all those named physical mechanism have a part in the net deviation, but it is unclear which is the most significant one.

(2) *The layering procedure* is another source for deviations, i.e. the initial state of the simulations does not represent a state in the experiments. Two strategies for the solution of this problem will be noted below.

First, the layering procedure could be modeled. Exactly, this would require solving the full cuvette geometry with an interaction of four phases: air, cuvette material, aqueous phase, organic phase. Or one may do a simplified model of the layering, which would require a combined experimental and theoretical study.

Secondly, a state of the system could be measured. This would demand the knowledge of the fully three-dimensional concentration field (while velocity is not needed due to the low Reynolds numbers), which would mean a considerable experimental effort. Or the experimental geometry is changed such that a constant concentration boundary condition could be used, which may lead to a statistical independence from the initial state, cf. experimental setup in [82]. Another strategy is to approximate the experimental shadowgraph s_{exp} image by setting a corresponding concentration field c such that it minimizes an appropriate functional E

$$E[s_{exp}(x, y) - \int_{[-1,d]} \Delta_2 c(x, y, z) dz], \quad (7.6)$$

that measures the deviation. The solution of such an inverse problem requires further "ad-hoc" constraints to derive a physical reasonable concentration field and very carefully prepared experimental data.

(3) *Representation of shadowgraph images* might be improved. Several optical effects are not modeled by Eq. (5.15) [160]. For instance, the index of refraction as a function of the

composition could be modeled (would require experimental characterization), or the impact of interfacial deformation may be taken into account. From an experimental point of view, optical artifacts should be reduced, and optical resolution increased.

One may also think of not using a commercial tool for deriving an optical flow, but rather using a strategy that can be better described theoretically. For instance, the optical flow of an image sequence $I(x, y, t) \in \mathbb{R}$ can be defined as the vector field (\mathbf{u}_{of}) for which

$$\|\partial_t I + \mathbf{u}_{of} \cdot \nabla_2 I\| = 0 \quad (7.7)$$

holds. Without further constraints, this provides not a unique definition [91] for \mathbf{u}_{of} . Now depending on the application, different constraints could be used, e.g. the minimization of the smoothness $\Delta_2 \mathbf{u}_{of}$.

7.7 Conclusion

With respect to the reported data and the central questions (R_1 - R_4) pointed out in Sec. 2.4.2 the following conclusion can be drawn:

(R_1) Our simulations show that the experimentally observed eruption regime is well predicted by the PM. Beside recent experimental observation that have been included in our presentation, also former observation of Schwarz [197, 198] are in qualitative agreement with our simulation.

(R_2) It is found that eruptions are triggered by the Rayleigh convection, causing a distribution of solute near the interface that is susceptible to the Marangoni effect.

(R_3) Simulations successfully reproduced key experimental observations in the water + isopropanol / cyclohexanol system. Especially, the chaotic appearance of the shadowgraph images – sometimes noted as interfacial turbulence – could be interpreted with the help simulations. A reproduction of the early experimental phase was not achieved since onset of convection and the layering procedure act on similar time scales, and the complex process of layering cannot be described by the PM. By analyzing the shadowgraph images in terms of optical flow, experiments show higher "interfacial" velocities, approximately twice the simulated value. A clear physical reason could not be identified due to the complexity of the physical system, the uncertainty of material properties and the numerous simplification in the PM, which are, however, necessary for an efficient numerical treatment.

(R_4) Simulations with varied initial concentrations suggested that the change in initial concentration can be partly accounted for by a scale transformation of time $T \propto c_0^{-2/3}$ for an early stage of mass transfer. This can be explained by our earlier consideration in Sec. 3.1. Physical quantities (e.g. transferred mass, rms velocity at the interface) at the scaled time seem to obey power laws with respect to Grashof numbers, whose explanation could be a vital issue for further work. In this respect, it seems a valuable task to study the "extreme" cases for which a prediction seem feasible, i.e. deep layers with only Rayleigh convection or a steady transfer with fixed concentration at the boundaries.

Furthermore, the simulations describe only one-third of the full equilibration process in the 3D setup for the experimental parameters (in the low cuvettes), which could be extended by spending more computational resources.

Simulations without the Marangoni effect (so pure Rayleigh convection) showed no eruptions and a retarded transfer of solute. However, evidence was also found that mass transfer could be retarded –in contrast – by the Marangoni effect for lower concentration differences. It is left open for further works, to determine additional requirements for such eruption regimes.

Chapter 8

Conclusion and Recommendations

Conclusion

In the first and largest part of this thesis, we have theoretically examined a case of stationary Marangoni instability under a stabilizing density stratification (Fig.2.3, type I). Especially, we employed the ternary system made of cyclohexanol and water with butanol initially dissolved in the lighter organic phase. Taking into account Linde's classification of patterns and former experimental observation by Schwarz, a comprehensive numerical study was carried out to reproduce and explain experimental observations.

Simulations based on the PM successfully reproduced a two-level hierarchy of convection cells that consist of large, slowly growing cells (called RC-IIs according to Linde's classification), which host smaller rapidly changing cells (named RC-Is). The main hypotheses of Linde (Sec. 2.4.1) regarding patterns in type I systems could be effectively applied. Nevertheless, his last hypothesis L_4 that the integral activity of convection may fluctuate on a large time scale in "cycles" was not encountered in the present material systems.

The experimental results of Schwarz and Schwarzenberger & Eckert have agreed in most aspects with our simulated results. Deviations were within a range that could be expected from the uncertainty of material properties and experimental conditions. In this way, it has been demonstrated that multiscale flow patterns can indeed be described by the PM, although a considerable amount of numerical resources had to be spent.

The formation of hierarchical patterns has been explained by the action of coarsening and local instability. It has been reasoned that the RC-IIs grow as a result of advancing equilibration of the butanol distribution (coarsening). The RC-IIs induce a distribution of solute near the interface that is susceptible to a continuous creation of smaller Marangoni cells (local instability).

By deriving new stability results, we attempted to predict the onset of convection by means of its time instant and characteristic wavelength. The predictions from our frozen time analysis underpredict the simulated onset times but were able to predict approximately the characteristic size of convection cells at onset. The predictions seemed to improve when it is required that the size of the concentration boundary layer be similar to the perturbation wavelength.

If buoyant effects and a geometrical confinement can be excluded, a change in the Marangoni number Ma could be accounted for by a scale transformation of the time unit $\tilde{T} \propto Ma^{-2}$ and the length unit $\tilde{L} \propto Ma^{-1}$. Parametric studies probed the deviation to this scaling laws by

systematically probing its requirements and comparing the respective simulations to a generic simulation (G.1.1), where requirements are fulfilled. By this, it has been found that non-zero Morton numbers perturb the application of scale transformation, except at the early time of convection. Later, it leads to a reduction of mass transfer.

For both situations of lateral and vertical confinement, a departure from the generic development (noted as deep layer regime) has been observed if convection cells reach the typical outer length, which is manifesting by a lower rate of mass transfer. For vertical confinement, this departure started approximately when one-half of possible solute was transferred through the interface. However, care has to be taken with a generalization of these findings to other material system; their behavior may especially depend on the Schmidt number.

Additionally, we performed simulations in the framework of a 2D Hele-Shaw model and compared these to experiments that were provided to us for four different configurations. For the thin (0.5mm gap) and vertical HS cell, the numerical results qualitatively represented the experiments, but the time evolution in the simulations appeared retarded as in the 3D simulation. Furthermore, it seems that three-dimensional flow effects have to be expected for a horizontal orientation and a large gap width (1 mm).

In the second part of this thesis, the transfer of isopropanol (classified as type III system in Fig. 2.3) that triggered eruptions was simulated. The physical mechanisms (before unclear) that led to eruptions have been explained by the coupling of Rayleigh and Marangoni convection. A comparison with recent experimental results showed a good qualitative agreement, but experimentally measured velocities were roughly two times as high as the simulated ones.

Simulations with varied initial concentrations suggested that the change in initial concentration can be partly accounted for by a scale transformation of time $T \propto c_0^{-2/3}$ for an early stage of the mass transfer. This scaling behavior has been explained by our theoretical consideration in Sec. 3.1. The actual change of quantities (e.g. transferred mass, rms velocity) at the scaled time also seems to obey a power law. Simulations without the Marangoni effect (pure Rayleigh convection) showed no eruptions and a retarded transfer of mass.

Recommendations

Some recommendations – mainly from the viewpoint of theoretical modeling – for future work are made in this section.

A *first* suggestion is that effort should be made to decrease the deviation between simulations and experiments in the same or similar chemical systems. Different aspects regarding this issue are already noted in Sec. 7.6.3, these suggestions also apply to the butanol system. We will not repeat them here in detail. Nevertheless, two main issues are noted: (1) Material properties should be characterized more accurate and also their dependence on composition. (2) The physical model can be extended in several respects, e.g. physical properties depending on composition, interfacial deformation, phase changes, wall effects. However, the inclusion of some physical mechanism may distinctly decrease numerical efficiency. In this respect, the Hele-Shaw system seems to be a promising configuration to simulate the effect of a curved interface and solid walls.

A *second* valuable task is to consider mass transport in a binary system of partially miscible liquids (like cyclohexanol and water). Fundamentally, the physical modeling ap-

pears easier since only two substances are involved. However, due to the phase rule, there is no degree of freedom for the composition at the interface (if pressure and temperature are constant). Thus, Marangoni convection is triggered by the heat of solution. Classical experiments [87, 158, 174, 244] and theoretical works [58, 90, 173, 216] are available in literature. Especially, note that the water-cyclohexanol system was reported unstable to convection in Ref. [174] (relevant parameters are given therein) for any situation, i.e. no matter which phase has an excess versus the equilibrium composition of its main component. In such a configuration, the shortcomings in physical modeling noted for the present ternary system might be accounted easier and more precisely. For example, the dependence of transport parameters or density on the composition can be characterized more certain in a binary system than in a ternary one. Disadvantages are that the thermal "boundary condition" had to be characterized, and one may encounter large interface deformations, which requires a different numerical strategy.

As a *third* direction, we propose to keep the present theoretical and numerical framework:

(1) The parameter analysis in the Rayleigh-Marangoni case showed a power-law behavior whose range of applicability is yet unclear. Its examination could be performed by further simulations and theoretical work. Additionally, a parameter study of the pure Rayleigh unstable case ($Ma=0$) should be done. It is of peculiar importance to determine what the conditions are for which an exact scaling behavior applies, i.e. are there conditions for that dynamics near the interface (e.g. the integral mass transport) are practically taking place in two semi-infinite layers?

(2) The classification of patterns in type I systems by Linde (quoted in Sec. 2.4.1) still addresses features that we have not seen in the present material systems. These features are the cyclic behavior L_4 and relaxations oscillations (ROs) beside those at the onset of convection. The transport of dioxane from a benzol-rich into a water-rich phase has shown these yet not simulated features, cf. Fig. 44-49 in Ref. [198]. Consequently, this might be a candidate to assess further the hypotheses of Linde.

(3) The study of more complex systems should go in hand with improvements in the numerical methods in terms of efficiency. On the one hand, the present code could be better parallelized by including a domain decomposition in both horizontal directions. On the other hand, the undesired clustering of collocation points at the top and bottom could be reduced by using another discretization for the z -direction or a mapping of collocation points [42, 176].

A *fourth* and last suggestion for further work, we like to make is treating other physical effects that were not present in the PM or to be expected in the studied material system but which could be studied in the current framework with some few extension of the numerical code. We like to point out two issues.

(1) Chemical reactions and electrochemistry: For instance, the ethyl acetate-water system with the transport of acetic acid out of the organic phase was estimated of type III (see Sec. 2.4.2) and corresponding observation of eruption were indeed done Ref. [9, 123, 166]. However, for the transport in the reversed direction, the same authors did not report on sustained Marangoni convection, which would be predicted by our simple scheme in Fig. 2.3. E.g., Bakker *et al.* [9] reported "cells faded away after some time, reappearing later". It seems possible that the electrochemical properties [25, 52] (ions of acetic acid might be partly dissociated in the aqueous but associated in the organic phase) of acetic acid have to be taken into account for a correct description. Thus, a further study of this material system might be

useful.

Furthermore, in recent years, several experimental observations [6, 59, 67, 149, 199] (in HS cells) were reported on different types of Marangoni convection that were triggered by chemical reactions. All these might be valuable candidates for numerical studies in order to advance our knowledge in the physical modeling of such systems since effects like a curved interface (HS-cell), diffusion of electrolytes, chemical kinetics, latent heat release, triple line motion are observed there. These issues are also related to the industrial application of reactive extraction [13].

(2) A last point we like to emphasize on is the modeling of surfactants for which the author already did some attempts to include them into the present numerical code – however not described in this thesis. The main new physical feature that had to be modeled is the interfacially adsorbed amount of solute $\Gamma(x, y, t)$ [69]. For a plane interface this amounts to revised matching conditions for the bulk concentration field in the form of

$$\partial_t \Gamma + \partial_x(u_x \Gamma) + \partial_y(u_y \Gamma) - D_g \Delta(\Gamma) = D^{(2)} \partial_z c^{(2)}(z=0) - D^{(1)} \partial_z c^{(1)}(z=0), \quad (8.1)$$

which poses some numerical difficulties due to its nonlinearity (e.g. by $\partial_y(u_y \Gamma)$). Besides numerous applications of surfactants, also experiments showed their impact on Marangoni convection (already noted in Sec. 2.1). Nevertheless, we like to indicate two experimental publications for a numerical study: Firstly, the mass-transfer experiments of Linde [144] with "ditalan" (mixture of different surfactants) showing interesting round cells and secondly the comprehensive study of Agble *et al.* reporting mass transfer rates in binary system with and without surfactants [2, 4].

Appendix A

Thermal model

The paradigmatic model, introduced in Sec. 2.2, is also able to describe the extensively studied thermal problem [50, 66, 99, 100, 165, 172, 182, 194, 217, 246], i.e. the model describing internal energy changes due to temperature gradients, but possessing a uniform composition. The necessary transformation rules are presented next.

The thermal two layer problem [50] – in the form of Boussinesq approximation – is mathematically isomorphic to the solutal PM. Consequently, works discussing the thermal problem are equally important to the solutal problem. The governing equations for thermal convection read as follows, for the bulk:

$$\partial_t \mathbf{u}^{(i)} + \mathbf{u}^{(i)} \cdot \nabla \mathbf{u}^{(i)} = T^{(i)} \beta_T^{(i)} \mathbf{g} - \frac{\nabla p_d^{(i)}}{\rho_{ref}^{(i)}} + \nu^{(i)} \Delta \mathbf{u}^{(i)}, \quad (\text{A.1})$$

$$\nabla \cdot \mathbf{u}^{(i)} = 0, \quad (\text{A.2})$$

$$\partial_t T^{(i)} + \mathbf{u}^{(i)} \cdot \nabla T^{(i)} = \kappa^{(i)} \Delta T^{(i)}, \quad (\text{A.3})$$

and matching conditions at the interface ($z = 0$)

$$u_x^{(1)} = u_x^{(2)}, \quad u_y^{(1)} = u_y^{(2)}, \quad u_z^{(1)} = u_z^{(2)} = 0, \quad (\text{A.4})$$

$$\lambda^{(1)} \partial_z T^{(1)} = \lambda^{(2)} \partial_z T^{(2)}, \quad T^{(1)} = T^{(2)}, \quad (\text{A.5})$$

$$\sigma_{ref} \alpha_T \partial_x T^{(1)} = -\mu^{(2)} \partial_z u_x^{(2)} + \mu^{(1)} \partial_z u_x^{(1)}, \quad (\text{A.6})$$

$$\sigma_{ref} \alpha_T \partial_y T^{(1)} = -\mu^{(2)} \partial_z u_y^{(2)} + \mu^{(1)} \partial_z u_y^{(1)}. \quad (\text{A.7})$$

Material laws are given by

$$\rho^{(i)} = \rho_{ref}^{(i)} + \rho_{ref}^{(i)} \beta_T^{(i)} T^{(i)}, \quad (\text{A.8})$$

$$\sigma = \sigma_{ref} + \sigma_{ref} \alpha_T T^{(1)} (z = 0) \quad (\text{A.9})$$

The former equations involve the temperatures in both layers $T^{(i)}$ with thermal diffusivity $\kappa^{(i)}$ and thermal conductivity $\lambda^{(i)}$. The notion of the thermal problem can be mapped into our "solute language" by the following identification

$$\kappa^{(i)} \cong D^{(i)}, \quad \lambda^{(2)} / \lambda^{(1)} \cong HD^{(2)} / D^{(1)}, \quad T^{(1)} \cong Hc^{(1)}, \quad T^{(2)} \cong c^{(2)}, \quad (\text{A.10})$$

$$\alpha_T \cong \alpha_c / H, \quad \beta_T^{(1)} \cong \beta_c^{(1)} / H, \quad \beta_T^{(2)} \cong \beta_c^{(2)}. \quad (\text{A.11})$$

Furthermore, note that the comprehensively studied one layer model [165, 172, 182] is also included in the formulation. Therefore only the lower layer $z \in [-d^{(1)}, 0]$ is considered. This single layer problem has been studied employing different boundary conditions.

The most prominent instance is the Rayleigh-Bénard setup [41, 45, 182, 212], which possesses two isothermal and no-slip boundaries at $(z = -1, 0)$. However, this model excludes the existence of Marangoni convection and its application to solute transport is sparse.

The second prominently studied setup is a liquid-layer bounded on the top by a gaseous layer. In the case of a thin gaseous upper layer, this can also be described by a single layer model [66]. Then the temperature boundary condition at the free surface are accounted by a *Biot number condition* and the viscous stress from the gaseous layer are neglected.

Appendix B

Material properties

B.1 Water-cyclohexanol-butanol system

This section provides details on the estimation of material properties of the cyclohexanol-water-butanol system used in Ch. 5. Finally, this estimation leads to the parameters introduced formerly in Tab. 5.1.

We assume isothermal conditions and will not distinguish between measurements of material parameters that have been taken at 20°C or 25°C. The volume and molar concentrations of butanol in the phase i are denoted as $y_b^{(i)}$ and $c_b^{(i)}$, and given in Vol% and mol/l, respectively. They are related by

$$c_b^{(i)} = \frac{\rho_b y_b^{(i)}}{M_b}, \quad (\text{B.1})$$

where M_b is the molar mass and ρ_b the density of pure butanol.

Density: The reference densities $\rho_{ref}^{(i)}$ of the two mutually saturated binary phases, i.e. for zero butanol concentration are reported in [198] to be $\rho_{ref}^{(1)} = 0.997\text{kg/l}$, $\rho_{ref}^{(2)} = 0.955\text{kg/l}$. According to our paradigmatic model, the density depends on the butanol concentration. In the aqueous phase (1), it may only change with zero excess volume of mixing, i.e.

$$\rho^{(1)} = \rho_{ref}^{(1)} + \frac{c_b^{(1)} M_b}{\rho_b} (\rho_b - \rho_{ref}^{(1)}). \quad (\text{B.2})$$

This linear relation is reformulated with the solutal expansion coefficient $\beta_c^{(1)}$ (Eq.(2.4)) to

$$\beta_c^{(1)} = \frac{M_b}{\rho_b \rho_{ref}^{(1)}} (\rho_b - \rho_{ref}^{(1)}). \quad (\text{B.3})$$

A linear relation is also applied for phase (2). However, in this case the solutal expansion coefficient $\beta_c^{(2)}$ can be determined more precisely, based on the data of Schwarz [198] for $\rho^{(2)} = 0.9416 \text{ kg/l}$ at $y_b = 0.1 \Rightarrow c_b^{(2)} = 1.093 \text{ mol/l}$ Eq. (B.1). For the values of ρ_b, M_b see Tab. 5.1, they are provided by Ref. [135].

Solute partition coefficient: The bulk concentrations at the interface are assumed to be in thermodynamic equilibrium with the local excess concentration of the interface Γ . Furthermore, we apply Henry's model, stating that the excess concentration depends linearly on the concentrations adjacent to the interface $\Gamma = K_1 c_b^{(1)}$ and $\Gamma = K_2 c_b^{(2)}$. Both relations yield the concentration partition coefficient or Henry's constant H ,

$$c_b^{(1)} = K_2 / K_1 c_b^{(2)} = c_b^{(2)} / H. \quad (\text{B.4})$$

H is approximated by means of a correlation method [132], which relies on the partition coefficient of 1-butanol in an octanol-water system $H_{OW} = 6.92$ [135] as input. This correlation method estimates the equilibrium concentration of butanol to be 31 times higher in the upper organic phase compared to the aqueous phase, i.e. $H = 31$. Thus, the absolute concentration of butanol in both layers changes only slightly for our configuration, making the applied linearizations and the further assumption of constant material properties more robust.

Interfacial tension dependence: General thermodynamic considerations [63, 69] imply that the excess concentration Γ of the interface is related to the interfacial tension σ by the Gibbs adsorption isotherm. For Henry's model this yields a linear relationship between the interfacial tension and the concentration,

$$\sigma = \sigma_{ref} + \sigma_{ref} \alpha_c c_b^{(1)}. \quad (\text{B.5})$$

This solutal surface tension coefficient α_c is determined from the measurements of Schwarz [198]. He measured an interfacial tension of $\sigma = 3.1 \cdot 10^{-3}$ N/m at a concentration of $c_b^{(1)} = 34.2 \cdot 10^{-3}$ mol/l and $\sigma_{ref} = 3.4 \cdot 10^{-3}$ N/m at zero concentration.

Note that Schwarz describes his measurements by an initial volumetric concentration of butanol $y_b^{(2)} = 0.1$, which is equivalent to a molar concentration of $c_b^{(2)} = 1.093$ mol/l. However, the corresponding equilibrium state (at which he measures interfacial tension) establishes after a sufficient long time and butanol spreads over both phases. The concentrations at equilibrium are calculated by using the global conservation of mass the formerly calculated Henry coefficient and taking into account that the volumes of individual phases may gradually change. These assumption lead to a concentration in equilibrium of $c_b^{(2)} = 1.061$ mol/l and $c_b^{(1)} = 34.2 \cdot 10^{-3}$ mol/l via a nonlinear relation (not presented here).

Viscosity: Schwarz [198] also listed the kinematic viscosity of phase (2) for different butanol concentrations. We use the value $\nu^{(2)} = 20 \cdot 10^{-6}$ m²/s corresponding to a volume concentration of $y_b^{(2)} = 0.075$. For the lower aqueous phase (1) without butanol, it is $\nu^{(1)} = 1.2 \cdot 10^{-6}$ m²/s [198].

Diffusivity: The diffusivity of butanol in the aqueous phase $D^{(1)}$ is approximated by the value in pure water [135] $D^{(1)} = 5 \cdot 10^{-10}$ m²/s. To estimate the diffusivity in the organic phase, we performed the methods discussed in Ref. [134]. Thus four different empirical formulas (corresponding to the Scheibel, Reddy-Doraiswamy, Lusi-Ratcliff and Wilke-Chang correlations) are applied to the organic phase, which yields $D^{(2)} = 7 \cdot 10^{-11}$ m²/s as a mean value. The lower diffusivity in layer (2) is mainly due to the higher viscosity since all correlations contain the relation $D \propto 1/\mu$.

B.2 Water-cyclohexanol-isopropanol system

In contrast to our sample water/cyclohexanol+butanol system used for the study of stationary Marangoni convection in Ch. 5, we replace the transferred solute from 1-butanol to isopropanol (also called 2-propanol), but keep the solvent binary phase (cyclohexanol/water). Why do we change to isopropanol? Isopropanol is solvable to a higher degree in the aqueous phase, resulting in a better visibility by shadowgraph optical methods. The remainder of this section is devoted to the estimation of the physical properties of this second sample system (say "isopropanol system"), which was used for numerical simulation (see Ch. 7).

Preparation of the isopropanol system proceed similar to the butanol system: First, the phases of a water and cyclohexanol ($C_6H_{11}OH$) mixture are produced – so both binary phases are in equilibrium due to mutual saturation. Secondly, isopropanol (C_3H_8O), which lowers interfacial tension, is dissolved in the aqueous phase. The material properties demanded to solve our paradigmatic model (see Sec. 2.2) will be derived below and collected in Tab. B.1.

Viscosity: The viscosity of the binary system (water+cyclohexanol) was measured by Schwarz [198]. These values are used for the present system, which is a bit different to the butanol case, where we took the viscosity measured with dissolved butanol in the organic phase.

Density: The density of the binary system and the ternary system is provided to us by pycnometric measurements from Karin Schwarzenberger (*personal communications*). The density of the binary system is determined to $\rho_{ref}^{(1)} = 0.9962$ kg/l, $\rho_{ref}^{(2)} = 0.9515$ kg/l at room temperature ($\approx 20^\circ C$) and typical atmospheric pressure. Note that this values slightly deviate from the values reported by Schwarz.

The ternary system (with addition of isopropanol) is probed at the first tie-line composition reported by Sayar [192] (see our Tab. B.1). In this table, $\omega_j^{(i)}$ is the mass fraction of component j in phase (i). These mass fraction have been measured for different compositions by Sayar [192]. After mixing (at the first tie-line of Sayar) the density is measured to $\rho^{(1)} = 993.78$ kg/m³, $\rho^{(2)} = 948.37$ kg/m³ with standard deviation (three samples, uncorrected) of $\sigma_{\rho^{(1)}} = 0.265$ kg/m³, $\sigma_{\rho^{(2)}} = 0.220$ kg/m³. So the isopropanol concentration can be calculated to $c_2^{(1)} = 0.2315$ mol/l, $c_2^{(2)} = 0.34715$ mol/l (generally it holds that mass fractions and molar concentration are related by $c_2^{(1)} = \rho^{(1)} \cdot \omega_2^{(1)} / M_2$). With this values and the data from the binary system, the soltual-expansion coefficients $\beta_c^{(i)}$ are derived (Tab. B.1) according to the linear model

$$\rho^{(i)} = \rho_{ref}^{(i)} + \rho_{ref}^{(i)} \beta_c^{(i)} c_2^{(i)}. \quad (B.6)$$

Equilibrium composition: Sayar [192] measured the equilibrium compositions of the water-cyclohexanol-isopropanol mixture. The mass fraction ratios of 2-propanol for the two lowest propanol concentration are $\omega_2^{(2)} / \omega_2^{(1)} = 0.022 / 0.014 = 1.57$, $0.038 / 0.021 = 1.81$ (first and second tie line [192]).

The molar concentration (mol/l) in phase (1) results from the mass fraction $\omega_2^{(1)}$ by $c_2^{(1)} = \rho^{(1)} \cdot \omega_2^{(1)} / M_2$. An analogous relation holds for phase (2), with this, the ratio of molar concentrations (Henry coefficient H) reads

$$H = c_2^{(2)} / c_2^{(1)} = \omega_2^{(2)} \rho^{(2)} / (\omega_2^{(1)} \rho^{(1)}). \quad (B.7)$$

Using the density ratio of the binary phases, $\rho \approx 0.96$, it yields $H \in \{1.53, 1.74\}$. We will use $H = 1.6$. as a rational mean. ^I

Generally, the density is a function of both concentrations, so for an improved modeling one may also solve the transport equation for the water concentration. In such an approach, the effects of multicomponent diffusion may be taken into account. Thus, diffusion of both constituents is coupled due to cross diffusion [225]. Without further elaboration of this point, we suspect that the error introduced with this *single solute* modeling has its main impact far from the interface in the phase where isopropanol [layer (1)] is introduced. Because departure from the equilibrium composition (we have implicitly employed) is highest there.

Surface tension: Schwarz [197, 198] measured for an overall mass fraction $m_2/m = 0.04$ of 1-propanol (i.e. an isomer of 2-propanol) the interfacial tension to $\sigma = 3.2\text{mN/m}$. We will use this value for 2-propanol. The knowledge of corresponding 1-propanol concentration in each phase requires additional calculations. So, an equilibrium ratio of mass fractions for 1-propanol of $H_\omega = \omega_2^{(2)}/\omega_2^{(1)} \approx 2.75$ (cf. measurements of Ref. [168] for low 1-propanol concentrations) is used and we assume the individual phases of Schwarz had the same mass, i.e. $m^{(1)} = m^{(2)}$ the corresponding mass fractions after equilibration are

$$\omega_2^{(1)} = 0.04/(1 + H_\omega), \quad (\text{B.8})$$

$$\omega_2^{(1)} = 0.0107 \rightarrow c_2^{(1)} = 0.1774\text{mol/l}. \quad (\text{B.9})$$

The interfacial tension is taken as a linear function of solute concentration

$$\sigma = \sigma_{ref} + \sigma_{ref}\alpha_c c_2^{(1)}, \quad (\text{B.10})$$

, thus,

$$\frac{\sigma(c_2^{(1)}) - \sigma_{ref}}{\sigma_{ref}c_2^{(1)}} = \alpha_c, \quad (\text{B.11})$$

$$\alpha_c = \frac{3.2\text{mN/m} - 3.4\text{mN/m}}{3.4\text{mN/m} \cdot 0.1774\text{mol/l}} = -0.3316\text{l/mol}. \quad (\text{B.12})$$

Evidence for the applicability of 1-propanol data to the 2-propanol system is given by the fact that the plait points (critical point) are located in both systems around $\omega_2 = 0.2 \rightarrow c_2 = 3.3\text{mol/l}$ (see [168] and [192]), which is in accordance with the calculated coefficient since there $\sigma = 0$ by our linear model. ^{II}

Diffusivity: is estimated as follows. For the aqueous phase we took the value from 1-propanol in water from [135] $D_2^{(1)} = 8.7 \cdot 10^{-10}\text{m}^2/\text{s}$ at $T = 15^\circ\text{C}$ and further extrapolated this for a higher temperature of 22.5°C , resulting to $D^{(1)} = 8.9 \cdot 10^{-10}\text{m}^2/\text{s}$.

For the organic phase (2), we use the methods reviewed in [134]. A prerequisite for all those methods is to know the molar volume of the involved pure substances at their normal boiling

^IAnother way could be calculating equilibrium data from the UNIFAC data [151], which is not straightforward as it needs some optimization calculations and care with the parameters.

^{II}Some methods for estimation of surface tension are available [205], but these might be too uncertain for the small interfacial tension change we have.

point. These are deduced for cyclohexanol($C_6H_{12}O$)(six membered ring), propanol(C_3H_8O) with the LeBas method [134]

$$V_{cyclo} = 6 \cdot 14.8 + 12 \cdot 3.7 + 7.4 - 15 = 125.6 \text{cm}^3/\text{mol}, \quad (\text{B.13})$$

$$V_{prop} = 3 \cdot 14.8 + 8 \cdot 3.7 + 7.4 = 79 \text{cm}^3/\text{mol}, \quad (\text{B.14})$$

$$V_{water} = 18.9 \text{cm}^3/\text{mol}. \quad (\text{B.15})$$

In [84] it is noted that the desired molar volumes at normal boiling point are related to the critical volume by $V_B = 0.285 * V_c^{1.048}$. Actually, the critical volume of 2-propanol is $V_c^{prop} = 222.5 \text{cm}^3/\text{mol}$, thus, $V_{prop} = 82.2$. Let us use $V_{prop} = 81 \text{cm}^3/\text{mol}$ as a mean value.

Just for checking the estimation methods, we estimate propanol diffusion in water. With the Wilke-Chang [134, 240] method it gives $D = 9.66 \cdot 10^{-10} \text{m}^2/\text{s}$, the Hayduk formula [52] with dissociation factor of 2.26 gives $9.89 \cdot 10^{-10} \text{m}^2/\text{s}$, both using $V_{prop} = 82 \text{ml}/\text{mol}$. So diffusivity is estimated a little higher than measured ($8.7 \cdot 10^{-10} \text{m}^2$).

To estimate diffusion in the organic phase, the mixing molecular volume is needed as an input value [134]. The molar volume of the binary solvent is calculated by

$$\bar{V}^{(2)} = x_3^{(2)} V_{cyclo} + x_1^{(2)} V_{water}, \quad (\text{B.16})$$

$$\bar{V}^{(2)} = 0.5925 \cdot 125.6 \text{cm}^3/\text{mol} + 0.4075 \cdot 18.9 \text{cm}^3/\text{mol} = 82.12, \quad (\text{B.17})$$

where $x_3^{(2)}$ is the molar fraction of constituent 3 in phase (2). The correlation of Scheibel [134] gives

$$D_2^{(2)} = \frac{8.2 \cdot 10^{-8} \cdot T[\text{K}]}{\mu^{(2)} [10^{-3} \text{Pas}] V_{prop}^{1/3} [\text{cm}^3/\text{mol}]} \left[1 + \left(3 \frac{\bar{V}^{(2)} [\text{cm}^3/\text{mol}]}{V_{prop} [\text{cm}^3/\text{mol}]} \right)^{2/3} \right], \quad (\text{B.18})$$

$$D_2^{(2)} = \frac{8.2 \cdot 10^{-8} \cdot 293 \text{K}}{23.68 \text{mPas} (81 \text{mL}/\text{mol})^{1/3}} \left[1 + \left(3 \frac{82.12 \text{mL}/\text{mol}}{81 \text{mL}/\text{mol}} \right)^{2/3} \right] \approx 7.3 \cdot 10^{-11} \text{m}^2/\text{s}, \quad (\text{B.19})$$

which is used in the following.

description	symbol	unit	value
molar mass water(H_2O)	M_1	kg/mol	$18.02 \cdot 10^{-3}$
molar mass propanol(C_3H_8O)	M_2	kg/mol	$60.10 \cdot 10^{-3}$
molar mass cyclohexanol($C_6H_{12}O$)	M_3	kg/mol	$100.12 \cdot 10^{-3}$
mass density H_2O sat. $C_6H_{11}OH$	$\rho_{ref}^{(1)}$	kg/m ³	$0.9962 \cdot 10^3$
mass density $C_6H_{11}OH$ sat. H_2O	$\rho_{ref}^{(2)}$	kg/m ³	$0.9515 \cdot 10^3$
mass density propan-2-ol	ρ_2^{pure}	kg/m ³	$0.781 \cdot 10^3$
kinematic viscosity (1) $c_2^{(1)} = 0$ [198]	$\nu^{(1)}$	m ² /s	$1.2 \cdot 10^{-6}$
kinematic viscosity (2) with $c_2^{(2)}=0$ [198]	$\nu^{(2)}$	m ² /s	$24.89 \cdot 10^{-6}$
partition coefficient $c^{(2)}/c^{(1)}$	H	(mol/l) / (mol/l)	1.6
diffusivity isopropanol (1)	$D^{(1)}$	m ² /s	$8.9 \cdot 10^{-10}$
diffusivity isopropanol (2)	$D^{(2)}$	m ² /s	$7.3 \cdot 10^{-11}$
interfacial tension of the binary system	σ_{ref}	N/m	$3.4 \cdot 10^{-3}$
change in interfacial tension per mol/l of $c^{(1)}$	$\sigma_{ref}\alpha_c$	N/m/(mol/l)	$1.13 \cdot 10^{-3}$
solubility expansion coefficient (1)	$\beta_c^{(1)}$	l/mol	-0.0104
solubility expansion coefficient (2)	$\beta_c^{(2)}$	l/mol	-0.0096
density change per surfactant conc. (1)	$\rho_{ref}^{(1)}\beta_c^{(1)}$	(kg/l)/(mol/l)	-0.0104
density change per surfactant conc. (2)	$\rho_{ref}^{(2)}\beta_c^{(2)}$	(kg/l)/(mol/l)	-0.0091
concentration for $y_2^{(1)}=(0.01, 0.025, 0.05)$	$c_2^{(1)}$	mol/l	(0.130 ,0.32, 0.65)
composition (aqueous) ($\omega_1, \omega_2, \omega_3$) 0th tie-line [192]	$\omega_i^{(1)}$	kg/kg	(0.961 0 0.039)
composition (organic)($\omega_1, \omega_2, \omega_3$) 0th tie-line [192]	$\omega_i^{(2)}$	kg/kg	(0.103 0 0.897)
composition (aqueous) ($\omega_1, \omega_2, \omega_3$) 1st tie-line [192]	$\omega_i^{(1)}$	kg/kg	(0.917 0.014 0.069)
composition (organic)($\omega_1, \omega_2, \omega_3$) 1st tie-line [192]	$\omega_i^{(2)}$	kg/kg	(0.136 0.022 0.842)

Table B.1: Properties of the system (cyclohexanol+2-propanol)/water. Phase 1 is the water rich phase marked with $(.)^{(1)}$ and phase 2 the organic, cyclohexanol-rich phase marked with $(.)^{(2)}$. The data sources are detailed in the text of Sec. B.2. The subscripts refer to the different constituents: $_1$ =water, $_2$ = isopropanol, $_3$ = cyclohexanol. Molar concentration is related to the volumetric concentration by $c_2^{(1)} = (\rho_2^{pure} y_2^{(1)})/M_2$.

Appendix C

Kinetic energy balance

In this Appendix, the kinetic energy balance in accordance with the PM (Sec. 2.2) is derived.

Generally, the momentum balance with the stress tensor \mathbf{T} and volume forces \mathbf{f} reads

$$\rho \frac{D\mathbf{u}}{Dt} = \nabla \cdot \mathbf{T} + \mathbf{f}. \quad (\text{C.1})$$

Multiplying every term with the velocity yields,

$$\rho \frac{D(\mathbf{u} \cdot \mathbf{u})}{2Dt} = (\nabla \cdot \mathbf{T}) \cdot \mathbf{u} + \mathbf{f} \cdot \mathbf{u}, \quad (\text{C.2})$$

which is the transport equation of kinetic energy of any material point in the respective bulk volume, see Ref. [57] on p.16.

The only external force considered is gravity ($\mathbf{f} = \mathbf{g}\rho$). Also we assume an incompressible Newtonian behavior and constant viscosity, so (C.2) leads to

$$\rho \frac{D(\mathbf{u} \cdot \mathbf{u})}{2Dt} + \nabla \cdot (\mathbf{u}p - 2\mu\mathbf{u} \cdot \mathbf{E}) = -2\mu(\mathbf{E} : \mathbf{E}) + \mathbf{g}\rho \cdot \mathbf{u}, \quad (\text{C.3})$$

cf. [178], p. 123. Here, the symmetric part of the velocity gradient is denoted by \mathbf{E} , given in a Cartesian basis \mathbf{e}_i by $E_{ij} = 1/2(\partial_{x_i}u_j + \partial_{x_j}u_i)$.

To be consistent with the Boussinesq approximations, the density before the material derivative has to be taken as a constant but the density related to the gravitational acceleration has to be assumed as spatial dependent. In what follows the integral kinetic energy balance of both phases is deduced by including boundary and matching conditions according to our PM. The time rate of change of kinetic energy in layer (2) is

$$\partial_t \int_{\Omega^{(2)}} \rho^{(2)} \frac{1}{2}(\mathbf{u}\mathbf{u}) = - \int_{\Omega^{(s)}} \mu^{(2)}(u_x^{(2)}\partial_z u_x^{(2)} + u_y^{(2)}\partial_z u_y^{(2)}) + \int_{\Omega^{(2)}} -2\mu^{(2)}\mathbf{E} : \mathbf{E} + \rho^{(2)}\mathbf{g} \cdot \mathbf{u} \quad (\text{C.4})$$

and for layer (1)

$$\partial_t \int_{\Omega^{(1)}} \rho^{(1)} \frac{1}{2}(\mathbf{u}\mathbf{u}) = \int_{\Omega^{(s)}} \mu^{(1)}(u_x^{(1)}\partial_z u_x^{(1)} + u_y^{(1)}\partial_z u_y^{(1)}) + \int_{\Omega^{(2)}} -2\mu^{(1)}\mathbf{E} : \mathbf{E} + \rho^{(1)}\mathbf{g} \cdot \mathbf{u}. \quad (\text{C.5})$$

Adding both layers and taking density as $\rho^{(i)} = \rho_{ref}^{(i)}(1 + \beta_c^{(i)}c^{(i)})$, the gravity to $\mathbf{g} = -g\mathbf{e}_z$, interfacial tension as $\sigma = \sigma_{ref} + \sigma_{ref}\alpha_c c^{(1)}(x, y, z = 0)$ yields

$$\partial_t \int_{\Omega^{(1)} \cup \Omega^{(2)}} \rho_{ref}^{(i)} \frac{1}{2}\mathbf{u}^{(i)} \cdot \mathbf{u}^{(i)} = \int_{\Omega^{(s)}} \nabla_s \sigma \cdot \mathbf{u} + \int_{\Omega^{(1)} \cup \Omega^{(2)}} -2\mu^{(i)}\mathbf{E}^{(i)} : \mathbf{E}^{(i)} - \rho_{ref}^{(i)}\beta_c^{(i)}c^{(i)}gu_z^{(i)}. \quad (\text{C.6})$$

The constant part in the density does not add to the energy [last term in (C.5)] since there is no mean vertical velocity. This is not true for a deformable interface with a density difference between the phase.

Now we introduce the usual nondimensional viscous units $d^{(1)}$, $(d^{(1)})^2/\nu^{(1)}$, $\mu^{(1)}\nu^{(1)}/(d^{(1)})^2$ and $\rho_{ref}^{(1)}(d^{(1)})^3$ for length, time, pressure and mass, respectively. Considering these units, the dimensionless kinetic energy balance reads

$$\frac{(\nu^{(1)})^3}{(d^{(1)})^4} \partial_t \int_{\hat{\Omega}} \rho_{ref}^{(i)} \frac{1}{2} (\hat{\mathbf{u}} \cdot \hat{\mathbf{u}}) = \frac{\sigma_{ref} \alpha_c c_0 \nu^{(1)}}{(d^{(1)})^3} \int_{\Omega^{(s)}} \nabla_s \hat{c} \cdot \hat{\mathbf{u}} - \int_{\hat{\Omega}} 2 \frac{\mu^{(i)} (\nu^{(1)})^2}{(d^{(1)})^4} \hat{\mathbf{E}}^{(i)} : \hat{\mathbf{E}}^{(i)} - \frac{\rho_{ref}^{(i)} \beta_c^{(i)} g c_0 \nu^{(1)}}{d^{(1)}} \hat{c}^{(i)} \hat{u}_z^{(i)}. \quad (\text{C.7})$$

For comparing different geometries, volume and interfacial ($\langle \cdot \rangle_s$) averaged quantities are introduced by dividing (C.7) by the base area $l_x l_y$ and multiplying by $\nu^{(1)} (d^{(1)})^4$

$$\begin{aligned} (\nu^{(1)})^2 \frac{1}{2} \partial_t \left[\langle \rho_{ref}^{(1)} (\hat{\mathbf{u}} \cdot \hat{\mathbf{u}}) \rangle_{\hat{\Omega}^{(1)}} + d \langle \rho_{ref}^{(2)} (\hat{\mathbf{u}} \cdot \hat{\mathbf{u}}) \rangle_{\hat{\Omega}^{(2)}} \right] = \\ d^{(1)} \sigma_{ref} \alpha_c c_0 \langle \nabla_s \hat{c} \cdot \hat{\mathbf{u}} \rangle_s \\ - (\nu^{(1)}) \left[\langle \mu^{(1)} 2 \hat{\mathbf{E}} : \hat{\mathbf{E}} \rangle_{\hat{\Omega}^{(1)}} + d \langle \mu^{(2)} 2 \hat{\mathbf{E}} : \hat{\mathbf{E}} \rangle_{\hat{\Omega}^{(2)}} \right] \\ - (d^{(1)})^3 g c_0 \left[\langle \rho_{ref}^{(1)} \beta_c^{(1)} \hat{c}^{(1)} \hat{u}_z^{(1)} \rangle_{\hat{\Omega}^{(1)}} + d \langle \rho_{ref}^{(2)} \beta_c^{(2)} \hat{c}^{(2)} \hat{u}_z^{(2)} \rangle_{\hat{\Omega}^{(2)}} \right]. \end{aligned} \quad (\text{C.8})$$

Furthermore, it is divide by $\rho_{ref}^{(1)}$ and $(\nu^{(1)})^2$, which reads as follows

$$\begin{aligned} \frac{1}{2} \partial_t \left[\langle (\hat{\mathbf{u}} \cdot \hat{\mathbf{u}}) \rangle_{\hat{\Omega}^{(1)}} + d \rho \langle (\hat{\mathbf{u}} \cdot \hat{\mathbf{u}}) \rangle_{\hat{\Omega}^{(2)}} \right] = \\ \frac{d^{(1)} \sigma_{ref} \alpha_c c_0}{\rho_{ref}^{(1)} (\nu^{(1)})^2} \langle \nabla_s \hat{c} \cdot \hat{\mathbf{u}} \rangle_s \\ - \left[2 \langle \hat{\mathbf{E}} : \hat{\mathbf{E}} \rangle_{\hat{\Omega}^{(1)}} + d \nu \rho 2 \langle \hat{\mathbf{E}} : \hat{\mathbf{E}} \rangle_{\hat{\Omega}^{(2)}} \right] \\ - \frac{(d^{(1)})^3 g c_0 \beta_c^{(1)}}{(\nu^{(1)})^2} \left[\langle \hat{c}^{(1)} \hat{u}_z^{(1)} \rangle_{\hat{\Omega}^{(1)}} + d \rho \beta_c \langle \hat{c}^{(2)} \hat{u}_z^{(2)} \rangle_{\hat{\Omega}^{(2)}} \right]. \end{aligned} \quad (\text{C.9})$$

Finally, this can be written by the Grashofnumber G , the Marangoni number Ma and Schmidt number Sc

$$\begin{aligned} \frac{1}{2} \partial_t \left[\langle (\hat{\mathbf{u}} \cdot \hat{\mathbf{u}}) \rangle_{\hat{\Omega}^{(1)}} + d \rho \langle (\hat{\mathbf{u}} \cdot \hat{\mathbf{u}}) \rangle_{\hat{\Omega}^{(2)}} \right] = \frac{Ma}{Sc} \langle \nabla_s \hat{c} \cdot \hat{\mathbf{u}} \rangle_s \\ - \left[2 \langle \hat{\mathbf{E}} : \hat{\mathbf{E}} \rangle_{\hat{\Omega}^{(1)}} + d \nu \rho 2 \langle \hat{\mathbf{E}} : \hat{\mathbf{E}} \rangle_{\hat{\Omega}^{(2)}} \right] \\ - G \left[\langle \hat{c}^{(1)} \hat{u}_z^{(1)} \rangle_{\hat{\Omega}^{(1)}} + d \rho \beta_c \langle \hat{c}^{(2)} \hat{u}_z^{(2)} \rangle_{\hat{\Omega}^{(2)}} \right] \end{aligned} \quad (\text{C.10})$$

We introduce the following abbreviations for power density due to gravitational force (positive if work is done on the system)

$$\omega_g = -G \left[\langle \hat{c}^{(1)} \hat{u}_z^{(1)} \rangle_{\hat{\Omega}^{(1)}} + d \rho \beta_c \langle \hat{c}^{(2)} \hat{u}_z^{(2)} \rangle_{\hat{\Omega}^{(2)}} \right], \quad (\text{C.11})$$

power density due to interface work

$$\omega_s = \frac{Ma}{Sc} \langle \nabla_s \hat{c} \cdot \hat{\mathbf{u}} \rangle_s \quad (\text{C.12})$$

and viscous dissipation (positive for heat production)

$$\epsilon = \left[2 \langle \hat{\mathbf{E}} : \hat{\mathbf{E}} \rangle_{\hat{\Omega}^{(1)}} + d\nu\rho 2 \langle \hat{\mathbf{E}} : \hat{\mathbf{E}} \rangle_{\hat{\Omega}^{(2)}} \right]. \quad (\text{C.13})$$

The factor relating interfacial work to buoyant work (see (C.10)) is the dynamic Bond number

$$Bo_d = G/(Ma/Sc^{(1)}) = \frac{\rho_{ref}^{(1)} \beta_c^{(1)} g (d^{(1)})^2}{\alpha_c \sigma_{ref}} \quad (\text{C.14})$$

Appendix D

Supplementary numerical results

D.1 Marangoni convection

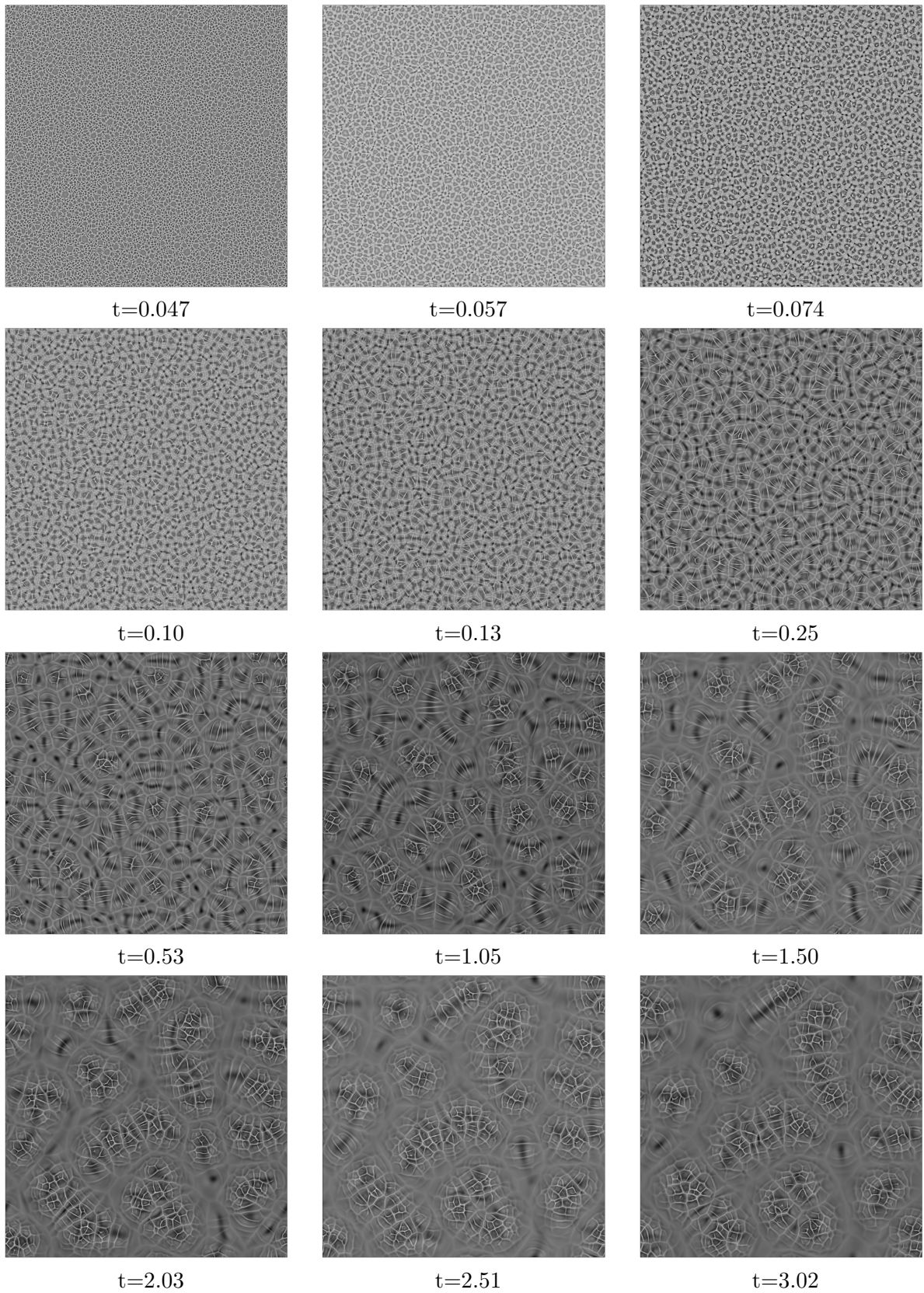


Figure D.1: Simulation G_1.1 (see Tab. 5.3) synthetic shadowgraph images $s(x, y)$ gray scale adapted to the extrem value (white \leftrightarrow maximum and black \leftrightarrow minimum) for consecutive times, full domain is shown $(x, y) \in [0, 0.5] \times [0, 0.5]$.

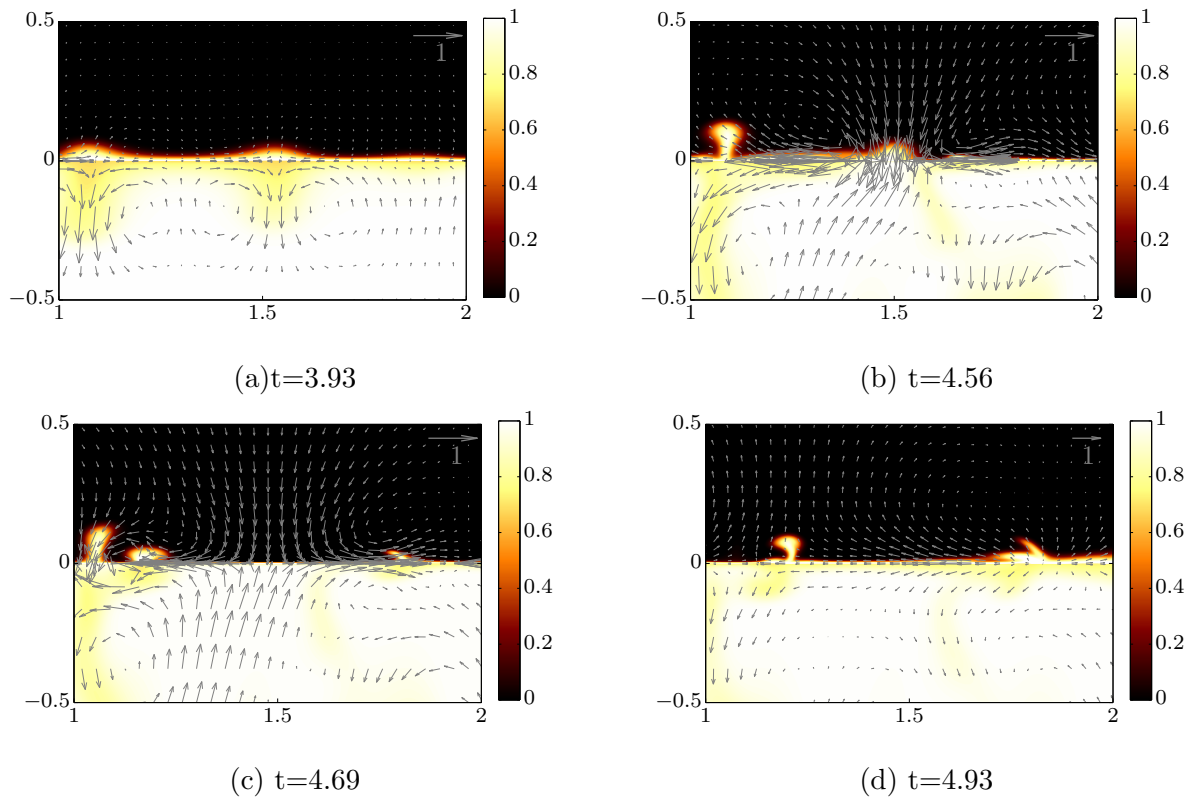


Figure D.2: Details of Fig.7.4 on the onset of convection for simulation RM_2a: Vertical cut at $y = 0$ showing concentration and velocity.

D.2 Rayleigh-Marangoni convection

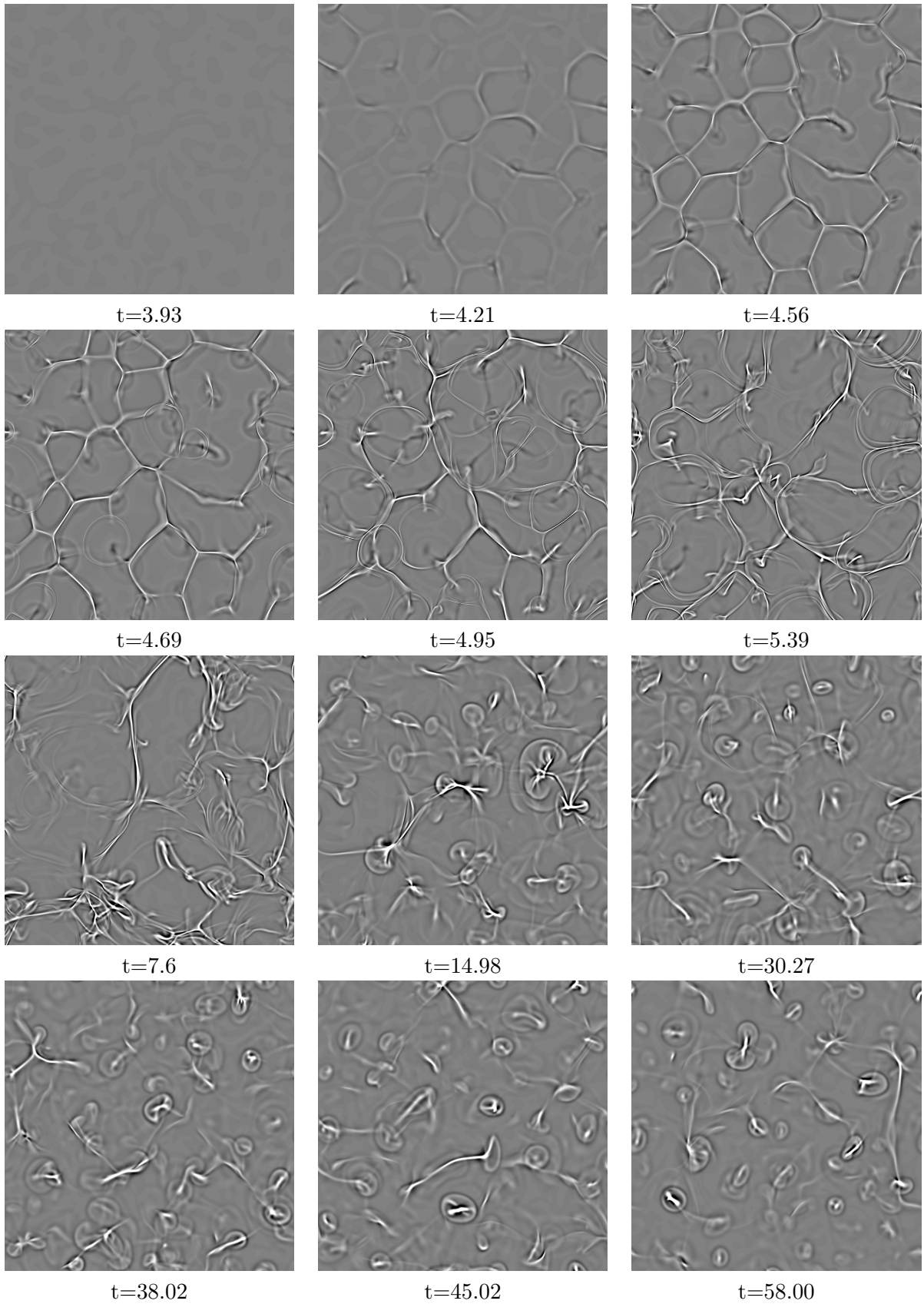


Figure D.3: Simulation RM.2a synthetic shadowgraph images $s(x, y)$ (black $\leftrightarrow s(x, y) = +200$; white $\leftrightarrow s(x, y) = -400$) for consecutive times, full domain is shown $(x, y) \in [0, l_x] \times [0, l_y]$.

Appendix E

Image processing

RC-I size λ_{RC-I}

This section provides details about the image analysis that we applied in the scope of Sec.5.3. After mapping the raw data $\partial_z u_z(x, y, z = 0)$ into the binary representation

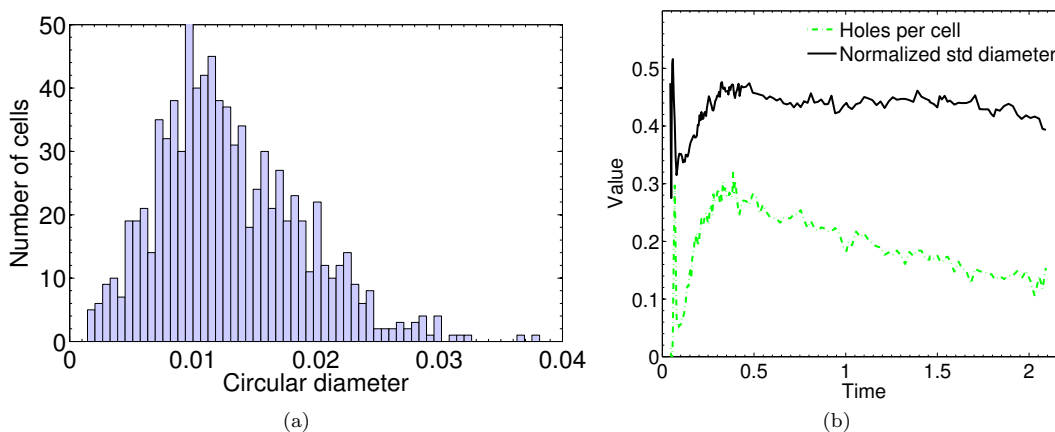


Figure E.1: Image processing of simulation E_1.1:(a) Histogram of circular diameters $\sqrt{A_j 4/\pi}$ corresponding to Fig. 5.16 and (b) time evolution of the standard deviation of diameter distribution and averaged number of white spots ("holes") included in a cell.

$I_0(\partial_z u_z)(x, y)$, we erase all connected inflow regions at the image boundary. This is apparent in Fig. 5.16. Otherwise, all cells at the boundary have to be merged with their periodic continuation, which is avoided for simplicity. The connected black subareas in Fig. 5.16 are defined as the individual cells C_j with $j \in [1, \dots, N_c]$. Some of the RC-Is exhibit a completely enclosed white spot in their middle, corresponding to surfactant fronts. They are included into the individual sets C_j . This identification of individual cells disregards the area of the white outflow zones, which constitute the periphery of the RC-Is. However, as can be seen from Fig. 5.16, the inflow zones (black) occupy most of the actual cell areas and therefore serve as an adequate approximation for the manual measurements of Schwarz. After the identification of cells C_j their area A_j is calculated and used in Eq. (5.20).

Our procedure does not distinguish between the RC-Is as the compact type of substructure and ROWs, which feature an elongated shape. Fig. E.1(a) shows the respective histogram of circular diameters $\sqrt{A_j 4/\pi}$ corresponding to Fig. 5.16. Additional parameters of the evalu-

ation procedure are depicted in Fig. E.1(b). These parameters are the normalized standard deviation of the RC-Is diameters and the number of erased white spots per cell (holes per cell).

RC-II size λ_F The RC-II cell size is calculated from the shadowgraph images $s(x, y)$ by the following procedure. The 2D FFT $\hat{s}(k_x, k_y)$ of the shadowgraph image is radially averaged,

$$\hat{s}_r(k_m) = \frac{1}{N_m} \sum_{k_m - \Delta k/2 < |\mathbf{k}| < k_m + \Delta k/2} |\hat{s}(k_x, k_y)|, \quad (\text{E.1})$$

and divided afterwards by the global maximum. This yields the single data points in Fig. E.2. The wavenumber intervals over which it is averaged have midpoints $k_m = 2\pi m/l_x$ and size $\Delta k = 2\pi/l_x$; the factors N_m denote the number of individual modes in interval m . The dominant length λ_F , cf. cross in Fig E.2, is determined as the maximum of the moving average (full line) from $\hat{s}_r(k_m)$, to smooth out fluctuations in the raw data. As can be seen from Fig. E.2, the large-scale structures in their fully developed state govern the signal of the averaged spectrum.

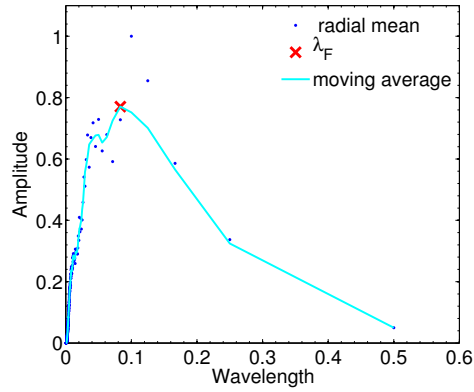


Figure E.2: Radially averaged spectrum of the synthetic shadowgraph distribution of $E_{1.1}$ at $t=1.44$.

Bibliography

- [1] R. Abraham, J. E. Marsden, and T. Ratiu. *Manifolds, tensor analysis, and applications*. Springer-Verlag, 3rd edition, 2001.
- [2] D. Agble and M.A. Mendes-Tatsis. The effect of surfactants on interfacial mass transfer in binary liquid-liquid systems. *International Journal of Heat and Mass Transfer*, 43(6):1025 – 1034, 2000.
- [3] D Agble and M.A Mendes-Tatsis. The prediction of Marangoni convection in binary liquid-liquid systems with added surfactants. *International Journal of Heat and Mass Transfer*, 44(7):1439 – 1449, 2001.
- [4] D. K. Agble. *Interfacial mass transfer in binary-liquid systems*. PhD thesis, Imperial College London (University of London), 1998.
- [5] I. Aharon and B.D. Shaw. Marangoni instability of bi-component droplet gasification. *Physics of Fluids*, 8(7):1820–1827, 1996.
- [6] C. Almarcha, P. M.J. Trevelyan, P. Grosfils, and A. De Wit. Chemically driven hydrodynamic instabilities. *Physical review letters*, 104(4):044501, 2010.
- [7] R. Aris. On the dispersion of a solute in a fluid flowing through a tube. *Proceedings of the Royal Society of London. Series A. Mathematical and Physical Sciences*, 235(1200):67–77, 1956.
- [8] S. Backhaus, K. Turitsyn, and R.E. Ecke. Convective instability and mass transport of diffusion layers in a Hele-Shaw geometry. *Physical review letters*, 106(10):104501, 2011.
- [9] C. A. P. Bakker, P. M. van Buytenen, and W. J. Beek. Interfacial phenomena and mass transfer. *Chemical Engineering Science*, 21:1039 – 1046, 1966.
- [10] C.A.P. Bakker, F.H. Fentener van Vlissingen, and W.J. Beek. The influence of the driving force in liquid-liquid extraction - a study of mass transfer with and without interfacial turbulence under well-defined conditions. *Chemical Engineering Science*, 22(10):1349 – 1355, 1967.
- [11] G.I. Barenblatt. *Scaling, self-similarity, and intermediate asymptotics*. Cambridge University Press, 1996.
- [12] J.L. Barron, D.J. Fleet, and S.S. Beauchemin. Performance of optical flow techniques. *International journal of computer vision*, 12(1):43–77, 1994.
- [13] H.-J. Bart. *Reactive extraction*. Springer, 2001.
- [14] N Bassou and Yahya Rharbi. Role of Bénard- Marangoni instabilities during solvent evaporation in polymer surface corrugations. *Langmuir*, 25(1):624–632, 2008.
- [15] D. Bedeaux. Nonequilibrium thermodynamics and statistical physics of surfaces. *Advances in Chemical Physics*, 64(47):47–109, 1986.
- [16] Henri Bénard. Les tourbillons cellulaires dans une nappe liquide.-Méthodes optiques d’observation et d’enregistrement. *J. Phys. Theor. Appl.*, 10(1):254–266, 1901.

- [17] J.C. Berg. *An introduction to interfaces & colloids: the bridge to nanoscience*. World Scientific, 2010.
- [18] J.C. Berg and A. Acrivos. The effect of surface active agents on convection cells induced by surface tension. *Chemical Engineering Science*, 20(8):737 – 745, 1965.
- [19] J.C. Berg, M. Boudart, and A. Acrivos. Natural convection in pools of evaporating liquids. *Journal of Fluid Mechanics*, 24(04):721–735, 1966.
- [20] J.C. Berg and C.R. Morig. Density effects in interfacial convection. *Chemical Engineering Science*, 24:937 – 946, 1969.
- [21] S. Berg. Marangoni-driven spreading along liquid-liquid interfaces. *Physics of Fluids*, 21:032105, 2009.
- [22] M. Bestehorn. Phase and amplitude instabilities for Bénard-Marangoni convection in fluid layers with large aspect ratio. *Physical Review E*, 48(5):3622–3634, 1993.
- [23] M. Bestehorn. Square patterns in Bénard-Marangoni convection. *Physical review letters*, 76(1):46–49, 1996.
- [24] W. Bi, X. Wu, and E.K.L. Yeow. Unconventional multiple ring structure formation from evaporation-induced self-assembly of polymers. *Langmuir*, 28(30):11056–11063, 2012.
- [25] R. B. Bird, W.E. Stewart, and E.N. Lightfoot. *Transport phenomena*. John Wiley & Sons, Singapore, 2002.
- [26] R.V. Birikh, A.L. Zuev, K.G. Kostarev, and R.N. Rudakov. Convective self-oscillations near an air-bubble surface in a horizontal rectangular channel. *Fluid Dynamics*, 41(4):514–520, 2006.
- [27] L.M. Blair and J.A. Quinn. The onset of cellular convection in a fluid layer with time-dependent density gradients. *J. Fluid Mech*, 36(part 2):385–400, 1969.
- [28] T. Boeck, A. Nepomnyashchy, and I. Simanovskii. Three-dimensional simulations of water–mercury anticonvection. *Fluid Dyn. Mater. Process*, 4(11), 2008.
- [29] T. Boeck, A. Nepomnyashchy, I. Simanovskii, A. Golovin, L. Braverman, and A. Thess. Three-dimensional convection in a two-layer system with anomalous thermocapillary effect. *Physics of Fluids*, 14:3899, 2002.
- [30] T. Boeck and A. Thess. Bénard-Marangoni convection at low prandtl number. *Journal of Fluid Mechanics*, 399:251–275, 1999.
- [31] Thomas Boeck. *Bénard-Marangoni convection at low Prandtl number: Results of direct numerical simulations*. PhD thesis, TU-Ilmenau, 2000.
- [32] W. Boos and A. Thess. Thermocapillary flow in a Hele-Shaw cell. *Journal of Fluid Mechanics*, 352:305–330, 1997.
- [33] R. Borcia and M. Bestehorn. Phase-field simulations for evaporation with convection in liquid-vapor systems. *The European Physical Journal B-Condensed Matter and Complex Systems*, 44(1):101–108, 2005.
- [34] R. Borcia and M. Bestehorn. Phase-field simulations for drops and bubbles. *Physical Review E*, 75(5):056309, 2007.
- [35] R. Borcia and M. Bestehorn. Different behaviors of delayed fusion between drops with miscible liquids. *Physical Review E*, 82(3):036312, 2010.
- [36] J. Bragard and M.G. Velarde. Bénard–Marangoni convection: planforms and related theoretical predictions. *Journal of Fluid Mechanics*, 368(1):165–194, 1998.
- [37] D.A. Bratsun and A. De Wit. On Marangoni convective patterns driven by an exothermic chemical reaction in two-layer systems. *Physics of Fluids*, 16:1082–1096, 2004.

- [38] D.A. Bratsun and A. De Wit. Buoyancy-driven pattern formation in reactive immiscible two-layer systems. *Chemical engineering science*, 66(22):5723–5734, 2011.
- [39] P. L. T. Brian, J. E. Vivian, and S. T. Mayr. Cellular convection in desorbing surface tension-lowering solutes from water. *Industrial & Engineering Chemistry Fundamentals*, 10(1):75–83, 1971.
- [40] M. A. Budroni, L. A. Riolfo, L. Lemaigre, F. Rossi, M. Rustici, and Anne De Wit. Chemical control of hydrodynamic instabilities in partially miscible two-layer systems. *The journal of physical chemistry letters*, 5(5):875–881, 2014.
- [41] F.H. Busse. Non-linear properties of thermal convection. *Reports on Progress in Physics*, 41(12):1929–1967, 1978.
- [42] C. Canuto, M.Y. Hussaini, A. Quarteroni, and T.A. Zang. *Spectral methods in fluid dynamics*. Springer-Verlag, 1988.
- [43] H.S. Carslaw and J.C. Jaeger. *Conduction of heat in solids*, volume 2. Clarendon Press Oxford, 1959.
- [44] P. Cerisier, C. Jamond, J. Pantaloni, and C. Perez-Garcia. Stability of roll and hexagonal patterns in Bénard–Marangoni convection. *Physics of Fluids (1958-1988)*, 30(4):954–959, 1987.
- [45] S. Chandrasekhar. *Hydrodynamic and hydromagnetic stability*. Courier Dover Publications, 2013.
- [46] F. Chauvet, S. Dehaeck, and P. Colinet. Threshold of Bénard-Marangoni instability in drying liquid films. *EPL (Europhysics Letters)*, 99:34001, 2012.
- [47] S. Chen, B. Fu, X. Yuan, H. Zhang, W. Chen, and K. Yu. Lattice Boltzmann method for simulation of solutal interfacial convection in gas-liquid system. *Industrial & Engineering Chemistry Research*, 51:10955–10967, 2012.
- [48] C.K. Choi, K.H. Kang, M.C. Kim, and I.G. Hwang. Convective instabilities and transport properties in horizontal fluid layers. *Korean Journal of Chemical Engineering*, 15(2):192–198, 1998.
- [49] P. Colinet, F. Chauvet, and S. Dehaeck. Genesis of Bénard-Marangoni patterns in thin liquid films drying into air. In R.G. Rubio, Y.S. Ryazantsev, V.M. Starov, G.-X. Huang, A. P. Chetverikov, P. Arena, A.A. Nepomnyashchy, A. Ferrus, and E.G. Morozov, editors, *Without Bounds: A Scientific Canvas of Nonlinearity and Complex Dynamics*, Understanding Complex Systems, pages 95–104. Springer Berlin Heidelberg, 2013.
- [50] P. Colinet, J.C. Legros, M.G. Velarde, and I. Prigogine. *Nonlinear dynamics of surface-tension-driven instabilities*. Wiley Online Library, 2001.
- [51] J. Crank. *The mathematics of diffusion*, Clarendon. Oxford, 1975.
- [52] E.L. Cussler. *Diffusion: mass transfer in fluid systems*. Cambridge university press, 2003.
- [53] H. Daiguji, E. Hihara, and T. Saito. Mechanism of absorption enhancement by surfactant. *International journal of heat and mass transfer*, 40(8):1743–1752, 1997.
- [54] P.C. Dauby and G. Lebon. Bénard–Marangoni instability in rigid rectangular containers. *Journal of Fluid Mechanics*, 329:25–64, 1996.
- [55] I.F. Davenport and C.J. King. Marangoni stabilization of density-driven convection. *Chemical Engineering Science*, 28(2):645–647, 1973.
- [56] S.H. Davis. Thermocapillary instabilities. *Annual Review of Fluid Mechanics*, 19(1):403–435, 1987.
- [57] P. De Groot, S.R. and Mazur. *Non-equilibrium thermodynamics*. Dover Publications, 1984.

- [58] E.S.P. De Ortiz and H. Sawistowski. Stability analysis of liquid-liquid systems under conditions of simultaneous heat and mass transfer. *Chemical Engineering Science*, 30(12):1527–1528, 1975.
- [59] A. De Wit, K. Eckert, and S. Kalliadasis. Introduction to the focus issue: Chemo-hydrodynamic patterns and instabilities. *Chaos-Woodbury*, 22(3):037101, 2012.
- [60] R.D. Deegan, O. Bakajin, T.F. Dupont, G. Huber, S.R. Nagel, and T.A. Witten. Capillary flow as the cause of ring stains from dried liquid drops. *Nature*, 389(6653):827–829, 1997.
- [61] C.R. Doering and J.D. Gibbon. *Applied analysis of the Navier-Stokes equations*, volume 12. Cambridge University Press, 1995.
- [62] F. Doumenc, E. Chénier, B. Trouette, T. Boeck, C. Delcarte, B. Guerrier, and M. Rossi. Free convection in drying binary mixtures: Solutal versus thermal instabilities. *International Journal of Heat and Mass Transfer*, 63(0):336 – 350, 2013.
- [63] S.S. Dukhin, G. Kretzschmar, and R. Miller. *Dynamics of adsorption at liquid interfaces: theory, experiment, application*, volume 1. Elsevier Science, 1995.
- [64] K. Eckert, M. Acker, and Y. Shi. Chemical pattern formation driven by a neutralization reaction. i. mechanism and basic features. *Physics of Fluids*, 16(2):385–399, 2004.
- [65] K. Eckert, M. Acker, R. Tadmouri, and V. Pimienta. Chemo-Marangoni convection driven by an interfacial reaction: Pattern formation and kinetics. *Chaos: An Interdisciplinary Journal of Nonlinear Science*, 22(3):037112–037112, 2012.
- [66] K. Eckert, M. Bestehorn, and A. Thess. Square cells in surface-tension-driven Bénard convection: experiment and theory. *Journal of Fluid Mechanics*, 356:155–197, 1998.
- [67] K. Eckert and A. Grahn. Plume and finger regimes driven by an exothermic interfacial reaction. *Physical review letters*, 82(22):4436, 1999.
- [68] K. Eckert, L. Rongy, and A. De Wit. $A + b \rightarrow c$ reaction fronts in Hele-Shaw cells under modulated gravitational acceleration. *Physical Chemistry Chemical Physics*, 14(20):7337–7345, 2012.
- [69] D.A. Edwards, H. Brenner, and D.T. Wasan. *Interfacial transport processes and rheology*. Butterworth-Heinemann, 1991.
- [70] A. Einstein. Über die von der molekularkinetischen Theorie der Wärme geforderte Bewegung von in ruhenden Flüssigkeiten suspendierten Teilchen. *Annalen der Physik*, 322(8):549–560, 1905.
- [71] R.F. Engberg, M. Wegener, and E.Y. Kenig. The influence of Marangoni convection on fluid dynamics of oscillating single rising droplets. *Chemical Engineering Science*, 117:114–124, 2014.
- [72] J.B. Engel, A. and Swift. Planform selection in two-layer Bénard-Marangoni convection. *Physical Review E*, 62(5):6540, 2000.
- [73] A. Fane and H. Sawistowski. Surface tension effects in sieve-plate distillation. *Chemical Engineering Science*, 23(8):943–945, 1968.
- [74] R. Finn. Capillary surface interfaces. *Notices of the AMS*, 46(7):770–781, 1999.
- [75] F. Gallaire, P. Meliga, P. Laure, and C.N. Baroud. Marangoni induced force on a drop in a hele shaw cell. *Physics of Fluids (1994-present)*, 26(6):062105, 2014.
- [76] A.N. Garazo and M.G. Velarde. Dissipative Korteweg-de Vries description of Marangoni-Bénard oscillatory convection. *Physics of Fluids A*, 3:2295–2300, 1991.
- [77] A.C. Giere. Transient heat flow in a composite slab-constant flux, zero flux boundary conditions. *Applied Scientific Research, Section A*, 14(1):191–198, 1965.

- [78] A.A. Golovin. Mass transfer under interfacial turbulence: kinetic regulaties. *Chemical Engineering Science*, 47(8):2069 – 2080, 1992.
- [79] A.A. Golovin, A. Nir, and L.M. Pismen. Spontaneous motion of two droplets caused by mass transfer. *Industrial & engineering chemistry research*, 34(10):3278–3288, 1995.
- [80] A. Grahn. Two-dimensional numerical simulations of Marangoni-Bénard instabilities during liquid-liquid mass transfer in a vertical gap. *Chemical Engineering Science*, 61:3586 – 3592, 2006.
- [81] Alexander Grahn. *Strömungsinstabilitäten bei Stoffübergang und chemischer Reaktion an der ebenen Grenzfläche zwischen zwei nicht mischbaren Flüssigkeiten*. PhD thesis, TU-Dresden, 2004.
- [82] B. Gross and A.N. Hixson. Interferometric study of interfacial turbulence accompanying mass transfer. water-acetic acid-benzene. *Industrial & Engineering Chemistry Fundamentals*, 8(2):296–302, 1969.
- [83] B. Gross and A.N. Hixson. Marangoni instability with unsteady diffusion in the undisturbed state. *Industrial & Engineering Chemistry Fundamentals*, 8(2):288–296, 1969.
- [84] J.S. Gulliver. *Introduction to chemical transport in the environment*. Cambridge University Press, 2007.
- [85] M. Hampe. Flüssig/Flüssig-Extraktion: Einsatzgebiete und Lösungsmittel-Auswahl. *Chemie Ingenieur Technik*, 50(9):647–655, 1978.
- [86] D. J. Harris and J. A. Lewis. Marangoni effects on evaporative lithographic patterning of colloidal films. *Langmuir*, 24:3681–3685, 2008.
- [87] H. Heines and J.W. Westwater. The effect of heats of solution on Marangoni convection. *International Journal of Heat and Mass Transfer*, 15(11):2109 – 2117, 1972.
- [88] A. Heinze, K. Eckert, M.J.B. Hauser, and S. Odenbach. A wavelet and Zernike-polynomial-based shearing interferometry approach to analyse hydrodynamic instabilities at interfaces. *Acta Astronautica*, 68(7):707–716, 2011.
- [89] M. Hennenberg, A. Sanfeld, and P. M. Bisch. Adsorption-desorption barrier, diffusional exchanges and surface instabilities of longitudinal waves for aperiodic regimes. *AIChE Journal*, 27(6):1002–1008, 1981.
- [90] K.-L. Ho and H.-C. Chang. On nonlinear doubly-diffusive marangoni instability. *AIChE journal*, 34(5):705–722, 1988.
- [91] B.K. Horn and B.G. Schunck. Determining optical flow. In *1981 Technical Symposium East*, pages 319–331. International Society for Optics and Photonics, 1981.
- [92] R.N Horne and F. Rodriguez. Dispersion in tracer flow in fractured geothermal systems. *Geophysical Research Letters*, 10(4):289–292, 1983.
- [93] M. Hozawa, J. Inoue, M. and Sato, T. Tsukada, and N. Imaishi. Marangoni convection during steam absorption into aqueous libr solution with surfactant. *Journal of chemical engineering of Japan*, 24(2):209–214, 1991.
- [94] H. Hu and R. G. Larson. Marangoni effect reverses coffee-ring depositions. *The Journal of Physical Chemistry B*, 110:7090–7094, 2006.
- [95] J.A.M. Huethorst and J. Marra. Motion of Marangoni-contracted water drops across inclined hydrophilic surfaces. *Langmuir*, 7(11):2756–2763, 1991.
- [96] N. Imaishi and K. Fujikawa. Theoretical study of the stability of two-fluid layers. *Journal of Chemical Engineering of Japan*, 7(2):81–87, 1974.

- [97] N. Imaishi, Y. Suzuki, M. Hozawa, and K. Fujinawa. Interfacial turbulence in gas-liquid mass transfer. *International Chemical Engineering*, 22(4):659–665, 1982.
- [98] N. Jarrige, I.B. Malham, J. Martin, N. Rakotomalala, D. Salin, and L. Talon. Numerical simulations of a buoyant autocatalytic reaction front in tilted Hele-Shaw cells. *Physical Review E*, 81(6):066311, 2010.
- [99] D. Johnson and R. Narayanan. A tutorial on the Rayleigh–Marangoni–Bénard problem with multiple layers and side wall effects. *Chaos: An Interdisciplinary Journal of Nonlinear Science*, 9(1):124–140, 1999.
- [100] A. Juel, J.M. Burgess, W.D. McCormick, J.B. Swift, and H.J. Swinney. Surface tension-driven convection patterns in two liquid layers. *Physica D: Nonlinear Phenomena*, 143(1):169–186, 2000.
- [101] K.H. Kang, C.K. Choi, and I.G. Hwang. Onset of solutal Marangoni convection in a suddenly desorbing liquid layer. *AIChE journal*, 46(1):15–23, 2000.
- [102] S. Karpitschka and H. Riegler. Noncoalescence of sessile drops from different but miscible liquids: Hydrodynamic analysis of the twin drop contour as a self-stabilizing traveling wave. *Physical Review Letters*, 109(6):066103, 2012.
- [103] S. Karpitschka and H. Riegler. Sharp transition between coalescence and non-coalescence of sessile drops. *Journal of Fluid Mechanics*, 743:R1, 2014.
- [104] M. Khosravi, B. Rostami, M. Emadi, and E. Roayaei. Marangoni flow: An unknown mechanism for oil recovery during near-miscible co 2 injection. *Journal of Petroleum Science and Engineering*, 125:263–268, 2015.
- [105] J. Kim, Y.T. Kang, and C.K. Choi. Effects of gas phase and additive properties on Marangoni instability for absorption process in a horizontal fluid layer. *International journal of refrigeration*, 27(2):140–149, 2004.
- [106] J.-K. Kim, J.Y. Jung, and Y.T. Kang. The effect of nano-particles on the bubble absorption performance in a binary nanofluid. *International journal of refrigeration*, 29(1):22–29, 2006.
- [107] M.C. Kim, D.Y. Yoon, and C.K. Choi. Onset of buoyancy-driven instability in gas diffusion systems. *Industrial & engineering chemistry research*, 45(21):7321–7328, 2006.
- [108] V.S. Kislik. *Solvent extraction: classical and novel approaches*. Elsevier, 2011.
- [109] H. Kitahata, N. Yoshinaga, K. H. Nagai, and Y. Sumino. Spontaneous motion of a droplet coupled with a chemical wave. *Phys. Rev. E*, 84:015101, 2011.
- [110] T. Köllner, M. Rossi, F. Broer, and T. Boeck. Chemical convection in the methylene-blue–glucose system: Optimal perturbations and three-dimensional simulations. *Physical Review E*, 90(5):053004, 2014.
- [111] T. Köllner, K. Schwarzenberger, K. Eckert, and T. Boeck. Multiscale structures in solutal Marangoni convection: Three-dimensional simulations and supporting experiments. *Physics of Fluids*, 25:092109, 2013.
- [112] T. Köllner, K. Schwarzenberger, K. Eckert, and T. Boeck. Solutal Marangoni convection in a Hele-Shaw geometry: Impact of orientation and gap width. *The European Physical Journal Special Topics*, 224(2):261–276, 2015.
- [113] T. Köllner, K. Schwarzenberger, K. Eckert, and T. Boeck. The eruptive regime of mass transfer-driven Rayleigh-Marangoni convection. *Journal of Fluid Mechanics*, in press.
- [114] E.L. Koschmieder and M.I. Biggerstaff. Onset of surface-tension-driven Bénard convection. *Journal of Fluid Mechanics*, 167:49–64, 1986.

- [115] E.L. Koschmieder and S.A. Prahl. Surface-tension-driven Bénard convection in small containers. *Journal of Fluid Mechanics*, 215(1):571–583, 1990.
- [116] K.G. Kostarev, A.V. Shmyrov, A.L. Zuev, and A. Viviani. Convective and diffusive surfactant transfer in multiphase liquid systems. *Experiments in Fluids*, 51(2):457–470, 2011.
- [117] N.M. Kovalchuk. Spontaneous oscillations due to solutal Marangoni instability: air/water interface. *Central European Journal of Chemistry*, 10(5):1423–1441, 2012.
- [118] N.M. Kovalchuk, V. Pimienta, R. Tadmouri, R. Miller, and D. Vollhardt. Ionic strength and pH as control parameters for spontaneous surface oscillations. *Langmuir*, 28(17):6893–6901, 2012.
- [119] N.M. Kovalchuk and D. Vollhardt. Marangoni instability and spontaneous non-linear oscillations produced at liquid interfaces by surfactant transfer. *Advances in Colloid and Interface Science*, 120(13):1 – 31, 2006.
- [120] N.M. Kovalchuk and D. Vollhardt. Spontaneous nonlinear oscillation produced by alcohol transfer through water/alkane interface: An experimental study. *Colloids and Surfaces A: Physicochemical and Engineering Aspects*, 291:101 – 109, 2006.
- [121] N.M. Kovalchuk and D. Vollhardt. Oscillation of interfacial tension produced by transfer of nonionic surfactant through the liquid/liquid interface. *The Journal of Physical Chemistry C*, 112(24):9016–9022, 2008.
- [122] H. Kroepelin and H.J. Neumann. Über die Entstehung von Grenzflächeneruptionen bei dem Stoffaustausch an Tropfen. *Naturwissenschaften*, 43(15):347–348, 1956.
- [123] H. Kroepelin and H.J. Neumann. Eruptiver Stoffaustausch an ebenen Grenzflächen. *Naturwissenschaften*, 44(10):304–304, 1957.
- [124] H.C. Kuhlmann and H.J. Rath. Hydrodynamic instabilities in cylindrical thermocapillary liquid bridges. *Journal of Fluid Mechanics*, 247:247–274, 1993.
- [125] I. Langmuir and D.B. Langmuir. The effect of monomolecular films on the evaporation of ether solutions. *The Journal of Physical Chemistry*, 31(11):1719–1731, 1927.
- [126] M. Lappa. *Thermal convection: patterns, evolution and stability*. John Wiley & Sons, 2009.
- [127] M. Lappa and C. Piccolo. Higher modes of the mixed buoyant-Marangoni unstable convection originated from a droplet dissolving in a liquid/liquid system with miscibility gap. *Physics of Fluids*, 16(12):4262–4272, 2004.
- [128] M. Lappa and L. Piccolo, C. and Carotenuto. Mixed buoyant-Marangoni convection due to dissolution of a droplet in a liquid–liquid system with miscibility gap. *European Journal of Mechanics-B/Fluids*, 23(5):781–794, 2004.
- [129] D. Lavabre, Vincent Pradines, Jean-Claude M., and Veronique Pimienta. Periodic Marangoni instability in surfactant (CTAB) liquid/liquid mass transfer. *The Journal of Physical Chemistry B*, 109(15):7582–7586, 2005.
- [130] M. Leconte, J. Martin, N. Rakotomalala, D. Salin, and Y.C. Yortsos. Mixing and reaction fronts in laminar flows. *The Journal of Chemical Physics*, 120(16):7314–7321, 2004.
- [131] K.S. Lee, N. Ivanova, V.M. Starov, N. Hilal, and V. Dutschk. Kinetics of wetting and spreading by aqueous surfactant solutions. *Advances in Colloid and Interface Science*, 144:54–65, 2008.
- [132] A.J. Leo and C. Hansch. Linear free energy relations between partitioning solvent systems. *The Journal of Organic Chemistry*, 36(11):1539–1544, 1971.
- [133] J.B. Lewis and H.R.C. Pratt. Oscillating droplets. *Nature*, 171:1155–1156, 1953.
- [134] J. Li and P.W. Carr. Accuracy of empirical correlations for estimating diffusion coefficients in aqueous organic mixtures. *Analytical chemistry*, 69(13):2530–2536, 1997.

- [135] D.R. Lide. *CRC handbook of chemistry and physics: a ready-reference book of chemical and physical data*. CRC Pr I Llc, 2004.
- [136] G. Liger-Belair. The physics behind the fizz in champagne and sparkling wines. *The European Physical Journal Special Topics*, 201(1):1–88, 2012.
- [137] H. Linde. Untersuchungen über den Stoffübergang an ebenen und waagerechten flüssig-flüssig-Phasengrenzen unter der Bedingung starker erzwungener Konvektion bei verschiedenartigem Einsatz grenzflächenaktiver Stoffe. *Fette, Seifen, Anstrichmittel*, 60(9):826–829, 1958.
- [138] H. Linde. Zur Kinetik des Stoffüberganges über die Grenzflächen zweier flüssiger Phasen: III. Freie Grenzflächenkonvektion bei lebhafter erzwungener Konvektion. *Monatsberichte der Deutschen Akademie der Wissenschaften zu Berlin*, 1:699–711, 1959.
- [139] H. Linde. Versuche zur Deutung des Einflusses der erzwungenen Konvektion auf die Grenzflächendynamik beim Stoffübergang. *Abhandlungen der Deutschen Akademie der Wissenschaften zu Berlin*, 6b:710–719, 1966.
- [140] H. Linde and M. Kunkel. Einige neue qualitative Beobachtungen beim oszillatorischen Regime der Marangoni-Instabilität. *Heat and Mass Transfer*, 2:60–64, 1969.
- [141] H. Linde, S. Pfaff, and C. Zirkel. Strömunguntersuchungen zur hydrodynamischen Instabilität flüssig-gasförmiger Phasengrenzen mit Hilfe der Kapillarspaltmethode. *Zeitschrift für physikalische Chemie*, 225:72–100, 1964.
- [142] H. Linde, P. Schwartz, and H. Wilke. Dissipative structures and nonlinear kinetics of the Marangoni-instability. In *Dynamics and Instability of Fluid Interfaces*. Springer, 1979.
- [143] H. Linde and E. Schwarz. Untersuchungen zur Charakteristik der freien Grenzflächenkonvektion beim Stoffübergang an fluiden Grenzen. *Zeitschrift für physikalische Chemie*, 224:331–352, 1963.
- [144] H. Linde and E. Schwarz. Untersuchungen zur Charakteristik der freien Grenzflächenkonvektion beim Stoffübergang an fluiden Grenzen. *Zeitschrift für physikalische Chemie*, 224:331–352, 1963.
- [145] H. Linde, E. Schwarz, and K. Gröger. Zum Auftreten des Oszillatorischen Regimes der Marangoni-Instabilität beim Stoffübergang. *Chemical Engineering Science*, 22(6):823 – 836, 1967.
- [146] H. Linde, K. Schwarzenberger, and K. Eckert. Pattern formation emerging from stationary solutal Marangoni instability: A roadmap through the underlying hierarchic structures. In R.G. Rubio, Y.S. Ryazantsev, V.M. Starov, G.-X. Huang, A.P. Chetverikov, P. Arena, A.A. Nepomnyashchy, A. Ferrus, and E.G. Morozov, editors, *Without Bounds: A Scientific Canvas of Nonlinearity and Complex Dynamics*, Understanding Complex Systems. Springer, 2013.
- [147] H. Linde, M. G. Velarde, W. Waldhelm, K. Loeschke, and A. Wierschem. On the various wave motions observed at a liquid interface due to Marangoni stresses and instability. *Industrial & Engineering Chemistry Research*, 44:1396–1412, 2005.
- [148] M. Loewenthal. XI. tears of strong wine. *The London, Edinburgh, and Dublin Philosophical Magazine and Journal of Science*, 12(77):462–472, 1931.
- [149] V. Loodts, C. Thomas, L. Rongy, and A. De Wit. Control of convective dissolution by chemical reactions: General classification and application to CO₂ dissolution in reactive aqueous solutions. *Physical review letters*, 113(11):114501, 2014.
- [150] Brendan D MacDonald. *The onset of Marangoni convection for evaporating liquids*. PhD thesis, University of Toronto, 2012.
- [151] T. Magnussen, P. Rasmussen, and Aage Fredenslund. Unifac parameter table for prediction of liquid-liquid equilibriums. *Industrial & Engineering Chemistry Process Design and Development*, 20(2):331–339, 1981.

- [152] Z. Mao, P. Lu, G. Zhang, and C. Yang. Numerical simulation of the Marangoni effect with inter-phase mass transfer between two planar liquid layers. *Chinese Journal of Chemical Engineering*, 16(2):161–170, 2008.
- [153] Carl Marangoni. Über die Ausbreitung der Tropfen einer Flüssigkeit auf der Oberfläche einer anderen. *Annalen der Physik*, 219:337–354, 1871.
- [154] J. Marra and J.A.M. Huethorst. Physical principles of Marangoni drying. *Langmuir*, 7(11):2748–2755, 1991.
- [155] J. Martin, N. Rakotomalala, and D. Salin. Gravitational instability of miscible fluids in a Hele-Shaw cell. *Physics of Fluids (1994-present)*, 14(2):902–905, 2002.
- [156] M. Medale and P. Cerisier. Numerical simulation of Bénard-Marangoni convection in small aspect ratio containers. *Numerical heat transfer. Part A, Applications*, 42(1-2):55–72, 2002.
- [157] M. Medale and P. Cerisier. Influence of container shape and size on surface-tension-driven Bénard convection. *The European Physical Journal Special Topics*, 224(2):217–227, 2015.
- [158] MA Mendes-Tatsis and ES Perez De Ortiz. Spontaneous interfacial convection in liquid-liquid binary systems under microgravity. *Proceedings of the Royal Society of London. Series A: Mathematical and Physical Sciences*, 438(1903):389–396, 1992.
- [159] D. Merkt and M. Bestehorn. Bénard–Marangoni convection in a strongly evaporating fluid. *Physica D: Nonlinear Phenomena*, 185(3):196–208, 2003.
- [160] W. Merzkirch. *Flow visualization*. Academic Press, 1987.
- [161] T. Míšek, R. Berger, and J. Schröter. Standard test systems for liquid extraction studies. *EFCE Publ. Ser*, 46(1), 1985.
- [162] A.A. Nepomnyashchy and M.G. Velarde. A three-dimensional description of solitary waves and their interaction in Marangoni–Bénard layers. *Physics of Fluids*, 6:187, 1994.
- [163] J.C. Nepomnyashchy, A. and Legros and I. Simanovskii. *Interfacial convection in multilayer systems*. Springer, 2006.
- [164] J.C. Nepomnyashchy, A. and Legros and I. Simanovskii. *Interfacial convection in multilayer systems*. Springer, 2012.
- [165] D.A. Nield. Surface tension and buoyancy effects in cellular convection. *Journal of Fluid Mechanics*, 19(03):341–352, 1964.
- [166] A. Orell and J. W. Westwater. Spontaneous interfacial cellular convection accompanying mass transfer: Ethylene glycol-acetic acid-ethyl acetate. *AIChE Journal*, 8:350–356, 1962.
- [167] O. Ou Ramdane and D. Quéré. Thickening factor in Marangoni coating. *Langmuir*, 13(11):2911–2916, 1997.
- [168] D. Özmen and S. Çehreli. Phase equilibria of water+ 1-propanol+ solvent (n-amyl acetate, cyclohexanol, and cyclohexyl acetate) at $t = 298.2$ k. *Fluid phase equilibria*, 253(1):61–66, 2007.
- [169] H.J. Palmer and J.C. Berg. Convective instability in liquid pools heated from below. *Journal of Fluid Mechanics*, 47(04):779–787, 1971.
- [170] H.J. Palmer and J.C. Berg. Hydrodynamic stability of surfactant solutions heated from below. *Journal of Fluid Mechanics*, 51(2):385–402, 1972.
- [171] J. Patterson and J. Imberger. Unsteady natural convection in a rectangular cavity. *Journal of Fluid Mechanics*, 100(01):65–86, 1980.
- [172] J.R.A. Pearson. On convection cells induced by surface tension. *Journal of Fluid Mechanics*, 4(05):489–500, 1958.

- [173] E.S. Perez de Ortiz and H. Sawistowski. Interfacial stability of binary liquid-liquid systems - I. Stability analysis. *Chemical Engineering Science*, 28(11):2051 – 2061, 1973.
- [174] E.S. Perez de Ortiz and H. Sawistowski. Interfacial stability of binary liquid-liquid systems - ii. stability behaviour of selected systems. *Chemical Engineering Science*, 28(11):2063 – 2069, 1973.
- [175] C.-Y. Petitjeans, P. and Chen, E. Meiburg, and T. Maxworthy. Miscible quarter five-spot displacements in a Hele-Shaw cell and the role of flow-induced dispersion. *Physics of Fluids (1994-present)*, 11(7):1705–1716, 1999.
- [176] R. Peyret. *Spectral methods for incompressible viscous flow*. Springer, 2002.
- [177] V. Pimienta, M. Brost, N. Kovalchuk, S. Bresch, and O. Steinbock. Complex shapes and dynamics of dissolving drops of dichloromethane. *Angewandte Chemie International Edition*, 50:10728–10731, 2011.
- [178] S.B. Pope. *Turbulent flows*. Cambridge university press, 2000.
- [179] C. Pozrikidis. *Boundary integral and singularity methods for linearized viscous flow*. Cambridge Univ Pr, 1992.
- [180] W.H. Press, S.A. Teukolsky, W.T. Vetterling, and B.P. Flannery. *Numerical recipes in C*, volume 2. Cambridge university press Cambridge, 1996.
- [181] S.J. Proctor, M.W. Biddulph, and K.R. Krishnamurthy. Effects of Marangoni surface tension forces on modern distillation packings. *AIChE journal*, 44(4):831–835, 1998.
- [182] Lord Rayleigh. Lix. on convection currents in a horizontal layer of fluid, when the higher temperature is on the under side. *The London, Edinburgh, and Dublin Philosophical Magazine and Journal of Science*, 32(192):529–546, 1916.
- [183] A. Rednikov, M.G. Colinet, P. and Velarde, and J.C. Legros. Rayleigh–Marangoni oscillatory instability in a horizontal liquid layer heated from above: coupling and mode mixing of internal and surface dilational waves. *Journal of fluid mechanics*, 405:57–77, 2000.
- [184] J. Reichenbach and H. Linde. Linear perturbation analysis of surface-tension-driven convection at a plane interface (Marangoni instability). *Journal of Colloid and Interface Science*, 84(2):433 – 443, 1981.
- [185] J.C. Robinson. *Infinite-dimensional dynamical systems: an introduction to dissipative parabolic PDEs and the theory of global attractors*, volume 28. Cambridge University Press, 2001.
- [186] L. Rongy and A. Assemat, P. and De Wit. Marangoni-driven convection around exothermic autocatalytic chemical fronts in free-surface solution layers. *Chaos: An Interdisciplinary Journal of Nonlinear Science*, 22(3):037106–037106, 2012.
- [187] Laurence Rongy. Influence of Marangoni and buoyancy convection on the propagation of reaction-diffusion fronts, 2008.
- [188] S. Ross and P. Becher. The history of the spreading coefficient. *Journal of colloid and interface science*, 149(2):575–579, 1992.
- [189] J.S. Rowlinson and B. Widom. *Molecular theory of capillarity*, volume 8. Dover Pubns, 2002.
- [190] C. Ruyer-Quil. Inertial corrections to the darcy law in a hele–shaw cell. *Comptes Rendus de l’Académie des Sciences-Series IIB-Mechanics*, 329(5):337–342, 2001.
- [191] H. Sawistowski. Interfacial phenomena. In C. Hanson, editor, *Recent Advances in Liquid-Liquid Extraction*. Pergamon Press, 1971.
- [192] A.A. Sayar. Liquid-liquid equilibria of some water+ 2-propanol+ solvent ternaries. *Journal of chemical and engineering data*, 36(1):61–65, 1991.

- [193] K. Schade, H. and Neemann. *Tensoranalysis*. Walter de Gruyter, 2009.
- [194] M.F. Schatz and G.P. Neitzel. Experiments on thermocapillary instabilities. *Annual review of fluid mechanics*, 33(1):93–127, 2001.
- [195] P.J. Schmid. Nonmodal stability theory. *Annu. Rev. Fluid Mech.*, 39:129–162, 2007.
- [196] B. Schmitt and W. von Wahl. Decomposition of solenoidal fields into poloidal fields, toroidal fields and the mean flow. applications to the boussinesq-equations. *The Navier-Stokes Equations II?Theory and Numerical Methods*, pages 291–305, 1992.
- [197] E. Schwarz. Zum Auftreten von Marangoni-Instabilität. *Wärme- und Stoffübertragung*, 3:131–133, 1970.
- [198] Erwin Schwarz. *Hydrodynamische Regime der Marangoni-Instabilität beim Stoffübergang über eine fluide Phasengrenze*. PhD thesis, HU Berlin, 1968.
- [199] K. Schwarzenberger, K. Eckert, and S. Odenbach. Relaxation oscillations between Marangoni cells and double diffusive fingers in a reactive liquid-liquid system. *Chemical Engineering Science*, 68:530–540, 2012.
- [200] K. Schwarzenberger, T. Köllner, T. Boeck, S. Odenbach, and K. Eckert. Hierarchical Marangoni roll cells: experiments and direct numerical simulations in three and two dimensions. In Mohammad Taeibi Rahni, Mohsen Karbaschi, and Reinhard Miller, editors, *Computational Methods for Complex Liquid-Fluid Interfaces*, number 5 in Progress in Colloid and Interface Science. CRC Press, 2015.
- [201] K. Schwarzenberger, T. Köllner, H. Linde, T. Boeck, S. Odenbach, and K. Eckert. Pattern formation and mass transfer under stationary solutal Marangoni instability. *Advances in Colloid and Interface Science*, 206:344 – 371, 2014.
- [202] K. Schwarzenberger, T. Köllner, H. Linde, S. Odenbach, T. Boeck, and K. Eckert. On the transition from cellular to wave-like patterns during solutal Marangoni convection. *The European Physical Journal Special Topics*, 219:121–130, 2013.
- [203] L.E. Scriven and C.V. Sternling. The Marangoni Effects. *Nature*, 187:186–188, 1960.
- [204] S. Semenov, V.M. Starov, R.G. Rubio, and M.G. Velarde. Computer simulations of evaporation of pinned sessile droplets: influence of kinetic effects. *Langmuir*, 28(43):15203–15211, 2012.
- [205] J.E. Seo, H.S. and McCray. Interfacial tension of chlorinated aliphatic dnapl mixtures as a function of organic phase composition. *Environmental science & technology*, 36(6):1292–1298, 2002.
- [206] Y. Sha, H. Chen, Y. Yin, S. Tu, L. Ye, and Y. Zheng. Characteristics of the Marangoni convection induced in initial quiescent water. *Industrial & Engineering Chemistry Research*, 49:8770–8777, 2010.
- [207] T. Sherwood and J. Wei. Interfacial phenomena in liquid extraction. *Industrial & Engineering Chemistry*, 49:1030–1034, 1957.
- [208] Y. Shi and K. Eckert. Acceleration of reaction fronts by hydrodynamic instabilities in immiscible systems. *Chemical Engineering Science*, 61:5523 – 5533, 2006.
- [209] Y. Shi and K. Eckert. A novel Hele-Shaw cell design for the analysis of hydrodynamic instabilities in liquid-liquid systems. *Chemical Engineering Science*, 63:3560–3563, 2008.
- [210] Ying Shi and Kerstin Eckert. Acceleration of reaction fronts by hydrodynamic instabilities in immiscible systems. *Chemical engineering science*, 61(17):5523–5533, 2006.
- [211] Y.D. Shikhmurzaev. *Capillary flows with forming interfaces*. CRC Press, 2007.

- [212] E.D. Siggia. High Rayleigh number convection. *Annual review of fluid mechanics*, 26(1):137–168, 1994.
- [213] K. Sigwart and H. Nassenstein. Vorgänge an der Grenzfläche zweier flüssiger Phasen. *Naturwissenschaften*, 42:458–459, 1955.
- [214] S. Slavtchev, M. Hennenberg, J.-C. Legros, and G. Lebon. Stationary solutal Marangoni instability in a two-layer system. *Journal of Colloid and Interface Science*, 203(2):354 – 368, 1998.
- [215] S. Slavtchev, P. Kalitzova-Kurteva, and M.A. Mendes. Marangoni instability of liquidliquid systems with a surface-active solute. *Colloids and Surfaces A: Physicochemical and Engineering Aspects*, 282283:37 – 49, 2006.
- [216] S. Slavtchev and M.A. Mendes. Marangoni instability in binary liquid-liquid systems. *International Journal of Heat and Mass Transfer*, 47(1416):3269 – 3278, 2004.
- [217] K.A. Smith. On convective instability induced by surface-tension gradients. *Journal of Fluid Mechanics*, 24(02):401–414, 1966.
- [218] M.K. Smith and S.H. Davis. Instabilities of dynamic thermocapillary liquid layers. part 1. convective instabilities. *Journal of Fluid Mechanics*, 132:119–144, 1983.
- [219] C.V. Sternling and L.E. Scriven. Interfacial turbulence: Hydrodynamic instability and the Marangoni effect. *AIChE Journal*, 5(4):514–523, 1959.
- [220] T. Still, P.J. Yunker, and A.G. Yodh. Surfactant-induced Marangoni eddies alter the coffee-rings of evaporating colloidal drops. *Langmuir*, 28(11):4984–4988, 2012.
- [221] C.-Y. Sun and G.-J. Chen. Measurement of interfacial tension for the CO₂ injected crude oil+reservoir water system. *Journal of Chemical & Engineering Data*, 50(3):936–938, 2005.
- [222] Z.F. Sun. Onset of Rayleigh–Bénard–Marangoni convection with time-dependent nonlinear concentration profiles. *Chemical Engineering Science*, 68(1):579–594, 2012.
- [223] R. Tadmouri, N.M. Kovalchuk, V. Pimienta, D. Vollhardt, and J.-C. Micheau. Transfer of oxyethylated alcohols through water/heptane interface: Transition from non-oscillatory to oscillatory behaviour. *Colloids and Surfaces A: Physicochemical and Engineering Aspects*, 354:134 – 142, 2010.
- [224] G. Taylor. Dispersion of soluble matter in solvent flowing slowly through a tube. *Proceedings of the Royal Society of London A: Mathematical, Physical and Engineering Sciences*, 219(1137):186–203, 1953.
- [225] R. Taylor and R. Krishna. *Multicomponent mass transfer*, volume 2. John Wiley & Sons, New York, 1993.
- [226] A. Thess and S.A. Orszag. Surface-tension-driven Bénard convection at infinite Prandtl number. *Journal of Fluid Mechanics*, 283:201–230, 1995.
- [227] A. Thess, D. Sporn, and B. Jüttner. A two-dimensional model for slow convection at infinite Marangoni number. *Journal of Fluid Mechanics*, 331:283–312, 1997.
- [228] U. Thiele and K. Eckert. Stochastic geometry of polygonal networks: An alternative approach to the hexagon-square transition in Bénard convection. *Physical Review E*, 58(3):3458, 1998.
- [229] J. Thomson. On certain curious motions observable at the surfaces of wine and other alcoholic liquors. *The London, Edinburgh, and Dublin Philosophical Magazine and Journal of Science*, 10(67):330–333, 1855.
- [230] W.A. Tokaruk, T.C.A. Molteno, and S.W. Morris. Bénard-Marangoni convection in two-layered liquids. *Physical review letters*, 84(16):3590, 2000.

- [231] K.E. Uguz and R. Narayanan. Instability in evaporative binary mixtures. I. the effect of solutal Marangoni convection. *Physics of Fluids*, 24:094101, 2012.
- [232] M. Wanschura, V.M. Shevtsova, H.C. Kuhlmann, and H.J. Rath. Convective instability mechanisms in thermocapillary liquid bridges. *Physics of Fluids (1994-present)*, 7(5):912–925, 1995.
- [233] A.F.H. Ward and L.H. Brooks. Diffusion across interfaces. *Trans. Faraday Soc.*, 48:1124–1136, 1952.
- [234] M. Wegener. A numerical parameter study on the impact of Marangoni convection on the mass transfer at buoyancy-driven single droplets. *International Journal of Heat and Mass Transfer*, 71:769–778, 2014.
- [235] M. Wegener, M. Fevre, A.R. Paschedag, and M. Kraume. Impact of Marangoni instabilities on the fluid dynamic behaviour of organic droplets. *International Journal of Heat and Mass Transfer*, 52(1112):2543 – 2551, 2009.
- [236] M. Wegener and A.R. Paschedag. The effect of soluble anionic surfactants on rise velocity and mass transfer at single droplets in systems with Marangoni instabilities. *International Journal of Heat and Mass Transfer*, 55(56):1561 – 1573, 2012.
- [237] M. Wegener, A.R. Paschedag, and M. Kraume. Mass transfer enhancement through Marangoni instabilities during single drop formation. *International Journal of Heat and Mass Transfer*, 52(1112):2673 – 2677, 2009.
- [238] Mirco Wegener. *Der Einfluss der konzentrationsinduzierten Marangonikonvektion auf den instationären Impuls-und Stofftransport an Einzeltropfen*. PhD thesis, TU Berlin, 2009.
- [239] J. Westerweel. Fundamentals of digital particle image velocimetry. *Measurement science and technology*, 8(12):1379, 1997.
- [240] C.R. Wilke and P. Chang. Correlation of diffusion coefficients in dilute solutions. *AIChE Journal*, 1(2):264–270, 1955.
- [241] C. Willert. Pivview 2c/3c user manual version 3.1.2. *Göttingen, Germany*.
- [242] S.G. Yiantsios and B.G. Higgins. A mechanism of Marangoni instability in evaporating thin liquid films due to soluble surfactant. *Physics of Fluids (1994-present)*, 22(2):022102, 2010.
- [243] Z. Yin, L. Chang, W. Hu, Q. Li, and H. Wang. Numerical simulations on thermocapillary migrations of nondeformable droplets with large Marangoni numbers. *Physics of Fluids*, 24(9):092101–092101, 2012.
- [244] W.E. Ying and H. Sawistowski. Interfacial and mass transfer characteristics of binary liquid-liquid systems. In *Proceedings of the International Solvent Extraction Conference*, volume 2, pages 840–851, 1971.
- [245] J. Zeng, Y.C. Yortsos, and D. Salin. On the Brinkman correction in unidirectional Hele-Shaw flows. *Physics of Fluids (1994-present)*, 15(12):3829–3836, 2003.
- [246] R.W. Zeren and W.C. Reynolds. Thermal instabilities in two-fluid horizontal layers. *Journal of Fluid Mechanics*, 53(02):305–327, 1972.
- [247] A. Zhang, J. and Oron and R.P. Behringer. Novel pattern forming states for Marangoni convection in volatile binary liquids. *Physics of Fluids*, 23:072102, 2011.
- [248] W.B. Zimmerman and G.M. Homsy. Nonlinear viscous fingering in miscible displacement with anisotropic dispersion. *Physics of Fluids A: Fluid Dynamics (1989-1993)*, 3(8):1859–1872, 1991.

List of Symbols

Acronyms

2D	two-dimensional
3D	three-dimensional
FFT	Fast Fourier Transformation
PIV	particle image velocimetry
PM	paradigmatic model, see Sec. 2.2
RBM	Rayleigh-Bénard-Marangoni
RC	(Marangoni) roll cell; except in Ch. 7 there Rayleigh convection
RO	chaotic relaxation oscillation
ROW	synchronized relaxation oscillation wave

Dimensionless groups

Re	Reynolds number
Sc	Schmidt number
G	Grashof number
Ra	Rayleigh number
Ma	Marangoni number
Pe	Péclet number
Mo	Morton number
Sh	Sherwood number
R	Enhancement factor

Mathematical terms

∇_2	gradient operator in the $x - y$ plane ($\mathbf{e}_x \partial_y + \mathbf{e}_y \partial_x$)
$q^{(i)}$	quantity related to the top ($i=2$) or the bottom layer ($i=1$)
\hat{q}	nondimensional quantity; or expansion coefficient
\tilde{q}	dimensional quantity
$\langle q(x, y, z) \rangle_{xyz}$	mean of field q over its three dimensional domain $\Omega \subset \mathbb{R}^3$, so $q : \Omega \rightarrow \mathbb{R}$. Then it is $\langle q(x, y, z) \rangle_{xyz} = \int_{\Omega} q dV / \int_{\Omega} 1 dV$.
$\langle q(x, y) \rangle_{xy}$	mean of field q over a horizontal slice $A \subset \mathbb{R}^2$ with $q : A \rightarrow \mathbb{R}$. Then it is $\langle q(x, y) \rangle_{xy} = \int_A q dA / \int_A 1 dA$.
$\langle q(x) \rangle_x$	mean of field q over a the interval $L \subset \mathbb{R}$ with $q : L \rightarrow \mathbb{R}$. Then it is $\langle q(x) \rangle_x = \int_L q dx / \int_L 1 dx$.
$\langle q(x, y, z) \rangle_s$	mean of field q at the interface $\langle q(x, y, z = 0) \rangle_{xy}$
$s_{xy}(q)$	standard deviation of field $q(x, y)$ over its domain $A = (0, l_x) \times (0, l_y)$; $s_{xy}(q(x, y)) = \sqrt{\langle [(q(x, y) - \langle q(x, y) \rangle_{xy})^2] \rangle_{xy}}$
$\langle q \rangle_e$	sample mean of quantity q , with samples q_i are $i \in [1, \dots, N]$: $\langle q \rangle_e = \frac{1}{N} \sum_{i=1}^N q_i$
$u_{rms}^{(i)}$	root-mean-squared velocity in layer (i) $u_{rms}^{(i)} = \sqrt{\langle \mathbf{u}^{(i)} \cdot \mathbf{u}^{(i)} \rangle_{xyz}}$
u_{rms}^s	root-mean-squared velocity at the interface) $u_{rms}^s = \sqrt{\langle \mathbf{u}^{(1)}(x, y, z = 0) \cdot \mathbf{u}^{(1)}(x, y, z = 0) \rangle_{xy}}$
u_{rms}	root-mean-squared velocity of both layers $u_{rms} = (u_{rms}^{(1)} + u_{rms}^{(2)})/2$
t_{c1}, t_{c2}, t_{c3}	onset times detected from full nonlinear simulation, definition in Eqs. (3.138)-(3.140)
\mathbf{u}_{of}	optical flow (see Sec. 5.3.5)
$\delta c_I^{(i)}$	concentration boundary layer width see Sec. 3.5
λ_F	wavelength of large convection cells definition in Sec. E
λ_{RC-I}	circular diameter of basic convection cells definition in Eq. (5.20)

Physical quantities

Description	Symbol	Unit
mass density - reference state	$\rho_{ref}^{(i)}$	kg/m ³
kinematic viscosity	$\nu^{(i)}$	m ² /s
partition coefficient (Henry constant)	H	(mol/l) / (mol/l)
diffusivity of solute	$D^{(i)}$	m ² /s
interfacial tension -reference state	σ_{ref}	N/m
change in interfacial tension per <i>mol/l</i> of $c^{(1)}$	$\sigma_{ref}\alpha_c$	N/m/(mol/l)
solubility expansion coefficient	$\beta_c^{(i)}$	l/mol
gravitational acceleration	g	m/s ²
dynamic pressure	$p_d^{(i)}$	N/m ²
concentration field	$c^{(i)}$	mol/l
initial concentration	c_0	mol/l
velocity field	$\mathbf{u}^{(i)}$	m/s
vorticity field	$\boldsymbol{\omega}$	1/s

Note that in the results chapter nondimensional physical quantities (according to Sec.3.1.2) are used without a change in the symbols.

Danksagung

Mein besonderer Dank gilt Dr. Thomas Boeck, welcher in vielerlei Hinsicht zur vorliegenden Arbeit beigetragen hat. Er war es der mir die Marangoni-Konvektion im Rahmen meiner Tätigkeit als wissenschaftlicher Mitarbeiter am Institut für Thermo- und Fluidodynamik der Technischen Universität Ilmenau anvertraute. Weiterhin konnte ich ideal auf den von ihm in mühevoller Arbeit programmierten Zweischicht-Solver aufbauen. Seine stets offene Tür für Diskussionen und sein kritisches Lektorat haben entscheidend zu dieser Arbeit beigetragen, ihm nochmals vielen Dank.

Eine besondere Bereicherung für mich war die Zusammenarbeit mit Karin Schwarzenberger (TU Dresden), welche einerseits mit ihren vielen interessanten experimentellen Beobachtungen diese Arbeit um einiges aufwertete, welche andererseits aber auch stets an den numerischen Ergebnissen interessiert war. Ebenso möchte ich Dr. Kerstin Eckert (TU Dresden) für die vielfältige Unterstützung bei der gemeinsamen Publikation unserer Resultate danken.

Die Bereitstellung von Rechenkapazitäten des Universitätsrechenzentrums der TU Ilmenau machten die zahlreich dokumentierten Resultate erst möglich. Außerordentlicher Dank gebührt daher Henning Schwanbeck, unserem Administrator, dafür dass es in den letzten vier Jahren zu keinem großen Crash kam, wie auch den anderen Nutzern denen ich viel eigenen Festplattenplatz abringen konnte. Auch dem FZ Jülich (NIC) möchte ich für die gewährten Rechenkapazitäten danken.

Weiterhin möchte ich Dr. Dmitry Krasnov danken, dass er mich solange ohne Beschwerden ertragen hat, für die guten Hinweise wenn der Fehlerteufel sich mal eingeschlichen hatte und die parallele I/O Routine. Allen Kollegen am Institut für Thermo- und Fluidodynamik möchte ich für die anregende und freundschaftliche Arbeitsatmosphäre danken. Besonders möchte ich Prof. Christian Karcher danken der mich früh durch die Aufnahme ins Graduiertenkolleg "Lorentzkraft" förderte.

Dank gebührt auch der Deutschen Forschungsgemeinschaft, welche im Rahmen des Schwerpunktprogrammes 1506 mein Auskommen gesichert und meinen Wissenschaftlichenhorizont erweitert hat.

Zum Schluss möchte ich mich bei meinen Eltern für ihre stete Unterstützung bedanken.